

COMPUTATIONAL CHEMISTRY APPLIED TO HYDROCARBON FUNCTIONALIZATION BY IRON CATALYSTS, OXIDATION STATE CHARACTERIZATION, AND ELECTRIDES DESIGN

Verònica Postils Ribó

Per citar o enllaçar aquest document:

Para citar o enlazar este documento:

Use this url to cite or link to this publication:

<http://hdl.handle.net/10803/663420>

ADVERTIMENT. L'accés als continguts d'aquesta tesi doctoral i la seva utilització ha de respectar els drets de la persona autora. Pot ser utilitzada per a consulta o estudi personal, així com en activitats o materials d'investigació i docència en els termes establerts a l'art. 32 del Text Refós de la Llei de Propietat Intel·lectual (RDL 1/1996). Per altres utilitzacions es requereix l'autorització prèvia i expressa de la persona autora. En qualsevol cas, en la utilització dels seus continguts caldrà indicar de forma clara el nom i cognoms de la persona autora i el títol de la tesi doctoral. No s'autoritza la seva reproducció o altres formes d'explotació efectuades amb finalitats de lucre ni la seva comunicació pública des d'un lloc aliè al servei TDX. Tampoc s'autoritza la presentació del seu contingut en una finestra o marc aliè a TDX (framing). Aquesta reserva de drets afecta tant als continguts de la tesi com als seus resums i índexs.

ADVERTENCIA. El acceso a los contenidos de esta tesis doctoral y su utilización debe respetar los derechos de la persona autora. Puede ser utilizada para consulta o estudio personal, así como en actividades o materiales de investigación y docencia en los términos establecidos en el art. 32 del Texto Refundido de la Ley de Propiedad Intelectual (RDL 1/1996). Para otros usos se requiere la autorización previa y expresa de la persona autora. En cualquier caso, en la utilización de sus contenidos se deberá indicar de forma clara el nombre y apellidos de la persona autora y el título de la tesis doctoral. No se autoriza su reproducción u otras formas de explotación efectuadas con fines lucrativos ni su comunicación pública desde un sitio ajeno al servicio TDR. Tampoco se autoriza la presentación de su contenido en una ventana o marco ajeno a TDR (framing). Esta reserva de derechos afecta tanto al contenido de la tesis como a sus resúmenes e índices.

WARNING. Access to the contents of this doctoral thesis and its use must respect the rights of the author. It can be used for reference or private study, as well as research and learning activities or materials in the terms established by the 32nd article of the Spanish Consolidated Copyright Act (RDL 1/1996). Express and previous authorization of the author is required for any other uses. In any case, when using its content, full name of the author and title of the thesis must be clearly indicated. Reproduction or other forms of for profit use or public communication from outside TDX service is not allowed. Presentation of its content in a window or frame external to TDX (framing) is not authorized either. These rights affect both the content of the thesis and its abstracts and indexes.



Doctoral Thesis:

**Computational Chemistry Applied to Hydrocarbon
Functionalization by Iron Catalysts, Oxidation State
Characterization, and Electrides Design**

Verònica Postils Ribó

2018

Doctoral Programme in Chemistry

Supervised by: Dr. Josep Maria Luis Luis and Prof. Miquel Solà Puig
Tutor: Dr. Josep Maria Luis Luis

Presented in partial fulfillment of the requirements for a doctoral degree from
the University of Girona



Dr. Josep Maria Luis Luis and Prof. Dr. Miquel Solà i Puig, from Universitat de Girona,

WE DECLARE:

That the thesis entitled "Computational Chemistry Applied to Hydrocarbon Functionalization by Iron Catalysts, Oxidation State Characterization, and Electrides Design", presented by Verònica Postils Ribó to obtain a doctoral degree, has been completed under our supervision and meets the requirements to opt for an International Doctorate.

For all intents and purposes, we hereby sign this document.

Signature

Dr. Josep Maria Luis Luis

Prof. Dr. Miquel Solà Puig

Girona, April 9, 2018

Déjame que recuerde esta historia que pasó hace ya mucho tiempo.

Déjame que les quite esta losa que tapó con su peso de silencio.

Déjame que las riegue de lágrimas para borrarles el miedo.

Déjame que las riegue de rabia por imaginar aquello.

Déjame que en estas líneas escritas regrese a los maestros,
que dieron su vida y su sangre por dar al pueblo conocimiento.

De nada sirvieron sus gritos de angustia antes del fusilamiento.

Iglesia y caciques, misas y estado los prefieren analfabetos.

Con ellos pelagra el tiempo que ocupan el crucifijo y la moral del clero.

Por eso estas líneas desordenadas van en dirección de su recuerdo.

Déjame que recuerde esta historia que pasó hace ya mucho tiempo.

Lo que entierran no son huesos, son las semillas que van creciendo.

Lo que entierran no son huesos, son las semillas que van creciendo.

*Los maestros, **Barricada.** (La tierra esta sorda)*

A tots els meus mestres de vida,

Acknowledgments

Aquesta tesi ha estat possible gràcies al finançament que he rebut amb la beca FPI (*Formación Personal Investigador*) amb referència BES-2012-052801 del *Ministerio de Economía y Competitividad* del *Gobierno de España*. Així, vull donar les gràcies a l'investigador principal del projecte CTQ2011-23156 que tenia aquesta beca associada, el Prof. Dr. Miquel Solà i Puig, per haver-me escollit en el seu moment, i al Dr. Josep Maria Luis i Luis per haver-me fet confinaça des d'uns inicis. Paral·lelament, els treballs que es presenten en aquesta tesi també s'han beneficiat d'altres fonts de finançament com els projectes CTQ2011-23156, CTQ2014-59212-P i CTQ2014-52525-P del MINECO, els projectes 2014SGR1202 i 2014SGR931 de la Generalitat de Catalunya, o el premi ICREA Academia 2014. Moltes gràcies a tots els organismes mencionats per la seva ajuda econòmica.

A part dels temes econòmics, m'agradaria seguir agraïnt especialment els meus directors de tesi, en Josep Maria Luis i en Miquel Solà. Estic molt contenta d'haver pogut treballar amb vosaltres aquests quatre anys. Agraïxo molt tot el què m'heu ensenyat, tant científicament, que és moltíssim, com personalment i de gestió de problemes. Sempre heu procurat que no em faltés de res; que pogués tenir algun contracte abans i després de la beca FPI, que pogués anar a congressos, que tingués un bon lloc de treball amb bones condicions i amb un bon ordinador (encara que sigui un Mac), que marxés dues vegades d'estada predoctoral, i podria seguir. De debò que estic encantada d'haver-vos tingut de pares científics.

A causa dels diferents projectes de tesi he pogut treballar amb moltes altres persones a part dels meus supervisors. En aquest sentit vull agrair molt especialment a en Pedro i a l'Edu per la paciència. Potser serà per la confiança, però no tinc cap dubte que tots dos heu patit la versió més pesada d'una Verònica quasi obsessiva amb algun aspecte del projecte. A tots dos us tinc una gran admiració i m'ha encantat poder aprendre de vosaltres i de les estones de converses que hem compartit. M'agradaria molt que es poguéssin tornar a repetir. Pel què fa als col·laboradors experimentals, vull agrair principalment a en Miquel Costas i a l'Anna Company (i en segona ronda a en Perdo Pérez i el seu grup de Huelva) per la confiança que sempre heu dipositat amb en Josep Maria i amb mi. El vostre Pitacín ja és part de la família i li tinc especial carinyo, encara que tingui un ferro! De les meves estades predoctorals, vull començar agraïnt els meus hosts, l'Odile i en Sam. Thank you Odile for all your kindness when I was in Montpellier, for everything you teach me with your energy, passion and criticism. It was a pleasure to spend these months with you, with a pioneer. Now, we still have

to publish the article... hehe, but I hope we can do soon! ;-) Truly, I was really lucky with my reasearch-stay hosts because Sam was also an excellent host. He was kind and comprehensive, because during my days in Manchester I was really stuck in Girona's projects. Thank you for everything Sam, for your comprehension and patience, and for your perseverance to wrap up the projects.

Pensant en com seguir aquests agraïments sento que no puc fer-ho de cap més manera que agraïnt tots els amics i companys del Parc per les hores de feina, dinars i aventures compartides. I clar, ja sóc gat vell i la llista és tan llarga que m'omple moltíssim recordar-vos a tots i no sé per on començar. Sílvia i Ferran, sou com uns germans grans, els companys incombustibles que hi heu estat des d'un principi i encara hi sou, tant per la recerca com per les aventures. No m'imagino l'IQC(C) sense vosaltres i m'alegro molt que durant aquests anys l'IQCC hagi estat AMB vosaltres. L'excursió a la neu, el casament de la Sílvia, sopars, sortides, congressos, assaigs per congressos, l'octubre passat, poder-vos venir a dir qualsevol cosa al despatx, etc. Trobaré a faltar molt aquests moments amb vosaltres perquè s'hi està molt bé aquí a Girona quan hi sou. Pero tampoc es queda curta altra gent que ja no hi és i que han fet de l'IQC un lloc ideal per fer la tesi. En Marc i la seva força; l'Eloy que les mata callant; l'Abril!!! mi compañerita de despacho que la trobo molt a faltar; l'incombustible Ouissam sempre disposat a ajudar-te; en Lorenzo i la seva alegria i els seus mil temes de conversa; en Pedrator perquè vull que torni a sortir també en la secció "aventures del dia a dia"; altres persones dels meus inicis com la Cristina Buchosa, l'Anna Díaz, en Yevhen, la Laia, en Sergi!! Que avui s'acaba de passar pel despatx i que m'alegra molt que ens vagi visitant de tant en tant!! O noves incorporacions com l'Adrià (no tant noves... ;-), en Miguel Àngel, l'Eila, en Christian, el Steven, en Miquel, en Javi, en Guillem, la Carla, etc. Gracies a tots per fer del Parc la pinya que som. Estic segura que vosaltres, com jo, guardareu especial estima a les persones amb qui heu compartit una cosa tan especial com és la tesi i amb aquest bon ambient.

Però la cosa no s'acaba aquí!! També hi ha altres persones que han estat claus perquè tot això funcioni, que les tinc molt presents, i a qui voldria agrair. Són o han estat més que l'engranatge perquè es pugui treballar. En Dani, la Carme i en Quim Antolin. Perquè m'heu donat molt més que la solució a un problema amb el beta, un registre a un congrés, o un mail informatiu de resposta. Moltes gràcies per la generositat, per fer dels nostres problemes els vostres problemes i per cuidar-nos més enllà de lo estrictament professional.

Fora de l'IQCC, però encara dins del món de la ciència, també m'agradaria mencionar a la Gudrun, en Nicola, la Yimei, en Marc Font i la Laia, en Fabian, i en Yomi, per haver-me fet les estades doctorals molt més divertides i alegres. Thank you! Al grup de Donostia, per haver-me permès treballar des dels seus despatxos durant les meves estades allà. Y a Xabi, Verena, Eli y Nacho per todos los ratos compartidos! La verdad es que me hacéis sentir como en casa! Tampoc em vull oblidar de la gent del màster. D'en Manel i les nostres converses via xat de gmail. M'alegro molt que seguim cuidant la nostra amistat. Del guerrer Mauricio, que porta ja uns anys entrenant a terres basques; i dels dos tresors que em vaig trobar fent al màster com són la Claudia i la Feñi. Noies, heu estat un su-

port increïble durant tota la tesi i encara molt més aquests últims mesos d'estrés màxim. Els nostres caps de setmana d'estiu eren reparadors i tinc moltíssimes ganes de que ens poguem retrobar. Com ja us he dit sou un tresor d'amigues i valeu un imperi!! Muaaks!!

També voldria agrair a tota la “colla del poble”, que és com ja us coneixen per aquí a Girona, farts de que us parli de vosaltres. És reconfortant que, després de tants anys, continuem cultivant les nostres quedades al bar, de turisme rural, sopars amb o sense futbol, excursions de mitja tarda, raquetes, etc. M'alegro moltíssim de poder venir a Casserres i saber que sempre hi haurà algú amb ganes de fer coses i de desconnectar de la feina! Lluís Costa, Pep Costa, Trumfet, Anna Ribera, Niku, Turri, Alba, Núria, Roko, Kanu, Laura, Isa, Ribe, Mauri... Moltíssimes gràcies per ser-hi i sempre estar disposats a escoltar-me! Ja sabeu que heu d'avisar quan vingueu per Girona i ara per Donostia!! També vull agrair molt especialment a l'Anna i l'Eva que quan vaig començar la tesi vàrem viure les tres moments complicats i des de llavors sempre, sempre hi han estat. Em sap greu que visquem cada una a puntes diferents de Catalunya i que costi tant quedar, per us tinc una estima grandíssima i no us vull fallar mai, com mai ho heu fet vosaltres.

Finalment vull agrair a la meva família. El meu pare, la meva mare, la meva àvia, la meva padrina, les meves tietes i en Joan. Moltes gràcies per cuidar de mi, per educar-me en la llibertat i la tolerància, permetent que m'equivoqui, i per la confiança que em mostreu sempre. I com no, per acabar, falta una de les persones més importants, l'Edu! Ets una de les millors coses que m'ha passat durant la tesi. T'he d'agrair infinit per aguantar-me, estimar-me, acceptar-me i complementar-me. Crec que quan estic amb tu sóc millor persona i ja saps que ets a qui m'emportaria al cul del món. T'ha tocat, ho sento... Us estimo molt a tots!!

Full list of publications

This thesis is presented as a compendium of publications.

Published and submitted articles included in the thesis:

1. Postils, V.; Company, A.; Solà, M.; Costas, M.; Luis, J.M. **Computational Insight into the Mechanism of Alkane Hydroxylation by Non-Heme Fe(PyTACN) Iron Complexes. Effects of the Substrate and Solvent.** *Inorg. Chem.* **2015**, 54, 8223-8236.
DOI: 10.1021/acs.inorgchem.5b00583. (JCR Impact Factor= 4.71; SJR position 3/66 in chemistry(inorganic), 1st quartile)
2. Postils, V.; Garcia-Borràs, M.; Solà, M.; Luis, J.M.; Matito, E. **On the existence and characterization of molecular electrides.** *Chem. Commun.* **2015**, 51, 4865-4868. DOI: 10.1039/c5cc00215j.
(JCR Impact Factor= 6.10; SJR position 16/415 in chemistry(multidisciplinary), 1st quartile)
3. Postils, V.; Rodríguez, M.; Sabenya, G.; Conde, A.; Díaz-Requejo, M.M.; Pérez, P.J.; Costas, M.; Solà, M.; Luis, J.M. **The Mechanism of the Selective Fe-Catalyzed Arene Carbon-Hydrogen Bond Functionalization,** *ACS Catal.* Just Accepted Manuscript.
DOI: 10.1021/acscatal.7b03935. (JCR Impact Factor= 10.30; SJR position 3/46 in chemical engineering(catalysis), 1st quartile)
4. Postils, V.; Delgado-Alonso, C.; Luis, J.M.; Salvador, P. **Reaching the new IUPAC definition of oxidation state by computational techniques,** submitted to *Angew. Chem. Int. Ed.*
(JCR Impact Factor= 11.18; SJR position 9/415 in chemistry(multidisciplinary), 1st quartile)

Other published articles not included in the thesis:

5. Prat, I.; Company, A.; Postils, V.; Ribas, X.; Que, L.; Luis, J.M.; Costas, M. **The Mechanism of Stereospecific C-H Oxidation by Fe(PyTANC) Complexes. Bioinspired Non Heme Iron Catalysts Containing cis-Labile Exchangeable Sites.** *Chem. Eur. J.* **2013**, 19, 6724-6738.
(JCR Impact Factor= 4.99; SJR position 17/415 in chemistry(multidisciplinary), 1st quartile)

FULL LIST OF PUBLICATIONS

6. Ramos-Cordoba, E.; Postils, V.; Salvador, P. **Oxidation States from Wave Function Analysis.** *J. Chem. Theory Comput.* **2015**, 11, 1501-1508. (JCR Impact Factor= 5.05; SJR position 5/149 in chemistry(physical and theoretical), 1st quartile)
7. Conde, A.; Sabenya, G.; Rodríguez, M.; Postils, V.; Luis, J.M.; Díaz-Requejo, M.M.; Costas, M.; Pérez, P.J. **Iron and Manganese Catalysts for the Selective Functionalization of Arene C(sp²)-H Bonds by Carbene Insertion.** *Angew. Chem. Int. Ed.* **2016**, 128, 6640-6644. (JCR Impact Factor= 11.18; SJR position 9/415 in chemistry(multidisciplinary), 1st quartile)
8. Li, X.X.; Postils, V.; Sun, W.; Faponle, A.S.; Solá, M.; Wang, Y.; Nam, W.; de Visser, S.P. **Reactivity patterns of (Protonated) Compound II and Compound I of Cytochrome P450: Which is the Better Oxidant?** *Chem. Eur. J.* **2017**, 23, 6406-6418. (JCR Impact Factor= 4.99; SJR position 17/415 in chemistry(multidisciplinary), 1st quartile)

Outreach publications:

9. Postils, V. **Electrurs. Compostos per al món del demà.** *Rev. Soc. Cat. Quim.* **2015**, 14, 83-90.

List of Abbreviations

Abbreviation	Description
AHP	Alkane Hydroxylation Process
ARPES	Angle-Resolved Photoemission Spectroscopy
BDE	Bond Dissociation Energy
BVS	Bond Valence Sum
CDA	Charge-Density Analysis
DFT	Density Functional Theory
EER	Exchange Enhance Reactivity
eff-AOS	effective-Atomic Orbitals
ELF	Electron Localization Function
EN	Electronegativity
EOS	Effective Oxidation State
EPR	Electron Paramagnetic Resonance
ESP	Electrostatic Potential
EXAFS	Extended X-ray Absorption Fine Structure
HAT	Hydrogen Atom Transfer
HAXPES	Hard X-ray Photoelectron Spectroscopy
HPE	High Pressure Electride
IA	Ionic Approximation
IRC	Intrinsic Reaction Coordinate
KIE	Kinetic Isotopic Effect
LA-LB	Lewis Acid - Lewis Base
MMO	Methane Monooxygenase
MO	Molecular Orbital
MO-LCAO	Molecular Orbital by Linear Combination of Atomic Orbitals
NCIs	Non-Covalent Interactions
NHC	N-heterocyclic Carbene
NNA	Non-Nuclear Attractor
NLOP	NonLinear Optical Properties
OS	Oxidation State
PyTACN	1-(2-pyridylmethyl)-4,7-dimethyl-1,4,7-triazacyclononane
QTAIM	Quantum Theory of Atoms In Molecules
SQUID	Superconducting Quantum Interference Devices
TSR	Two State Reactivity
XRD	X-Ray Diffraction

List of Figures

1.1	Composition of crude oil.	13
1.2	Basic petroleum refining operations.	13
1.3	Evolving algorithms in organic synthesis.	14
1.4	Selected C-H bond activation and functionalization reactions.	15
1.5	First oxidation reactions of n-alkanes by cobalt(III) salts.	16
1.6	Selected C=C bond activation and functionalization reactions.	17
1.7	Elements' abundance and availability.	18
1.8	Chronological timeline for some of the most important achievements in hydrocarbons' activation and functionalization processes in the 20th century.	19
1.9	Types of metal-mediated C-H bond functionalization mechanisms.	20
1.10	Examples of C(sp ³)-H bond functionalization by "true" organometallic activation of the C-H bond.	22
1.11	The catalytic cycle of cytochrome P450.	23
1.12	Nonheme oxygenases enzymes.	24
1.13	Porphyrin-based ligands.	25
1.14	Oxoiron(IV) complexes supported by cyclam and related ligands.	26
1.15	Examples of <i>S</i> =1 oxoiron(IV) complexes supported by pentadentate ligands.	27
1.16	Examples of oxoiron(IV) complexes supported by tetradentate ligands.	27
1.17	Examples of oxoiron(V) complexes.	29
1.18	General representation of the TSR scenario of the HAA reaction by Fe ^{IV} (O) complexes.	30
1.19	Electron shifts diagrams for all the viable pathways of the C-H abstraction reaction by Fe ^{IV} oxo complexes.	31
1.20	Electron shift diagrams and Gibbs energy profile (kcal/mol) of the HAA reaction by an Fe ^V oxo complex.	32
1.21	Mechanisms of the C-H bond functionalization by metal carbene catalysts.	33
1.22	First examples of catalytic intermolecular functionalization reactions by carbene insertion using diazo compounds as the carbene source.	34
1.23	Rhodium acetate, (Rh ₂ (OAc) ₄ , and other examples of Rh ₂ (L) ₄ catalysts for the C-H bond functionalization by carbene insertion.	34
1.24	Examples of regioselective, chemoselective, and intramolecular reactions by dirhodium(II) carbene catalysts.	35

LIST OF FIGURES

1.25	Examples of enantioselective and diastereoselective intramolecular reactions by dirhodium(II) carbene catalysts.	36
1.26	Structures of trispyrazolylborane and trispyrazolylmethane complexes.	36
1.27	Classification of different groups of diazo compounds and an overview of their properties.	37
1.28	Examples of chemoselectivity in intermolecular carbene insertion reactions.	38
1.29	Structures of some NHC ligands used by Prof. Pérez group in carbene-transfer reactions and examples of the reactivity of the corresponding catalysts.	39
1.30	Fe and Mn catalysts with a complete chemoselective carbene insertion reactivity.	39
1.31	Redox noninnocent behavior of carbene ligands in an initial $M^{II}(\text{por})$ catalyst.	40
1.32	Classic carbene insertion mechanisms of alkyl and aromatic substrates.	41
1.33	Approaches to determine the OS by using the IA.	44
1.34	Schematic representations of the dominant orbital interactions to carbene formation, and the carbene double-bond decomposition to OS assignment in Fischer-type carbene complexes and Schrock-type carbene complexes.	46
1.35	<i>1H</i> -pentazole, HN_5 . Calculated bond lengths (in Å), and OS assignment in the two limiting Lewis formulas: aromatic and localized.	47
1.36	LOBA plots for the ClMnO_2MnO core of complexes.	52
1.37	Crystal structure of C12A7.	57
2.1	The hierarchy of DFT approximations represented by Jacob's ladder.	67
2.2	Schematic representation of how to obtain the energy terms of the classical Marcus formalism.	75
2.3	Electron distribution analyses of the SO_2 molecule.	81
7.1	Postulated reaction mechanisms for alkane hydroxylation processes.	149
7.2	Gibbs energy profile (in kcal/mol) of the alkane hydroxylation process for the different analyzed substrates by 21.	151
7.3	Gibbs energy profiles (in kcal/mol) of the alkane hydroxylation process for cyclohexane at solvent phase, and at gas phase including single-point dispersion and solvent corrections.	153
7.4	Gibbs energy profiles, ΔG , (kcal/mol) of the metal-carbene bond formation.	155
7.5	Studied pathways for the formation of insertion and addition products.	156
7.6	Comparative Gibbs energy profile, ΔG , (kcal/mol) of the formation of addition (VI) and insertion (V) products from II	157
7.7	Examples of three types of sulfur bonding in SO_2 ligands.	160
7.8	Above, schematic representation of the dominant orbital interactions in Fischer-type and Schrock-type carbene complexes. Below, their respective methods of deconstruction are schematically represented.	161

LIST OF FIGURES

7.9 QTAIM topological analysis, $\nabla^2\rho=-0.001$, and ELF=0.75 representations of TCNQLi₂. 164

List of Tables

1.1	Structural Data for all the Crystalline Electrides synthesized up to date.	59
7.1	Relative Gibbs Energies (ΔG_{solv} , in kcal/mol) for radical and cation iron-bishydroxo intermediates.	149
7.2	Relative Gibbs Energies at gas-phase (ΔG_g) and at gas-phase including single-point dispersion and acetonitrile solvent corrections (ΔG_{g+corr}) (kcal/mol) for radical and cation iron-bishydroxo catalyst intermediates.	152
7.3	Summary of the agreement between the OSs predicted by EOS analyses and the ones reported in Karen's reports or prior literature.	162
7.4	Summary of the criteria used to characterize electrides.	164

Contents

Abstract	1
Resum	3
Resumen	7
1 Introduction	13
1.1 Functionalization of Hydrocarbons	13
1.1.1 Historical survey	14
1.2 Activation and functionalization of C-H bonds	20
1.2.1 Oxidation by Metal Oxo Complexes of C(sp ³)-H bonds	20
1.2.2 Aromatic C(sp ²)-H bond Functionalization by Metal Carbene Complexes	33
1.3 Oxidation States	42
1.3.1 The oxidation state concept	42
1.3.2 Computational determination of OSs	48
1.4 Electron Distribution in Chemical Systems	55
1.4.1 Electron Distribution Analysis by Electron Partitioning Schemes	55
1.4.2 A particular case of electron localization: isolated electrons in electrides	56
2 Methodology and Computational Chemistry Tools	63
2.1 Theoretical framework	64
2.1.1 Density Functional Theory	65
2.1.2 Deficiencies of DFT	67
2.1.3 Which functional should I use?	69
2.2 Good computational practices for chemical reactivity studies	72
2.3 Tools for electron distribution analyses	78
2.3.1 Molecular-space partitions	78
2.3.2 Hilbert-space partitions	85
2.3.3 Effective Oxidation States Analysis	87
3 Objectives	91
4 Functionalization of C-H bonds of hydrocarbons by iron catalysts	93
4.1 Computational Insight into the Mechanism of Alkane Hydroxylation by Non-Heme Fe(PyTACN) Iron Complexes. Effects of the Substrate and Solvent	95

CONTENTS

4.2	The Mechanism of the Selective Fe-Catalyzed Arene Carbon-Hydrogen Bond Functionalization	111
5	Computational determination of OSs	125
5.1	Reaching the new IUPAC definition of oxidation state by computational techniques	127
6	Theoretical characterization of molecular electrides	139
6.1	On the existence and characterization of molecular electrides . . .	141
7	Results and Discussion	147
7.1	Functionalization of C-H bonds of hydrocarbons by iron catalysts .	148
7.1.1	Effects of the substrate and solvent in the alkane hydroxylation mechanism. The nonheme [(PyTACN)Fe ^V] ²⁺ complex case study.	148
7.1.2	Elucidating the reaction mechanism of the chemoselective carbene-insertion reaction into C-H bonds by iron-carbene catalysts.	154
7.2	Theoretical characterization of the oxidation state property by effective oxidation state (EOS) analysis	158
7.3	Electron distribution in molecular electrides	163
8	Conclusions	167
9	Bibliography	171
Annex		186
	Supporting Information Section 4.1	187
	Supporting Information Section 4.2	209
	Supporting Information Section 5	231
	Supporting Information Section 6	261

Abstract

According to F. Jensen quote:

“Chemistry is the science dealing with construction, transformation and properties of molecules.”

Introduction to Computational Chemistry, Second Edition. Frank Jensen. Page 1.

In this thesis, the three constituent parts of chemistry (in agreement with Jensen’s quotation) are addressed by means of theoretical and computational tools. In this sense, only the global knowledge given by the three different aspects of chemistry provides an enough detailed picture for the absolute understanding of any chemical system. It is necessary to know the molecular construction (atomic and electronic) to rationalize molecular properties, and, in turn, molecular properties govern the reactivity and molecular transformations. This thesis encompasses different computational studies that together cover all the three parts of chemical science. For each part, we have selected a different research project, whose major feature is related with construction, transformation or properties of the chemical systems. The different research projects have been chosen taking into account their general chemical interest and the insights that computational chemistry can provide to the up-to-date knowledge of the topic. In that way, the study of the C-H bond functionalization of non-activated hydrocarbons by iron catalysts has been chosen as the research project for the molecular transformations section; the oxidation state is the property we focus on; and, regarding molecular construction, we describe the electronic structure of molecular electrides.

Achieving direct and selective C-H bond functionalizations of non-activated hydrocarbons by organometallic catalysts is still a challenging work in synthetic chemistry. Nowadays it constitutes the main drawback to overcome in order to achieve efficient strategies in organic synthesis or to use alkanes as direct precursors for more important chemicals for the industry. Thus, currently, this research topic is focus of much activity and there is still plenty of room for development. The use of iron catalysts in such reactions has a special interest in the sense that iron is an economic, environmental friendly, and nontoxic metal. The main role of computational chemistry in this field falls to the determination of the reaction mechanisms. In this thesis two C-H bond functionalization processes that share complementary interest are studied (**Chapter 4**). The first one is the hydroxylation of alkanes by a nonheme $\text{Fe}^{\text{V}}=\text{O}$ catalyst. Although this reaction has been widely studied computationally, the different studies report several reaction mechanisms that differ among them, the origin of their variability was not completely understood. Therefore, we investigate the effects of the substrate

ABSTRACT

and solvent in these processes in order to try to rationalize the differences on the reaction mechanisms reported in literature. The different stability at gas and in solvent phase of the reaction intermediate is revealed as the key reason for the existence of different reaction mechanisms. The second studied process is the functionalization of C-H bonds of non-activated arenes by carbene-insertion reactions. Unlike hydroxylation reactions, this process has not been widely studied. Specifically, a chemoselective carbene-insertion reaction into benzene by an iron-carbene catalyst was reported in 2016 by the experimental groups of Dr. Miquel Costas and Prof. Pedro J. Pérez for the first time (*Angew. Chemie Int. Ed.* 2016, **55**, 6530-6534). In this sense, in the fourth chapter of this thesis we elucidate the reaction mechanism of this unprecedented reactivity and we also identify the features and reasons that favor this reactivity over other possible reactions such as the carbene addition into benzene.

The oxidation state (OS) concept has utmost relevance in chemistry. In reaction mechanisms of organometallic catalysis, for example, it is an intrinsic descriptor and the fingerprint of the chemical reaction is not complete until the determination of the OSs of all the involved species. The OS concept is also an important concept in chemical nomenclature, or, in spectroscopic characterizations, where it is related to *d*-electron configurations of TM. The role of computational chemistry in determining the OSs from first principles has been little explored. However, the group of Dr. Pedro Salvador recently presented a new computational tool for the determination of OS, the so-called Effective Oxidation State (EOS) method (*J. Chem. Theory Comput.* 2015, **11**, 1501-1508). In **chapter 5**, we present a benchmarking study about the applicability of the EOS method to determine OSs. Moreover, new key insights about the OS property based on data of the benchmarking study are provided.

Electrides are a relatively new class of ionic compounds with an intriguing electronic structure: isolated electrons act as the stoichiometric anionic part of the crystal. This interesting feature, however, hinders the classical assignation of oxidation states in such compounds, for example. Despite just thirteen solid electrides have been synthesized up to date (only six stable at room temperature), their interesting properties have led to the development of a plethora of amazing applications for those compounds. Thus, electrides are, without doubt, one of the promising research fields for the development of new materials which still has many room for development. Computational chemistry has always had an important role in the development of electrides and in the understanding of their electronic structure. In **chapter 6** we present the first computational study about the existence of electrides beyond the solid state. Despite many theoretical works have been addressed to the study of the electron confinement of electrides in the solid lattice, no other work before focused on the characterization of electrides in the gas phase. Herein, we investigate whether the electronic structure of molecular electrides truly contain isolated electrons or if it is actually just a formal picture to represent these molecules. Furthermore, we provide an unambiguous criterion to distinguish molecular electrides from other similar species.

Overall, this thesis is divided into eight chapters. The first one is an introduction where the reasons of the chemical interest of the different topics selected

ABSTRACT

in this thesis are exposed. Furthermore, the first chapter also summarizes the contributions that the quantum chemist community has provided to these topics up to date. Chapter 2 presents the theoretical methods, tools, and the different computational chemistry strategies used in the thesis to carry out the studies or to properly analyze the results. Chapter 3 lists the aims of the thesis. Chapters 4, 5, and 6 include the abovementioned publications presented in this thesis. Chapter 7 presents the discussion of the reported results and, finally, in chapter 8 the main conclusions drawn from this thesis are summarized.

Resum

Segons F. Jensen:

“La química és la ciència que tracta la construcció, la transformació i les propietats de les molècules.”

traduït de, *Introduction to Computational Chemistry*, Second Edition. Frank Jensen. Pàg. 1.

En aquesta tesi s’han tractat les tres parts constituents de la química (segons la cita de F. Jensen) mitjançant eines teòriques i computacionals. En aquest sentit, únicament un coneixement global de les tres parts assegura una visió suficientment detallada com per garantir l’absoluta comprensió de qualsevol sistema químic. És necessari conèixer la construcció molecular (atòmica i electrònica) per racionalitzar les propietats moleculars i, al mateix temps, les propietats moleculars governen la reactivitat i les transformacions moleculars. Aquesta tesi engloba diferents estudis computacionals que, conjuntament, cobreixen les tres parts constituents de la química mencionades. Per cada part constituent de la química hem seleccionat diferents projecte de recerca, la principal característica dels quals està relacionada amb la construcció, transformació o propietats dels sistemes químics. Els diferents projectes de recerca han estat seleccionats tenint en compte el seu interès químic i els coneixements que la química computacional pot aportar al camp considerant el coneixement actual existent en cada cas. D’aquesta manera, l’estudi de la funcionalització d’hidrocarburs no activats mitjançant catalitzadors de ferro s’ha escollit com a projecte d’investigació per a la secció de reactivitat; l’estat d’oxidació és la propietat en la qual ens centrarem; i, pel que fa referència a la construcció molecular, s’ha estudiat l’estructura electrònica dels electrurs moleculars.

Aconseguir una funcionalització directa i selectiva d’enllaços C-H d’hidrocarburs no activats mitjançant catalitzadors organometàl·lics constitueix encara una feina complexa en l’àmbit de la química sintètica. A dia d’avui aquest és l’obstacle principal a superar per aconseguir estratègies més eficients per a la síntesi orgànica o per poder utilitzar alcans simples com a precursors directes d’altres compostos químics més importants per a la indústria. Així, aquest tema d’investigació constitueix un centre d’interès que concentra molta activitat científica i on encara hi ha espai pel desenvolupament. La utilització de catalitzadors de ferro en aquest tipus de reaccions té un interès especial ja que el ferro és un metall econòmic, respectuós amb el medi ambient i no tòxic. El paper principal de la química computacional en aquest camp recau en la determinació dels mecanismes de reacció. En aquesta tesi s’estudien dos processos de funcionalització d’enllaços

C-H que tenen interessos complementaris (**Capítol 4**). El primer és la hidroxilació d'alcans mitjançant catalitzador no-hemo $\text{Fe}^V=\text{O}$. Tot i que aquesta reacció ha estat àmpliament estudiada computacionalment, els diferents estudis presenten diversos mecanismes de reacció diferents, l'origen de la variabilitat dels quals no era clar. Així, hem investigat els efectes del substrat i el solvent en aquests processos per tal d'intentar determinar les diferències en els mecanismes de reacció recollits en la literatura. S'ha observat que la diferent estabilitat en fase gas i en solvent d'un intermedi de la reacció és el motiu principal de l'existència de la variabilitat de mecanismes. El segon procés estudiat és la funcionalització d'enllaços C-H d'arens no activats mitjançant la inserció de carbens. A diferència de les reaccions d'hidroxilació, aquest procés no ha estat àmpliament estudiat. Concretament, la reacció d'inserció quimioselectiva de carbens en benzè mitjançant un catalitzador de ferro es va publicar per primera vegada l'any 2016 pels grups experimentals del Dr. Miquel Costas i el Prof. Pedro J. Pérez (*Angew. Chemie Int. Ed.* 2016, **55**, 6530-6534). En aquest sentit, en el capítol 4 de la tesi s'elucida per primera vegada el mecanisme d'aquesta reacció i també s'identifiquen les característiques i motius que afavoreixen aquesta reactivitat sobre altres possibles reaccions com serien l'adició del carbè en el benzè.

El concepte d'estat d'oxidació (EO) té una importància primordial en la química. En els mecanismes de reacció de catàlisi organometàlica, per exemple, l'estat d'oxidació és un descriptor intrínsec i la descripció de la reacció química no és completa fins que no s'han determinat els estats d'oxidació de les espècies involucrades. El concepte d'EO també és important en la nomenclatura química, o en processos de caracterització espectroscòpica, on es relaciona amb la configuració dels electrons *d* del metall de transició. El paper de la química computacional en la determinació d'EOs a partir de principis fonamentals no ha estat gaire explorat. No obstant, el grup del Dr. Pedro Salvador recentment va presentar una nova eina computacional per la determinació d'EOs, l'anomenat mètode dels estats d'oxidació efectius (EOS, per les seves sigles en anglès, *effective oxidation states*) (*J. Chem. Theory Comput.* 2015, **11**, 1501-1508). En el **capítol 5** presentem un anàlisi comparatiu sobre l'aplicabilitat del mètode EOS en la determinació d'EOs. A més a més, també es presenten nous importants descobriments sobre aquesta propietat basats en els resultats obtinguts en l'estudi.

Els electrurs són un tipus de compostos iònics relativament nous amb una estructura electrònica fascinant: electrons aïllats actuen de manera estequiomètrica com la part aniónica del cristall. Aquesta interessant característica, no obstant, obstaculitza l'assignació dels EOs de manera clàssica en aquests compostos, per exemple. Tot i que fins a dia d'avui únicament s'han sintetitzat tretze electrurs sòlids (només sis dels quals estables a temperatura ambient), les seves interessants propietats han comportat que es puguessin desenvolupar un gran nombre d'aplicacions sorprenents per aquests compostos. Així, els electrurs constitueixen, sens dubte, un dels camps de recerca més prometedors en el desenvolupament de nous materials, on encara hi ha molt camp per recórrer. La química computacional sempre ha tingut un paper important en el desenvolupament de nous electrurs i en la comprensió de la seva estructura electrònica. En el **capítol 6** presentem el primer estudi computacional sobre l'existència d'electrurs més enllà de l'estat sòlid. Tot i l'existència d'un gran nombre de treballs teòrics enfocats

RESUM

en l'estudi del confinament dels electrons dels electrurs en l'entramat sòlid, cap altre treball abans s'havia centrat en la caracterització d'electrurs en fase gas. En aquesta tesi investiguem si l'estructura electrònica d'electrurs molecular realment conté electrons aïllats o si això és simplement un model formal per representar aquestes molècules. A part, també es presenta un criteri clar per diferenciar electrurs moleculars d'altres espècies similars.

Globalment aquesta tesi es divideix en vuit capítols. El primer és una introducció on s'exposen els motius de l'interès químic dels projectes d'investigació seleccionats. A més, el primer capítol també resumeix les contribucions que la química teòrica ha aportat als corresponents temes d'investigació fins a dia d'avui. El capítol 2 presenta els mètodes teòrics, eines i les diferents estratègies computacionals que s'han fet servir en aquesta tesi per portar a terme els estudis o per analitzar els resultats adequadament. El capítol 3 llista els objectius de la tesi. Els capítols 4, 5 i 6 inclouen les publicacions, mencionades en els paràgrafs previs, que es presenten en aquesta tesi. El capítol 7 presenta la discussió dels resultats i, finalment, en el capítol 8 es resumeixen les principals conclusions que es deriven de la tesi.

Resumen

Según F. Jensen:

“La química es la ciencia que trata la construcción, la transformación y las propiedades de las moléculas.”

traducido de, *Introduction to Computational Chemistry*, Second Edition. Frank Jensen. Pág. 1.

En esta tesis se han abordado las tres partes constituyentes de la química (según la cita de F. Jensen) mediante herramientas teóricas y computacionales. En este sentido, únicamente un conocimiento global de las tres partes de la química asegura una visión suficientemente detallada como para garantizar una comprensión total de cualquier sistema químico. Se necesita conocer la construcción molecular (atómica y electrónica) para racionalizar las propiedades moleculares y, al mismo tiempo, las propiedades moleculares gobiernan la reactividad y las transformaciones moleculares. Esta tesis engloba distintos estudios computacionales que, conjuntamente, cubren las tres partes constituyentes de la química anteriormente mencionadas. Se han seleccionado diferentes proyectos de investigación, cuya principal característica está relacionada con la construcción, transformación o propiedades de las moléculas. Los distintos proyectos de investigación han sido seleccionados considerando su interés químico y los conocimientos que la química computacional puede aportar al campo considerando el conocimiento actual existente en cada campo. De esta manera, el estudio de la funcionalización de hidrocarburos no activados mediante catalizadores de hierro se ha escogido como proyecto de investigación para la sección de reactividad; el estado de oxidación es la propiedad en la cual nos hemos centrado; y, referente a la construcción molecular, se ha estudiado la estructura electrónica de los electruros moleculares.

Conseguir una funcionalización directa y selectiva de enlaces C-H en hidrocarburos no activados mediante catalizadores organometálicos constituye aún un trabajo complejo en el ámbito de la química sintética. Hoy en día éste es el obstáculo principal a superar para conseguir estrategias más eficientes en síntesis orgánica o para poder utilizar alcanos simples como precursores directos de otros complejos químicos más importantes para la industria. Así, este tema de investigación constituye un centro de interés donde se concentra mucha actividad científica y donde aún hay espacio para el desarrollo. La utilización de catalizadores de hierro en este tipo de reacciones tiene un interés especial ya que el hierro es un metal económico, respetuoso con el medio ambiente y no es tóxico. El rol principal de la química computacional en este campo de investigación recae en la determinación de mecanismos de reacción. En esta tesis se estudian dos procesos de funcionalización de enlaces C-H con intereses complementarios

(**Capítulo 4**). El primero es la hidroxilación de alcanos mediante catalizadores no-hemo $\text{Fe}^{\text{V}}=\text{O}$. A pesar de que esta reacción ha sido ampliamente estudiada computacionalmente, los diferentes estudios presentan diversos mecanismos de reacción, el origen de la variabilidad de los cuales no estaba claro. Por lo tanto, se han investigado los efectos del sustrato y el solvente en estos procesos con el objetivo de intentar racionalizar las diferencias en los mecanismos de reacción recogidos en la literatura. Se ha observado que la distinta estabilidad en fase gas y en solvente de un intermedio de la reacción es el motivo principal de la existencia de la variabilidad de mecanismos. El segundo proceso estudiado es la funcionalización de enlaces C-H en arenos no activados mediante la inserción de carbenos. A diferencia de las reacciones de hidroxilación, este proceso no ha sido ampliamente estudiado. Concretamente, la reacción de inserción quimioselectiva de carbenos en benceno mediante catalizadores de hierro se publicó por primera vez el año 2016 por parte de los grupos experimentales del Dr. Miquel Costas y el Prof. Pedro J. Pérez (*Angew. Chemie Int. Ed.* 2016, **55**, 6530-6534). En este sentido, en el capítulo 4 de la tesis se explica por primera vez el mecanismo de reacción de esta reactividad sin precedentes, y también se identifican las características y motivos que favorecen esta reactividad por encima de otras posibles reacciones como serían la adición del carbeno en el benceno.

El concepto de estado de oxidación (EO) tiene una importancia primordial en química. En los mecanismos de reacción en catálisis organometálica, por ejemplo, el estado de oxidación es un descriptor intrínseco y la descripción de la reacción química no está completa hasta que no se han determinado los estados de oxidación de todas las especies involucradas. El concepto de EO también es importante en nomenclatura química, o en procesos de caracterización espectroscópica, donde se relaciona con la configuración de los electrones d del metal de transición. El papel de la química computacional en la determinación de EOs no ha sido muy explorado. No obstante, el grupo del Dr. Pedro Salvador recientemente presentó una nueva herramienta computacional para determinar EOs, el denominado método de los estados de oxidación efectivos (EOS por sus siglas en inglés, *effective oxidation states*) (*J. Chem. Theory Comput.* 2015, **11**, 1501-1508). En el **capítulo 5** presentamos un análisis comparativo de la aplicabilidad del método EOS en la determinación de estados de oxidación. Además, también se presentan nuevos importantes descubrimientos sobre esta propiedad en base los resultados obtenidos en el estudio.

Los electruros son un tipo de compuestos iónicos relativamente nuevos con una estructura electrónica fascinante: electrones aislados actúan estequiométricamente como la parte aniónica del cristal. Esta interesante característica, no obstante, obstaculiza la asignación de los EOs de manera clásica en estos compuestos, por ejemplo. A pesar de que actualmente sólo se han sintetizado trece electruros sólidos (únicamente seis de los cuales estables a temperatura ambiente), sus interesantes propiedades han propiciado el desarrollo de muchas sorprendentes aplicaciones. Así, los electruros constituyen, sin duda, uno de los campos de investigación más prometedores en el desarrollo de nuevos materiales, donde aún queda mucho camino por recorrer. La química computacional siempre ha tenido un papel importante para el desarrollo de nuevos electruros y en la comprensión de su estructura electrónica. En el **capítulo 6** presentamos el primer estudio

RESUMEN

computacional sobre la existencia de electruros más allá del estado sólido. A pesar de la existencia de un gran número de trabajos teóricos sobre el confinamiento de electrones en el estado sólido, ningún otro trabajo antes se había centrado en la caracterización de electruros en fase gas. En esta tesis investigamos si la estructura electrónica de los electruros moleculares realmente consiste en electrones aislados o si ésto es simplemente un modelo formal para representar estas moléculas. A parte, también se presenta un criterio para diferenciar electruros moleculares de especies similares.

Globalmente esta tesis se divide en ocho capítulos. El primero es una introducción donde se exponen las razones del interés químico de los proyectos de investigación seleccionados. Además, el primer capítulo también resume las contribuciones que la química teórica ha aportado en los distintos temas de investigación hasta el día de hoy. El capítulo 2 presenta los métodos teóricos, herramientas y las distintas estrategias computacionales que se han utilizado en esta tesis para llevar a cabo los estudios o para analizar los resultados adecuadamente. El capítulo 3 lista los objetivos de la tesis. Los capítulos 4, 5 y 6 incluyen las publicaciones, mencionadas en los párrafos anteriores, que la tesis presenta. El capítulo 7 presenta la discusión de los resultados y, finalmente, en el capítulo 8 se resumen las principales conclusiones que se derivan de la tesis.

Chapter 1

Introduction

1.1 Functionalization of Hydrocarbons

Mastering the functionalization of unactivated hydrocarbons is regarded as the "Holy Grail" to achieve efficient strategies in organic synthesis and selective transformations of petroleum to more valuable and expensive products. Nowadays, the main application of hydrocarbons is as an energy source through petroleum or crude oil combustion (Figure 1.1). At high temperatures alkanes and cycloalkanes react with O_2 producing the thermodynamically stable and economically unattractive products, carbon dioxide and water. However, the potential use of alkanes as precursors for other more important chemicals has not yet been fully exploited, mainly as a consequence of the relatively inertness of C-H and C-C bonds.

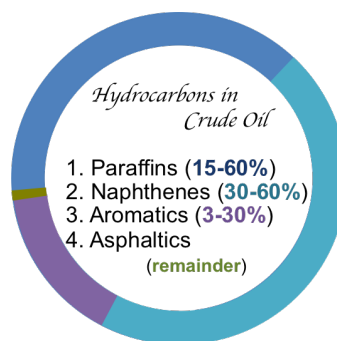


Figure 1.1: Composition of crude oil.

The standard process to transform alkanes to other "useful" chemicals starts with cracking or dehydrogenation processes (thermal or catalytic) (Figure 1.2).^{1,2} These processes, although being energy-intensive, non-selective, and fairly inefficient in many occasions, form valuable olefins that will be transformed to other petrochemicals, especially oxygenates such as alcohols, aldehydes, and carboxylic acids.^{3,4} These new chemicals are used as essential building blocks in organic synthesis processes. In traditional organic synthesis, they are typically used and

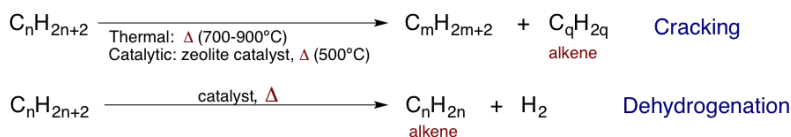


Figure 1.2: Examples of petroleum refining operations to transform alkanes to olefins. $q=n-m$

incorporated by means of multiple transformations to achieve the final products. Thus, the starting reagents are rather unlike from the final products and pre-determine the synthetic strategy (Figure 1.3).⁵ In this sense, the development of new strategies to directly functionalize C-H, C-C and C=C bonds unlocks opportunities for new synthetic strategies and for efficient and better-controlled conversions of alkanes into olefins, that may offer economic benefits.

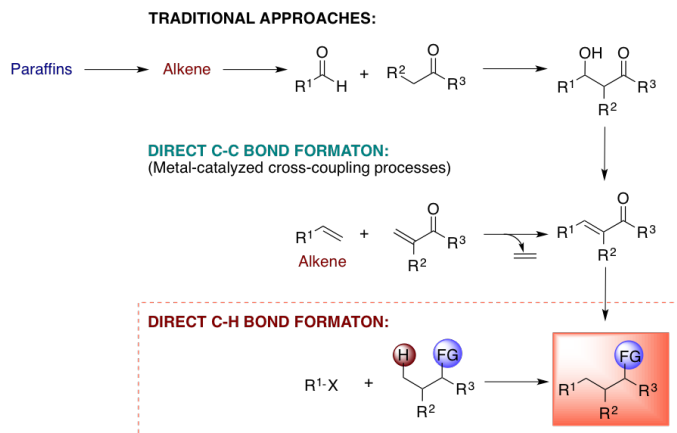


Figure 1.3: Evolving synthetic procedures of functionalizations in organic synthesis. R, alkyl or aryl groups.

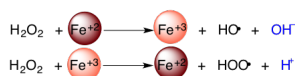
1.1.1 Historical survey

The controlled activation and functionalization of hydrocarbons (C-H and C-C bonds) has been a ubiquitous theme throughout the entire 20th century. From the very beginning, transition metals were associated with and used for that purpose and, by the middle of the last century, with the raise of coordination chemistry and transition metal catalysis, is when the area experiences further progress. Figure 1.8 shows a timeline with a historical overview of the progress made in hydrocarbons' activation and functionalization. The selected achievements related with C-H bond activation and functionalization are displayed below the timeline, whereas, above the timeline, the selected achievements related with C-C or C=C bond formation and functionalization are cited.

The first metal-containing systems which were able to react with C-H bonds of hydrocarbons were described as early as the end of 19th century by means of Fenton's reagents,⁶ which are solutions of hydrogen peroxide with ferrous iron (usually sulphate) that can oxidize (hydroxylate) arenes (Figure 1.4.a). Another early example, already in the 1930s, is the report of electrophilic auration of arenes.⁷ From that point, we have to wait until the 1960s to find a second spurt in this research field, when the description of metalations or cyclometalations of arenes (Figure 1.4.b),^{8,9} and the first reports about alkenes and arenes' C-H bond functionalization are described. These first reports about alkenes and arenes' C-H bond functionalization include: i) the oxidative coupling of arenes (Figure 1.4.c1),¹⁰ ii) the arylation of alkenes, i.e., the Fujiwara-Moritani reaction

1.1 FUNCTIONALIZATION OF HYDROCARBONS

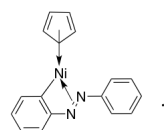
a) Fenton's reagents



Ex.:

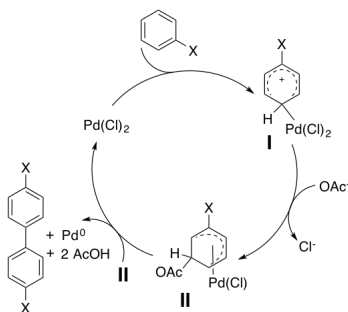


b) Metalation of arenes



c) Arenes' C-H bond functionalization

c1. Oxidative coupling of arenes (1965)



c2. Fujiwara-Moritani reaction. Arylation of alkenes (1969)

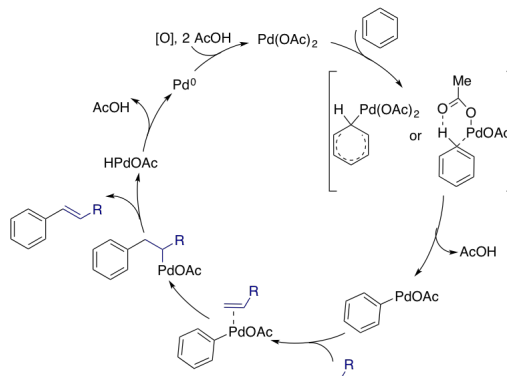


Figure 1.4: C-H bond activation and functionalization. a) **Fenton's reagents.** Net effect of Fenton's reagents⁶ (solution of hydrogen peroxide with ferrous ions). It results with the desproportionation of H_2O_2 to create two different oxygen-radical species. Example: hydroxylation of benzene into phenol. b) **Metalation of arenes.** **1.** $(\eta^5\text{-cyclopentadienyl})(o\text{-phenylazo})\text{phenylnickel}$.⁸ **2.** Hydrido(aryl)-complex. $\text{PP}=\text{Me}_2\text{PCH}_2\text{CH}_2\text{PMe}_2$, bidentate ligand.⁹ c) **Arenes' C-H bond functionalization.** **c1.** Oxidative coupling of aromatic compounds with Palladium salts.¹⁰ **c2.** The Fujiwara-Moritani reaction. Cross coupling reaction between an aromatic C-H bond and an olefin C-H bond.¹¹

(Figure 1.4.c2),¹¹ (both using palladium(II) salts as catalysts), or iii) the H/D exchange between benzene and D_2O by platinum(II) derivatives.¹² In all these examples, the C-H bond reaction with the transition metal proceeds successfully because it is assisted by π orbitals of arene substrates. The first C-H bond activation reaction (not functionalization) of alkanes was not reported until 1969.¹³ However, despite the late onset, new achievements were quick in coming during the 1970s and 1980s; when vigorous development of the activation and functionalization of alkanes and arenes by, mainly, low-valent metal complexes took place.¹⁴ Examples include: i) the H/D exchange between methane or its analogs and D_2O at 100-160 °C by platinum(II) or titanium(II) salts, or iridium(III) solutions;¹⁵ ii) the deuteration of methane by D_2 at room temperature by the $\text{CoH}_3(\text{PPh}_3)_3$ complex; and iii) first oxidation reactions by palladium(II),¹⁶ platinum(IV),¹⁷ ruthenium(IV),¹⁸ or cobalt(III) (Figure 1.5).^{19,20}

A typical problem of the coordination of alkane or alkyl groups in organometallic compounds with high oxidation-state metals is the formation of highly stable alkane-metal coordination intermediates that may stop the reaction and the desired functionalization. This is the main reason for the far fewer number of publi-

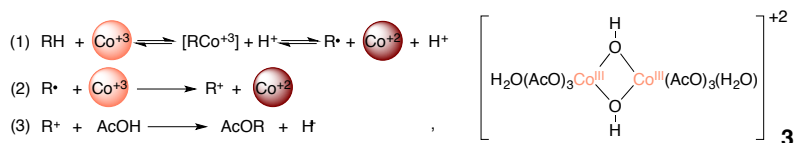


Figure 1.5: Suggested procedure of n-alkanes oxidation by cobaltic acetate complexes in acetic acid in the presence of strong acids.²⁰ In the first stage, an alkyl radical is produced (1), which is further oxidized into a carbonium ion (2), that reacts with the solvent (3). **3**. Suggested structure of the cobaltic acetate complex.

cations focused on high-valent metal complexes, compared with low-valent metal complexes. Nevertheless, at the end of the 1980s, the tendency began to change. Low-valent metal complexes were gradually replaced by high-valent metal-oxo complexes.¹⁴ It was a new biomimetic strategy to improve the performance on alkane oxidation reactions. Unlike previous complexes, the organometallic compound presented a metal-oxo group, that facilitates the C-H bond cleavage without direct contact between the metal and the C-H bond.

During the last 30-40 years a lot of knowledge about the factors that control the activity and selectivity of several catalytic C-H bond activation and functionalization reactions, as well as important mechanistic insights, have been gained.^{21,22} There is a large amount of information available about different C-H bond functionalization reactions, but is beyond the scope of this thesis to cover them all. In this thesis we will focus on [C-H bond hydroxylations](#) and [carbene insertions](#).

If we now focus on the above part of the timeline (Figure 1.8), we see the selected feats related with C-C or C=C bond functionalization. An early example on C=C bond functionalization took place already in the 1930s, when using anhydrous solution of hydrogen peroxide and tertiary butyl alcohol in the presence of osmium tetroxide, hydroxylations of the double bond of alkenes and arenes were observed.²³ However, it was during the 1950s when the revolution of transition metal catalysis able to functionalize plain olefins arrived. The chemical companies DuPont, Standard Oil, and Philips Petroleum discovered transition-metal catalyzed olefin metathesis when they reported that propene reacted to form ethylene and 2-butene when passed over a molybdenum on alumina catalyst at high temperature (Figure 1.6.a);²⁴ or, in turn, in 1953, the German chemist Karl Ziegler discovered a catalytic system able to polymerize olefins, specifically ethylene into linear, high molecular weight polyethylene (Figure 1.6.b).²⁵ Karl Ziegler, along with Giulio Natta, were awarded the Nobel Prize in Chemistry in 1963 for this achievement. Another finding for the industrial functionalization of the C=C bond of plain olefins took place during the 1960s and 1970s with the development of the Wacker process, which involves the oxidation of ethylene into acetaldehyde using a Pd(II) catalyst (Figure 1.6.c).^{26,27} Finally, it is also worth noting that in the late sixties and early seventies mechanistic breakthroughs related with olefin metathesis were reported. Examples include the discovery of the olefin metathesis mechanism in 1971 by Yves Chauvin,²⁸ or the isolation of the first metal-carbene complex (M=C) by Ernst Otto Fischer in 1964.²⁹ Chauvin's proposed mechanism involves a metal-carbene complex (Figure 1.6.d), thus the

1.1 FUNCTIONALIZATION OF HYDROCARBONS

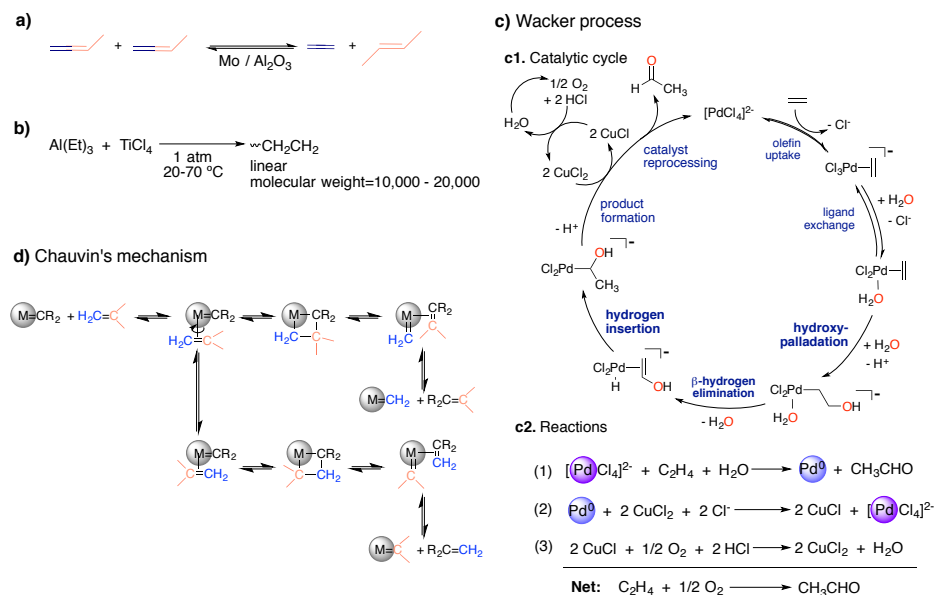


Figure 1.6: C=C bond activation and functionalization. **a)** Olefin-metathesis reaction reported by DuPont, Standard Oil, and Philips Petroleum in the 1950s. **b)** Chemical reaction of the Ziegler's catalytic system to polymerize ethylene into linear polyethylene. **c) Wacker process.** **c1.** Overall catalytic cycle of the Wacker process. **c2.** Individual reactions of the overall process. **d) Chauvin's mechanism.** Initiation of the olefin metathesis mechanism proposed by Chauvin in 1971 involving metal alkylidene and metallacyclobutane intermediates.

previous isolation and characterization of this structure was essential for Chauvin's proposal. Fischer received the Nobel Prize in Chemistry in 1973 and Yves Chauvin, together with Robert H. Grubbs and Richard R. Schrock, awarded the Nobel Prize in Chemistry in 2005 for the development of the metathesis method in organic synthesis.

Thus, alkane and alkene (or arene) transformation chemistry are clearly in different development stages. While the development of industrial processes for plain alkene's transformation and processing was already developed during the 20th century and have received a lot of attention, the development of efficient strategies for the direct industrial-scale conversion of alkanes remains challenging. For example, reconciling the constraints inherent in alkane chemistry with thermodynamic, economic and engineering requirements is being problematic and precludes the development of a process for the direct conversion of methane to methanol or other liquid fuels that could significantly improve methane utilization.

The vast majority of the catalytic processes previously described use 2nd and 3rd row transition-metal elements, mainly the 4d metal, palladium. It is worth noticing that the development of palladium-catalyzed cross coupling reactions in the manufacture of pharmaceutical and electronic materials was recognized by the Nobel Prize in Chemistry in 2010, awarded to Richard F. Heck, Ei-ichi Negishi, and Akira Suzuki.³⁰⁻³² However, the dominance of these precious metals in metal catalysis is not sustainable for a number of reasons, mainly related

to low abundance on Earth, limited availability (see Figure 1.7), as well as high price and significant toxicity. Thus, nowadays, the main research on hydrocarbon functionalization seeks to use 1st row transition-metal catalysts to obtain novel reactivity and selectivity that may enable the development of new mechanisms.³³ Transition metals (TM) of the 1st row are, in general, more affordable, sustainable and cheaper than precious metals. These considerations have motivated chemists to replace precious metals with 1st-row TM. However, working with 1st-row TM catalysts implies differences with second- or third-row transition metal catalysts. Mainly, the weak ligand field of many first-row complexes often gives paramagnetic complexes ($S > 0$) that involve special considerations for the experimental characterization of the complex and for the computational studies of the reaction mechanism. From the computational point of view, the fact that first-row metals often have multiple spin states with similar energies requires the characterization of multiple potential energy surfaces, the study of potential-energy surface crossings, and benchmark studies to validate the theoretical methodology.³⁴ All the mechanistic studies presented in this thesis are based on 1st row transition metals (iron).

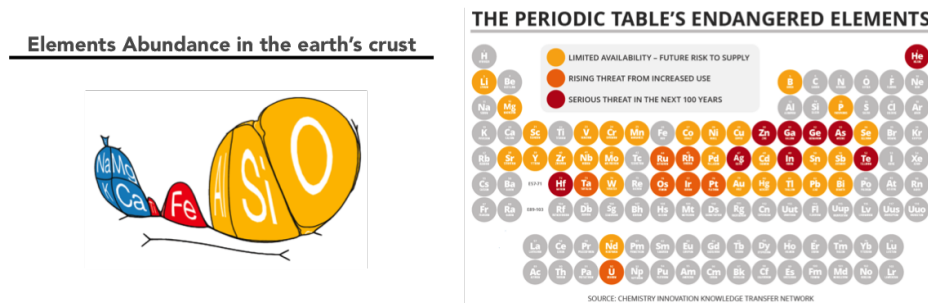


Figure 1.7: **Left.** Difussion cartogram representing elements abundance in the earth's crust by weight.³⁵ **Right.** Periodic Table where the elements that will face supply limitations in the coming years are represented. The research was conducted by the Chemical Innovation Knowledge Transfer Network.³⁶

Regarding hydrocarbon substrates, among all the possible hydrocarbon types (i.e., alkanes, cycloalkanes or naphthenes, alkenes, alkynes, and aromatics), this thesis includes mechanistic studies on the functionalization of three of them: alkanes, cycloalkanes, and aromatics. Regarding hydrocarbons' functionalization, this thesis will focus on C-H bond functionalization reactions by iron catalysts. These reactions are still in an early stage of development, where efficient synthetic strategies remain challenging and still have progress to make.

1.1 FUNCTIONALIZATION OF HYDROCARBONS

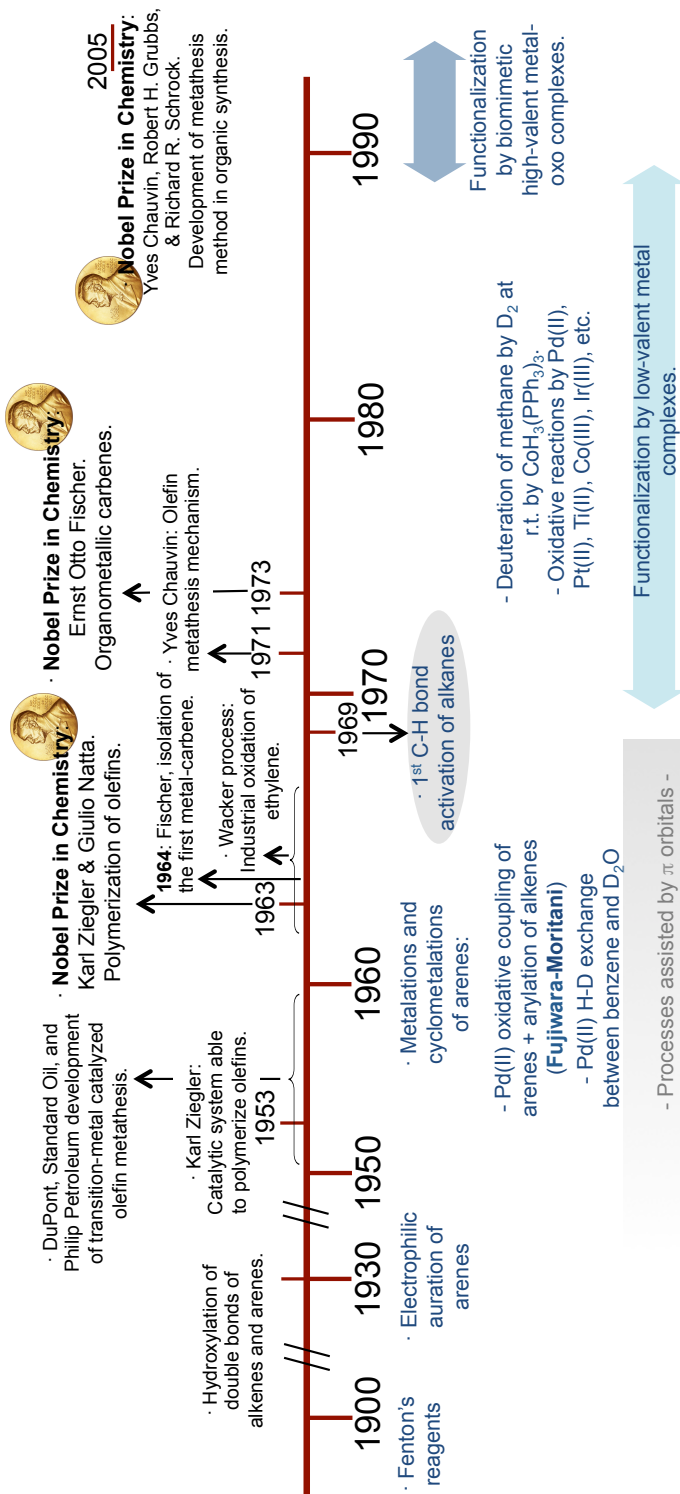
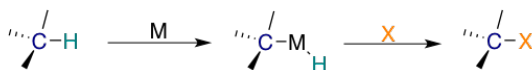


Figure 1.8: Chronological timeline for some of the most important achievements in hydrocarbons' activation and functionalization in the 20th century. *r.t.* accounts for room temperature.

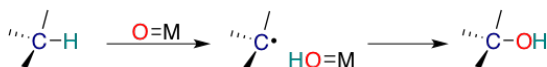
1.2 Activation and functionalization of C-H bonds

We can divide all the C-H functionalization processes promoted by metal complexes into three types taking into account the mechanism involved (Figure 1.9).³⁷ The first type includes reactions involving a "true" activation, where an organometallic derivative, i.e., a compound containing a M-C σ -bond, is formed as an intermediate or as a final product. The second type includes reactions in which there is no direct contact between the metal and the C-H bond; the contact between the complex and the C-H bond occurs only through a ligand of the complex. The function of the metal complex in these reactions usually consists in abstracting an electron or a hydrogen atom from the hydrocarbon. In the processes that belong to the third type there is no interaction between the complex (albeit via the ligand) and the molecule with the C-H bond. These complexes activate in advance some other reactants (e.g., O₂ or H₂O₂) to form reactive species which are able to attack the hydrocarbon molecule.

"True" organometallic activation of the C-H bond



Activation and functionalization of the C-H bond via the *rebound* mechanism



Activation and functionalization of the C-H bond via attack by a free radical



Figure 1.9: Three types of metal-mediated C-H bond functionalization mechanisms. On top, a "true" activation mechanism where an intermediate with a M-C bond is formed. In the middle, a second-type mechanism which entails direct contact between the complex (not the metal) and the C-H bond. Below, a third-type mechanism where there is no interaction between the complex and the molecule. The complex has formed the reactive species (HO•) in advance.

The vast majority of metal-containing enzymes in living organisms that are able to functionalize C-H bonds proceed through a second or third type mechanism.³⁸ According to today's research interests in hydrocarbons' functionalization, the two reactions types presented in this thesis that involve a C-H bond functionalization evolve through the second type mechanism.

1.2.1 Oxidation by Metal Oxo Complexes of C(sp³)-H bonds

To contextualize...

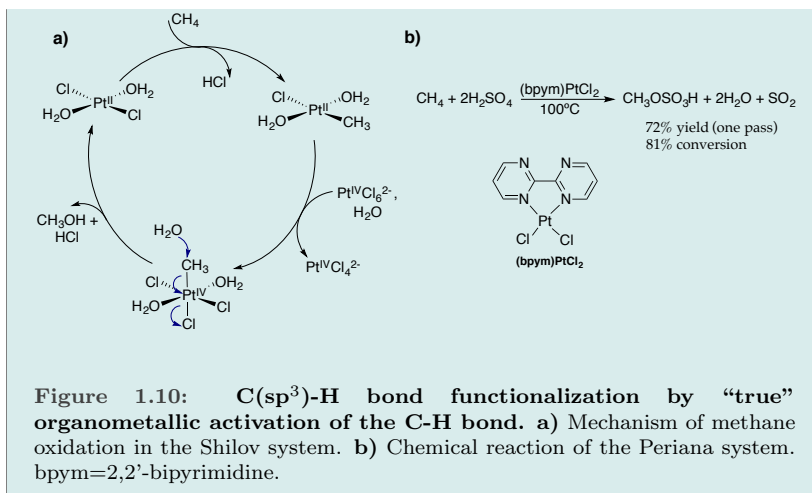
In this subsection we are going to develop the current strategies used

to functionalize C(sp³)-H bonds. As already stated, current strategies involve the use of biomimetic catalysts that react through a second-type mechanism seen above. Here, in particular, strategies that involve the use of metal-oxo units to achieve biological and synthetic C(sp³)-H bond oxidation reactions will be commented.

Concerning the achievements already commented about the functionalization of C-H bonds of hydrocarbons (achievements presented in the lower part of the timeline in [Figure 1.8](#)), just the use of Fenton's reagents allows C(sp³)-H bond functionalization. All the other commented achievements refer to alkenes or arenes C-H bond functionalization. I would like to note some further events related with C(sp³)-H bond functionalization before focusing on C(sp³)-H bond oxidation reactions by metal oxo complexes. Moreover, I would like to contextualize these achievements in terms of the reaction mechanisms (first-type, second-type, or third-type according [Figure 1.9](#)) that are used.

Besides Fenton system, another system that imply the C-H bond functionalization (oxidation) by radical mechanisms is the Barton system. The Barton system uses iron powder and dioxygen in pyridine solvent to achieve the oxidation of C(sp³)-H bonds. The reaction was first observed in 1983 with the oxidation of adamantane to adamantanone.³⁹ Subsequent studies on several variations of this system have demonstrated that iron salts in the presence of a reducing agent, or in combination with peroxides, can catalytically oxidize alkanes, sometimes with interesting selectivities. For example, the so-called Gif chemistry, developed by Barton at Gif-sur-Yvette, in France, represents an improvement on the initial Barton system. The Gif chemistry uses Fe(II) salts, picolinic acid (used as ligand), and an oxidand (tBuOOH, H₂O₂, O₂) in Pyr/AcOH as solvents. However, experimental observations refute the possibility of a radical mechanism in Gif Chemistry; and there is agreement about the oxidation occurs via Fe^V=O species.⁴⁰ Thus, Gif chemistry is an early example of C(sp³)-H bond functionalization by means of a second-type reaction mechanism.

Regarding metal complexes able to oxidize C(sp³)-H bonds by a first-type reaction mechanism (*i.e.*, forming an intermediate with a M-C bond), the so-called Shilov chemistry and the Periana system should be commented. Shilov chemistry (discovered in 1969 and 1972) oxidizes methane to methanol by a Pt(II) catalyst in an aqueous solution if stoichiometric amounts of Pt^{IV}Cl₆²⁻ complex are added.³⁸ The catalytic cycle in which σ -methyl complexes of platinum(II) and platinum(IV) are involved is shown in [Figure 1.10](#). Separately, the Periana system also involves a platinum complex, but derived from the bidiazine ligand family, that catalyze the oxidation of methane to a methanol derivative by sulfuric acid (see [Figure 1.10](#)).⁴¹



As noted in [section 1.1](#), the field of catalyzed oxidation reactions of saturated nonactivated hydrocarbons is of enormous importance not only for synthetic organic chemistry but also for biochemistry and industrial applications, e.g., the oxidation of methane to methanol. Unlike synthetic procedures, in biological systems, where reduced hydrocarbons are abundant in the environment, enzymes that catalyze the oxygenation of alkanes are relatively easy to find. Oxygenases perform alkane functionalization at ambient temperature, and sometimes with great selectivity. Regarding oxygenases reaction mechanisms, two important papers by Mason and Hayaishi in the fifties altered the understanding known so far. Before their work, the enzymatically catalyzed oxygen incorporated into substrates was thought to come from water. However, both researchers proved, with $^{18}\text{O}_2$ oxygen isotopes, that direct incorporation of oxygen into organic compounds occurred. For Mason, the dioxygen incorporation was observed through the tyrosinase oxygenase reaction,⁴² and, for Hayaishi, the reaction was observed through a catechol oxygenase.⁴³ These enzymes, originally referred to as oxygen transferases, are today referred to as oxygenases. There are different types of oxygenases according to their structure or function, but all of them catalyze the chemo-, regio- and stereoselective oxygenations of alkanes and many other compounds, producing alcohols, aldehydes, epoxides and carboxylic acids.⁴⁴

We can divide enzyme systems capable of activating saturated hydrocarbon under aerobic conditions in the following main groups: i) heme oxygenases like cytochrome P450 enzymes; ii) nonheme oxygenases; and the special case of iii) methane monooxygenases. There are many other enzymes not considered here able to oxidize hydrocarbons, but they can not oxidize C(sp³)-H bonds (e.g., Rieske Dioxygenases, cyclooxygenases (COX), tryptophan 2,3-dioxygenases (TDO), etc.).

Cytochrome P450 enzymes are the most studied biological oxygenases. There is a number of books and reviews describing them, the reactions they can perform and the mechanism of action.⁴⁵⁻⁵¹ More than 4000 P450 enzymes are known to date, but only a few of them have been characterized. The active iron-oxo species in alkane hydroxylations, the $\text{Fe}^{\text{IV}}\text{O}$ porphyrin π -cation radical intermediate, called compound I (CpdI), is known to perform hydroxylation of lin-

1.2 ACTIVATION AND FUNCTIONALIZATION OF C-H BONDS

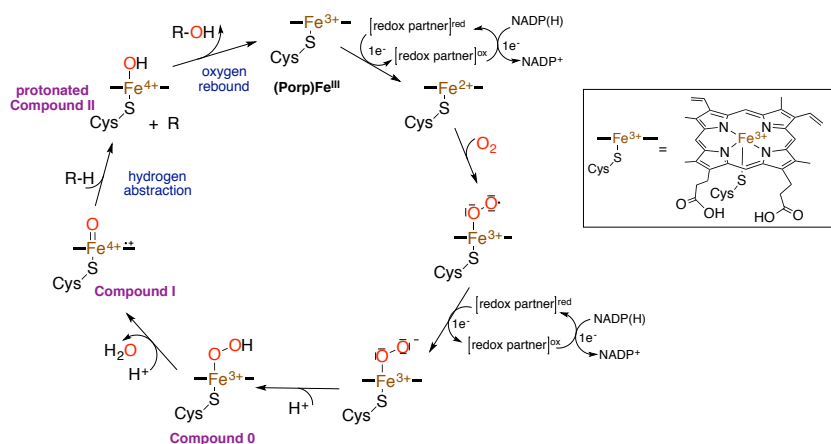


Figure 1.11: The catalytic cycle of cytochrome P450. The heme macrocycle is depicted with bold lines, as indicated in the inset. The cycle shows the activation of the heme iron by O_2 , 2H^+ and two extra electrons from the initial ferric state ($(\text{Porp})\text{Fe}^{\text{III}}$) until the achievement of the ferric hydroxoperoxo form (also known as Compound 0) and the ferryl-oxo species with a porphyrin radical cation (Compound I). The latter is likely to be the catalytically relevant oxidant in most P450 reactions. The second part of the cycle shows the hydroxylation mechanism of alkanes by CpdI intermediate, the so-called Groves' mechanism, which entails an initial hydrogen abstraction, followed by an oxygen rebound.

ear and branches alkanes, arenes, and their derivatives such as aliphatic acids. Moreover, the catalytic power and activity of other porphyrinic species (CpdI, Cpd0 or CpdII - see species in Figure 1.11) in the oxidation of varied organic substrates have also been studied.⁵²⁻⁵⁵ The reaction mechanism that P450 enzymes follow to hydroxylate hydrocarbon substrates was first suggested in 1976 by Groves and McClusky,⁵⁶ and it is known as the Groves' mechanism or the rebound mechanism. At present, the Groves' mechanism has been resolved in detail and it is strongly supported and well-established in enzymatic reactions by experimental⁴⁹ and theoretical evidences. In the rebound mechanism of P450-enzymes, $(\text{Porp}^+)\text{Fe}^{\text{IV}}\text{O}$ species, CpdI, starts the alkane hydroxylation by a rate-determining hydrogen abstraction step, which is followed by an oxygen rebound step between the resulting $(\text{Porp})\text{Fe}^{\text{IV}}\text{OH}$ and the substrate radical species. (Figure 1.11)

Regarding nonheme oxygenases, there are several enzymes able to perform C-H or C-C bond oxidation. However, most of the nonheme oxygenases able to catalyze *alkane* hydroxylation reactions are related to the integral-membrane nonheme di-iron protein AlkB (Figure 1.12.a). AlkB protein was first discovered in a hexane-degrading fluorescent pseudomonas that is known as *P. putida* GPo1.^{57,58} However, AlkB homologs have been currently identified in many alkane-degrading α -, β -, and γ -Proteobacteria. These enzymes have different substrate ranges: some oxidize alkanes from C_5 to C_{12} , whereas others oxidize C_{10} - C_{16} *n*-alkanes. They require one or two rubredoxin domains and, such as cytochrome P450, use NADH as the electron-providing source.

Just focusing in methane monooxygenases, two types of them are known: the fully characterized, but relatively rare, soluble di-iron methane monooxy-

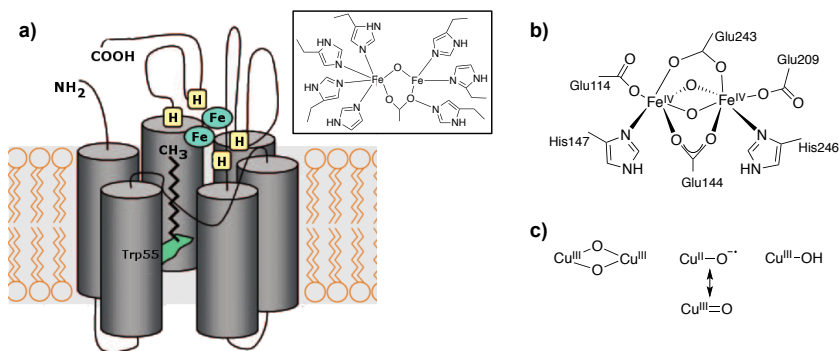


Figure 1.12: Nonheme oxygenases enzymes. **a)** Model for the AlkB alkane hydroxylase in *P. putida* GPo1. The enzyme is proposed to have six transmembrane helices forming a hexagonal distribution with a long, hydrophobic pocket into, where the linear alkane molecule can slip. The four histidine (H) squares represent sets of histidine ligands believed to bind the two iron atoms (Fe), allegedly in agreement with the illustration of the active site presented in the inset.⁵⁹ In *P. putida* GPo1 AlkB, the side chain of Trp55 extends its bulky arm towards the hydrophobic pocket, which hampers the proper insertion of alkanes longer than C₁₃. Figure modified from ref. 60. **b)** Structure of intermediate **Q**, which is the key reaction cycle intermediate of the soluble methane monooxygenase (sMMO). Intermediate **Q** is predicted to possess a symmetrical *cis*-μ-1,2-peroxo bridge, formed after the homolytic O-O bond cleavage of the bridging oxygens originate from O₂. **c)** Proposed copper-oxo/hydroxo reactive intermediates in the catalytic cycles of copper-containing oxygenases.

genase (sMMO) and the not well understood but ubiquitous copper-containing membrane-bound methane monooxygenase (pMMO). sMMOs are characterized by diiron centers with two histidines and four carboxylates. However, the characterization of the highly unstable pMMO complexes have not been achieved. Concerning sMMOs, a bis(μ-oxo)diiron(IV) compound has been trapped and identified as active intermediate in the oxidation of methane,^{61–63} and equivalent dicopper active species (bis(μ-oxo)dicopper(III)) have been suggested and controversially discussed in the literature for pMMO enzymes (Figure 1.12.b and .c).^{64–66} Besides the activation of methane, sMMOs are able to oxidize other saturated and unsaturated alkanes up to C₁₀ and halogenated, aromatic, and heterocyclic compounds. By contrast, pMMOs have a lower substrate range, restricted to alkanes and alkenes with lengths up to C₅.

The application of MMOs for synthetic purposes is limited owing to the low regio- and stereoselectivities of these enzymes. Furthermore, in general, large-scale applications of oxygenases are not yet feasible. By one hand, *in vitro* enzyme applications are restricted by cofactor requirements and their often-multicomponent nature. By the other hand, if whole cells are used, significant engineering challenges appear, such as how to deal with the toxicity of substrates and products, oxygen mass transfer, or the absorption of lipophilic substrates.⁴⁴ Thus, the development of biomimetic catalysts has become an attractive target due to the important advantages of the oxidation reactions that high-valent iron- and copper-oxo proteins are able to catalyze. It is also worth emphasizing that owing to the fact that most of alkane oxygenases enzymes are Fe-containing oxygenases, this triggered the development of biomimetic catalytic systems of Mn, Fe, and Cu for aliphatic C-H hydroxylation reactions and spurred the achieve-

1.2 ACTIVATION AND FUNCTIONALIZATION OF C-H BONDS

ments in the field of base-metal catalysts. These catalytic systems have been reviewed extensively^{67,68} and, in the next section, I am just going to focus on iron catalysts.⁶⁹

Biomimetic metal(iron)-oxo complexes

The first biomimetic metal-oxo complex was already synthesized in 1981 by Groves *et al.* via oxidation of the $[(\text{TMP})\text{Fe}^{\text{III}}(\text{Cl})]$ compound (TMP = *meso*-tetramesityl porphinate dianion), **4**.⁷⁰ **4** was an heme complex, based on cytochrome P450 enzymes, which showed the characteristic features of the CpdI intermediate after its oxidation; namely, an oxoiron(IV) porphyrin π -radical cation (d^4) species $[(\text{TMP}^+\bullet)\text{Fe}^{\text{IV}}(\text{O})(\text{CH}_3\text{OH})]^+$, **5**, (Figure 1.13.a).^{71,72} **5** was found to be a competent oxidant in alkane hydroxylations and also in olefin epoxidation.^{71,73} Since then, a number of oxoiron(IV) TMP derivatives have been prepared in an effort to understand the electronic effects of the porphyrin ligands on the chemical properties of oxoiron(IV) intermediates and the role of the axial ligand bound trans to the iron-oxo moiety (Figure 1.13.b).^{74,75}

While the first paper on an oxoiron(IV) porphyrin species appeared in 1981, subsequent papers on nonheme biomimetic oxoiron complexes had not appeared until two decades later in the 2000s, when Grapperhaus *et al.* generated a terminal nonheme oxoiron(IV) species, $[(\text{cy-ac})\text{Fe}^{\text{IV}}(\text{O})]^+$, **7**, by the ozonolysis of $[(\text{cy-ac})\text{Fe}^{\text{III}}(\text{CF}_3\text{SO}_3)]^+$, **6**, (cy-ac = cyclam-acetato = 1,4,8,11-tetraazacyclotetradecane-1-acetate) (see Figure 1.14).⁷⁶ However, the instability of the compound prevented its spectroscopic characterization. The first X-ray structure of a mononuclear nonheme oxoiron(IV) complex was not reported until three years later, in 2003, when Rohde *et al.*⁷⁷ characterized the $S=1$ $[(\text{TMC})\text{Fe}^{\text{IV}}(\text{O})(\text{CH}_3\text{CN})]^2+$, **8** complex (where TMC = 1,4,8,11-tetramethylcyclam). This compound also had a macrocyclic polyamino ligand and it became the prototypical

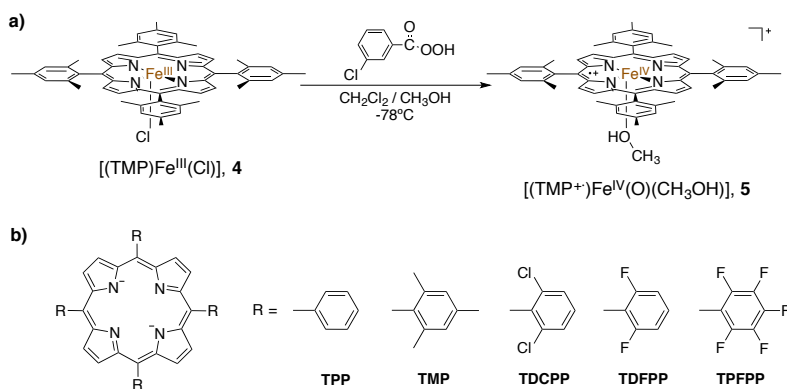


Figure 1.13: Porphyrin-based ligands. **a)** Chemical reaction of the oxidation of $[(\text{TMP})\text{Fe}^{\text{III}}(\text{Cl})]$ to $[(\text{TMP}^+\bullet)\text{Fe}^{\text{IV}}(\text{O})(\text{CH}_3\text{OH})]^+$ by *m*-chloroperoxybenzoic acid in $\text{CH}_2\text{Cl}_2/\text{CH}_3\text{OH}$ (4:1) at -78°C . **b)** Examples of porphyrin-based ligands according to the R substituent of the porphinate anion. TPP = *meso*-tetraphenyl porphinate dianion; TMP = *meso*-tetramesityl porphinate dianion; TDCPP = *meso*-tetrakis(2,6-dichlorophenyl)porphinate dianion; TDFPP = *meso*-tetrakis(2,6-difluorophenyl)porphinate dianion; TPFPP = *meso*-tetrakis(pentafluorophenyl)porphinate dianion.

example of $S=1$ oxoiron(IV) complexes (Figure 1.14).

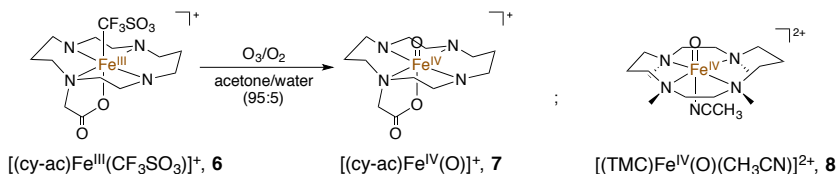


Figure 1.14: Oxoiron(IV) complexes supported by cyclam and related ligands. Left-hand side. Chemical reaction of the ozonolysis of $[(\text{cy-ac})\text{Fe}^{\text{III}}(\text{CF}_3\text{SO}_3)]^+$ to $[(\text{cy-ac})\text{Fe}^{\text{IV}}(\text{O})]^+$ in acetone/water mixture. **Right-hand side.** Structure of the $[(\text{TMC})\text{Fe}^{\text{IV}}(\text{O})(\text{CH}_3\text{CN})]^{2+}$ complex.

Since the report of **8**, a handful of nonheme $S=1$ oxoiron(IV) complexes have been synthesized using various tetradentate and pentadentate ligand systems, containing pyridine and amine nitrogen donors. The second $\text{Fe}^{\text{IV}}=\text{O}$ complex to be crystallized was supported by the pentadentate N4Py ligand, (N4Py=(1,1-di(pyridin-2-yl)-N,N-bis(pyridin-2-ylmethyl)methanamine)) (see Figure 1.15). Indeed, the $[(\text{N4Py})\text{Fe}^{\text{IV}}(\text{O})]^{2+}$ complex, **9**, where Fe is coordinated to four equatorial pyridines and a donor tertiary amine *trans* to the $\text{Fe}=\text{O}$ moiety, was the first nonheme $\text{Fe}^{\text{IV}}=\text{O}$ complex shown to cleave the C-H bonds of cyclohexane, albeit quite slowly.^{78,79} Currently, similar complexes where the N4Py ligand was substituted by Bn-TPEN, Py_2TACN , BP1 or BP2 ligands (other pentadentate ligands which keep a donor tertiary amine *trans* to the $\text{Fe}=\text{O}$ moiety) have been synthesized to study the effect of equatorial ligands on the reactivity of oxoiron(IV) complexes (Figure 1.15).^{80–82} The catalysts differ only with respect to the extent of equatorial donation from the ligands to the Fe center, which results in a difference in the $\text{Fe}^{\text{III}}\text{-OH}/\text{Fe}^{\text{IV}}=\text{O}$ reduction potentials, that affects the hydrogen atom abstraction (HAA) reaction rate. In $S=1$ oxoiron(IV) complexes supported by pentadentate ligands, a higher reactivity is associated with complexes that exhibit higher redox potentials and that have pyridine rings (those highlighted in gray in Figure 1.15) perpendicular to the $\text{Fe}=\text{O}$ unit.^a

Regarding nonheme oxoiron(IV) complexes supported by tetradentate ligands, many complexes have been achieved, giving rise to diverse groups of catalysts which, due to different factors, tend to have higher oxidative activities than catalysts with pentadentate ligands. For example, the TPA (tris(2-pyridylmethyl)amine) ligand could be seen as the equivalent tripodal amine of N4Py. Tuning or replacing pyridine groups in TPA by other nitrogenated compounds, several related ligands such as tpa^{Ph} , TQA, or H_3buea have been synthesized (Figure 1.16). All of them form $S=2$ oxoiron(IV) complexes and exhibit high reactivities in C-H hydroxylation and oxo-transfer reactions. For example, the $[(\text{TQA})\text{Fe}^{\text{IV}}(\text{O})(\text{NCMe})]^{2+}$ complex, related to **15**, obtained by substituting the pyridine moieties of the TPA ligand with weaker-field quinoline ligands, is one of the most reactive oxoiron(IV) complexes synthesized to date.⁸³ De-

^a Catalysts with perpendicular pyridine rings to the $\text{Fe}=\text{O}$ unit are less stable^{78,82} than other equivalent complexes that do not have them. The difference in stability has been attributed to steric effects of the α -H on the pyridine donor, that results in longer Fe-N distances. Then, the donation character of the equatorial ligand is lower, which increases the redox potential of the oxo-group and its reactivity.

1.2 ACTIVATION AND FUNCTIONALIZATION OF C-H BONDS

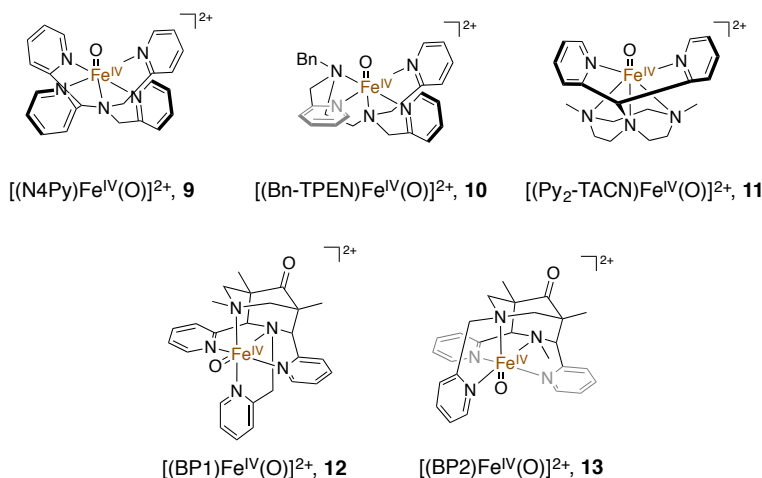


Figure 1.15: Examples of $S=1$ oxoiron(IV) complexes supported by pentadentate ligands. Abbreviations: Bn-TPEN accounts for the *N*-benzyl-*N,N',N'*-tris(2-pyridylmethyl)-1,2-diaminoethane ligand; Py_2TACN for Me_2Py_2TACN , 1-di(2-pyridyl)methyl-4,7-dimethyl-1,4,7-triazacyclononane; BP1 and BP2 ligands are conformational isomers.

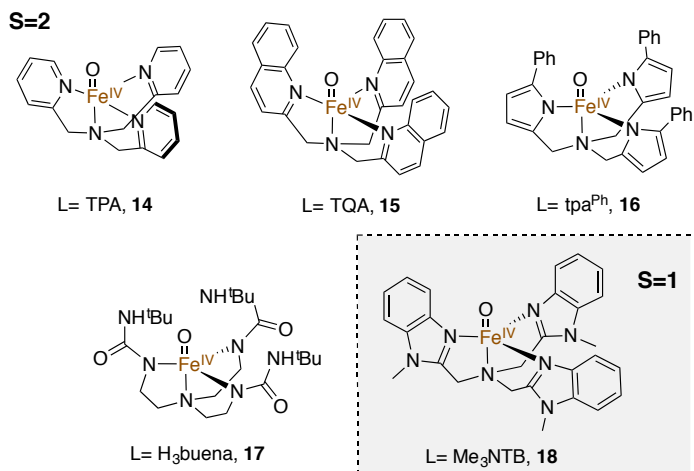


Figure 1.16: Examples of oxoiron(IV) complexes supported by tetradentate ligands, L. Abbreviations: TPA = tris(2-pyridylmethyl)amine; TQA = tris(2-quinolylmethyl)amine; tpa^{Ph} = tris(5-phenylpyrrol-2-ylmethyl)amine; H_3buena = tris(*tert*-butylureaylethylene)aminato; Me_3NTB = tris(*N*-methylbenzimidazol-2-yl)methyl)amine.

spite all theoretical studies have predicted that the ferryl species are better oxidants on the quintet-state than the corresponding triplet-state; the paucity of synthetic examples of $S=2$ oxoiron(IV) complexes makes it difficult to confirm it experimentally and there is a long-term debate on how to rationalize it.^{83–89} A counter-example can be found in the $[(Me_3NTB)Fe^{IV}(O)]^{2+}$ complex, **18**, (with Me_3NTB = tris(*N*-methylbenzimidazol-2-yl)methyl)amine), (see [Figure 1.16](#)), that despite being an $S=1$ complex, it is the most reactive species among oxoiron(IV) complexes reported so far.⁹⁰ In the next subsection, the main controversies over the C-H bond hydroxylation mechanism will be discussed, fo-

cusing also in the triplet-, quintet-state reactivity.

A different set of tetradentate ligands is formed by those that result in oxoiron(V) complexes. One notable example is the tetraamido macrocyclic ligand (TAML), which form the spectroscopically characterized $[(\text{TAML})\text{Fe}^{\text{V}}(\text{O})]^-$ anion, **19**, (Figure 1.17). The iron(V) oxidation state was confirmed on the basis of its characteristic Mössbauer spectrum, the EPR spectrum revealed an $S=1/2$ ground state, and EXAFS provided evidence of a short Fe-O distance. $[(\text{TAML})\text{Fe}^{\text{V}}(\text{O})]^-$ is the only known isolable oxoiron(V) species in the literature but not the highly reactive oxoiron complex despite following the Bordwell/Polanyi correlation.^b Other remarkable oxoiron(V) species are $\text{Fe}^{\text{V}}(\text{O})(\text{OH})$ catalysts. The main ligands that can form $\text{Fe}^{\text{V}}(\text{O})(\text{OH})$ complexes are tetradentate ligands able to form octahedral Fe complexes with two *cis* coordination labile positions (Figure 1.17). Examples of such ligands are some TPA-based or TACN-based ligands, such as PyTACN (1-(2-pyridylmethyl)-4,7-dimethyl-1,4,7-triazacyclononane). The involvement of $\text{Fe}^{\text{V}}(\text{O})(\text{OH})$ intermediates in oxygenation reactions remained doubtful until Prat *et al.* provided unequivocal evidences for such a reactive intermediate, $[(\text{PyTACN})\text{Fe}^{\text{V}}(\text{O})(\text{OH})]^{+2}$, **21**, using variable temperature mass spectroscopy.⁹⁴

The hydroxylation mechanism by biomimetic nonheme Fe(IV)=O and Fe(V)=O catalysts

The mechanism of alkane hydroxylation reactions catalyzed by biomimetic Fe(IV)=O and Fe(V)=O catalysts follows the same general scheme than the already described Groves' or rebound mechanism by CpdI (Figure 1.11). However, in contrast to enzymes, the nonheme model complexes synthesized offer high structural versatility, as we have already seen in the previous section, which affects their electronic properties. This structural versatility, combined with the typical multi state reactivity of iron, results in a versatile reactivity susceptible of changes in the reaction mechanism. There are many works addressed to the study of how the electronic structure or experimental conditions may change the mechanism and reactivity of such complexes.^{64,95-97} Below, the most important factors that determine the reaction mechanism of hydrocarbon hydroxylation processes catalyzed by Fe(V)=O are commented.

^b Neese and co-workers⁹¹ demonstrated that the Bordwell/Polanyi correlation (Equation 1.1) can be applied to rationalize the predicted electrophilic trend (that the reaction barriers decrease in the order $\text{Fe}^{\text{IV}} > \text{Fe}^{\text{V}} > \text{Fe}^{\text{VI}}$) in the reactivities of oxo-iron(IV), iron(V), and iron(VI) complexes with nearly identical coordination geometry to oxidize alkanes.

$$D(\text{O}-\text{H}) = 23.06E_{1/2} + 1.32pK_a + C \quad (1.1)$$

The Bordwell/Polanyi relationship represents a development of the Evans-Polanyi principle (or Brønsted-Evans-Polanyi principle) for C-H activation reactions mediated by metal-oxo cores. According Bordwell/Polanyi relationship,⁹² the rates of alkane oxidations by metal-oxo cores correlate with the thermodynamic affinity of the hydrogen atom abstraction reaction, which is the rate determining step of the alkane oxidation process. The thermodynamic affinity is defined as the strength of the O-H bond formed ($D(\text{O}-\text{H})$ in kcal/mol) upon reduction of the metal-oxo. Thus, following the thermochemical cycle defined by Bordwell,⁹³ the O-H bond strength is equivalent to the affinity of the oxidized metal-oxo species for an electron (redox potential $E_{1/2}$ for the $\text{M}^n=\text{O}/\text{M}^{n-1}=\text{O}$ couple) and the affinity of the reduced metal-oxo species for a proton (acid dissociation constant K_a of the conjugate base $\text{M}^{n-1}-\text{OH}$).

1.2 ACTIVATION AND FUNCTIONALIZATION OF C-H BONDS

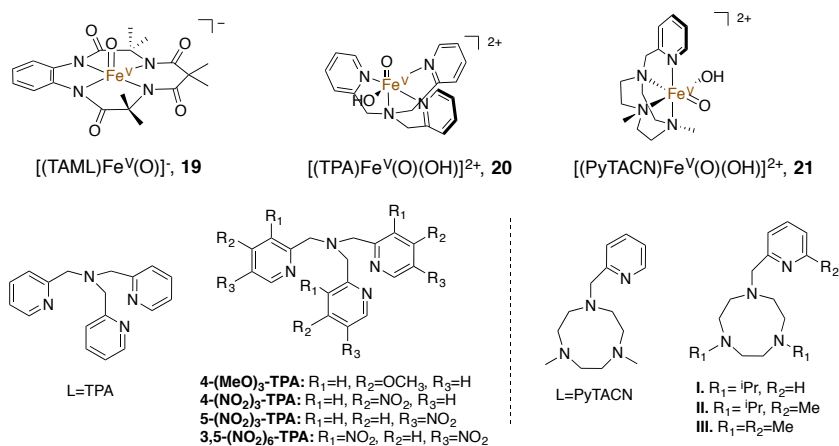


Figure 1.17: Oxoiron(V) complexes. In the first line there are the structures of the oxoiron(V) complexes commented in the text; TAML= Tetraamido macrocyclic ligand. Depicted below, there are possible structures of TPA and TPA-based ligands, on the left hand side, and PyTACN and PyTACN-based ligands, on the right hand side, which can form $\text{Fe}^{\text{V}}(\text{O})(\text{OH})$ complexes.

The first handicap is to ensure the generation of the iron-oxo species. Common synthetic routes for iron-oxo complexes include oxidation of the iron(II) precursor with an oxygen atom donor, like PhIO, peracids, hydrogen peroxide, elemental oxygen or other oxygen-atom donors. For example, it is well known that the combination of iron(II) and H_2O_2 for oxidative transformations often raises the generation of Fenton's reagents (hydroxyl radicals) as the incipient oxidants (see Figure 1.4.a). Hydroxyl radicals are highly reactive but unselective, while iron-oxo species are much more stereo- and regioselective. A thorough analysis of the reaction products, as well as obtaining spectroscopic or experimental evidences of the $\text{Fe}=\text{O}$ species, are the standard processes used to verify the formation of active iron-oxo species and to rule out that the reactivity is due to Fenton's reagents.

Once the $\text{Fe}(\text{IV})=\text{O}$ or $\text{Fe}(\text{V})=\text{O}$ catalysts are formed, the commonly accepted first step for the alkane's hydroxylation is the rate-determining hydrogen atom abstraction (HAA) step, with the formation of iron-hydroxo species and intermediate alkyl radicals. The rate-determining-step role of the HAA process is usually deduced from kinetic isotopic effect (KIE) studies between protio and deuterio substrates, and/or from a linear correlation of the reaction rate constants with substrate C-H BDEs, the strength of the O-H bond formed, or the enthalpy of the reaction, based on the Brønsted-Evans-Polanyi relationship.^{98,99} Despite there is agreement on the initial C-H bond activation and HAA reaction, emphasis has been placed on a proper electronic description of this step.

Regarding $\text{Fe}(\text{IV})=\text{O}$ species, intermediate-spin $S=1$ state species are usually experimentally detected as the ground state for the majority of model compounds. However, computationally, it has been predicted that the quintet ferryl species are much more potent oxidants for C-H bond cleavage than their triplet

counterparts. The higher reactivity of the $S=2$ spin state has been well-studied and it has been demonstrated that exchange correlation plays a crucial role in modulating the reactivity of such complexes.¹⁰⁰⁻⁸⁹ Shaik and coworkers rationalize the effect of the exchange correlation by the two-state-reactivity (TSR) and the exchange enhance reactivity (EER) models (see Figure 1.18). The EER model is based on the decrease of the repulsion energy between the electrons with the same spin. Therefore, in a chemical reaction involving an open-shell transition metal and an open-shell molecule (like an alkyl radical) with all unpaired electrons with the same spin, the stabilizing exchange interaction between the two molecules will increase when the distance between them decreases, reaching a maximum in the transition state. This effect will stabilize the transition state relative to the reactants. Figure 1.19 shows schematic electron-shift diagrams for $S=1$ and $S=2$ viable pathways of C-H bond oxidation by Fe^{IV} oxo complexes. The exchange interactions on the d block that affect the HAA barrier can be observed on it. The upper figures show the possible pathways (σ and π -following Solomon and Neese terminology-)^{101,102} for the $S=1$ state. If we take into account the π -attack, where a β -electron shifts to the $\pi_{xz/xy}^*$

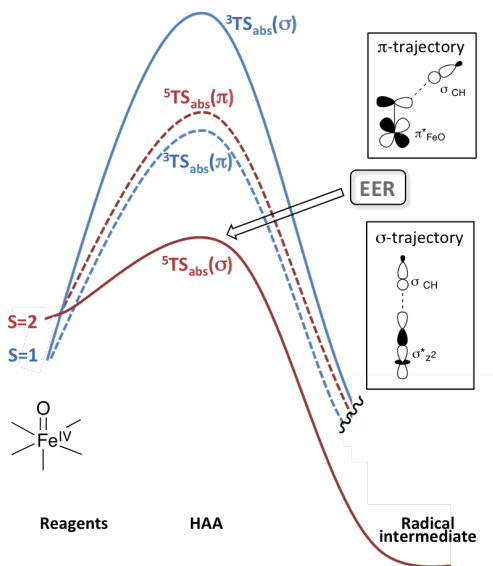


Figure 1.18: General representation of the TSR scenario of the HAA reaction by $\text{Fe}^{IV}(\text{O})$ complexes. σ - and π -trajectory labels refer to the acceptor orbitals during the electron shift, as it is represented in the orbital-overlap cartoons. In turn, σ - and π -trajectories are represented with plain and dashed lines, respectively, in the general energy profile.

d orbital, the exchange stabilization of ${}^3\text{TS}_{\text{abs}}(\pi)$ is downsized by one exchange term relative to the $S=1$ iron-oxo reactant. By contrast, in the $S=2$ state, if we take into account the σ -attack where an α -electron has shifted to the σ_z^* d orbital, the d block of ${}^5\text{TS}_{\text{abs}}(\sigma)$ contains five α -electrons, entailing that the number of exchange interactions has increased by four exchange terms in the metal center, relative to the $S=2$ iron-oxo reactant. Therefore, ${}^5\text{TS}_{\text{abs}}(\sigma)$ is stabilized by EER, which lowers its net energy barrier for the HAA making the high-spin $S=2$ complex more reactive than the corresponding $S=1$ species.

Besides the exchange stabilization, the relative energy of two spin states also depends on the energy gaps between the electron donating and electron accepting orbitals of the reagents and the orbitals' rearrangement during the HAA reaction. The orbital-energy gaps rely on the transition metal and the coordination sphere. However, in general, the calculations showed that, taking into account the interplay of exchange and orbital promotion energies, the reactivity of all

1.2 ACTIVATION AND FUNCTIONALIZATION OF C-H BONDS

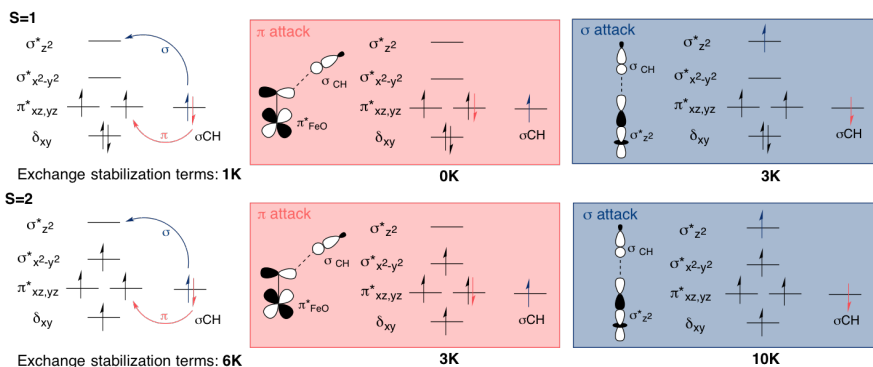


Figure 1.19: Electron shifts diagrams for all the viable pathways of the C-H abstraction reaction by Fe^{IV} oxo complexes. The σ and π trajectory labels refer to the acceptor orbitals during the electron shift, as shown in the orbital-overlap cartoons. The number of exchange stabilization terms on the d block for each MO representation is stated below each one.

viable pathways for C-H bond oxidation by Fe^{IV} oxo intermediates exhibits the order ${}^5\sigma_{abs} > {}^5\pi_{abs} \approx {}^3\pi_{abs} > {}^3\sigma_{abs}$.^{97,103}

Inasmuch as exchange-stabilization and orbital-promotion energies are general principles, the HAA energy barriers of different-spin $\text{Fe}(\text{V})=\text{O}$ species are also affected by them. However, TSR situations are uncommon. In Figure 1.20 the exchange contribution energies for alkane HAA reactions by the nonheme $\text{Fe}(\text{V})=\text{O}$ catalyst **21**, $[(\text{PyTACN})\text{Fe}^{\text{V}}(\text{O})(\text{OH})]^{+2}$, are analyzed and commented.

Finally, a further consideration regarding the hydroxylation mechanism of nonheme iron-oxo catalyst is the existence of the rebound step. Despite the reaction products experimentally detected are usually in agreement with the oxygen rebound mechanism, there exist several studies where the generation of dissociation products (*i.e.* products that can just be explained through the dissociation of the alkyl radical substrate and the catalytic intermediate) has been argued. These examples cover $\text{Fe}(\text{IV})$ -oxo ($[(\text{Bn-TPEN})\text{Fe}^{\text{IV}}\text{O}]^{2+}$, **10**, and $[(\text{N4Py})\text{Fe}^{\text{IV}}\text{O}]^{2+}$, **9**)^{105,106} as well as $\text{Fe}(\text{V})$ -oxo catalysts ($[(\text{TAML})\text{Fe}^{\text{V}}\text{O}]^{-}$, **19**).¹⁰⁷

Taking into account the previous and some other considerations, in the section 4.1 of this thesis, the substrate and solvent effects on the alkane hydroxylation mechanism by the nonheme $[(\text{PyTACN})\text{Fe}^{\text{V}}(\text{O})(\text{OH})]^{+2}$ catalyst are revised.

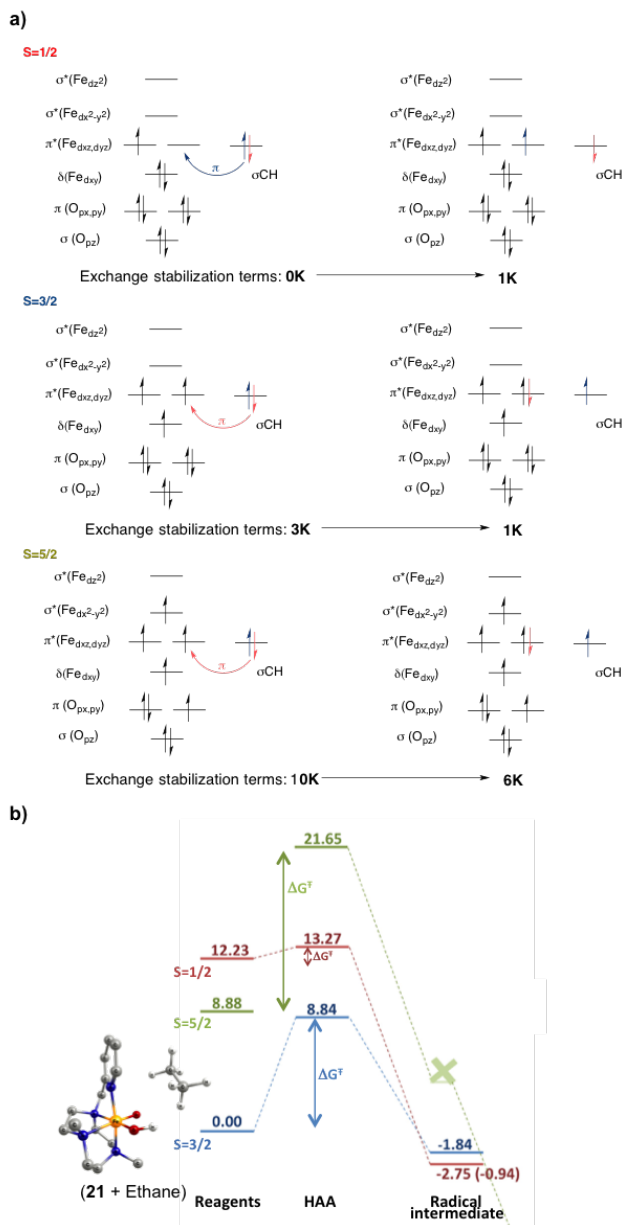


Figure 1.20: Gibbs energy profile and electron shift diagrams of the HAA reaction by an Fe^{V} oxo complex. a) Schematic representations of the d - and bonding $\text{Fe}=\text{O}$ orbitals and their occupancy evolution for all viable π pathways of the HAA reaction by Fe^{V} oxo complexes. b) Gibbs energy profile of the HAA step for ethane by **21**.¹⁰⁴ Although the linear σ -channels for the HAA reaction were searched, all attempts led to TSs of the angular π -channel. According to the orbital occupancy-evolution diagrams, i) the number of exchange interactions on the d block for the $S=1/2$ state has increased by one exchange term after the electron-shift; ii) for the $S=3/2$ state, the number of exchange interactions is reduced by two after the HAA reaction; and, iii) for the $S=5/2$ state, the number of exchange interactions is reduced by four terms. Thus, the exchange stabilization involves a relative energy barrier of the transition state that is in agreement with the energy barriers presented in figure b), *i.e.* $\Delta G^\ddagger(^6\text{TS}_\pi) > \Delta G^\ddagger(^4\text{TS}_\pi) > \Delta G^\ddagger(^2\text{TS}_\pi)$. However, $\Delta G^\ddagger(^4\text{TS}_\pi)$ is not high enough to be overtaken by $^2\text{TS}_\pi$ and to undergo two-state reactivity.

1.2.2 Aromatic C(sp²)-H bond Functionalization by Metal Carbene Complexes

In this section we introduce another approach to functionalize C-H bonds with, instead of an oxo group, a divalent carbon (carbene). As in the previous subsection, we are just going to focus on C-H bond functionalization reactions that evolve through a second type mechanisms (*i.e.* the contact between the catalytic complex and the C-H bond occurs only through the carbene coordinated to the metal complex).

The classic C-H functionalization via a metal carbene approach evolves, precisely, through a second type mechanism. It uses a high-energy diazo compound as the carbene source and the metal-induced extrusion of nitrogen from the high-energy diazo compound provides the driving force for the energetically unfavourable formation of the carbene. Finally, the highly reactive carbene species inserts into a C-H bond to form the C-H activation product and liberates the metal catalyst for another cycle (see shaded part of Figure 1.21).^{108,109} However, there has recently appeared a new approach toward aromatic C(sp²)-H functionalization by metal (Ir and Pd) carbenes that is proposed to involve a different reaction mode.¹¹⁰ The reaction mechanism consists of C-H bond metalation followed by metal carbene formation and migratory insertion (lower part of Figure 1.21).^{110,111}

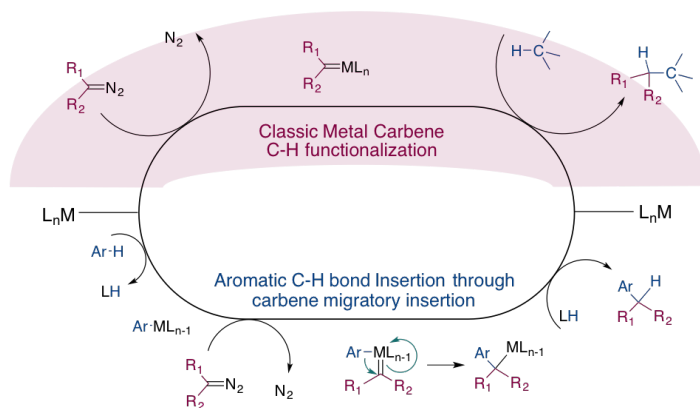


Figure 1.21: Mechanisms of the C-H bond functionalization by metal carbene catalysts. Classical mechanism versus the new approach that involves an initial C-H bond metalation followed by a carbene migratory insertion.

Historical survey of the C-H bond functionalization by metal carbene catalysts

C-H bond functionalization by metal carbene insertion is a research field itself with its own set of achievements. We are going to review some of them below in order to contextualize part of the research presented in this thesis.^{109,112,113}

The first examples of C-H bond functionalize by metal carbenes were based in copper sulfate and Cu(acac)₂ (acac=acetylacetonate) in the 1970s (see chemical

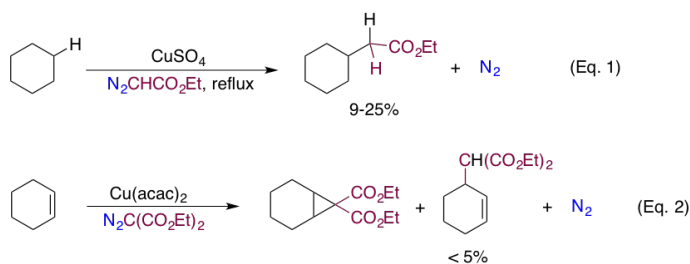


Figure 1.22: First examples of catalytic intermolecular functionalization reactions by carbene insertion using diazo compounds as the carbene source.

equations (1) and (2) in Figure 1.22).^{114,115} Although the initial reactions sought C(sp³)-H bond functionalization and their yields were low in both catalysts (e.g. Cu(acac)₂ catalyst just promoted the functionalization of the allylic C-H bond of cyclohexene as a side reaction in the cyclopropanation of the cyclic olefin), these results suppressed the opening of this research area.

Shortly after, several groups discovered the potential of rhodium acetate and Rh₂(L)₄ (L=bidentate ligand) related complexes as good catalysts for the diazo compound decomposition and subsequent insertion of the carbene group into a C-H bond (Figure 1.23).¹¹² For the rest of the 20th century, most of the advances in this field were ruled by the use of these rhodium-based catalysts in both inter- and intramolecular reactions.

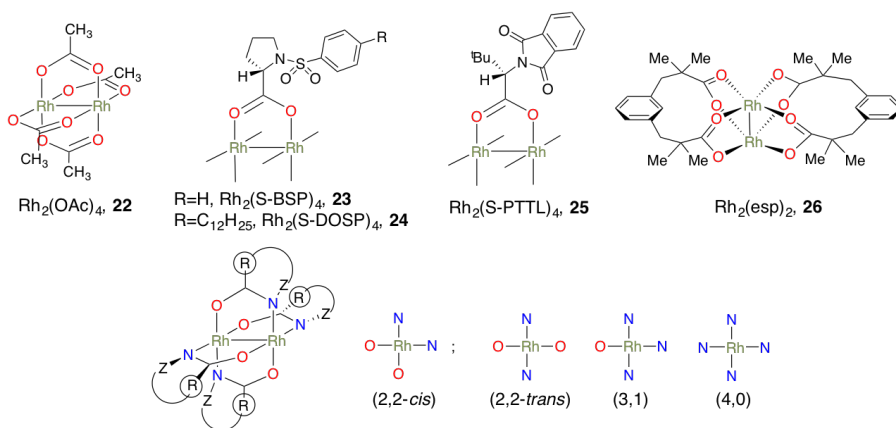


Figure 1.23: Rhodium acetate, (Rh₂(OAc)₄, **22), and other examples of Rh₂(L)₄ catalysts for the C-H bond functionalization by carbene insertion.** The top line shows, besides the structure of rhodium acetate complex, the structures of four dirhodium (II) carboxylates: Rh₂(S-BSP)₄ (**23**),¹¹⁶ Rh₂(S-DOSP)₄ (**24**),¹¹⁷ Rh₂(S-PTTL)₄ (**25**),¹¹⁸ and Rh₂(esp)₂ (**26**).¹¹⁹ In the lower line, the dominant structure of dirhodium(II) carboxamides (*i.e.* 2,2-*cis*) is represented by a full scheme. In addition, the other three possible isomers of chiral dirhodium(II) carboxamides are mapped. Because of the chiral carboxamide ligands are unsymmetrical bridges, four different geometries, based on the positioning of nitrogens and oxygens on each rhodium, are possible. Abbreviations: BSP=1-benzenesulfonyl piperidine; DOSP=N-[(4-dodecylphenyl)-sulfonyl]proline; PTTL=N-1,8-naphthaloyl-(*S*)-*tert*-leucine; esp=α,α,α',α'-tetramethyl-1,3-benzenedipropionate.

1.2 ACTIVATION AND FUNCTIONALIZATION OF C-H BONDS

The first successful synthetic applications for C-H insertion reactions by dirhodium(II) carbene catalysts were for intramolecular reactions. The preferential insertion of the carbene into the C-H bond of the gamma position of the carbene, *i.e.* the formation of five-membered ring compounds, dominates the regioselectivity of intramolecular C-H insertion reactions (see chemical equation (3) in Figure 1.24). This allowed the initial progress in synthetic applications. Subsequent achievements in chemoselectivity and stereoselectivity were also accomplished fiddling with the ligands.

Regarding the chemoselectivity, ligands have significant influences, often leading to a complete change in the chemoselectivity (see chemical equations (4) and (5) in Figure 1.24). In general, decreasing the electron-withdrawing ability of the ligand, decreases the electrophilic character of the metal carbene, which leads to an enhancement in the selectivity of the carbene for the less nucleophilic substrates.

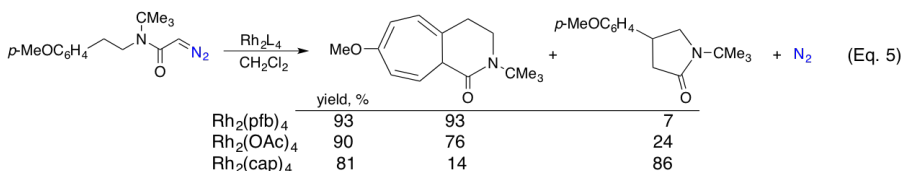
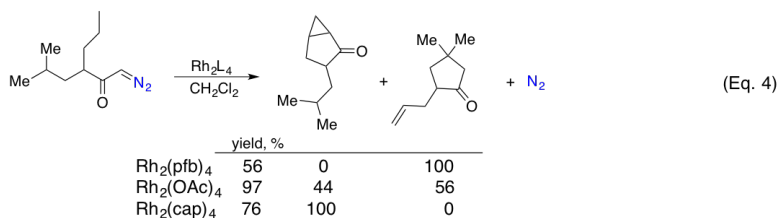
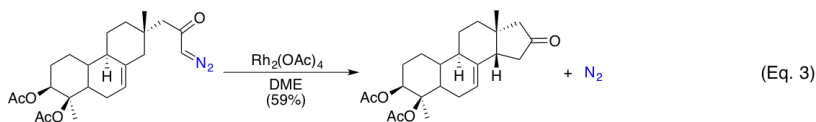


Figure 1.24: Examples of regioselective, eq. 3,¹²⁰ chemoselective, eq. 4 and 5,¹²¹ intramolecular reactions by dirhodium(II) carbene catalysts. Abbreviations: pfb=perfluorobutyrate; cap=caprolactamate.

In terms of stereoselectivity, the C-H insertion can be enantioselective by using chiral catalysts (see chemical equation (6) in Figure 1.25). The use of chiral ligands may also provide significant ligand-dependent diastereocontrol. This is illustrated in the lower part of Figure 1.25 with the reaction of a chiral nonracemic 2-methylcyclohexyl with a dirhodium catalyst with a chiral carboxamide ligand, **28**. The configuration of the chiral carboxamide ligand on the catalyst determines the direction of approach of the C-H bond to the carbene center, which produces different diastereomeric ratio of products.

Being able to control intermolecular transformations is better than having to perform intramolecular reactions for synthetic applications in terms of molecular and synthetic economy because the sequence of steps and reagents required to

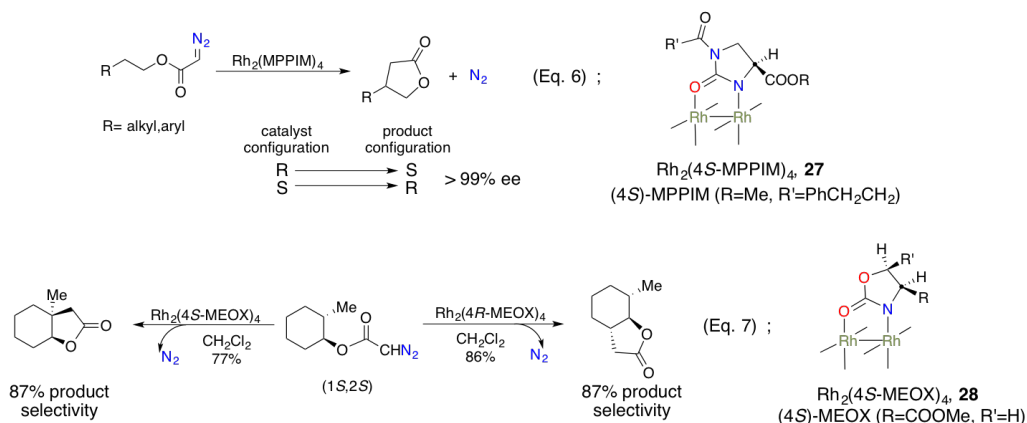


Figure 1.25: Examples of enantioselective, eq. 6,¹¹² and diastereoselective, eq. 7,¹²² intramolecular reactions by dirhodium(II) carbene catalysts. Catalysts **27** and **28**¹²³ are chiral dirhodium(II) carboxamidate catalysts, formed by chiral imidazolidinate and chiral oxazolidinate ligands, respectively. Abbreviations: 4*S*-MPPIM=methyl 1-(3-phenylpropanoyl)-2-oxoimidazolidine-4(*S*)-carboxylate; 4*S*-MEOX=methyl 2-oxooxazolidine-4(*S*)-carboxylate.

synthesize the substrate for an intramolecular reaction would no longer be needed. However, controlling the chemoselectivity and regioselectivity of intermolecular carbene C-H insertions has been a more difficult challenge. On the basis of early investigations, it was said that “Intermolecular C-H insertion reactions... are not synthetically useful”¹⁰⁸ because regioselective and chemoselective reactions could not be obtained. The typical carbene source used in intermolecular transformation was ethyl diazoacetate (EDA), an electron acceptor diazo compound (see Figure 1.27). Using EDA as the carbene source, the electrophilic character of metal carbenoids is reinforced by the corresponding electron-withdrawing ester group of the EDA and the system strengthens its high reactivity and poor chemo- and regioselectivity. It was not until the 2000s when successful strategies to attenuate the carbenoid too high reactivity were reached. First advances were obtained by Pérez and Lovely who, keeping EDA as the carbene source, reported cooper-^{124,125} and silver-based¹²⁶ complexes containing trispyrazolylborate and trispyrazolylmethane ligands able to functionalize cycloalkanes (Figure 1.26). These works served as renaissance of copper as catalyst for such transformation and reported a suitable new family of ligands to be explored for intermolecular C-H bond functionalizations. However, the major breakthrough to achieve intermolecular C-H bond functionalizations was the discovery that carbenoids functionalized with donor and acceptor groups (Figure 1.27) were much more

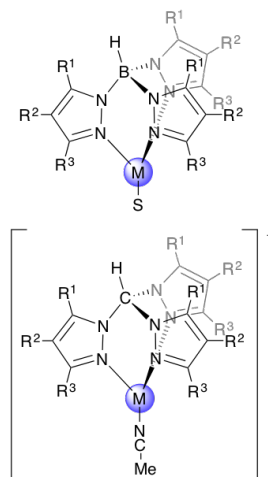


Figure 1.26: Structures of cooper- and silver-trispyrazolylborane (above) and trispyrazolylmethane (below) complexes reported as catalysts for the functionalization of C-H bonds by carbene insertion.

1.2 ACTIVATION AND FUNCTIONALIZATION OF C-H BONDS

regio- and chemoselective than the traditional carbenoids.

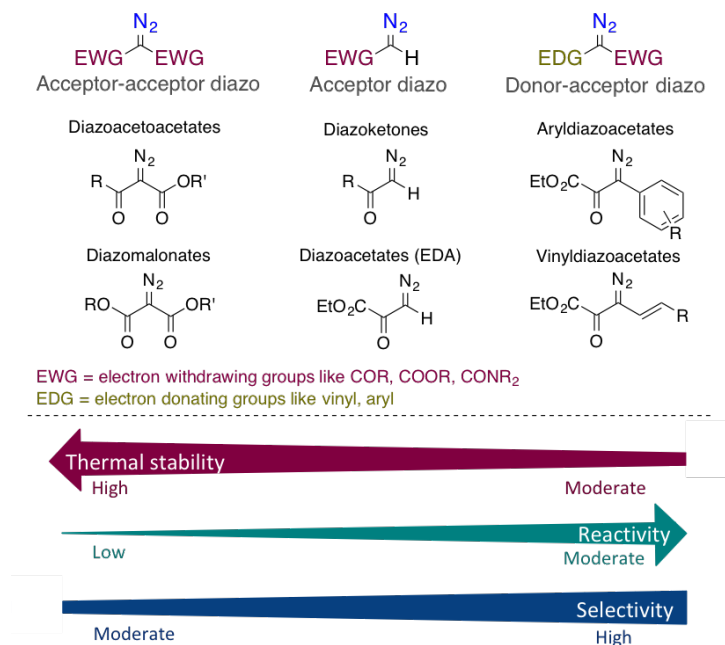
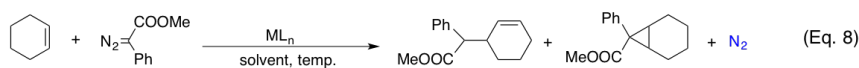


Figure 1.27: Classification of different groups of diazo compounds with a couple of examples for each group (upper part). Below, an overview of their properties is presented.

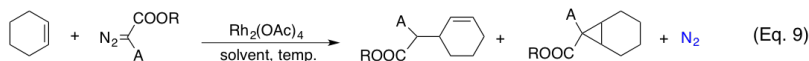
Typical donor/acceptor-substituted metal carbenes used were aryl- and vinyl-diazoacetates.¹²⁷ Phenyl and vinyl groups bound to the carbene carbon are able to dissipate charge so that the intermediate metal carbene has a later C-H activation transition state than their counterparts with diazoacetates. In general, the success of metal-carbene selectivity is due to a balance between activation and stabilization caused by the ligated metal and carbene substituents, and the steric and electronic demands of the C-H bond that is activated.

An example of the scope of catalyst and carbene chemoselectivity in intermolecular carbene insertion reactions is illustrated in Figure 1.28. The scheme shows the competition between the allylic C-H insertion and cyclopropanation of cyclohexene.¹²⁸ When double bonds are present in the hydrocarbon substrate, cyclopropanation reactions are usually the preferred option. Despite the ratio of products obtained reveals dependence on the dirhodium(II) catalyst, the dependence on the diazo compound is highly important because some diazo compounds are able to reverse the trend towards cyclopropanation, leading to a favorable allylic C-H insertion.

In Figure 1.28, irrespective of the diazo compound used, no complete chemoselective reactions are achieved (chemical equation (9)). However, other examples where complete chemoselective reactions are achieved just using donor/acceptor-substituted metal carbenes are reported. For example, with 1,4-cyclohexadiene, the product from C-H insertion is the sole outcome from dirhodium(II)-catalyzed



Rh ₂ (OAc) ₄ , 22	75	25
Rh ₂ (pfb) ₄	87	13
Rh ₂ (5S-PHOX) ₄ , 29	66 (4% ee)	34
Rh ₂ (5S-MEPY) ₄ , 30	93 (45% ee)	7
Rh ₂ (S-PTTL) ₄ , 25	50 (53% ee)	50
Rh ₂ (S-DOSP) ₄ , 24	80 (75% ee)	20



R = Et, A = H	20	80
R = BHT, A = H	67	33
R = Me, A = COOMe	38	62
R = Me, A = Ph	75	25
R = Me, A = 4-NO ₂ C ₆ H ₄	69	31

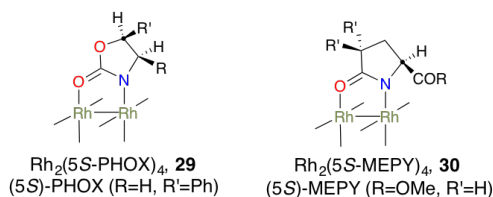


Figure 1.28: Examples of chemoselectivity in intermolecular carbene insertion reactions.¹²⁸ Chemical equation (8) illustrates catalyst chemoselectivity, while chemical equation (9) illustrates carbene chemoselectivity. Below, the structures of catalysts **29** and **30** are presented. Both are chiral dirhodium(II) carboxamide catalysts, formed by chiral oxazolidinate and chiral pyrrolidinate ligands, respectively. Abbreviations: 5S-PHOX= 5-phenyloxazolidin-2-one; 5S-MEPY= methyl 2-pyrrolidone-5(*S*)-carboxylate.

reactions with methyl phenyldiazoacetate.^{127,128} In intermolecular reactions, regioselectivity is also highly influenced by the electronic effects produced by groups adjacent to the C-H bond of the substrate.¹¹²

In terms of stereoselectivity, similar strategies than in intramolecular reactions are used. The use of chiral catalysts and/or substrates, chiral auxiliaries on phenyldiazoacetates, or substituents on the aryl group of aryldiazoacetates can influence diastereoselectivity.¹¹² Enantiocontrol is generally enhanced at lower temperatures and in hydrocarbon solvents.^{129–132}

Carbene insertion into aromatic C(sp²)-H bonds

The formal insertion of the carbene moiety into aromatic C(sp²)-H bonds deserves a particular mention. This is a reaction that can be readily promoted in an intramolecular manner,¹⁰⁹ but achieving a chemoselective intermolecular reaction has been a challenge until very recently. The few precedents of carbene-insertion reactions into aromatic C(sp²)-H bonds were obtained using rhodium-based catalyst and elaborate diazo compounds.^{133,134} However, its selectivity was very low and a significant advance arrived from the use of a new group of catalysts that contains an N-heterocyclic carbene (NHC) ligand by Prof. Pérez group (see Figure 1.29).¹³⁵ In this new group of catalysts, the ligand coordinates the metal

1.2 ACTIVATION AND FUNCTIONALIZATION OF C-H BONDS

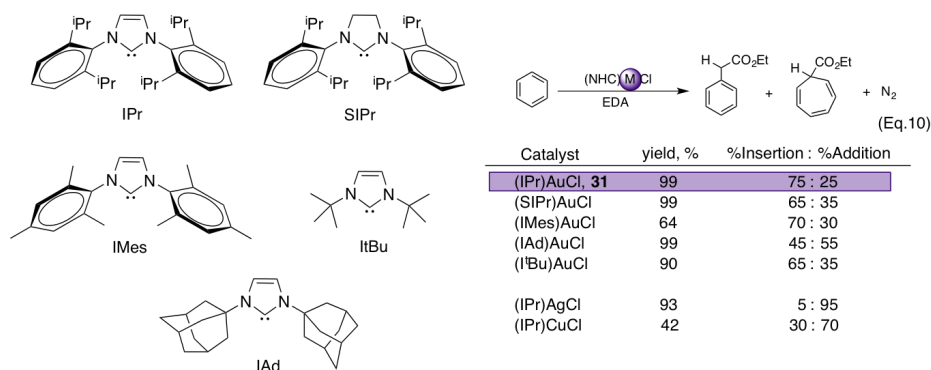


Figure 1.29: Structures of some NHC ligands used by Prof. Pérez group for carbene-transfer reactions (left) and examples of the reactivity of the corresponding catalysts (right). Reactivity data from refs. 136,137 and 139. Abbreviations: IPr= 1,3-bis(2,6-diisopropylphenyl)imidazol-2-ylidene; SIPr= 1,3-bis(diisopropylphenyl)imidazol-2-ylidene; IMes= 1,3-bis(2,4,6-trimethylphenyl)imidazol-2-ylidene; ItBu= 1,3-di-*t*-butylimidazol-2-ylidene; IAd= 1,3-di(1-adamantyl)imidazol-2-ylidene.

through just one carbon donor from an N-heterocyclic carbene. Its selectivity has been tested by several reaction conditions and metals (Cu, Ag, and Au) and the best results were obtained using the IPrAuCl (**31**) + NaBAR₄ system, where insertion products were obtained with 75% yield, along with some amount of cycloheptatriene products (see Figure 1.29).^{136–139}

A complete chemoselective reaction using plain benzene as substrate was not achieved until the past year, 2016, when our collaborators reported >99% insertion selectivity using Fe and Mn catalyst and a family of tetradentate N-based ligands that leave two *cis* vacant coordination positions (Figure 1.30).¹⁴⁰ Beside achieving a total insertion chemoselectivity, this work expanded to Fe and Mn the direct functionalization of aromatic C(sp²)-H bonds by metal-carbenes, a reaction that was usually performed by rhodium- or gold-based catalysts.

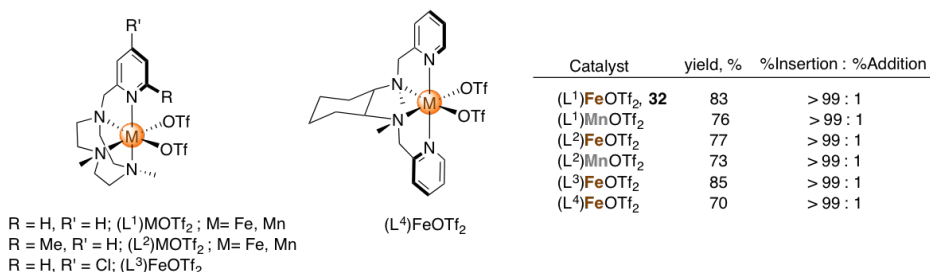


Figure 1.30: Examples of the complexes employed as catalysts in ref. 140 (left) and an overview of their reactivity towards carbene-transfer reactions (right).

A different strategy to achieve a chemoselective insertion of the carbene group into aromatic C(sp²)-H bonds consists in using electron-rich benzene derivatives such as phenols or anisole. The addition of these π-electron-donating groups (-OH and -OCH₃) to benzene enhances the nucleophilic character of the aromatic

ring and favors the electrophilic attack of the carbene moiety to the low reactive aromatic C(sp²)-H bonds. The combination of activated benzene substrates with electron-deficient phosphite derivative ligands that increase the electrophilic character of the carbene moiety in gold catalysts enabled chemoselective functionalization of aromatic C-H bonds.^{141,142} However, the inclusion of substituents in benzene can promote the reaction of the carbene with the substituents instead of the carbene insertion into the aromatic C(sp²)-H bond.^{143–145} Specifically, gold-catalysts have been the only ones able to functionalize aromatic C-H bonds using this strategy, unlike copper, palladium, and rhodium catalysts.

Finally, a new trend in metal-carbene catalysts that is worth to mention is the use of biomimetic porphyrin ligands. A pioneer study of You appeared in 2002,¹⁴⁶ but a revival of porphyrin carbenes as catalytic reagents was not reported until the current decade. However, research using these catalysts is still at an early stage where their electronic structures and associated reactivities are poorly understood. Thus, most of the reported studies focus on their electronic structure and basic reactivity. The broadest studied porphyrin carbene catalysts use iron and cobalt metals, and they reveal a quite remarkably electronic property: an intrinsic “redox noninnocent” behavior of the carbene ligand, which has a clear carbon-radical (carbene-radical) character (Figure 1.31).^{147–152} Regarding reactivity, the reaction most often reported is the cyclopropanation of olefins (C=C bond functionalization),^{146,147,153} while C-H bond functionalization reactions by carbene insertion using these catalysts have just occasionally been described. For example, Bas de Bruin described intramolecular C-H bond functionalization by cobalt porphyrin carbenes¹⁵³ and You, already in 2002, described intermolecular C-H bond insertion reaction by iron porphyrin carbenes with alkenes or tetrahydrofuran.¹⁴⁶

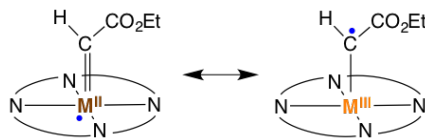


Figure 1.31: Redox noninnocent behavior of carbene ligands in an initial $M^{II}(\text{por})$ catalyst. M accounts for Co, Rh, or Fe, and the ellipse represents a porphyrinic ligand.

Nevertheless, perhaps the major achievement related with iron-phorphyrin carbenes’ catalysis has been achieved moving from biomimetic catalysts to biocatalysts. It was accomplished by Arnold’s group, that developed a biocatalytic method for cyclopropanation of styrenes in the presence of diazo compounds using engineered variants of cytochrome P450.^{154,155} Despite carbene transfer processes to olefins have no biological counterpart, this work highlighted the capacity to adapt existing enzymes for the catalysis of synthetically important reactions not previously observed in nature and motivates further studies focused on biomimetic iron porphyrin carbenes.

On the mechanism of C-H bond carbene insertion

The [fourth chapter](#) of this thesis addresses the carbene insertion mechanism into aromatic C(sp²)-H bonds. Specifically, the studied reaction involves the [(PyTACN)FeX₂] catalyst, **32**, (where X=Cl or OTf) in a solvent mixture of benzene:dichloromethane, using ethyl diazoacetate as carbene source and an ex-

1.2 ACTIVATION AND FUNCTIONALIZATION OF C-H BONDS

cess of NaBAR_4^F . This system belongs to a series of iron and manganese catalysts with tetradentate aminopyridine ligands that are the only ones reported as far able to chemoselectively functionalize non-activated-benzene $\text{C}(\text{sp}^2)\text{-H}$ bonds by carbene insertion.¹⁴⁰

Taking into account previous studies, once the carbene moiety is formed, aromatic $\text{C}(\text{sp}^2)\text{-H}$ and alkyl $\text{C}(\text{sp}^3)\text{-H}$ bonds follow different pathways for the C-H bond activation and functionalization (Figure 1.32). While $\text{C}(\text{sp}^2)\text{-H}$ bonds follow a stepwise mechanism where the aromatic carbons (C_{bz}) undergoes an initial electrophilic addition by the carbene carbon (C_{carb}) which leads to an intermediate with a $\text{C}_{carb}\text{-C}_{bz}$ bond; $\text{C}(\text{sp}^3)\text{-H}$ bonds follow a concerted mechanism via a three-centered transition state that directly leads to the insertion product. This conclusion has been recently reported comparing aromatic $\text{C}(\text{sp}^2)\text{-H}$ and alkyl $\text{C}(\text{sp}^3)\text{-H}$ bonds activation for gold carbenes,¹⁵⁶ and can also be obtained comparing the mechanistic literature of the reactions of Au, Cu, Ag or Rh carbenes with alkanes^{157,158} and with aromatic compounds.^{139,159} Assuming the stepwise mechanism, when the intermediate with the $\text{C}_{carb}\text{-C}_{bz}$ bond is formed, it can evolve through two different products: toward final insertion products or toward expansion ones. The classical mechanism to achieve insertion products involves the direct hydrogen migration between the two carbons that form the $\text{C}_{carb}\text{-C}_{bz}$ bond, the called [1,2]-H shift. Conversely, the classical mechanism to achieve expansion products involves a second $\text{C}_{carb}\text{-C}_{bz}$ bond formation with an adjacent carbon of the phenyl. These mechanisms and others had been taken into account in section 4.2 to reveal the mechanistic reasons why our nonheme iron carbene catalysts perform chemoselective aromatic $\text{C}(\text{sp}^2)\text{-H}$ bond carbene insertion on single benzene substrates.

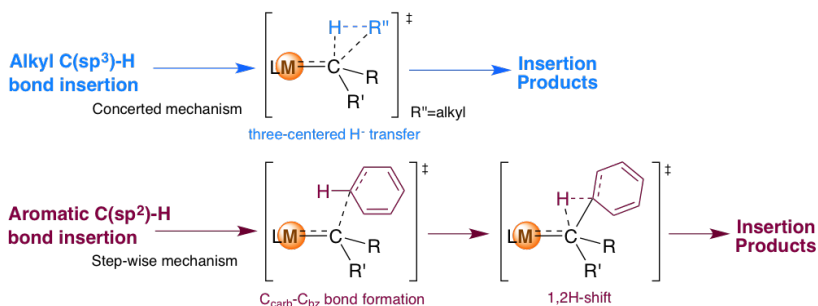


Figure 1.32: Classic carbene insertion mechanisms of alkyl and aromatic substrates.

1.3 Oxidation States

As we have already introduced in [subsection 1.1.1](#), transition metals can play a very important role in catalytic reactions where oxidation and reduction processes are crucial, like in C-H and C-C bonds functionalization reactions. Therefore, the use of TM represented the main revolution in synthetic chemistry throughout the entire 20th century. One of the most important attributes to determine in these reactions is the assignment of the proper formal oxidation state, OS, of the catalyst and key intermediates. The changes in the OS are key information to properly understand the mechanism and to predict the reactivity of the catalyst and the transformations it may perform.

The OS concept is essential in chemistry for various purposes. In organometallic catalysis, for example, the OS concept is: i) the formalized basis for balancing redox equations; ii) an intrinsic descriptor of the reaction mechanism; iii) a parameter in chemical nomenclature; and iv) a value related to *d*-electron configurations of TM compounds that can be obtained from spectroscopic characterizations. Thus, the complete fingerprint of a chemical reaction is not complete until the determination of the OSs of the species involved. Therefore, it is relevant to focus part of this thesis on the work we developed in Girona related with oxidation state's determination ([chapter 5](#)).

1.3.1 The oxidation state concept

Within the fundamental ordering principle of the Periodic Table, the concept of oxidation states is one of the most important classifications in Chemistry,^{160,161} and other branches of science like physics (spectroscopy), biology, and medicine. The origin of the oxidation state concept is prior to the development of the electronic theory of chemical bonding; thus, and not surprisingly, there had been many words devoted to this topic over the years.

Its origin dates back about 200 years ago, when it was described as the increase in the amount of oxygen bound by elements that form more than one oxide. Wöhler spoke about "oxydationsstufe" (an older German spelling for oxidation grade) in his textbook *Unorganische Chemie* already in 1835;¹⁶² and this expression remains in use for oxidation state in several languages. Skipping to the 20th century, Latimer appears to be the first to officially introduce "oxidation number" or "oxidation state" concept within the context of redox half-reactions.¹⁶³ And later, Jørgensen devoted a whole book to the concept,¹⁶⁴ where he distinguished between the formal oxidation state, defined by a number of well-known, simple rules, and a physical or spectroscopic oxidation state.

If we focus on transition metal complexes, already Jørgensen in his book,¹⁶⁴ and later Hegedus¹⁶⁵ defined the formal oxidation state of the central atom of the TM complex as "*the charge remaining when the ligands have all been removed in their most stable closed-shell form*". This definition implies that the bonding electron pairs between the central atom and the ligands have been assigned exclusively to the most electronegative bonding partner, assuming that ligands are *always* more electronegative than the TM. However, at that time, IUPAC's "Gold Book" was just offering a general set of rules on how to assign OSs and no formal

1.3 OXIDATION STATES

definition.^{166,167} Rather than giving a formal OS definition, only the so-called oxidation number was defined for compounds with central atoms and ligands. The terse dedication to the topic by IUPAC till 2014 may have contributed to some of the debate and polemics about oxidation state misconceptions and meaning.

Already in the 21st century, Jansen and Wedig¹⁶⁸ point out the heuristic nature of the oxidation-state assignation and suggest that “*concepts need to be defined as precisely as possible, and these definitions must always be kept in mind during applications*”. A pertinent example for bioinorganic chemistry is the famous “Compound I” in the heme enzyme P450_{cam}. This important reactive intermediate has often been described as an oxo-Fe^V-porphyrin complex. However, closer examinations by quantum-chemical methods indicated that the system is more appropriately described as a Fe^{IV} oxo complex with a porphyrin radical cation (the Fe^V-type state is computed too high in energy to play a significant mechanistic role).^{169,170} In this direction, many other authors have advocated for a consensual approach to determine formal OSs. Steinborn¹⁷¹ and Loock,¹⁷² for example, recommended Pauling’s approach of assigning shared electron pairs to the more electronegative atom to determine OSs. ^c Finally, in 2014, an IUPAC Technical Report on OS was published to provide a new unambiguous generic definition of OS.¹⁷³

According ref. 173, the oxidation state is “*the atom’s charge after ionic approximation of its heteronuclear bonds*”. This definition, however, implies that, at least, two terms have to be clarified: “atom’s charge” and “ionic approximation”.^d

The atom’s charge is the difference between the current count of electrons and the electrons of the free atom. However, the oxidation state is a quantitative concept that operates on integer values of counted electrons. Thus, to get the number of electrons that define the OS, it may require idealizing visual representations or rounding off numerical results per bond.¹⁷⁵ So, in this context, the determination of the *atom’s charge* as partial or average atomic charges obtained by experimental or theoretical analysis of the electron density without performing any kind of ionic approximation will not retrieve the formal OS except for the most ionic situations.¹⁷⁶ In this sense, the ionic approximation is the criteria used to assign all the electrons of the system to properly define the oxidation states.

The ionic approximation is illustrated in [Figure 1.33](#) according the MO-LCAO scheme (LCAO = linear combination of atomic orbitals). In the MO-LCAO scheme, the contribution by atom to the bonding MO is used as the criterion for ionic approximation. Thus, the atom contributing more to each bonding molecular orbital receives all their electrons under the ionic approximation. That is to say, each MO defining a bond is considered as it was in an ionic situation.

^cThis recommendation from Steinborn and Loock was the first advance of the use of electronegativities (EN) as an approach to assign OSs.

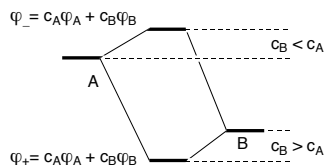
^d Since the end of June 2017 Karen’s definition of OS already appears in IUPAC, *Compendium of Chemical Terminology*.¹⁷⁴ However, for more than 20 years, the OS was just defined as the number resulting from an agreed-upon set of rules.

- **Bondless approach. Direct Ionic Approximation:** Electrons assigned to individual atoms according to their decreasing EN until the complete number of valence electrons.



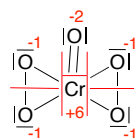
- **Bond Approach:** Requires a structural formula and the definition of bonds.

MO coefficients



Allen Electronegativity, EN

Moving Bonds



Summing ionized bond orders

$$\text{OS} = \text{iBOS} + \text{FC}$$

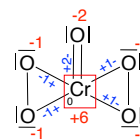
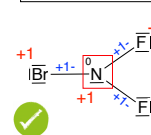


Figure 1.33: Approaches to determine the OS by using the IA. In the bondless approach the OS is determined from the empirical formula of the compound, without building the structural formula, and avoiding bonds. There are two variants of the application of the EN-based approach. In the *algorithm of summing bond orders* the iBOS (ionized bond order sum) term is the sum of bond orders weighted with the ionic-approximation sign (blue values); and the FC term is the formal charge of the atom in the Lewis formula (black values). Red values are OS values and red lines are bonding partitions related with the assignment of OSs.

However, complicate MO schemes will make the above criterion impracticable in many cases. For example, when the LCAO is too complex or when theoretical post-HF methods are used to figure out them. Moreover, it should be noted that orbital energies are strongly method dependent. Therefore, among several possible approaches to assign the bonding electrons, at the end the electronegativity (EN) difference was chosen as the best viable option to capture the essence of the ionic approximation. Nevertheless, the existence of several EN scales that assign different EN values to an element, leads the need to choose the appropriate one for the ionic approximation scheme. In a nutshell, Allen electronegativity is chosen in ref. 173 as the most suitable one. Allen EN is defined as the average one-electron energy of the valence-shell electrons of the *free* atom in its ground state.^{177–179} Thus, Allen EN can be considered an intrinsic *free* atom property, rather than an *in situ* atom-in-molecule property dependent on the atom environment or, even more important, on the atom's OS.^e The Mulliken EN scale, for example, depends on OS and it is an example of an inappropriate EN scale for this issue. The values of Mulliken EN depend on the orbital hybridization of the atom which, in turn, could depend on the OS assignment. For example, the Mulliken EN values for the carbon atom are: $C(\text{sp}^3)=2.45$, $C(\text{sp}^2)=2.69$, and $C(\text{sp})=3.17$. Therefore, the use of EN scales that depend on OS to assign OS implies a circular argument and a dilemma that invalidate their use for OS assignments.^f

Figure 1.33 overviews the approaches to assign OS using the ionic approximation scheme according ref. 173. We can distinguish two main options: a) by

^e The advantage of Allen EN of being expressed as an intrinsic *free* atom property that is independent of the atom environment also entails a shortcoming because, as we will see and it can be expected, the chemical environment may affect the OS assignment.

^f Providing a short overview of the vast field of EN is out from the scope of this thesis and interested readers are directed to relevant reviews.^{180–182} There are ongoing discussions concerning what exactly EN is and which is the best way to obtain it.

1.3 OXIDATION STATES

using the generic definition, which means the mixing coefficients approach; or b) by using the EN-based approach. In turn, the application of the EN-based approach can be carried out using a bond approach or a bondless approach (also called direct ionic approximation (DIA) algorithm). Further details of the different approaches presented in [Figure 1.33](#) to apply the IA will not be commented in detail here in order to not move too far away from our topic.

Although the need of an unambiguous definition of OS and schemes to obtain its numerical value has been covered with the publication of the last IUPAC Technical Report on OS;¹⁷³ ambiguities and exceptions of the IA scheme have already been encountered. Some of the exceptions set out were already commented on ref. 173, but others have not been previously commented and they are part of the work we have been done in Girona on quantum-chemical predictions of OSs.

One of the most important exceptions, already commented in Karen's work,^{173,175} is the use of the EN-based approach to determine the OS in Lewis acid (LA) - Lewis base (LB) adducts where the more electronegative atom is the reversibly bonded Lewis acid (the so called Z-ligand). If we apply the EN-based approach to determine the OS of these type of adducts, the electrons of the adduct are assigned to the LA ligand. On the contrary, using the generic definition of IA, *i.e.*, the mixing coefficient approach, the acceptor orbital of the LA atom is high, and the less-electronegative LB donor atom retains the electrons because of its larger contribution to the bonding MO. Therefore, using the mixing coefficient approach, the adduct electrons are assigned to the LB ligand, and there is a mismatch between the two approaches. In these cases the correct OS is given by the mixing coefficients approach, since its results usually agree more with spectroscopic (Mössbauer) data.¹⁸³⁻¹⁸⁵

Other important limitation of using the EN-based approach to determine the OS takes places when carbene complexes are analyzed. Allen EN of carbon is higher than TM electronegativities. Thus, the electrons of the metal-carbene bond are always assigned to the carbene moiety and its OS will be -2, while the OS of the metal is always increased by a +2 charge. However, this rigid description is clearly insufficient because it cannot depict the two typical bonding situations described for Fischer or Schrock carbenes. The metal-carbene bonding in Schrock carbenes is described as a covalent double bond between a triplet carbene and a triplet metal fragment (see top right of [Figure 1.34](#)). This model does not imply pure donor-acceptor interactions and, after the double bond deconstruction, the sigma and pi bond electrons are assigned to the carbene moiety. Therefore, the carbene is viewed as a four-electron donor carbene, CR_2^{2-} , and the metal fragment as a cationic L_nM^{q+2} moiety ([Figure 1.34](#)). Thus, the carbene complex can also be defined as an alkylidene and the assignation of OSs using the EN-based approach of IA agrees with the Schrock carbene model. However, the metal-carbene bonding in Fischer carbenes has a different nature. On one side, the unbounded electrons of the singlet carbene ligand form a ligand→metal σ donation bond. On the other side, a metal→ligand π back-donation bond arises from the *d* electrons of the metal (see top left of [Figure 1.34](#)). A dominant influence of the metal fragment on the π back-donation bond of Fischer carbenes

has been already postulated by Cundari and Gordon¹⁸⁶ and by Vyboshchikov and Frenking,^{187–189} by means of charge-density analysis (CDA),¹⁹⁰ during the nineties. Therefore, Fischer carbenes after the double bond deconstruction are viewed as a neutral carbene, CR_2^0 , and a $q+0$ metal fragment, L_nM^{q+0} (*i.e.*, σ bond electrons are assigned to the carbene whereas the π bond electrons are assigned to the metal) (Figure 1.34). Thus, the EN-based approach of IA is not able to retrieve this situation, where each bond of a double bond

has its own opposite ionic decomposition. Besides, despite the use of the mixing coefficient approach may work for the correct description of the OSs of Fischer and Schrock carbenes, it is not considered a possibility in ref. 173.

Apart from the previous commented exception and limitations of EN-based IA, other situations where IA leads to ambiguous OS (multiple OS or intermediate OS values are possible) have already been encountered and reported in ref. 173. Examples of such situations are complexes with non-innocent ligands, haptocomplexes or molecules with hard-to-resolve bond orders.

A direct consequence of operating a bond based approach of IA (*i.e.* the mixing coefficients approach or the EN-based approach) is that the OS analysis is dependent on the connectivity or the initial Lewis structure we awarded to the molecule. Thus, non-innocent ligands that allow several chemically feasible electronic configurations or molecules with ambiguous bond orders agree with several bonding patterns that, in turn, may originate different OSs after the application of the IA. The NO ligand, the hemoglobin's heme ligand, or the case of 1*H*-pentazole (HN_5) are examples of these situations. Regarding the non-innocent NO ligand, for example, it can act either as an $|\text{N}\equiv\text{O}|^+$ cation with $\text{OS}_\text{N} = +3$,[§] as an $|\text{N}=\text{O}|^-$ anion with $\text{OS}_\text{N} = +1$, or as the radical octet-violating yet neutral nitrogen-monoxide with $\text{OS}_\text{N} = +2$. In this ligand, however, the MNO bond angle varies in between linear for the $|\text{N}\equiv\text{O}|^+$ case to bent (tetrahedral-angle values) for $|\text{N}=\text{O}|^-$. Then, the corresponding electronic configuration can be easily de-

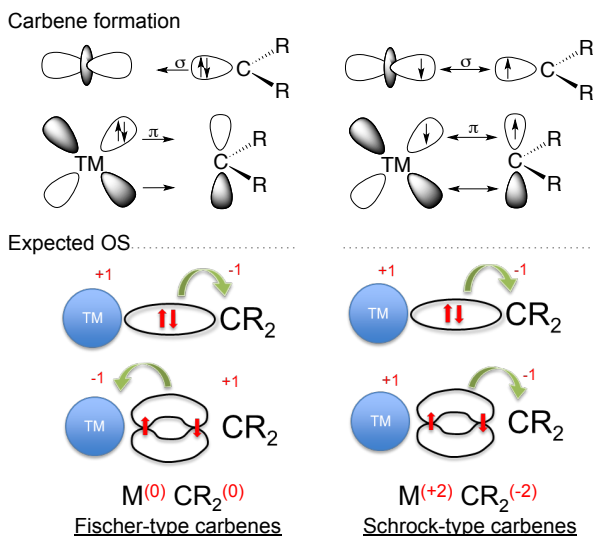


Figure 1.34: Schematic representations of the dominant orbital interactions to carbene formation (upper part), and the carbene double-bond decomposition to OS assignment (lower part) in: (left) Fischer-type carbene complexes and (right) Schrock-type carbene complexes.

[§] Subscript denotes the atom or fragment for which the OS is defined.

1.3 OXIDATION STATES

terminated by means of X-ray spectroscopy.^{191,192}

For the *1H*-pentazole, in contrast, ambiguity results from changes in the geometrical parameters. With almost equal NN bond distances along the ring,¹⁹³ a Lewis formula with full aromatic conjugation is the one that agrees more with the experimental data. However, a fully aromatic configuration is not enough to describe the molecule according its bond distances (left in [Figure 1.35](#)), and an alternative localized Lewis structure is also necessary. Thus, two limiting connectivity and Lewis formulas can be drawn, leading to two different valid OS sets by the IA ([Figure 1.35](#)). The OS set on the localized formula agrees with the rule that an atom bonded solely to atoms of the same element has OS=0 if the 8-N rule is obeyed. The OS set on the aromatic formula would be the one to use for electrochemistry. Therefore, the IA criteria lead to an ambiguous OS assignment in this situation.

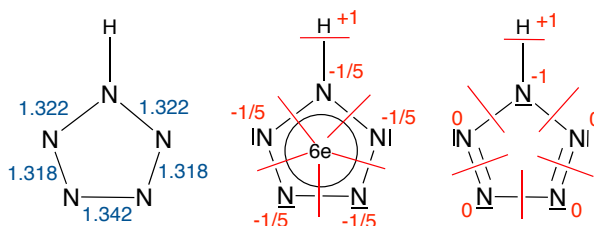


Figure 1.35: *1H*-pentazole, HN_5 . Calculated bond lengths (in Å) (left),¹⁹⁴ and OS assignment in the two limiting Lewis formulas: aromatic (center) and localized (right)

Haptocomplexes, TM π -complexes of aromatic rings or conjugated chains, can also lead to ambiguous OS. According to ref. 173, some additional rules for Lewis formula construction are needed to assign the ionic charge of the haptoligand, which may lead to ambiguous situations. However, when the ionic charge and the hapticity are assigned, a straightforward OS assignment is proposed. As it will be explained in [chapter 5](#), the simple scheme suggested in ref. 173 is insufficient and originates mismatches between predicted and experimental OSs.^{195,196} According our results, we suggest that other considerations such the local spin state or the flatness of the haptoligand also must be taken into account for the OS assignment.

The general overview on OS assignment described above has prompted the use of state-of-the-art quantum-chemical methods for the OS determination. Jørgensen in the 1980s already suggested the use of quantum-chemical methods for that goal, however being pessimistic then about the practical implementation.¹⁹⁷ Nevertheless, since then, quantum-chemical methods have achieved a level of accuracy that allows the successful prediction of the existence or nonexistence of certain non-usual molecular species with different OSs. Then, the achievement of getting accurate information is done, and the computational prediction of OSs should be possible.

1.3.2 Computational determination of OSs

Many methods have been used to determine the OS. The use of geometry parameters may well be the simplest way to characterize them in metal complexes. Geometry and OS often tend to correlate and, in this sense, the bond valence sum (BVS) method is used.¹⁹⁸ This method uses the metal-ligand distance (R_1), which is compared with empirical reference values (R_0) of systems with known OSs to determine them. However, the determination of R_0 values limits the applicability of the method to systems with known bonding patterns. Furthermore, it is known that, for some species (particularly for species with bulky ligands), there is not a correlation pattern between metal-ligand distances and OS.¹⁹⁹ Therefore, bearing in mind that the oxidation state is a direct consequence of the electronic structure of the compound, different techniques for estimating OSs from analyses of the local electron distribution have been proposed.

Regarding electronic-structure based techniques, a typical scheme is the allocation of partial atomic charges by computational schemes and use the results to infer the OS.

Partial atomic charges are computed as the difference between the atomic Z number and the integrated number of electrons per atom (\mathbf{N}_A), (1.2).

$$Z_A - N_A = q_A \quad (1.2)$$

Then, \mathbf{N}_A , the average number of electrons per atom, is the term that should be quantified. It can be obtained by the partition of the electron density function in atomic terms since the whole function integrates to the total number of electrons of the system (\mathbf{N}_e), (1.3).

$$\int \rho(\vec{r}) d\vec{r} = N_e \quad (1.3)$$

There are many schemes to decompose the electron density in atomic contributions. According to Sit *et al.*²⁰⁰ those schemes may be classified into the following categories: a) partition of the space (topological partitions) with integration of the total charge density within the space allocated to each atom (e.g. Bader or Voronoi charges); b) projection techniques of Hilbert space basis to each atom (e.g. Mulliken,²⁰¹ Löwdin,²⁰² or NBO²⁰³ charges); and c) matching techniques aimed at reproducing a computed property of the system (e.g. electrostatic potential (ESP) and restrained electrostatic potential (RESP) charges).

Each category has his main specific shortcoming in the determination of atomic contributions. In projection schemes, for example, there can be basis-set dependence or dependence on cutoffs used in some methods. In matching schemes, concerning ESP fitting methods, there is no good conformational transferability and unreasonable partial atomic charge values can be assigned to some buried atoms.^{204–207} Furthermore, despite topological partition schemes are the most suitable ones since they are not affected by the shortcomings already mentioned, there is no agreement between different topological partition methods, and different results may be obtained.

Besides the aforementioned practical drawbacks to determine \mathbf{N}_A or q_A , the key point is whether a relationship between partial atomic charges and oxidation

1.3 OXIDATION STATES

$$N_A = \int_A \rho(\vec{r}) d\vec{r} \quad (1.4a)$$

$$= \sum_{\mu \in A} \sum_{\nu} D_{\mu\nu} \chi_{\mu}^*(\vec{r}) \chi_{\nu}(\vec{r}) \quad (1.4b)$$

$$\Theta(\vec{r}) = \Theta_{el} + \sum_{ij} P_{ij} (\psi_i | V | \psi_j) \quad ; \quad (1.4c)$$

$$V(\vec{r}) = \sum_A \frac{Z_A}{|\vec{r} - \vec{R}_A|} - \sum_{ij} P_{ij} \int \frac{\Psi_i \Psi_j}{|\vec{r} - \vec{r}'|} d\vec{r}'$$

General expressions to obtain \mathbf{N}_A or q_A using topological schemes (1.4a), Hilbert-space-based schemes (1.4b), and a matching scheme (ESP)(1.4c).

states can be established. For example, in matching schemes, in many cases, there is no clear connection between the property matched and the OS, *e.g.* electrostatic potential surfaces. In partition schemes, in principle, an overall averaged partial atomic charge is obtained for each atom. Taking into account that the formal oxidation state is defined as the charge of the atom after applying the **ionic approximation** to its bonds, this means that a rounding off to obtain integer values is an inherent feature of OS and that working with pure non-integer values or averages is not a matching choice. However, aside from the conceptual inconsistencies of using atomic charges to infer OSs, the key motive of the disagreement is physical.

Several studies point that there is no physical relationship between static electric atom charges and oxidation states.²⁰⁸⁻²¹⁰ Raebiger *et al.*²⁰⁹ perform a series of theoretical first-principle calculations of the charges on single transition-metal atoms embedded in a large semiconducting or ionic matrix. They considered different oxidation states of the transition metal and studied how the net electronic charge belonging to the transition-metal atom was changing. The authors argued that the small changes in the net electronic charge belonging to a TM atom was essentially independent of its oxidation state due to the "negative feedback" mechanism. Thus, when a TM ion is reduced by any gain in local electron density, the metal-ligand orbital mixing between orbitals of the TM ion and those of the surrounding atoms compensate the gain in the local electron density of the metal by decreasing the electron donation to it, and vice versa. This leads to the conclusion that the allocated charge is a poor measure of the oxidation state of TM ions.

Another fundamental investigation of these two concepts (OS and atomic charges) was published by Aullon and Alvarez in 2009.²¹⁰ They studied several isoelectronic (d^0) compounds along the 3d transition-metal row (which all represent the highest possible oxidation state of the given metal) and compute the atomic charges of the central metallic atom. They observed that computed partial atomic charges show much less variability than the formal molecular oxidation state, conclusion in agreement with Raebiger *et al.* work.²⁰⁹ Furthermore, they also observed that the partial metal charge varies continuously as

the electronegativity of the ligands is varied, only becoming close to the formal oxidation state when the ligands have a high electronegativity. Thus, it means that the electronegativity difference between the ligand and the TM influences the final charge of the central atom and, again, that partial atomic charges must not be equated with the formal oxidation state except for the most ionic situations.

“What is the relationship between static electric charges and oxidation states? None.”

Resta, R. *Nature*, 2008, 453, 735.

Therefore, the procedure based on computing atomic charges (or the complementary integrated electron-density value per atom) to assign OS is not reliable, although unfortunately they are still used by some chemists to assign the OS.²¹¹

A different strategy that is also used to infer OS is checking the local spin density. The number of unpaired electrons in an atom (or fragment) can be used to deduce the OS. For example, if we have an organometallic Fe compound that could be Fe^{2+} or Fe^{3+} in an octahedral-like structure, three spin states are possible: low, intermediate, and high spin. In an ideal situation, these spin states correlate with singlet, triplet, and quintet spin-density values, respectively, in the Fe^{2+} situation; and with doublet, quartet, and sextuplet spin-density values in the Fe^{3+} situation. Thus, checking local atomic spin-density values, we could distinguish between oxidation states.

Despite local spin density could a priori be used to infer OS, on the contrary that partial atomic charges, in some cases there are also shortcomings that difficult their practical application for this purpose. For example, local spin-density values are not highly dependent on the partitioning scheme used; however, they highly depend on the level of theory and on the electronic state predicted. Other obvious but unavoidable *shortcoming* arises in closed-shell singlets, where the local spin-density value is zero in the whole compound and no extra information about the system is given by the spin-density matrix. Thus, despite local spin-density values may be enough to distinguish between two oxidation states in some cases, in other cases it may represent a limitation for the analysis, as it is pointed out in the above example. However, one of the main drawback of using local spin densities to infer OSs is that a prior knowledge of the system is necessary for the correct interpretation of the results. Prior knowledge about the global spin state, the geometry of the system and how this affects MO distribution, for example, is essential to determine which OS matches with the local spin-density values obtained.

The absence of a rigorous quantum-mechanical theory to determine the OS has questioned the status of OS as a physical quantity or merely as a “book-keeping tool” for a set of experimental properties.²¹² In turn, other investigation groups have proposed other schemes or methods to predict OS not based on atomic charges. Most of these schemes use the following features at some point: i) generation of some sets of localized orbitals; and ii) assignation of integer electrons of these orbitals to atoms. Thus, these proposed schemes seek to recover the rounding scheme of the OS concept.

As far as I know, four quantum-mechanical methods for OS determination are described in literature. In the following lines a brief description of them is given, comparing their applicability, strengths, and weaknesses.

1. Centroids of Localized Orbitals:

This method was originally described to be used in plane-wave codes,²¹³ but it has recently been applied in MO-LCAO calculations, too.²¹⁴ In both situations, the method follows the same scheme. A new set of optimally localized orbitals (OLOs) are generated by using the Boys algorithm (*i.e.* by minimizing the radial extend of the corresponding functions/orbitals).²¹⁵ In plane-wave codes, these functions are called maximally localized generalized Wannier functions (MLWFs)²¹⁶ because they are obtained from the corresponding Wannier functions and span the same space as the specified set of Bloch bands. Then, the center of gravity of the MLWFs (or equivalent localized molecular orbitals) are determined, the Wannier centers (WCs). The corresponding electrons of OLOs are entirely assigned to the atom closest to the center of gravity, based on the criterion of proximity.

Despite it is argued that the centroids obtained from localized molecular orbitals and their displacements may be used to determine OSs, as a fingerprint of the electronic structure, or to follow the movement of electrons during chemical reactions; benchmarking and deeper studies to confirm its applicability are missing. For example, all the published studies are based on organometallic bonds, no challenging systems (*e.g.* bimetallic systems, carbenes, haptocomplexes, LA-LB adducts, etc.) are studied, and it has not been discussed yet what may happen when covalent systems are analyzed.

Dr. Pedro Salvador personal communication: In X-H bonds (where X accounts for any atom except H), the center of gravity appears closest to the hydrogen atom in most situations, even in water. This issue, presumably due to an important difference between the size of X-atom electronic basin and the electronic basin of H, involves that hydrogens are always defined as hydrides. Thus, in the water molecule situation, the method defines hydrogens as H^- and the oxygen as O^0 , which is completely wrong. Therefore, the criterion of proximity to assign electrons is not always valid to assign the correct OS and should, at least, evolve and introduce general considerations.

2. Localized Orbital Bonding Analysis, LOBA:

This method, developed by Thom *et al.*²¹⁷ to be used in molecular codes, also creates a new set of localized orbitals using the Edmiston-Ruedenberg (ER) scheme, which maximize the electrostatic self-interaction of each orbital.²¹⁸ Then, to extract the chemical information from localized orbitals, they are decomposed in atomic contributions. A typical LOBA plot of the population analysis of generated localized orbitals is presented in [Figure 1.36](#). In order to finally assign electrons on atoms, a criterion to define the minimum contribution from which any given electron should be considered *localized* on an atom is needed, *i.e.* a threshold. The OS is calculated from the difference between the atomic Z number and the number of electrons the method assigns or *localizes* on the atom.

This method provides a pragmatic way to determine OS and uses a scheme (orbital localization + analysis of the atomic contributions of the orbitals) that resembles the OS definition. However, there is no rigorous criterion to support the choice of the cutoff percentage. Moreover, the method have just been only applied to a series of transition-metal complexes without further studies.²¹⁹

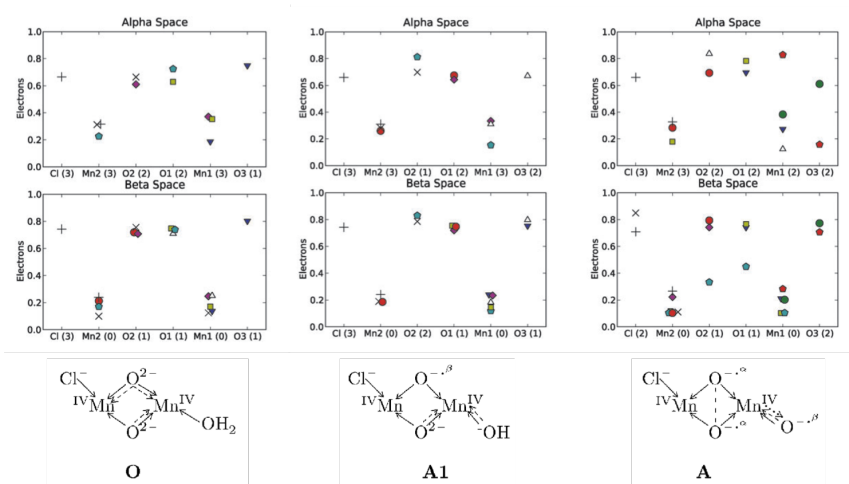


Figure 1.36: LOBA plots for the ClMnO₂MnO core of complexes **O**, **A1**, and **A** (from left to right) calculated with unrestricted B3LYP in a 6-31G* basis. O2 and O1 are bridging oxygens. Mn2 has the Cl ligand and Mn1 the initial water ligand, whose oxygen is labelled O3. Each symbol corresponds to a different localized orbital, plotting its population on each atom. For **A**, the definition of a threshold becomes subtle. Figure adapted with permission (ref. 217).

3. Projection on auxiliary basis:

This approach for determining OS was also developed by Sit et al. (as the Centroids-of-Localized-Orbitals method).²⁰⁰ Its applicability is limited to TM of the *d* block because it is based on determining the *d*-orbital contribution of TM-ligand bonds. In order to determine OS, the method follows these steps: i) occupied orbitals are projected onto an auxiliary set of atomic *d*-orbitals of the TM; ii) the occupation numbers obtained on the auxiliary atomic *d*-orbitals are calculated; and iii) the number of *d*-orbitals with full (or almost full) occupancy equates to the number of *d* electrons assigned to the metal ion. To conclude, from the number of *d* electrons assigned to the metal, the OS is determined. The same scheme was used by Knizia to determine oxidation states of transition-metal complexes using orthonormal intrinsic atomic orbitals (IAOs), instead of the *d*-orbitals basis, to project onto them the MO.²²⁰

The authors argue that, unlike LOBA method, this projection approach does not need a threshold because of the splitting between high and low occupation numbers of the *d*-orbitals is always high enough. Nevertheless, there is not any benchmark study dealing with challenging systems to support this point, because mainly standard systems (metal aquo, metal

1.3 OXIDATION STATES

carbonyl, or metal ciano complexes) have been studied. In addition, one of the main weakness of the method is related to its applicability: limited to systems with just one TM of the d -block. On systems with significant metal-metal bonds, the approach can introduce ambiguities and it is not recommended. On the other side, this method has not been described for f -block metals. Despite projections onto an auxiliary set of atomic f -orbitals might also work as an strategy to determine OS, the authors did not discuss this possibility.

4. **Effective Oxidation States, EOS:**²²¹

This method was developed at the University of Girona by the group of Dr. Pedro Salvador. The main characteristics of this approach are the set of localized orbitals used and how their occupation numbers are handled.

Regarding the set of localized orbitals, EOS method is based on the so-called **effective atomic orbitals** (eff-AOs) of Mayer, introduced for the first time by I. Mayer in 1996.²²² Conceptually, due to their construction, eff-AOs recover the “intraatomic” component of every MO from the diagonalization of the so-called atom’s net population.

Equations 1.5 show the expressions of atom A gross population (eq. 1.5a) and atom A net population (eq. 1.5b) into a 3-D space partitioning in the framework of the “fuzzy” or disjoint atom.

$$\rho^A = w_A(\vec{r})\rho(\vec{r}) \quad ; \text{Gross population} \quad (1.5a)$$

$$\rho^{AA} = w_A(\vec{r})w_A(\vec{r})\rho(\vec{r}) \quad ; \text{Net population} \quad (1.5b)$$

w^A accounts for the “fuzzy”-atom or disjoint-atom concept. It is a weight function that assigns a proportion of the global density to atom A on each point of the 3D space satisfying the requirement:

$$\sum_A w_A(\vec{r}) = 1. \quad (1.6)$$

Equations 1.5a and 1.5b allow us to clearly differentiate between gross and net population. While gross atomic populations recover the total electron density when they are summed over all atoms of the system, the net atomic population is a measure of the intraatomic density and, in order to recover the total electron density of the system, the overlap population has also to be taken into account. In subsection 2.3.2 these concepts are addressed in detail and contextualized in terms of space partitioning.

Once eff-AOs orbitals (or spin-orbitals if necessary) and their occupation numbers are generated, these are the ones used to determine OS. Specifically, **all** eff-AOs of the system are arranged by decreasing occupation number and filled by entire electrons until electrons are exhausted. From this procedure, the OS of each atom is determined as its atomic Z number minus the electrons assigned. Using this assignation scheme no threshold is needed. The *threshold* or limiting occupation-number value is different

in every case because it depends on all the other occupation-number values of the system.

However, using this procedure, when the number of atoms of the system is large or when the system involves many apolar bonds, pseudodegeneracies of the occupation numbers of the eff-AOs are likely to occur, which makes the assignation of EOS difficult. Also, in most cases, one is not interested in the OS of all atoms forming the system, but only in some of them or in groups of them, *i.e.* ligands of TM complexes. Therefore, EOS method also developed a fragment/ligand approach where, instead of eff-AOS, effective fragment orbitals can be defined.²²¹ The fragment approach allows us to focus the study in polar bonds where the concept of OS makes sense and extends the application of the method in most chemical systems.

Besides the aforementioned benefits of the EOS method against the other methods discussed in this section, EOS method is the only one that works with post-Hartree-Fock methods and correlated wavefunctions. Moreover, despite it has been developed to be used in molecular systems that use the LCAO formalism, it is potentially applicable to periodic systems that use plane-waves formalism.

In the [chapter 5](#) of this thesis, a detailed benchmarking study about EOS-method's applicability is presented.

1.4 Electron Distribution in Chemical Systems

In the [previous section](#) we have already introduced the use of partitioning techniques to analyze a feature derived from the electron distribution, the oxidation-state property. Stepping forward in the topic, we will devote this new section to general analyses of the electron distribution in chemical systems. A brief overview of quantum chemical techniques to study the electronic structure of chemical systems is presented, ending with a particular example of electron localization, the isolated electrons in electriles.

According to F. Jensen quotation: “*Chemistry is the science dealing with construction, transformation and properties of molecules.*”²²³ Thus, this section deals with the building block of chemistry according the previous quotation that has not yet been discussed in the thesis: the construction of molecules. In [section 1.2](#) we have considered molecule’s transformations, specifically the activation and functionalization of C-H bonds in hydrocarbons. In [section 1.3](#) we have discussed a molecular property, the oxidation state. Finally, in this section, we are going to focus on the electronic structure of matter by the analysis of the electron distribution.

1.4.1 Electron Distribution Analysis by Electron Partitioning Schemes

Once the chemical composition and the atomic coordinates of molecules are given, the remaining issue that should be defined to obtain the whole picture of the molecule is the electron distribution or the bonding pattern. Most interpretative analyses of the electron distribution (electron localization and delocalization) are based on partitioning techniques. In quantum chemistry, there are mainly two different types of partitioning analyzes according the function that is scrutinized: i) Hilbert-space partitions; and ii) real-space or molecular-space partitions.^h

When we work in the Hilbert-space, due to the fact that for non-periodic chemical systems the wavefunction is usually built using base functions centered in atoms, the electron partitioning of molecular system tends to be divided into atomic regions (or fragments formed by the addition of atomic regions). The typical example of a Hilbert-space partition that is centered on atoms is the Mulliken population analysis based on the MO-LCAO approach. In the MO-LCAO approach, the one-electron molecular orbitals (MO) are expanded on a finite set of atomic-centered functions $\{\chi_\mu(\vec{r})\}$ according:

$$\phi_i^{MO}(\vec{r}) = \sum_{\mu} c_{\mu i} \chi_{\mu}(\vec{r}) \quad . \quad (1.7)$$

The set of functions centered on a given atom conform an atomic Hilbert subspace $\{\chi_{\mu}(\vec{r})\}_{|\mu \in A}$.

^h A complete theoretical description of Hilbert-space and molecular-space partition is given in [section 2.3](#)

Other examples of Hilbert-space partitions centered on atoms are those derived from natural bond orbitals (NBOs),²⁰³ or many other localized orbitals that result from unitary (or similarity) transformations of MOs (or AOs). Examples of other atomic orbital-based partitions are those derived from the (charge) density localized molecular orbitals (DLMOs), which were defined by Niessen, W. von²²⁴ and are the orbitals that result from the unitary transformation of the canonical molecular orbitals (CMOs) that minimize the sum of the charge density overlap integrals between the orbitals. Or the Foster-Boys localized orbitals,²²⁵ which result from maximizing the sum of the distances between the centroids of localized orbitals.

In real-space, we find several kind of partitions of the electron distribution beyond the atomic-based ones. The type of partition achieved in real-space functions depends on the topology of the analyzed function. For example, when we split the electron density ($\rho(\vec{r})$), its topology (*i.e.*, maximum, minimum, and so on) is determined by the electron accumulation and matches with atomic positions; *i.e.*, it usually leads to the definition of atomic regions (see [Figure 2.3.d](#)). Indeed, the Quantum Theory of Atom in Molecules (QTAIM) of Richard Bader²²⁶ is based on this approach (as explained in [subsection 2.3.1](#)). Nevertheless, if we topologically analyze other real-space molecular functions like the electrostatic potential,²²⁷ or the Electron Localization Function (ELF) of Becke and Edgecombe,²²⁸ other regions or partitions will be achieved. Analyzing the ELF function, for example, the partitions match with localized electrons (*e.g.*, core electrons, bond pairs, or lone pairs). In all cases, the topological partitions provide a qualitative and quantitative picture about how and where the electron density is distributed and localized in different finite volumes called basins.

Atomic partitions, defined whether using a Hilbert-space or a real-space partition, are well-defined methods to subdivide the molecule into its constituting atoms. In fact, atomic partitions are the most commonly used because, besides being useful to rationalize the electronic structure of a given molecule (atomic populations, partial charges, etc.), are also used to envision the atomic contributions of molecular properties such as energies,^{229–232} aromaticity,^{233,234} magnetic susceptibilities,²³⁵ dipole moments,²³⁶ or the abovementioned oxidation states.²³⁷

1.4.2 A particular case of electron localization: isolated electrons in electrides

As mentioned at the beginning of this section, the challenging examples of electron distribution that are addressed in this thesis by means of electron partitioning schemes are the isolated electrons in electrides.

Electrides are a relatively new class of ionic compounds with exotic anions; specifically, the anionic part is just occupied by stoichiometric isolated electrons. In these compounds such electrons are neither localized in specific atoms, nor delocalized as in metals, nor solvated by the solvent, but rather they are independent entities separated from the cationic part of the compound to which are

1.4 ELECTRON DISTRIBUTION

bounded by electrostatic forces.

The uncommon nature of electrides, their thermal instability, and air and water sensitivity are the main reason for their late development. Specifically, the first crystalline electride, $\text{Cs}^+(\text{18-crown-6})_2\text{e}^-$, was synthesized by Dye *et al.* in 1983,²³⁸ and, since then, a series of similar unstable-at-room-temperature organic electrides were reported during the 20th century (see [Table 1.1](#)).²³⁹ However, at the beginning of the 21st century, this research field went through a revolution with the synthesis of the first room-temperature stable electrides and their characterization, highly promoted by theoretical studies. The first room-temperature stable electride synthesized was inorganic, the $[\text{Ca}_{24}\text{Al}_{28}\text{O}_{64}]^{4+}(4\text{e}^-)$ compound, C12A7, synthesized in 2003 by Hosono's group ([Figure 1.37](#)).²⁴⁰ In terms of thermal stability, its organic equivalent was synthesized just two years later, in 2005, by Dye's group. It is the $\text{Na}^+[\text{tri-pip-aza}(222)]\text{e}^-$ compound.²⁴¹

With unique structures, electrides have broad applications. Aside from being the first stable electride synthesized, the $[\text{Ca}_{24}\text{Al}_{28}\text{O}_{64}]^{4+}(4\text{e}^-)$ compound has been used to test several of their potential applications. With a low work function of 2.4 eV,²⁴² this electride can be used as an electron emitter for displays,²⁴³ and as an efficient electron injection in organic light-emitting diodes (OLED).²⁴⁴ Considering that this electride is an excellent electron donor, it could catalyze electron-injection limited reactions, such the activation of CO_2 ²⁴⁵ and N_2 .^{246,247} For example, the Ru-loaded $[\text{Ca}_{24}\text{Al}_{28}\text{O}_{64}]^{4+}(4\text{e}^-)$ has the best catalytic performance for ammonia synthesis among Ru-based catalysts reported so far.²⁴⁶ In general, inorganic electrides are promising in electronics, and organic electrides exhibit high hyperpolarizabilities^{248,249} and they are proposed as a new type of high-performance nonlinear optical (NLO) materials. Electrides also show particular magnetic properties (exalted susceptibilities), however, none of the existing already tested applications take advantage of the magnetic properties so far.

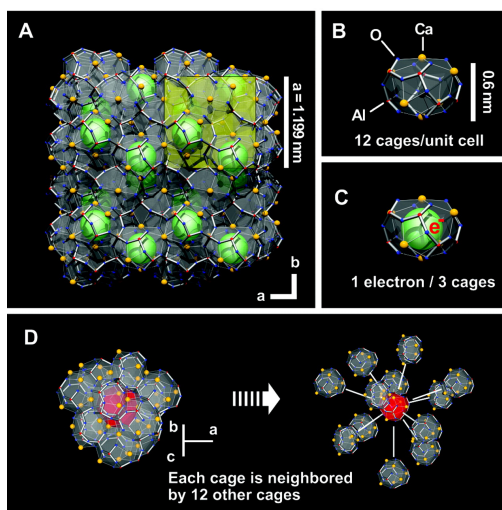


Figure 1.37: (A) Crystal structure of C12A7. (B) The framework of stoichiometric C12A7 is composed by 12 cages. (C) In the compound, 4 out of 12 cages are occupied by electrons in place of O^{2-} ions. Reproduced with permission (ref. 240).

Up until now, a few other inorganic electrides have been synthesized, each one more remarkable than the previously ones (see [Table 1.1](#)). For example, in 2013,

a layered-structure electride of dicalcium nitride described by the chemical formula of $[\text{Ca}_2\text{N}]^+\text{e}^-$ was reported.²⁵⁰ Until then, reported confining sites consist only of zero-dimensional cavities or weakly linked channels,²³⁹ but $[\text{Ca}_2\text{N}]^+\text{e}^-$ was the first electride whose structure possessed a two-dimensional anionic electron layer with confined electrons. A recent study suggest to use the Ca_2N electride as a new anode material of sodium-ion batteries tapping into its electrochemical properties.²⁵¹ In 2014 another important achievement in the field of electrides was reached, the synthesis of the first transition-metal electride, Y_2C . This new hypocarbide electride again presents a layered-structure with quasi-two-dimensional anionic electrons confined in the interlayer space.²⁵² Finally, in 2016 two new electrides were described. The first was Y_5Si_3 , the first silicide-related electride stable in both air and water. Its anionic electrons are confined in quasi-one-dimensional holes and, as distinct from the previously studied electrides, the anionic electrons strongly hybridize with yttrium 4d electrons, giving rise to its improved chemical stability. It was also realized that Ru-loaded Y_5Si_3 could be a promising ammonia synthesis catalyst.²⁵³ The second type of electrides described in 2016 were hydride-based electrides with the general formula LnH_2 , where $\text{Ln}=\text{La}, \text{Ce}, \text{ or } \text{Y}$. Although these compounds were already well-known materials, their electronic structure were clarified using the knowledge that has been gained in previous studies of electrides. These new hydride-based chemical systems are extremely rare anion-rich electrides having itinerant electrons populating cages surrounded by hydride ions.²⁵⁴

Thus, little more than a handful of electrides have been synthesized since nowadays and only about half of them are room-temperature stable and suitable for supporting chemical applications. Undoubtedly, electrides still are a relatively young field of research and many questions remain pending. However, theoretical and computational studies of electrides have had a crucial role in the understanding of their chemical structure, in demonstrating and quantifying the presence of localized electrons, and in the design of new electrides and corresponding novel applications. In the next section, I will present how theoretical studies have driven the development of the field, and how the application of partition schemes have been essential for electrides' characterization.

Compound	Type	RT Stability	Space Group	Cell Parameters (pm)
Cs ⁺ (18C6) ₂ ·e ⁻ [a]	Org.	×	Monoclinic C2/c	1307.5, 1584.0, 1735.9; β = 92.30°
K ⁺ (C222)·e ⁻ [a]	Org.	×	Monoclinic C2/c	1212.9, 2069.2, 2151.9; β = 95.23°
Cs ⁺ (15C5) ₂ ·e ⁻ [a]	Org.	×	Triclinic P $\bar{1}$	859.7, 888.6, 994.1; α = 102.9°, β = 90.06°, γ = 97.74°
Cs ⁺ [(15C5)(18C6)] ₆ ·(18C6) [a]	Org.	×	Hexagonal R $\bar{3}$	3310.8, 3310.8, 1626.6
K ⁺ (15C5) ₂ ·e ⁻ [a]	Org.	×	Triclinic P $\bar{1}$	862.8, 891.4, 912.6; α = 76.31°, β = 89.16°, γ = 80.99°
Li ⁺ (C211)·e ⁻ [a]	Org.	×	Orthorhombic Pbcn	1006.0, 2312.4, 838.0
Rb ⁺ (C222)·e ⁻ [a]	Org.	×	Triclinic P $\bar{1}$	873.0, 1156.5, 1394.7; α = 64.20°, β = 71.93°, γ = 84.74°
Na ⁺ [tri-pip-aza(222)]·e ⁻ [a]	Org.	✓	Orthorhombic Pccn	1070.3, 1460.8, 1860.6
[Ca ₂₄ Al ₂₈ O ₆₄] ⁴⁺ ·(4e ⁻)	Inorg.	✓	– [f]	– [f]
[Ca ₂ N] ⁺ ·e ⁻ [b]	Inorg.	✓	Hexagonal R $\bar{3}m$	360, 360, 191
[Y ₂ C] ^{1.8+} ·(1.8e ⁻) [c]	Inorg.	✓	Hexagonal R $\bar{3}m$	361.7, 361.7, 179.6
[Y ₅ Si ₃] ^{0.79+} ·(0.79e ⁻) [d]	Inorg.	✓	Hexagonal P6 ₃ mcm	840.8, 840.8, 634.1
LaH _{~2.6} [e]	Inorg.	✓	Cubic Fm $\bar{3}m$	~ 560

Table 1.1: **Structural Data for all the Crystalline Electrides synthesized up to date.** Extended version of Table 1 in ref. 255. RT accounts for room temperature. [a] Data from ref. 239. [b] Data from ref. 250. [c] Data from ref. 252. [d] Data from ref. 253. [e] Data from ref. 254. [f] [Ca₂₄Al₂₈O₆₄]⁴⁺·(4e⁻) crystals are amorphous and they settle on surfaces as single crystals.

Computational characterization and theoretical design of electrides

The main and first goal of theoretical studies of electrides was demonstrating and quantifying the presence of localized and isolated electrons that are independent of any particular atom. Thus, analyzing whether electride definition was a real fact or just a formal picture to explain these intriguing chemical species. The main trouble of experimental investigations is that the density of a free electron is not large enough to obtain a convincing evidence for its existence. Thus, experimental techniques can only infer (not verify) the presence of localized electrons, and theoretical studies become an essential tool to obtain a full description of the electronic structure of electrides.

In spite of this, several experimental methods are used (and have been refined)²⁵⁶ to characterize electride materials. X-ray diffraction (XRD) is the most direct experimental method to obtain their atomic structures. For some organic electrides, XRD measurements provide plausible experimental evidences of the isolated electron character when structures can be compared with their alkali counterparts.^{257,258} Hard X-ray photoelectron spectroscopy (HAXPES) and angle-resolved photoemission spectroscopy (ARPES) provide also useful experimental measurements.²⁵⁹ HAXPES is a powerful tool to investigate the bulk electronic properties of materials and ARPES can directly measure electronic band dispersion with high energy and momentum resolutions. Thus, the comparison of ARPES and DFT results can provide convincing experimental evidences for the existence of anionic electrons. Last but not least, the scanning tunneling microscopy (STM) technique was optimized to obtain atomic resolution and provide images for electride-materials surface.²⁵⁶ ⁱ

Aside from previous techniques that seek to obtain direct data about the molecular and electronic structure of electrides, all other techniques used in electride characterization are indirect and deal with the study of their properties. Examples would be the use of electron paramagnetic resonance (EPR) spectroscopy and superconducting quantum interference devices (SQUID) to obtain magnetic data (e.g. magnetic susceptibilities, spin-coupling constants, or electrical conductivities), measures of transport properties such as electrical resistivity, and measures of optical properties as optical reflectance.

Back to theoretical methods, several approaches can be used to characterize electrides. The most direct methods are based on calculating electron density maps and electronic band structure diagrams of electrides (using plane-wave codes). When band structure diagrams are obtained, the band-decomposed charged density can be computed to get a clue of the existence of anionic electrons. The band-decomposed charge density is obtained projecting the total electron density over atom-centered spherical harmonics. Typically, excess electrons occupy bands close to the Fermi level, whose density distribution confirms the presence of anionic electrons. Although visual analysis of the topology of charge and electron density is very intuitive, it may not give a conclusive crite-

ⁱ STM observations on surface are generally only carried out for the examination of materials that develop clear cleavages. Materials that do not have cleavage nature, such as $[\text{Ca}_{24}\text{Al}_{28}\text{O}_{64}]^{4+}(4e^-)$, were not studied in surface science until 2011, when Hosono's group optimized the experimental conditions to achieve this goal.

1.4 ELECTRON DISTRIBUTION

tion to judge if a compound is an electrider or not, mainly because it provides data about the electron distribution but not about its localization or isolation. Thus, more specific analysis that include the examination of other quantities, electron partitions, or the measurement of sharing indices have been used.

As it has been discussed, the AIM approach of Bader,²⁶⁰ where the total electron density is topologically split into *atomic* regions, is the standard 3D-space partition used to study electron localization directly from the electron density. As will be further explained in the [methodological section](#), quantum theory of atoms in molecules (QTAIM) analysis identify maximum points of the electron density and the boundaries of their regions. When a maximum of the electron density is found in a non-nuclear position, it is called a non-nuclear attractor (NNA), and it constitutes one of the required conditions to prove the existence of isolated electrons.^{261,262} Through the integration of the electron density of these atomic and NNA regions and the further statistical interpretation of the electron sharing indices, the isolated character of electrons can be quantified.

Regarding other quantities used to characterize the electronic structure of electrideres, it is worth noting the study of the electron localization function (ELF),²⁶³ the Laplacian of the electron density ($\nabla^2\rho$), noncovalent interactions (NCIs),²⁶⁴ or electrostatic potentials (ESPs). In ELF analysis, a new function that pinpoints regions with electron localization is created. Usually, these regions or basins correspond to chemical regions such as core electrons, valence electrons, bond pairs or lone pairs. However, isolated electrons also display their basins and can be identified and quantified by a further integration and statistical interpretation of their electron density. In $\nabla^2\rho$ analysis, concern is focused on regions with negative values of the Laplacian since they determine electron localization. Consequently, a negative value of the Laplacian in a void space is a sign of electrider nature. In NCI studies, electron density (ρ) and its reduced density gradient ($s(\vec{r})$)^j are checked simultaneously. Typically, in regions far from a molecule, ρ decays to zero exponentially, which gives large s values. In the case of electrideres, the localized electron in the void presents a non-nuclear maximum in the density, which is also characterized by a region with low density (ρ) and low reduced density gradient ($s(\vec{r})$).²⁶⁵ Electrostatic potentials give an idea about the charge distribution in molecules. Low or negative ESP energy values indicate an abundance of electrons such as lone pairs, aromatic clouds, etc. To understand the nature of electronic distribution in electrideres and differentiate it from other kinds of electron localizations, extensive studies that examine the eigenvalues and eigenvectors of ESP Hessian have been done.^{266,267} However, from our experience with ESP calculations, ESP calculations are not always able to retrieve the presence of isolated electrons in electrideres. When other regions with abundance of electrons such lone pairs are close to the isolated electron region, the formers hinder the identification of the latter, which have lower abundance of electrons.

All previous theoretical analysis have been gradually incorporated in characterization studies of electrideres. These in turn have allowed a deeper understanding of electrider's electronic structure by abolishing any doubts about the physical existence of anionic isolated electrons.

$$^j s(\mathbf{r}) = \frac{|\nabla\rho(\vec{r})|}{2(3\pi^2)^{1/3}\rho(\vec{r})^{4/3}}$$

In addition to *ab initio* characterization of existing electrides, an important part of the recent theoretical work on electrides focuses on examining their properties and on proposing new compounds. Regarding the examination of electride properties, besides the collaborative works between theoretical and experimental groups, it is worth stressing the pure theoretical work done by Dale and Johnson. They studied the magnetic properties of electride crystals and their thermodynamics.^{265,268} Regarding the theoretical identification of new electrides, progresses have been mainly made in 2D electrides, in high-pressure electride (HPE) design, and also in electride-based material development. By examining crystallographic databases, seven 2D electrides were theoretically identified: three nitrides (Ca_2N , Sr_2N , and Ba_2N) and four carbides (Y_2C , Tb_2C , Dy_2C , and Ho_2C).²⁶⁹ Among them, Y_2C and Ca_2N have already been synthesized and their electride character has already been experimentally verified.^{250,252} Moreover, the new 1D inorganic electride with $[\text{La}_8\text{Sr}_2(\text{SiO}_4)_6]^{4+}:4e^-$ configuration has also been reported on the basis of theoretical calculations.²⁷⁰ Finally, however the existence of HPEs and how the electrons in a way play the role of atomic anions in these materials have been widely known;^{271–274} there has been a recent revival of this research field. HPE are generated when confined spaces between atoms in HPE host lattice are filled by quantized orbitals under an extreme pressure. With the increasing pressure, the energy levels of atoms on lattice sites and of interstitial spaces change. Therefore, valence electrons move to the interstitial space when the energy levels of the interstitial space is lower than energy levels of the valence orbital of the lattice site atoms. To this day, a predictive chemical and physical theory to explain which elements will form HPEs at moderately elevated pressure has been built²⁷⁵ and the chemical nature of interactions of the interstitial electrons has been deeply explored.²⁷⁶

Throughout this section we have described the characterization of synthesized solid-state electrides with isolated electrons occupy hollow cavities, tunnels, or layers where they can be hosted and stabilized by the environment. This thesis presents a pioneering study on electrides beyond the lattice, on the molecular level. Many molecules have been labeled as electrides according to their properties (presence of large nonlinear optical properties (NLOPs) such as second hyperpolarizabilities),^{248,277,278} or by the characterization of the frontier molecular orbital (presence of delocalized diffuse excess electrons on high-lying occupied orbitals). However, unlike solid-state electrides,^{250,279,280} the presence of NNAs of the electron density or even ELF basins were not studied for such molecules. Thus, if molecular electride's structure truly consists of isolated electrons or not had not been properly explored. Moreover, other molecules present these properties (NNAs or ELF basins in non-nuclear regions) without the presence of an isolated electron. Accordingly, in the work presented here ([chapter 6](#)) we wanted to show whether molecular electrides can exist and to provide unambiguous criterion to distinguish them from other similar species. State-of-the-art electronic characterization is applied to molecular electrides. For the first time molecular electrides are doubtless characterized through QTAIM, ELF, and Laplacian of the electron density analysis.

Chapter 2

Methodology and Computational Chemistry Tools

In this chapter the main theoretical framework in which this thesis has been developed is briefly commented and discussed. Afterwards, the different computational chemistry tools, methodologies, and strategies used to carry out the studies or to properly analyze the results of this thesis are presented.

2.1 Theoretical framework

All studies included in this thesis involve organometallic compounds or compounds with more than 100 atoms. To properly calculate and critically analyze these compounds, their electronic structure (chapter 5 and chapter 6) or the reaction pathways they can undergo (chapter 4), a flexible, accurate and fast quantum mechanical modelling method is needed. Thus, the vast majority of calculations presented in this thesis use density functional theory (DFT).

The studies presented in chapter 4 use DFT as the only enough flexible, accurate and computationally efficient method for the prediction of the structure, energetics and reaction mechanisms of (open-shell) organometallic complexes.^{281–285} Surprisingly in view of its technical simplicity (as a single-determinant method, operationally but not conceptually similar to Hartree-Fock (HF) theory), the Kohn-Sham version of DFT performs very well in organometallic and bioinorganic arenas. Specifically, organometallic complexes presented in Chapters 4 of this thesis involve iron. As a first-row transition metal, iron has a very compact 3*d* electron shell, which produces strong electron-electron interactions and requires a good treatment of electron correlation, balanced with the treatment of electron exchange. Moreover, the metal-ligand bonding of iron complexes can be strong or weak field, with resulting effects on spin states and metal-ligand covalency. This last problem is worse in first-row metal series than for the second or third transition metal series, where, conversely, relativistic effects are higher. Thus, in practice, standard HF methods are totally inadequate for this task since electron correlation is neglected, post-HF methods are impractical, *i.e.* too computationally expensive, and DFT methods take over the primary role.

Regarding studies presented in chapter 5 and chapter 6, DFT methods are used for consistency reasons. These studies involve both large and small molecules and, in order to treat all of them with similar accuracy and to obtain comparable results, DFT methods have been, again, the choice made. However, if necessary, post-HF methods have been used to reinforce DFT results. For example, if we suspected that the system may present dynamic correlation effects, the coupled-cluster method with single and double (and preferably also perturbative triple) excitations [CCSD(T)] would be the post-HF method of choice. Conversely, if we thought that our system may present static correlation effects, a multireference method such as CASSCF (complete active space self-consistent field) should be, in turn, the starting choice. However, the need for relatively small active spaces is a serious limitation for CASSCF calculations. Likewise, the high-quality CCSD(T) method is currently limited to small systems (of fewer than 20 atoms or so) for optimization and frequency calculations.^a Overall, the wavefunction community appears not to be able to extend the fully applicability (to the determination

^a Regarding this point we should mention the domain based local pair natural orbital (DLPNO) implementation of CCSD(T), published in 2013 by Neese and co-workers.²⁸⁶ This method, which includes a variety of approximations for calculating the (T) correction of CCSD(T) with associated thresholds that control the accuracy, absolutely rooted out the size limit of CCSD(T) in energy calculations. It has been shown that the DLPNO-CCSD(T) method is accurate enough (*i.e.*, it recovers the 99.9% of the CCSD(T) correlation energy) to predict enthalpies of formation as accurate as you can measure in molecules up to 30 atoms, and it is fast enough to treat an entire protein, such Cambrin with 644 atoms and more than 6400 basis functions.²⁸⁶

2.1 THEORETICAL FRAMEWORK

of geometries, energies, and vibrations) of their methods in an accurate way to relatively large (*i.e.*, 50-100 atoms) open-shell systems. In turn, in many studies it ends up choosing DFT methods as the level of theory for consistency reasons.

In the following paragraphs of this section, density functional theory is briefly lectured and its main deficiencies are commented, with a particular focus on organometallic compounds.

2.1.1 Density Functional Theory

Density Functional Theory (DFT) is a computational quantum mechanical modelling method, alternative to conventional *ab initio* methods, which is based on using the electron density function of the system to describe their properties.

The basis of DFT are Hohenberg and Kohn's theorems, by which: i) electronic energy and any other property of the ground state can be totally determined by *functionals* of the exact electron density of the system (1st theorem); and ii) the exact electron density of the system is the one that minimized the electronic energy of the ground state, following the variational principle (2nd theorem),

$$E[\rho] \geq E[\rho_{exact}] = E_{min} \quad . \quad (2.1)$$

A *functional* is any mathematical expression that applies to a function (the electron density, here) to retrieve a number. Since the electron density function ($\rho(r)$) only depends on three spatial coordinates ($r=x,y,z$), the DFT approach is potentially able to reduce the computational cost of quantum many-electron calculations with respect to wavefunction-based methods because HF and post-HF methods depend on $3N$ variables ($4N$ taking into account the spin), where N is the number of electrons. Thus, the final step in the development of DFT is to design the form of the functional that connects the electron density of the system with its energy. However, this has not been an easy task, which has not yet been fully resolved.

Compared with the wavefunction mechanics approach, it seems logical that the electronic energy functional may be divided into three parts: kinetic energy, $T[\rho]$, attraction between the nuclei and electrons, $E_{ne}[\rho]$, and electron-electron interaction, $E_{ee}[\rho]$ (the nuclear-nuclear repulsion is assumed constant within the Born-Oppenheimer approximation). Furthermore, the $E_{ee}[\rho]$ term may be divided into Coulomb and exchange parts, $J[\rho]$ and $K[\rho]$, respectively, implicitly including correlation energy in all the terms.²²³

$$E[\rho] = T[\rho] + E_{ne}[\rho] + J[\rho] + K[\rho] \quad (2.2)$$

Although several attempts at constructing *orbital-free* functionals depending directly only on the electron density have been developed, the accuracy achieved with these methods is still too low to be of general use,^{287,288} mainly because of the accuracy of T and K functionals.

The foundation for the general use of DFT methods in computational chemistry came in 1965, when Kohn and Sham devised a practical method to calculate

ρ and $E[\rho]$.²⁸⁹ They introduced orbitals and defined the kinetic functional under molecular-orbital approximation. Since the exact density matrix is not known, the approximate density is written in terms of a set of auxiliary one-electron functions, the KS orbitals,

$$\rho(r) = \sum_{i=1}^N |\phi_i(r)|^2 \quad (2.3)$$

The price to be paid with the re-introduction of orbitals is the increasing of the complexity from 3 to $3N$ variables, analogous to Hartree theory, but still much less complicated than post-HF (correlation) wavefunction models.

Regarding the approximation that was used to retrieve the energy of the system from their electron density, Kohn and Sham considered a fictitious reference system of non-interacting electrons with the same electron density as the real system, moving in a local effective external potential, called the *Kohn-Sham potential* ($\mathbf{V}_{eff}(r)$). The KS model is closely related to the HF method in the sense that HF uses an independent-electron wavefunction (Slater determinant), whose electrons interact through the HF potential. Then, for example, the kinetic electronic energy of non-interacting electrons can be calculated by an equivalent expression to the expression used in HF theory (first term in eq. 2.4). Other components that also have equivalent expressions to the ones used in HF theory are the classical electron-nucleus attraction (second term in eq. 2.4) and the classical Coulomb repulsion between charges (third term in eq. 2.4). Finally, the remaining kinetic energy (the difference between the exact kinetic energy of the real system and the kinetic energy of non-interacting electrons) and all non-classical interactions between electrons (both electron-electron repulsion potential correlation and exchange energy) are absorbed into an exchange-correlation term (E_{xc}).

$$E[\rho] = -\frac{\hbar^2}{2m_e} \sum_{i=1}^n \int \phi_i^*(r) \nabla^2 \phi_i(r) dr - \sum_{I=1}^N \int \frac{Z_I e^2}{4\pi\epsilon_o |R_I - r|} \rho(r) dr + \frac{1}{2} \iint \frac{\rho(r)\rho(r')e^2}{4\pi\epsilon_o |r - r'|} dr dr' + E_{xc}[\rho] \quad (2.4)$$

The E_{xc} is the only unknown energetic term in the KS formalism of DFT. Then, the major problem in DFT is to derive accurate expressions to describe the exchange-correlation term. Assuming that the exact E_{xc} functional would exist, DFT-KS would be able to provide the exact total energy of the system at a similar computational cost that the one needed for determining the uncorrelated HF energy.

The main difference between the large number of different DFT functionals described so far is the nature of the approximation for the exchange-correlation functional. The simplest approximation for the exchange-correlation energy used in DFT is the ‘local density approximation’ (LDA), which approximates the exchange-correlation energy density at a given position as a function of the electron density at that same local position. At the next level of sophistication comes the ‘generalized gradient approximation’ (GGA), for which the energy

2.1 THEORETICAL FRAMEWORK

density approximation also depends on the gradient of the density at that given position. A level above this is ‘meta-GGA’, for which the energy density also depends on the local kinetic energy density of the calculated Kohn-Sham orbitals. All these approximations (*i.e.*, LDA, GGA, and meta-GGA) scale with N^3 , which is the same as Hartree theory. Higher-order approximations such as hybrid functionals or fully non-local functionals further improve the accuracy, but at the price of non-locality in the density dependence and higher computational cost.²⁹⁰ In hybrid DFT methods, the exchange-correlation functional includes a fraction of the Hartree-Fock exchange; while in fully non-local functionals or double hybrid functionals, the energy density approximation also depends on unoccupied orbitals, as for example in the scheme called random phase approximation (RPA).

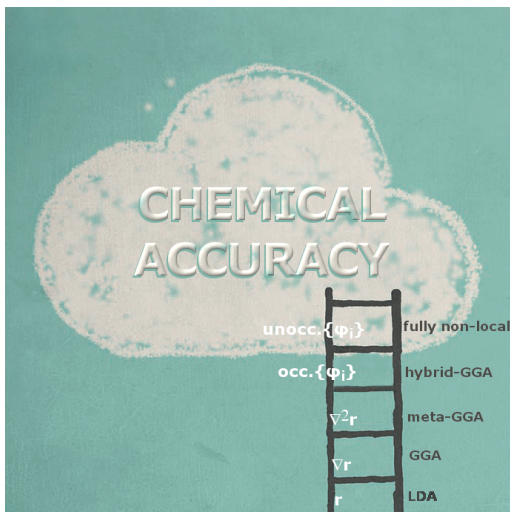


Figure 2.1: The hierarchy of DFT approximations represented by Jacob’s ladder.

Despite a systematic improvement of the exchange-correlation term in DFT does not exist, the previous approximations are ordered according the so-called Jacob’s ladder,²⁹¹ which sort DFT methods by their costs in terms of computational requirements to achieve the *heaven* of chemical accuracy.

2.1.2 Deficiencies of DFT

There are mainly three-four formal deficiencies of DFT. The first one is the so-called self-interaction error (SIE). In ab initio methods like HF, the artificial term corresponding to a Coulomb repulsion between an electron and itself is exactly cancelled by an exchange term. In DFT, Coulomb terms are described exactly (third term in eq. 2.4), but the exchange is described by an approximate functional (fourth term in eq. 2.4). Since these terms do not exactly cancel, a SIE remains:

$$\frac{1}{2} \iint \frac{\rho(r_1)\rho(r_2)}{r_{12}} dr_1 dr_2 + E_{xc}[\rho] \neq 0 \quad . \quad (2.5)$$

Classical examples of SIE are radical dissociations in homonuclear compounds, charge transfer complexes, systems with two-center three-electron bonds or the transition states (TSs) of some chemical reactions. SIE artificially stabilizes delocalization. In the next section about computational chemistry practices for chemical reaction studies (section 2.2), an strategy how to detect and quantify SIE in quantum mechanic calculations is presented, as well as strategies to prevent its occurrence.

The second error in DFT is due to the inherent description of the wavefunction as a single determinant, which leads to near-degeneracy errors, also termed an error in the nondynamical (static) correlation energy. The first suggested attempt to deal with near degeneracies is the use of a spin-unrestricted description, where spin-up (α) electron density occupies a different region of space from the spin-down (β) electron density. In general, in DFT studies of first-row transition metal complexes, an unrestricted description should always be used. When there is no interaction between the open shell electrons, the unrestricted solution will provide a proper energy, despite incorrect spin eigenvalues (*e.g.* asymptotic region of the H_2 dissociation). However, when there is a nonzero interaction between the open shell electrons, the unrestricted DFT solution no longer gives a proper energy and DFT starts to have energetic error. This energetic error arises because the described coupling between the open-shell electrons in these situation (when there is an interaction between them) is too weak. Then, for example, the triplet and broken-symmetry singlet determinants will give nearly the same energy (within 0.5 kcal/mol) and near-degeneracy errors occur.²⁹² Nevertheless, the spin-contamination in DFT is lower than in the equivalent HF calculation because the former includes the electron correlation.

Since the self-interaction error tends to decrease barriers while the lack of nondynamic correlation increases them, there is a substantial cancellation effect between these two errors of DFT. For that reason, trying to remove just one of the error sources when both are present could lead to larger errors than before.²⁹³ In this thesis, Yamaguchi’s approach to correct the electronic energy when there is a mixing of spin states due to the single determinant representation of the wavefunction is used. Yamaguchi’s approach will be developed in the next section about computational chemistry tools for chemical reaction studies (section 2.2). It is worth to mention that Yamaguchi’s approach has been used in the context of no SIE situations.

Near-degeneracy errors could be consider a particular case of a more general DFT problem which is spin-state energy gaps or spin-crossover. It has been observed that DFT energy errors of different spin states that arise from different electronic configurations (*e.g.* high-spin/low-spin problems) can be substantial and may exceed 10 kcal/mol.^{294,295} In an *ab initio* context, these situation (the comparison between situations with different number of unpaired electrons) requires extensive dynamic correlation treatments in order to arrive at good energetic predictions.^b Thus, while we can relate near-degeneracy errors with static correlation, errors related with prediction of spin-state energy gaps can be related with dynamic correlation.

Therefore, it is not surprising that hybrid functionals are a better choice than either the HF or the GGA methods. The high-spin/low-spin gap has been found to be a nearly linear function of the fraction of HF exchange mixed in the DFT functional. Even, for a given spin state, the electron configuration of the ground state can also be modified as a function of the HF exchange.^{296,297} General tips about which kind of functional should be use according the requirements of the

^b The term dynamic electron correlation is perhaps most easily understood as a correction to the mean-field electron-electron repulsion included in HF theory arising from instantaneous electron-electron interactions; its accurate calculation is the major challenge of *ab initio* quantum chemistry.

2.1 THEORETICAL FRAMEWORK

chemical system are given later. However, experimental data is extremely useful when we suspect that a potential problem of spin-crossover can take place. It is to be noted that any experimental evidence is of much help to the theoretician in such situations and that it is necessary to search for as close similarity to experimental data as possible in the theoretical investigations. The main outstanding problem here is that, while the spin ground states can be experimentally determined (if the compound is enough stable), much less is known experimentally about the energy differences between the different spin multiplets. Then, benchmarking studies between different functionals and a case-by-case examination is necessary and recommended in many situations.

The third error in most of current DFT functionals is the lack of a description of long-range dispersion interactions (such van der Waals). These long-range interactions can be viewed as instantaneous electron correlations when ‘charge fluctuations’ on one region of the system induce dipole moments on the other fragment. In a more precise picture, electromagnetic zero-point energy fluctuations in the vacuum lead to ‘virtual’ excitations to allowed atomic or molecular electronic states. The corresponding (pseudo)densities interact electrostatically (with exchange-type modifications at smaller distances) and these interactions are not represented by conventional (hybrid) DFT functionals that only consider electron exchange but do not employ virtual orbitals.²⁹⁸ All this means that, for example, bonding due to π -stacking cannot be studied by DFT if a dispersion correction approach is not considered. In this thesis a dispersion corrections approach has been used: the semiclassical correction approach by Stefan Grimme.^{299–301} Because the dispersion correction is an add-on term, if a geometry is given, it does not directly alter the wavefunction or any other molecular property. However, geometry optimizations with dispersion correction will lead to a different geometry because the energetic dispersion correction contributes to the forces acting on the atoms.

2.1.3 Which functional should I use?

The accuracy of DFT is quite uniformly good, bearing in mind the general deficiencies already commented. However, the functional of choice should depend on the property we want to predict, e.g., geometries, vibrational frequencies, energies or spectroscopic properties.

Regarding geometry optimizations, different DFT functionals generally behave similarly as long as at least gradient corrections are taken into account (*i.e.* one has to go beyond the local density approximations, LDA). In many cases, geometries predicted by GGA functionals are slightly better than those predicted by hybrid functionals. However, there are exceptions to this statement. In order to achieve good geometries, the basis set size plays an important role. Small basis sets without polarization functions are not recommended and, for first-row transition metals, the use of effective core potentials is neither necessary nor particularly desirable. In general, double zeta plus one set of polarization functions for the ligands and triple zeta plus one set of p-functions and one set of f-functions for the metal are enough to get good geometry descriptions. Overall, short, strong and stiff metal-ligand bonds are predicted with excellent accuracy, while the weaker metal-ligand bonds are typically predicted too long by approx-

imately 5 pm.²⁸²

Close related to the problem of predicting equilibrium geometries is the prediction of vibrational frequencies and IR spectra. In general GGA functionals give better results than hybrid functionals from error cancellation between the neglect of anharmonicities and systematic errors in the prediction of the true harmonic frequencies.³⁰² On the other hand, hybrid functionals provide harmonic frequencies of slightly higher quality and, since anharmonicities are neither considered, the resulting vibration frequencies agree somewhat worse than experimental results for global frequencies.

Regarding the accuracy and reliability of different DFT functionals for the predictions of reaction energies and energy barriers, the general deficiencies of DFT provided above should be bear in mind. However, in general, hybrid functionals, such as the B3LYP exchange-correlation functional,^{303,304} are more recommended than GGA functionals.³⁰⁵ Indeed, B3LYP has been the most popular quantum chemical method for studying mechanisms of complexes containing transition metals. The reasons behind its popularity are mainly two: i) B3LYP has been shown to be the most accurate of the DFT functionals in several benchmark tests regarding energetic descriptions;^c ii) despite being a hybrid functional, the computational cost of B3LYP calculations is low enough to treat rather large models, even up to a few hundred atoms.

DFT calculations on open-shell transition metal systems are less routine than DFT calculations on organic molecules and, every now and then, one stumbles across a system that is imperfectly described by DFT or, specifically, by B3LYP. There are no reasons for a blind trust in DFT and a careful comparison of calculated and measured observables may grey increase the trust one can have in the results of computations. An example where B3LYP is not doing a good job compare with the pure GGA BP86 is the description of the Co-C bond dissociation of alkylcobalamins.³¹⁰ Likewise, while the PW91 GGA seems to correctly reproduce the $S=0$ ground state of Mn^VO porphyrins and corroles, B3LYP seems to exhibit an undue preference for higher spin states.^{311–313}

As it has been already commented, one notorious exception of the good performance of DFT methods is the calculation of spin-state splitting energies. This issue is particularly relevant in Chapter 4 of this thesis where hydrocarbon functionalizations by an iron complex are studied. An interesting study of Swart et al.³¹⁴ addressed this issue in Fe complexes. The study recommends the use of the GGA type OPBE functional to properly describe spin-state splitting energies. When OPBE results were compared with the reference CASPT2 data of the study, OPBE's mean absolute deviation energies were an order or magnitude smaller than those of the other studied functionals. Moreover, OPBE results

^c On the basis of benchmark calculation on the so-called G2 set of test molecules, the B3LYP functional presents an average deviation from experiments of only 2.20 kcal/mol for the atomization energies.³⁰⁶ Also on the extended G3 set, when only the 301 entries that are most relevant are included, the atomization energies predicted by the B3LYP functional presents an average error of 3.3 kcal/mol.^{307,308} B3LYP has also shown excellent descriptions of a variety of Fe(IV) intermediates such as nonheme iron-oxo intermediates and iron-containing enzymes (e.g., cytochrome P450 and soluble methane monooxygenases).^{50,309}

2.1 THEORETICAL FRAMEWORK

lie well within the estimated accuracy of the reference CASPT2 data. However, among the other functionals, B3LYP results are one of the best. On this basis, to ensure a proper description of the spin-state splitting energy, the articles reported in Chapter [chapter 4](#) of this thesis include benchmarking studies with the OPBE functional.

Hybrid functionals are also recommended for the prediction of magnetic spectroscopic properties over GGA functionals. However, this thesis does not include spectroscopic studies and I will not flesh out further the reasons why hybrid functionals tend to behave better than GGA functionals in magnetic spectroscopic properties.

In agreement with the previous paragraphs, B3LYP is the main functional used in this thesis. It is worth noting that the studies presented in this thesis are mainly focused in: i) describing the thermodynamics and kinetics of reaction mechanism, for which the achievement of accurate energy values requires the use of hybrid functionals; and in ii) describing electron-distribution patterns by means of the analysis of the electron density, which is uniformly accurate from different DFT functionals.³¹⁵ Nevertheless, readers will find comparative analysis between B3LYP results and the results of other functionals and methods when it was considered necessary.

2.2 Good computational practices for chemical reactivity studies

Once the theoretical framework, its deficiencies and strengths, are clear, it can be understood that, in some situations, specific strategies or special considerations about how to process the data are necessary. In this section, some specific strategies used in this thesis to achieve reliable results for chemical reactivity studies are exposed.

General calculation of Gibbs free energies, G

Gibbs free energies are always calculated in a two-step process. In the first step, geometries are optimized at the so-called B1 level of theory. In the second step a higher level of theory is used (which will be referred to as B2) in order to improve electronic energies and, sometimes, the solvent description. The general expression of the final total Gibbs free energy (G) may be defined as:

$$G = E_{spin_corr(B2)} + E_{disp} + G_{solv(B1/B2)} + G_{corr(B1)} + \Delta G^{o/*} \quad (2.6)$$

where subscripts B1 and B2 refer to the level of theory at which the final energetic term is obtained.

$G_{corr(B1)}$ is the free energy correction, which includes the zero-point energy, enthalpic and entropic contributions. This energetic term is obtained from B1 level of theory because the study of vibrational frequencies and their contributions to the internal thermal energy, enthalpy and entropy, only makes sense if they are studied in a stationary point. Otherwise, the vibrational frequencies obtained are incorrect, and the energetic contributions derived therefrom would be wrong.

$G_{solv(B1/B2)}$ is the energetic term that accounts for the solvation energy (i.e., electrostatic and non-electrostatic terms triggered by the interactions between solute and solvent, the formation of a solvent cavity, etc.). This term can be computed at B1 and/or B2 level of theory, depending on which methodological scheme is used. For example, if the geometry optimization is performed using the desired (experimental) solvent, solvation energy correction will be already included at the B1 level of theory. Otherwise, if the geometry optimization is performed in gas-phase or if we want to improve the solvent description to mimic the experimental conditions, solvation energy corrections may be included at the B2 level of theory.^d

The E_{disp} (dispersion energy) term does not present any associated subscript related with the level of theory because this semiempirical correction only depends on the molecular geometry. However, as it was explained in previous section, if this energetic contribution is considered during the optimization process, it affects the general forces acting on atoms and, therefore, a different geometry

^d Many times, geometry optimizations are already done in solvent but, nevertheless, the final G_{solv} energetic term is included at the B2 level of theory because the solvent correction is basis dependent.

2.2 COMPUTATIONAL PRACTICES FOR REACTIVITY STUDIES

is obtained as stationary point.

The $E_{spin_corr(B2)}$ is the electronic energy term obtained from the highest level of theory used, B2. The subscript *spin_corr* states that when near-degeneracy errors are detected, the Yamaguchi's approach to correct the electronic energy is applied. It is worth remembering that Chapter 4 includes computational studies on iron complexes where near-degeneracy problems tend to occur.

Finally, the $\Delta G^{o/*}$ term is the free energy change associated with the conversion from a standard-state gas phase pressure of 1 atm to a given standard-state solvent phase concentration of X M (where X is the molarity concentration of reagents and products in agreement with experimental data). It should not be forgotten that the principles used for the conventional thermodynamic treatment of energetic data assume gas-phase non-interacting particles in standard-state conditions (*i.e.*, 1 atm and 298.15K). Thus, for going from gas-phase values to solvent-phase values, some considerations have to be taken into account. If the reaction keeps the molecularity (e.g. $A+B \rightarrow C+D$), the $\Delta G^{o/*}$ energy term has a zero value due to cancellation of terms (see equation 2.9). Otherwise, when the chemical reaction implies changes in the molecularity (e.g., $A + B \rightarrow C$), or the compounds of the chemical reaction have different concentrations with each other; the $\Delta G^{o/*}$ energy term is non-zero due to entropic effects.^e

The relation between the free energy change of different concentration conventions (standard-state gas phase (*)) and the desired concentration in solvent (°)) can be expressed as:

$$\Delta G^o = \Delta G^* + RT \ln \left(\frac{Q^o}{Q^*} \right) \quad (2.7)$$

where Q is the reaction quotient (*i.e.*, the ratio of concentrations that appear in the equilibrium constant) evaluated with all species at their standard-state concentrations, expressed so that the logarithm is dimensionless; *R* is the universal gas constant (1.987 cal/(Kmol)); and *T* is the temperature in Kelvin.³¹⁶

For example, considering the following reaction,



the reaction quotient Q is $[C]/[A][B]$ and A, B, and C concentrations at the standard-state gas phase ($[A]^*=[B]^*=[C]^*$) of 1 atm may be derived from the ideal gas law as $\frac{1}{24.5}$ mol/L. Then, if we assume a standard-state solvent phase concentration of 1M, Eq. (2.7) becomes:

$$\begin{aligned} \Delta G^o &= \Delta G^* + RT \ln \left(\frac{\frac{[C]^o}{[A]^o[B]^o}}{\frac{[C]^*}{[A]^*[B]^*}} \right) = \Delta G^* + RT \ln \left(\frac{\frac{1}{(24.5)}}{\left(\frac{1}{24.5}\right)\left(\frac{1}{24.5}\right)} \right) = \\ &\Delta G^* + RT \ln \left(\frac{\frac{1}{24.5 \cdot 24.5}}{24.5} \right) = \Delta G^* - RT \ln(24.5) \quad (2.9) \end{aligned}$$

^e The entropy of translation requires concentration specifications.

To ensure the most accurate results, we should work with the experimental concentration in solvent for each compound. An equivalent compound-by-compound equation to equation (2.7) can be expressed as:

$$G_A^o = G_A^* + RT \ln \left(\frac{Q^o}{Q^*} \right) = G_A^* + RT \ln \left(\frac{[A]_{exp}}{\frac{1}{24.5}} \right) \quad (2.10)$$

where subscript A refers to the chemical compound.

Kinetics of redox reactions

The kinetic of electron transfer (ET) processes in homogeneous phase requires expensive multiconfigurational calculations in order to describe electronic states properly. Then, in order to calculate electron transfer rates in outer-sphere processes, it is widely accepted to use the classical Marcus formalism.³¹⁷⁻³¹⁹ According to this approximation, the energy barrier of an electron transfer reaction depends on its thermodynamics (ΔG) and the total reorganization energy (λ_t) of the system involved in the redox reaction. The free energy barrier for an electron transfer process can be approximated as:

$$\Delta G^\ddagger = \frac{(\Delta G + \lambda_t)^2}{4\lambda_t} \quad (2.11)$$

The total reorganization energy is expressed as the sum of the inner (λ_{int}) and outer (λ_{out}) reorganization energies. The λ_{int} refers to the energy contribution due to geometrical changes of the molecules when the electronic state change, *i.e.*, it is the energy necessary to reorganize the geometry of the molecule in the equilibrium position of its redox counterpart, while λ_{out} is related with solvent reorientations and polarizations around the species involved in the redox reaction.

Using Klimkans and Larsson formula, λ_{int} can be expressed as (in accordance with colors of Figure 2.2):

$$\lambda_{int} = \frac{\lambda_{int(OX)} + \lambda_{int(RED)}}{2} = \frac{E_{OX}(\mathbf{x}_{red}) - E_{OX}(\mathbf{x}_{ox}) + E_{RED}(\mathbf{x}_{ox}) - E_{RED}(\mathbf{x}_{red})}{2} \quad (2.12)$$

where $\lambda_{int(OX)}$ is the energy difference of the oxidized species between their optimized geometry (\mathbf{x}_{ox}) and the geometry of reduced species (\mathbf{x}_{red}) evaluated at the oxidized species potential electronic surface. In turn, $\lambda_{int(RED)}$ is the energy difference of the reduced species between their optimized geometry (\mathbf{x}_{red}) and the geometry of oxidized species (\mathbf{x}_{ox}) evaluated at the reduced species potential electronic surface (Figure 2.2).

The outer reorganization energy has been calculated assuming a continuum solvent model as:

$$\lambda_{out} = (\Delta q)^2 \left(\frac{1}{2r_1} + \frac{1}{2r_2} - \frac{1}{R} \right) \left(\frac{1}{\epsilon_{op}} - \frac{1}{\epsilon_s} \right) \quad (2.13)$$

where Δq is the charge transferred, r_1 and r_2 are the effective radii of the precursor molecules, R is the effective radius of the whole precursor complex, and ϵ_s

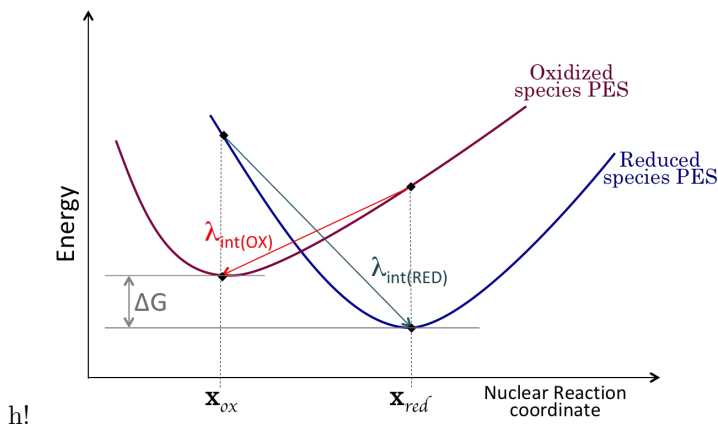


Figure 2.2: Schematic representation of how to obtain the energy terms of the classical Marcus formalism.

and ϵ_{op} are the static and high frequency (optical) dielectric constants of the solvent. r_1 , r_2 , and R are obtained from the molecular volume of the corresponding species (keyword “volume” in Gaussian09) and assuming a spherical shape.

Evaluation of the Self-Interaction Error, SIE

As previously noted in the “*Deficiencies of DFT*” section, SIE artificially stabilizes delocalization to minimize the incorrect excess of Coulomb interaction that is not cancelled by the approximate exchange-correlation term (E_{xc}). The third term of equation 2.4 shows that the classical Coulomb repulsion has a quadratic dependence of the density ($J[\rho] \propto \rho^2$). Thus, if instead of having repulsion between units of density localized in one of the two non-interacting centers (ρ^2), the charge is delocalized between the two non-interacting centers having half unit density each ($2 \cdot (\frac{\rho}{2})^2 = \frac{\rho^2}{2}$), the Coulomb repulsion decreases and the system is stabilized.

Whether or not a calculation is suffering SIE effects can be evaluated using the following equation, where the delocalization error is computed at 60\AA :³²⁰

$$\Delta E_{deloc(60\text{\AA})} = E(A-B)_{60\text{\AA}} - E(A) - E(B) - \frac{1}{4\pi\epsilon_0} \frac{Q_1 Q_2}{60\text{\AA}} \quad (2.14)$$

The first term of the equation refers to the energy of the whole system, where the two centers that may be effected by density delocalization (center A and center B) are separated by 60\AA . The third and fourth terms refer to the energies of the isolated center A and B, respectively, and the last term is the Coulomb interaction between charges Q_1 and Q_2 at the given distance, 60\AA . Q_1 and Q_2 charges concern the charges of the A and B centers, and the ϵ_0 term refers to the relative dielectric constant of the media where the analysis is performed (1.0 at vacuum, 37.5 at acetonitrile solution, etc.).

If there is no self-interaction error, the energy of the first term of equation 2.14 will cancel with the other ones (i.e., the sum of the energy of the two isolated

centers plus the classical Coulomb interaction between them will be the same as the energy of the whole system) and $\Delta E_{deloc(60\text{\AA})}$ will retrieve a zero value. Meanwhile, if there is SIE, the first term will be overstabilized (will present a more negative electronic energy that it should be) and equation 2.14 will retrieve negative values.

When SIE takes place, there are several options to try to improve the energetic description of the system. Several self-interaction corrected (SIC) functionals have been constructed. However, their use may worsen the description of the system in other components. Then, alternative options to avoid SIE effects in energetic terms are the addition of solvent (if it was still not considered) and/or the addition of counterions or point charges in the calculation.

Non-singlet-determinant state energies

As stated above, in order to recover the nondynamic correlation energy that is associated with the multi-determinantal wavefunction, single-determinantal models like HF and DFT are allowed to break the *spin* symmetry, i.e., to use different spatial orbitals for α and β spins. However, this approach do not avoid energetic errors due to near-degeneracy problems.

The resulting two sets of spatial orbitals are not orthogonal and the unrestricted determinant resultant is not an eigenfunction of the total spin operator $\langle S^2 \rangle$. In fact, the evaluation of $\langle S^2 \rangle$ does not return the expected eigenvalue (e.g., $\langle S^2 \rangle = 0$ for singlet states, $\langle S^2 \rangle = 0.75$ for doublet states, and so on) but a value proportional to the mixture of spin states. We can express the computed value of the $\langle S^2 \rangle$ operator of the broken-symmetry situation (BS) as:

$$\langle S^2 \rangle_{BS} = \alpha \langle S^2 \rangle_{(S+1)} + (1 - \alpha) \langle S^2 \rangle_{pure} \quad , \quad (2.15)$$

where $\langle S^2 \rangle_{(S+1)}$ is the value of the total square spin angular momentum operator of the afterward spin state which is near-degenerated with the spin state we are studying, $\langle S^2 \rangle_{pure}$ is the the expected value of the operator for the spin state we are studying, and α is the proportionality weight factor.

The same mixture of spin states depicted on the value of the $\langle S^2 \rangle$ operator is carried over to the energy value. Thus, an equivalent expression of equation 2.15 can be expressed for the energy:

$$E_{BS} = \alpha E_{S+1} + (1 - \alpha) E_{pure} \quad , \quad (2.16)$$

where α is the same proportionality weight factor as in equation 2.15, and E_{S+1} and E_{pure} are the energy of the afterward spin state which is mixed with the spin state we are studying and the expected non-contaminated energy of the spin state we are studying, respectively.

From the combination of equations 2.15 and 2.16 results the Yamaguchi expression to compute the energy of the spin-purified state (E_{pure}) in situations of BS with near-degeneracy problems:³²¹⁻³²³

$$E_{pure} = \frac{E_{BS}(\langle S^2 \rangle_{S+1} - \langle S^2 \rangle_{pure}) - E_{S+1}(\langle S^2 \rangle_{BS} - \langle S^2 \rangle_{pure})}{\langle S^2 \rangle_{S+1} - \langle S^2 \rangle_{BS}} \quad , \quad (2.17)$$

2.2 COMPUTATIONAL PRACTICES FOR REACTIVITY STUDIES

which is equivalent to the following two practical equations:

$$E_{pure} = \frac{E_{BS} - \alpha E_{S+1}}{1 - \alpha} \quad (2.18)$$

$$\alpha = \frac{\langle S^2 \rangle_{BS} - \langle S^2 \rangle_{pure}}{\langle S^2 \rangle_{S+1} - \langle S^2 \rangle_{pure}} \quad (2.19)$$

Yamaguchi's approach has been proven effective for the prediction of spin state energy splittings in metal coordination complexes.^{281,324}

2.3 Tools for electron distribution analyses

The last section of the methodology chapter is addressed to electron distribution analyses. Just as there has been introduced in [subsection 1.4.1](#), in order to obtain a whole picture of the construction of molecules, it is necessary to know the electron distribution or the bonding pattern. Since Lewis theory³²⁵ (or since the basics of quantum chemistry) most of chemistry is rationalized by the use of atoms (or electrons) as building blocks of the molecular system. Thus, conceptually, molecular partitions (in atomic regions or in regions with high electron localization, for example) have an irrefutable utility because they allow us to connect the final chemical system with their constituents.

As I hope to have been able to reflect in Chapter 1, studies of the construction and properties of molecules based on analyses of the electron distribution represent an important part of this thesis. Besides, electron distribution analyses are key supplementary studies of chemical reactivity.

Following the same scheme to classify electron partitioning strategies as described in [subsection 1.4.1](#), the partitioning strategies will be divided and defined as: i) Hilbert-space partitions; and ii) molecular-space partitions.

2.3.1 Molecular-space partitions

There are different molecular-space functions that can be used to define different electronic regions. However, the molecular function that has certainly been the most examined on electron distribution analyses is the electron density. The selection of the electron density has two main advantages: i) when it is studied by topological techniques, atomic partitions are naturally recovered; and ii) the atomic partitions are one of the best well-defined approach to divide the molecule into its constituents and to rationalize the electronic structure and properties.

Topology of the electron density

The topological analysis of the electron density was introduced by Richard F. W. Bader in 1990²²⁶ and a whole theory has been developed based on this analysis, the Quantum Theory of Atoms in Molecules, QTAIM. Within the framework of QTAIM, atomic populations and charges, electron localization indices, or population variances, among other chemically relevant information, can be defined.

In order to perform the QTAIM study, the electron density is analyzed through the identification of critical points (CPs), *i.e.*, points where the first derivative of the electron density function is equal to zero.

$$\vec{\nabla}\rho(\vec{r}) = \vec{i}\frac{\partial\rho(\vec{r})}{\partial x} + \vec{j}\frac{\partial\rho(\vec{r})}{\partial y} + \vec{k}\frac{\partial\rho(\vec{r})}{\partial z} = \vec{0} \quad (2.20)$$

Then, in order to characterize these CPs, the second derivatives of the density are analyzed at those positions. All these second derivatives of the density are

2.3 TOOLS FOR ELECTRON DISTRIBUTION ANALYSES

collected in the so-called Hessian matrix, \mathbf{H} :

$$\mathbf{H}(\vec{r}_c) = \left(\begin{array}{ccc} \frac{\partial^2 \rho(\vec{r})}{\partial x^2} & \frac{\partial^2 \rho(\vec{r})}{\partial x \partial y} & \frac{\partial^2 \rho(\vec{r})}{\partial x \partial z} \\ \frac{\partial^2 \rho(\vec{r})}{\partial y \partial x} & \frac{\partial^2 \rho(\vec{r})}{\partial y^2} & \frac{\partial^2 \rho(\vec{r})}{\partial y \partial z} \\ \frac{\partial^2 \rho(\vec{r})}{\partial z \partial x} & \frac{\partial^2 \rho(\vec{r})}{\partial z \partial y} & \frac{\partial^2 \rho(\vec{r})}{\partial z^2} \end{array} \right) \Bigg|_{\vec{r}=\vec{r}_c} \quad (2.21)$$

The Hessian Matrix is a real symmetric matrix, thus, it can be transformed into its diagonal representation via unitary transformation, $\mathbf{U}^{-1}\mathbf{H}\mathbf{U} = \Lambda$.

Once diagonalized, the diagonal values are the eigenvalues λ_1 , λ_2 and λ_3 and they correspond to the curvatures of the density with respect to the three principal axes, x' , y' , and z' , respectively, at the given point, \vec{r}_c .

$$\Lambda = \left(\begin{array}{ccc} \frac{\partial^2 \rho(\vec{r})}{\partial x'^2} & 0 & 0 \\ 0 & \frac{\partial^2 \rho(\vec{r})}{\partial y'^2} & 0 \\ 0 & 0 & \frac{\partial^2 \rho(\vec{r})}{\partial z'^2} \end{array} \right) \Bigg|_{\vec{r}'=\vec{r}_c} = \left(\begin{array}{ccc} \lambda_1 & 0 & 0 \\ 0 & \lambda_2 & 0 \\ 0 & 0 & \lambda_3 \end{array} \right) \quad (2.22)$$

Interestingly, the trace of the Hessian matrix is invariant with respect to the rotation of the coordinate system and it is known as the Laplacian of the one-electron density, $\vec{\nabla}^2 \rho(\vec{r})$:

$$\vec{\nabla}^2 \rho(\vec{r}) = \frac{\partial^2 \rho(\vec{r})}{\partial x^2} + \frac{\partial^2 \rho(\vec{r})}{\partial y^2} + \frac{\partial^2 \rho(\vec{r})}{\partial z^2} \quad (2.23)$$

The values and signs of the eigenvalues λ_1 , λ_2 and λ_3 characterize the critical points. In QTAIM the complete nomenclature for critical points is denoted as (ω, σ) . The ω term is the rank, which is the number of non-zero curvatures of the Hessian. In our compounds the rank is typically 3 because neither λ_1 , nor λ_2 , nor λ_3 are equal to zero. The σ term is the signature and it refers to the difference between the number of positive and negative eigenvalues. Each positive curvature contributes +1 to the signature and each negative curvature adds -1. According to ω and σ definitions, we can classify the critical points as maxima, minima, or saddle points, giving four CP types:

(3,-3) Nuclear Critical Point (NCP), Attractor or Atomic Critical Point: All the curvatures of the Hessian are negative and the point is a local maximum. These points usually coincide with an nucleus position and every atom-in-molecule within QTAIM is characterized by one, and only one, (3,-3) attractor. Although it is not highly usual, one may localize local maxima of the electron density not related with any atomic position. As stated before in the Introduction chapter, these CP are called **Non-Nuclear Attractors (NNAs)**, and it will be a widely-used concept in [chapter 6](#).

(3,-1) Bond Critical Point (BCP): BCPs show two negative curvatures of the Hessian and a positive one. Bond critical points are found between two NCP and, in general, indicate the presence of a chemical bond.

(3,+1) Ring Critical Point (RCP): RCPs show two positive curvatures of the Hessian and a negative one. RCP can be found on the vicinity of the center of chemical rings.

(3,+3) Cage Critical Point (CCP): In CCP, all the curvatures of the Hessian are positive, that is, it is a local minimum of the electron density. Its presence indicates a cage structure and the CCP locates close to its center.

If a proper characterization of the topology of the electron density has been possible, CPs will fulfill the Poincaré-Hopf relationship:

$$n_{NCP} - n_{BCP} + n_{RCP} - n_{CCP} = 1 \quad , \quad (2.24)$$

and the definition of natural partitions of *atoms in molecules* by the QTAIM framework will be possible. In order to define the boundaries of each atomic region, the gradient vector field of the electron density, $\vec{\nabla}\rho(\vec{r})$, is analyzed. The gradient vector field describes trajectories, also called gradient paths, that originate and terminate at a critical point, *i.e.*, where $\vec{\nabla}\rho(\vec{r}) = 0$ (see [Figure 2.3.a](#)). Then, the boundaries of the atomic regions are determined by the *zero*-flux surface in the gradient vector field of the electron density, given by:

$$\vec{\nabla}\rho(\vec{r}) \cdot \vec{n}(\vec{r}) = 0 \quad \forall \vec{r} \in S(\vec{r}), \quad (2.25)$$

where $\vec{n}(\vec{r})$ is the unit vector normal to $S(\vec{r})$, the surface.

The QTAIM method has strengths and weaknesses. Since a complex topological analysis is necessary, for example, for defining complex-shaped atomic domain or for integrating the electron population of each atomic partition, the QTAIM method usually implies high computational costs. Furthermore, the QTAIM method is very sensible to bad descriptions of the electron density function. For example, if the basis set used originates spikes or discontinuities on the electron density function, a bad topological description will be obtained. Usually, this kind of anomalies (spikes or discontinuities) of the electron density description are the main reason that leads to spurious NNA. On the contrary, the high versatility of QTAIM enables the localization of non-spurious NNA.

Other atomic partition of the electron density

By the QTAIM approach, the molecular space is divided into atomic regions defined by sharp boundaries. An alternative is to consider a continuous transition from one region to another, the so-called *fuzzy* atom schemes. Hence, part of the physical space is assumed to be shared to some extent by two or more atoms, and overlapping or “fuzzy” boundaries are introduced.

As stated in subsection [1.3.2](#), the common way to represent “fuzzy” schemes is by introducing a non-negative weight function $w_A(\vec{r})$ for each atom A and each point of the 3D space, which satisfies the requirement of equation [\(1.6\)](#).

There are several fuzzy atom schemes that can be used to define atomic partitions of the electron density such as Hirshfeld,³²⁶ Hirshfeld-Iterative,³²⁷ the simplest Becke atoms,³²⁸ or the topological fuzzy Voronoi cells (TFVC).³²⁹ The difference between those fuzzy schemes is how the weight function is defined.

2.3 TOOLS FOR ELECTRON DISTRIBUTION ANALYSES

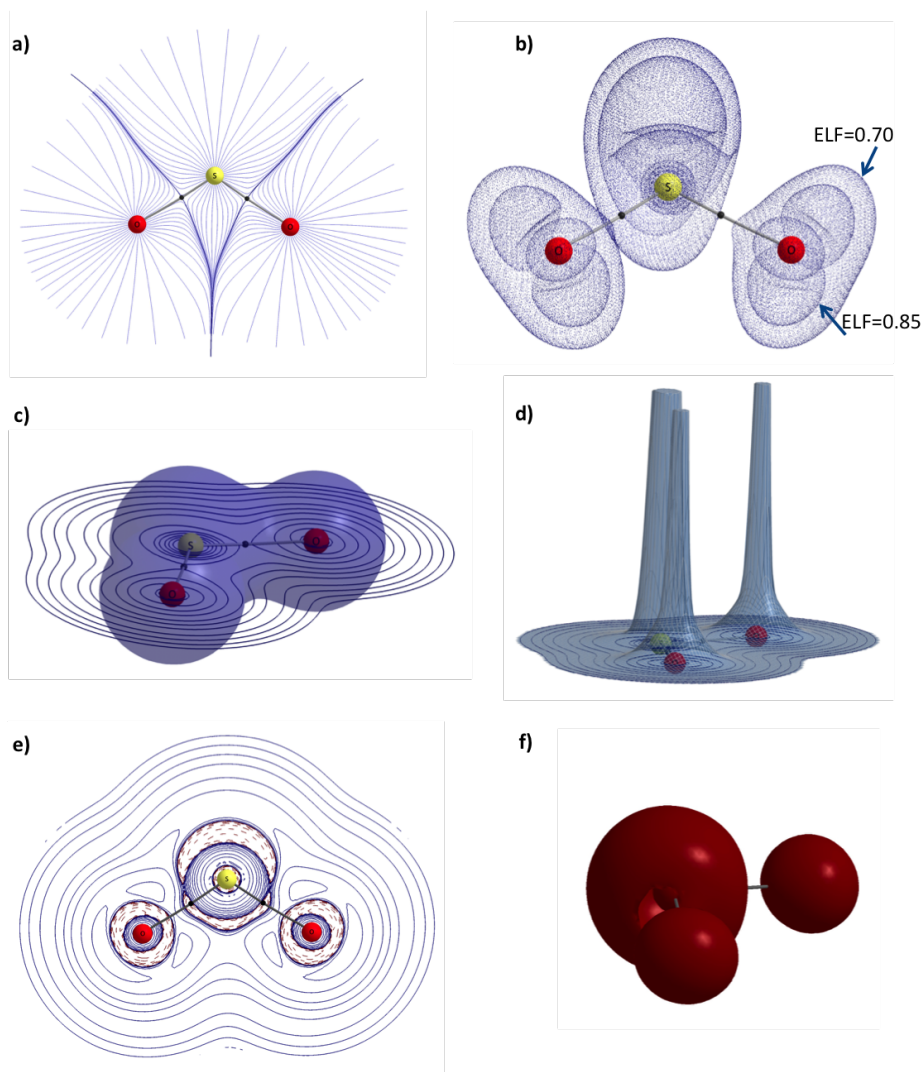


Figure 2.3: Electron distribution analyses of the SO₂ molecule. **a)** Topology of the electron density and trajectories of the gradient of the electron density ($\vec{\nabla}\rho(\vec{r})$) (in blue). BCP in black and bond paths in gray. **b)** ELF isosurfaces with contour values 0.70 and 0.85. **c)** Contour map of the electron density and isosurface with $\rho=0.07$. **d)** Relief map of the electron density. **e)** Contour map of the Laplacian of the electron density, $\vec{\nabla}^2\rho(\vec{r})$. Blue isocontour lines represent positive values and red isocontour lines represent negative values. **f)** $\vec{\nabla}^2\rho(\vec{r})=-0.05$ isosurface.

In Hirshfeld partitioning scheme, the atomic weight of atom A at a given point in the space is determined by the ratio:

$$w_A(\vec{r}) = \frac{\rho_A^0(\vec{r})}{\sum_{B=1}^N \rho_B^0(\vec{r})} \quad , \quad (2.26)$$

where $\rho_A^0(\vec{r})$ is the so-called pro-atomic electron density, a spherically-averaged atomic electron density of the neutral atom A, and the denominator accounts for the total sum of the pro-atomic electron density, which defines the pro-molecular density of the system.

In the standard Hirshfeld scheme, the resulting shape of atomic domains in the molecule are strongly dependent on the choice of the pro-atomic densities. The iterative Hirshfeld scheme is an extension of the original Hirshfeld method that corrects this strong dependency. By an iterative process, in the Hirshfeld-Iterative method, the final pro-atomic densities are modified in order to integrate the same number of electrons as do the atoms in the molecule. The N_A parameters (eq. 1.4a), *i.e.*, the actual population of atom A in the molecule, are computed iteratively. In the first iteration, the populations are computed like in the original Hirshfeld scheme. The obtained N_A are used to define the new pro-atomic electron densities, which are used in the second iteration to compute the new N_A . This procedure is repeated until the atomic populations (and the pro-atomic electron densities) converge, *i.e.*, until when the maximum value of the difference in atomic populations between two iterations drops below a predefined threshold.

Another alternative to compute atomic weights is to use Becke's atoms; *i.e.*, the fuzzy atomic Voronoi cells introduced by Becke.³²⁸ In Becke's atoms, the definition of the atomic weights follows the same general strategy as in Hirshfeld scheme:

$$w_A(\vec{r}) = \frac{P_A(\vec{r})}{\sum_{B=1}^N P_B(\vec{r})} \quad , \quad (2.27)$$

but using cell functions, $P_A(\vec{r})$, instead of pro-atomic densities.

Becke's cell-functions are algebraic functions which strictly satisfy the sum rule (eq. 1.6) and also fulfill $w_A(\vec{R}_A) = 1$ and $w_B(\vec{R}_A) = 0$. That is, the weight function becomes zero in the vicinity of the other nuclei.^f

In Becke's approach, each atom of the system has its cell function, $P_A(\vec{r})$, defined as the product of a series of switching functions, $s_{AB}(\vec{r})$.

$$P_A(\vec{r}) = \prod_{B \neq A} s_{AB}(\vec{r}) \quad (2.28)$$

In turn, switching functions, $s_{AB}(\vec{r})$, are defined by each pair of atoms of the system and are mainly determined by two parameters: the fixed atomic radii used and the stiffness parameter. The former determines the size of the atomic Voronoi cells, whereas the latter controls the shape of the cutoff profile, *i.e.*,

^f This characteristic of the weight function is not necessarily true for Hirshfeld-based fuzzy atom definitions.

2.3 TOOLS FOR ELECTRON DISTRIBUTION ANALYSES

to which extent two neighboring atoms share the physical space between them. In the original paper, Becke used the set of empirical atomic radii of Bragg and Slater³³⁰ on the basis of a better performance of his numerical integration scheme.

An alternative to Becke-atom definition that uses the same scheme was proposed by Salvador and Mayer.³³¹ The main criticism in Becke’s atom definition is the use of a fixed set of empirical radii because this might not allow the method to be flexible enough to properly study some systems. Thus, instead of fixed radii, Mayer *et al.* proposed a new criterion based on the position of the extremum (typically a minimum) of the density along the internuclear axis connecting every two neighboring atoms to define the location of the corresponding interatomic cell boundary. That scheme was later referred to as Becke- ρ ,³³² and can be considered as a good adaptation of Bader’s partitioning.

In this thesis several of these atomic partitions of the electron density have been used to study electron distribution and molecular properties. Obviously, in order to determine the electronegativity character, in [chapter 6](#), none of the fuzzy schemes exposed above is appropriate because the fuzzy schemes presented cannot define regions different from the atomic ones. However, in the determination of oxidation states, several *fuzzy* methods to define atomic partitions of the electron density have been used, being the topological version of the Becke’s atoms, *i.e.*, the topological fuzzy Voronoi cells (TFVC) approach, the atomic partition of choice.

Other molecular-space functions and their partitions

Besides the electron density, there are other molecular functions from which additional electronic partitions can be defined. Examples of these functions are, for instance, the Laplacian of the electron density, $\nabla^2\rho(\vec{r})$, the electron localization function (ELF), or the electrostatic potential (ESP). In the three previous functions, the topological partitions that arise are not atomic and depend on each function. In the following paragraphs, the Laplacian of the electron density and the ELF will be developed because they have been used in this thesis.

The **Laplacian of the electron density**, $\nabla^2\rho(\vec{r})$, is already defined in [eq. 2.23](#). It is obtained as the trace of the Hessian matrix and, together with the electron density, it is one of the most extensively used functions to analyze the electron distribution. Negative values of the Laplacian account for positions where the one-electron density function has a local maximum; thus, where electrons tend to be locally concentrated. On the contrary, positive values account for positions where the one-electron density function has a local minimum; thus, where electrons move away from (in a given molecular context). Hence, a global evaluation of the Laplacian gives us a complete map of the electron distribution that complements the topological analysis of the electron density performed within the QTAIM framework (see [Figure 2.3.e](#) and [.f](#)).

Although being possible, in this thesis the topological characterization of the Laplacian of the electron density (*i.e.*, the identification of maxima, minima, the boundaries of the electronic regions, and so on) has not been done. In this thesis the Laplacian of the electron density has been taken just for analyzing (and visualizing) the regions where it presented negative values as indicators of electron

localization.

The **Electron Localization Function**, ELF, is another molecular function based on the same-spin conditional pair probability. The ELF was introduced in 1990 by Becke and Edgecombe who used this function to generate interesting pictures of the electron localization in the atomic shell structure, as for instance the core, lone pairs, and binding regions.²²⁸ In this thesis, the ELF and its topological characterization are used to study the electron distribution.

The conditional probability is the probability that event A will occur given event B . Bayes' theorem provides the formula to calculate it:

$$P(A|B) = \frac{P(A \cap B)}{P(B)} \quad (2.29)$$

where $P(B)$ is the probability of event B and $P(A \cap B)$ is the probability both events A and event B occur. ELF measures the probability of having an electron in the sphere of radius $(\vec{r} + \vec{s})$ when one electron of the same spin is known to be at the reference position \vec{r} , $P(\vec{r}, \vec{r} + \vec{s})$.

In order to define the probability of finding two electrons simultaneously at two positions close in the space, we use the two-electron density or pair density, $\gamma^{\sigma_1\sigma_2}(\vec{r}_1, \vec{r}_2)$.³³³ After spin integration of $\gamma^{\sigma_1\sigma_2}(\vec{r}_1, \vec{r}_2)$, one gets the spinless pair density, which is:

$$\gamma^{(2)}(\vec{r}_1, \vec{r}_2) = N(N-1) \int |\psi(\vec{r}_1, \vec{r}_2, \vec{r}_3, \dots, \vec{r}_N)|^2 d\vec{s}_1 d\vec{s}_2 d\vec{r}_3 \dots d\vec{r}_N. \quad (2.30)$$

In order to obtain the conditional pair density we just have to divide the pair density by $\rho(\vec{r}_1)$:

$$P(\vec{r}_1, \vec{r}_2) = \frac{\gamma^{(2)}(\vec{r}_1, \vec{r}_2)}{\rho(\vec{r}_1)} \quad (2.31)$$

Since $\gamma^{(2)}(\vec{r}_1, \vec{r}_2)$ can be further partitioned in the same spin and the unlike-spin electron contributions,

$$\gamma(\vec{r}_1, \vec{r}_2) = \gamma^{\alpha\alpha}(\vec{r}_1, \vec{r}_2) + \gamma^{\alpha\beta}(\vec{r}_1, \vec{r}_2) + \gamma^{\beta\alpha}(\vec{r}_1, \vec{r}_2) + \gamma^{\beta\beta}(\vec{r}_1, \vec{r}_2), \quad (2.32)$$

it is possible to write the $P^{\sigma\sigma}(\vec{r}_1, \vec{r}_2)$ and $P^{\sigma\sigma'}(\vec{r}_1, \vec{r}_2)$ contributions to the conditional pair density as

$$P^{\sigma\sigma}(\vec{r}_1, \vec{r}_2) = \frac{\gamma^{\sigma\sigma}(\vec{r}_1, \vec{r}_2)}{\rho(\vec{r}_1)} \quad (2.33)$$

and

$$P^{\sigma\sigma'}(\vec{r}_1, \vec{r}_2) = \frac{\gamma^{\sigma\sigma'}(\vec{r}_1, \vec{r}_2)}{\rho(\vec{r}_1)}, \quad (2.34)$$

where $\sigma, \sigma' = \alpha, \beta$.

In order to construct the ELF expression, the same-spin conditional pair probability is expanded around the reference electron, *i.e.*, where $\vec{s} = \vec{0}$. This is done

in terms of a Taylor series.

Finally, with the defined spherically averaged same-spin pair density, D_σ , which it was defined just taking the leading term of the Taylor expansion (eq. 2.35), Becke and Edgcombe calculated the relative ratio with respect to the same quantity for the homogeneous electron gas, D_σ^0 (eq. 2.36).

$$D_\sigma = \frac{1}{2} \nabla_s^2 P^{\sigma\sigma}(\vec{r}, \vec{r} + \vec{s})|_{\vec{s}=\vec{0}}, \quad (2.35)$$

$$D(\vec{r}) = \frac{D_\sigma(\vec{r})}{D_\sigma^0(\vec{r})}. \quad (2.36)$$

The probability of observing an electron with spin α when there is already another electron with the same spin nearby is lower when the latter electron is localized. Thus, the more electron localization the lower the same-spin conditional pair probability values ($D_\sigma \downarrow \rightarrow D(\vec{r}) \downarrow$). Thus, although the relative ratio can recover the chemical structure, Becke and Edgcombe considered necessary to scale the aforementioned ratio in order to range the electron localization measure in the interval $[0,1]$:

$$ELF(\vec{r}) = \eta(\vec{r}) = \frac{1}{1 + D(\vec{r})^2} = \frac{1}{1 + \left(\frac{D_\sigma(\vec{r})}{D_\sigma^0(\vec{r})}\right)^2}, \quad (2.37)$$

where $ELF=1$ corresponds to a completely localized situation, $ELF=0$ corresponds to a delocalized system, and $ELF=0.5$ is the value one should obtain for the homogeneous electron gas (see Figure 2.3.b).

2.3.2 Hilbert-space partitions

In molecular-space partitions, the partition is achieved by the topological study of the molecular functions. In contrast, in Hilbert-space partitions, the partition is based on the basis set used to define the wavefunction. In principle, one can use any basis set from the Hilbert-space to expand a wavefunction (for instance atomic orbitals constructed from Slater or Gaussian primitive functions, or plane waves); however, since these basis functions are usually centered in atoms, Hilbert-space partitions tend to divide the molecular system into atomic regions.

In this context, any molecular quantity can be decomposed in terms of atomic contributions by means of a Hilbert-space analysis by expressing the quantity in terms of the basis functions. For instance, a molecular orbital can be rewritten as a sum of its atomic counterparts as:

$$\phi_i^{MO}(\vec{r}) = \sum_A \phi_i^A(\vec{r}) = \sum_A \sum_{\mu \in A} c_{\mu i} \chi_\mu(\vec{r}), \quad (2.38)$$

where χ_μ are the basis functions centered in atom A and $c_{\mu i}$ are the coefficients of the atomic orbitals.

Such kind of atomic decomposition is available in most of the computational softwares under the name of Mulliken's population analysis, who was the first to suggest this procedure already in 1955.²⁰¹

We can apply the same decomposition procedure to the electronic density. It can be written in terms of the atomic orbital basis as:

$$\begin{aligned}
 \rho(\vec{r}) &= \sum_{i=1}^N |\phi_i(\vec{r})|^2 = \sum_{i=1}^N \phi_i^*(\vec{r})\phi_i(\vec{r}) \\
 \rho(\vec{r}) &= \sum_{i=1}^N \sum_{\nu} c_{\nu i}^* \chi_{\nu}^*(\vec{r}) \sum_{\mu} c_{\mu i} \chi_{\mu}(\vec{r}) \\
 \rho(\vec{r}) &= \sum_{i=1}^N \sum_{\nu} \sum_{\mu} c_{\mu i} c_{i\nu}^* \chi_{\nu}^*(\vec{r}) \chi_{\mu}(\vec{r}) \\
 \rho(\vec{r}) &= \sum_{\mu\nu} D_{\mu\nu} \chi_{\nu}^*(\vec{r}) \chi_{\mu}(\vec{r})
 \end{aligned} \tag{2.39}$$

where \mathbf{D} is called first-order density matrix and it is a matrix representation of the electron density in terms of molecular orbitals

$$D_{\mu\nu} = \sum_{i=1}^N \omega_i c_{\mu i} c_{i\nu}. \tag{2.40}$$

In order to define a more general first-order density matrix of the system (*i.e.*, valid for different types of molecular orbitals), the occupation numbers of the molecular orbitals, ω_i , have to be also taken into account.

By integrating eq. 2.39 one obtains the total number of electrons of the system,

$$N = \int \rho(\vec{r}) d\vec{r} = \sum_{\mu\nu} D_{\mu\nu} \int \chi_{\nu}^*(\vec{r}) \chi_{\mu}(\vec{r}) d\vec{r} = \sum_{\mu\nu} D_{\mu\nu} S_{\nu\mu} = \sum_{\mu} (DS)_{\mu\mu} \tag{2.41}$$

The integration in equation 2.41 refers to the entire space, and the involved integrals over the basis set are the overlap integrals, the scalar products over the basis functions:

$$S_{\nu\mu} = \int \chi_{\nu}^*(\vec{r}) \chi_{\mu}(\vec{r}) d\vec{r}. \tag{2.42}$$

Note that the summations at the equation 2.39 run over all basis functions (ν and μ), irrespective of where they are centered. However, one of the summations can run over only the basis functions attached to one atom (*e.g.*, A):

$$\mu \in A; \quad \sum_{\mu \in A} \sum_{\nu} D_{\mu\nu} \chi_{\nu}^*(\vec{r}) \chi_{\mu}(\vec{r}) = \rho^A(\vec{r}). \tag{2.43}$$

If we integrate (to the entire space) the above expression we obtain the so-called Mulliken Gross atomic population of atom A.

$$\int \rho^A(\vec{r}) d\vec{r} = \sum_{\mu \in A} \sum_{\nu} D_{\mu\nu} S_{\nu\mu} = \sum_{\mu \in A} (DS)_{\mu\mu}. \tag{2.44}$$

2.3 TOOLS FOR ELECTRON DISTRIBUTION ANALYSES

Besides, if both μ and ν summations run over only the basis function attached to one atom, we obtain the Hilbert-space definition of intraatomic densities:

$$\mu \in A, \nu \in A : \quad \sum_{\mu \in A} \sum_{\nu \in A} D_{\mu\nu} \chi_{\nu}^*(\vec{r}) \chi_{\mu}(\vec{r}) = \rho^{AA}(\vec{r}) \quad , \quad (2.45)$$

which, despite being integrated to the entire space, give rise to the intraatomic population, the Mulliken Net atomic population of atom A

$$\int \rho^{AA}(\vec{r}) d\vec{r} = \sum_{\substack{\mu \in A \\ \nu \in A}} D_{\mu\nu} S_{\nu\mu}. \quad (2.46)$$

Equations 2.43 and 2.45 are the equivalent Hilbert-space expressions of equation 1.5a and 1.5b, respectively, which are the 3-D or molecular-space expressions within the *fuzzy* formalism of the Gross and Net atomic densities.

2.3.3 Effective Oxidation States Analysis

The last *tool* for electron distribution analysis that has been used in this thesis is the Effective Oxidation State, EOS, approach (chapter 5).

The EOS approach relies on the achievement of the effective atomic orbitals (eff-AOs) of Mayer and their occupations for each atom (or fragment) of the system. The eff-AOs were introduced by Prof. Mayer with the aim of recovering the classical concept of the electron configuration (1s, 2s, 2p orbitals or their hybrids) of an atom within a molecule from the *a posteriori* analysis of the wavefunction.³³⁴ Specifically, eff-AOs are obtained by the diagonalization of the Net atomic population of each atom (or each fragment).

As we have just seen above, net atomic populations can be expressed within a Hilbert-space or 3D-(molecular-)space formalism:

$$\int \rho^{AA}(\vec{r}) d\vec{r} = \sum_{\substack{\mu \in A \\ \nu \in A}} D_{\mu\nu} S_{\nu\mu} = \mathcal{Q}_{\mu\nu}^A \quad ; \text{Hilbert-space formalism} \quad (2.47)$$

$$\int \rho^{AA} d\vec{r} = \int w_A(\vec{r}) w_A(\vec{r}) \rho(\vec{r}) d\vec{r} = \mathcal{Q}_{ii}^A \quad ; \text{3D-space formalism} \quad (2.48)$$

In both situations, to obtain the eff-AOs, the Net atomic population matrix, \mathcal{Q}^A , can be diagonalized by the unitary matrix U^A

$$U^{A,\dagger} \mathcal{Q}^A U^A = \text{diag}\{\lambda_{\mu}^A\}. \quad (2.49)$$

Then, the eff-AOs, $\chi_{\mu}^A(\vec{r})$, for each atom are defined as linear combinations of the intraatomic parts $\phi_i^A(\vec{r})$ of the MOs as:

$$\chi_{\mu}^A(\vec{r}) = \frac{1}{\sqrt{\lambda_{\mu}^A}} \sum_{i=1}^{n_A} U_{i\mu}^A \phi_i^A(\vec{r}); \quad \mu = 1, 2, \dots, n_A, \quad (2.50)$$

where n_A is the number of non-zero eigenvalues λ_μ^A . The latter are the corresponding occupation numbers of the eff-AOs, with $0 < \lambda_\mu^A \leq 1$.

Once eff-AOs and their occupations are obtained, a fundamental part of the EOS approach is how this information is used. As it has been already commented in section 1.3.2, all eff-AOs of the system are arranged by the decreasing occupation number and filled by electrons until electrons are exhausted. However, one could think that the easiest avenue would have been to simply round up the occupation numbers of the eff-AOs to the nearest integer. Such a naive approach would have several disadvantages. First, one may end up with different number of electrons than were originally in the molecule (typically less because the sum of the net populations is smaller than the number of electrons). Second, the values of the occupation numbers may differ from one atomic definition to another, leading to an undesired strong dependence upon the particular atomic definition used in the eff-AO construction.

Thus, the comparative approach used to assign the electron (comparing the occupation numbers of all the eff-AOs of the system) appears more appropriate than the independent rounding of the occupation numbers of the eff-AOs.

Another consideration, in order to conserve the number of alpha and beta electrons of the system in the process, is that one should obtain the eff-AOs associated with the alpha and beta intraatomic density separately. Thus, working with the spin-resolved version of equation 2.50, the following expression, should be our choice if our system is not a closed-shell singlet spin state:

$$\chi_\mu^{A,\sigma}(\vec{r}) = \frac{1}{\sqrt{\lambda_\mu^{A,\sigma}}} \sum_{i=1}^{n_\sigma} U_{i\mu}^{A,\sigma} \phi_i^{A,\sigma}(\vec{r}); \quad \mu = 1, 2, \dots, n_A \quad (2.51)$$

where $\sigma = \alpha, \beta$, and $\lambda_\mu^{A,\sigma}$ are the corresponding occupation numbers of the spin-resolved eff-AOs.

Finally, another feature introduced by the EOS approach was a simple global index to quantify the reliability of the formal picture of the OSs obtained. The occupation numbers of the *frontier* eff-AOs, namely, the last occupied, λ_{LO}^σ , and the first unoccupied, λ_{FU}^σ , eff-AOs, can be used to indicate how close the formal picture given by the EOS is to the electronic distribution of the system. Ideally, these occupations should be close to 1 and 0, respectively, but such values are only expected for non-interacting atoms. Since the EOS are determined by integer electrons, we assume that when λ_{LO}^σ and λ_{FU}^σ differ by more than *half* an electron the assignation of EOS is considered as indisputable. Thus, for each spin state, we proposed the following expression for the spin reliability index:

$$R_\sigma(\%) = 100 \min(1, \max(0, \lambda_{LO}^\sigma - \lambda_{FU}^\sigma + 1/2)) \quad (2.52)$$

and then $R = \min(R_\alpha, R_\beta)$; that is, the overall R index is the minimum value obtained for either the alpha or beta part. The larger the R value, the closer the overall assignation of the EOS is to the actual electronic structure of the system. Note that R can take values from 0 to 100%; where a value of 50% indicate absolute competition among the description of two possible OSs, and where

2.3 TOOLS FOR ELECTRON DISTRIBUTION ANALYSES

values below 50% indicate that the assignation of the electrons has not followed an *aufbau* principle according to the occupation numbers of the eff-AOs.

Chapter 3

Objectives

In this thesis state-of-the-art computational tools are applied to the different constituents of chemical science, *i.e.*, reactivity, properties, and construction of molecules. The knowledge in this varied set of constituents provides a detailed general pictures of any studied system. The computational chemistry allows a more accurate description of some aspects of the chemical processes than experimental chemistry since many intermediates and transition states of the chemical reaction cannot be detected by experimental techniques. Moreover, computational chemistry also allows a more detailed description of molecular structures than experimental techniques since the physical electron distribution (expressed in terms of wavefunction or electron density function) can be easily obtained from quantum-chemical calculations. Finally, computational chemistry also provides a deep understanding of molecular properties by correlating them with direct operators of physical observables or different indicators (*e.g.*, the correlation of the aromaticity with electron delocalization indices, or the correlation of oxidation states with indices that retrieve the localization and ionicity). Thus, in order to delve deeper into the overall description of chemical systems by theoretical means, this thesis encompass different computational studies that together cover all the three divisions of chemical science. For each division (reactivity, properties, and construction of molecules) specific goals that have a general interest were set out. These specific goals are summarized in the following lines.

Reactivity: Homogeneous catalysis by first-row transition metals has become a central research area in the last decades, especially when it deals with functionalization of non-activated hydrocarbons. Two functionalization processes of complementary interest are: i) the hydroxylation of alkanes by M=O units, and ii) the functionalization of non-activated arenes by M=C units. While the former has been widely studied (Cyt P450s, the most studied biological oxygenases, catalyze this reaction, whose mechanism was already described in 1976), the first biological examples of the latter (using a TM of the first row) were not reported until 2014. The experimental groups of Dr. Miquel Costas and Prof. Pedro J. Pérez proved that the biomimetic aminopyridine iron catalyst $[(\text{PyTACN})\text{Fe}^{\text{V}}]^{2+}$ shows catalytic power on these two processes. In view of this situation, we set two different objectives ([chapter 4](#)):

- Understand the effects of the substrate and solvent in the alkane hydroxy-

lation mechanism of biomimetic Fe(V)=O catalysts. Rationalize if these effects (substrate or solvent) can explain the key differences on the reaction mechanisms of alkane hydroxylation processes by Fe(V)=O catalysts reported in literature (section 4.1). Mainly, there is controversy if the reaction mechanism is always stepwise or concerted in some cases.

- Elucidate the reaction mechanism of the chemoselective functionalization of the C-H bond of benzene by carbene-insertion. Provide a deeper insight of the features that allowed our iron-carbene catalyst to achieve the first chemoselective carbene-insertion reaction into C-H bonds (section 4.2). Up to now, reactions between benzene and metal-carbene catalysts always produced a mixture of insertion and addition products that prevented its application in the synthetic chemical industry.

Properties: The oxidation state (OS) concept has utmost relevance in many branches of chemistry and it is a central cross-cutting property. Coinciding with the new *era* of the OS concept (new IUPAC's definition as well as practical algorithms to its determination), Dr. Pedro Salvador's group has published a new computational tool for the determination of OSs (the so-called EOS method). Little attention has been paid to the resolution of OS from first principles beyond the tacit assumption that their role is merely to provide partial atomic charges. Thereby, we proposed (chapter 5):

- Ascertain the applicability of the EOS method to determine OSs.
- Provide new insights about the OS property based on a benchmarking study (*e.g.*, provide new understandings in those situations where the ionic approximation (IA) proposed by the IUPAC shows ambiguities or limitations).

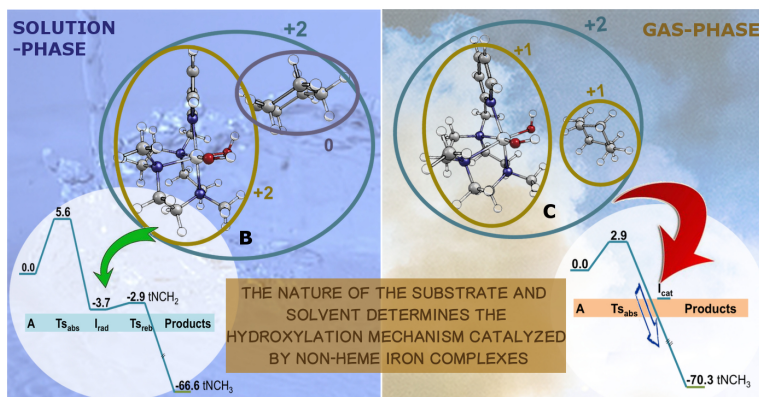
Construction: Electrides are among the most intriguing species lately discovered in terms of electronic structure. The feature of an isolated electron constituting the anionic part of electrides has been widely studied in the solid lattice. However, the possibility of the existence of truly electrides beyond the solid state, *i.e.*, molecular electrides at gas phase, had never been studied in detail before. The assignation of molecules as molecular electrides was done according to the presence of diffuse excess electrons on high-lying occupied orbitals or large values on nonlinear optical properties (NLOPs), but not determining the presence of isolated electrons in the electronic structure. Thus, we proposed (chapter 6):

- Examine the electronic structure of molecules previously labeled as electrides by means of different methods that are consistent with the presence of an isolated electron.
- Investigate if molecular electrides can exist and provide means to characterize and distinguish them from other similar species.
- Provide some guidance on the design of new electrides.

Chapter 4

Functionalization of C-H bonds of hydrocarbons by iron catalysts

4.1 Computational Insight into the Mechanism of Alkane Hydroxylation by Non-Heme Fe(PyTACN) Iron Complexes. Effects of the Substrate and Solvent



Postils, V.; Company, A.; Solà, M.; Costas, M.; Luis, J.M. **Computational Insight into the Mechanism of Alkane Hydroxylation by Non-Heme Fe(PyTACN) Iron Complexes. Effects of the Substrate and Solvent.** *Inorg. Chem.* **2015**, *54*, 8223-8236. DOI: 10.1021/acs.inorgchem.5b00583.

Reproduced with permission from:

Postils, V.; Company, A.; Sola, M.; Costas, M.; Luis, J.M. Computational Insight into the Mechanism of Alkane Hydroxylation by Non-Heme Fe(PyTACN) Iron Complexes. Effects of the Substrate and Solvent. *Inorg. Chem.* 2015, 54, 8223-8236.

<http://dx.doi.org/10.1021/acs.inorgchem.5b00583>

Copyright © 2015 American Chemical Society

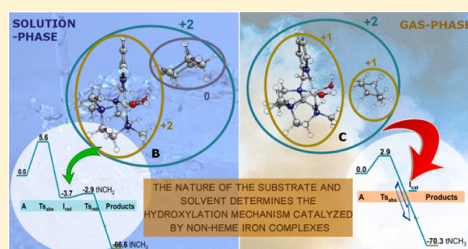
Computational Insight into the Mechanism of Alkane Hydroxylation by Non-heme Fe(PyTACN) Iron Complexes. Effects of the Substrate and Solvent

Verònica Postils, Anna Company, Miquel Solà,* Miquel Costas,* and Josep M. Luis*

Institut de Química Computacional i Catàlisi (IQCC) and Departament de Química, Universitat de Girona, Campus de Montilivi, 17071 Girona, Catalonia, Spain

Supporting Information

ABSTRACT: The reaction mechanisms for alkane hydroxylation catalyzed by non-heme Fe^VO complexes presented in the literature vary from rebound stepwise to concerted highly asynchronous processes. The origin of these important differences is still not completely understood. Herein, in order to clarify this apparent inconsistency, the hydroxylation of a series of alkanes (methane and substrates bearing primary, secondary, and tertiary C–H bonds) through a Fe^VO species, [Fe^V(O)(OH)(PyTACN)]²⁺ (PyTACN = 1-(2'-pyridylmethyl)-4,7-dimethyl-1,4,7-triazacyclononane), has been computationally examined at the gas phase and in acetonitrile solution. The initial breaking of the C–H bond can occur via hydrogen atom transfer (HAT), leading to an intermediate where there is an interaction between the radical substrate and [Fe^{IV}(OH)₂(PyTACN)]²⁺, or through hydride transfer to form a cationic substrate interacting with the [Fe^{III}(OH)₂(PyTACN)]⁺ species. Our calculations show the following: (i) except for methane in the rest of the alkanes studied, the intermediate formed by R⁺ and [Fe^{III}(OH)₂(PyTACN)]⁺ is more stable than that involving the alkyl radical and the [Fe^{IV}(OH)₂(PyTACN)]²⁺ complex; (ii) in spite of (i), the first step of the reaction mechanism for all substrates is a HAT instead of hydride abstraction; (iii) the HAT is the rate-determining step for all analyzed cases; and (iv) the barrier for the HAT decreases along methane → primary → secondary → tertiary carbon. The second part of the reaction mechanism corresponds to the rebound process. Therefore, the stereospecific hydroxylation of alkane C–H bonds by non-heme Fe^V(O) species occurs through a rebound stepwise mechanism that resembles that taking place at heme analogues. Finally, our study also shows that, to properly describe alkane hydroxylation processes mediated by Fe^VO species, it is essential to consider the solvent effects during geometry optimizations. The use of gas-phase geometries explains the variety of mechanisms for the hydroxylation of alkanes reported in the literature.



I. INTRODUCTION

Reactions involving functionalization of alkane C–H bonds are of interest because they enable reactivity into otherwise inert molecules.^{1,2} Alkane hydroxylation processes (AHPs) have importance in enzymatic oxidations that participate in metabolic paths, xenobiotic detoxification, and biodegradation, among others.^{3–6} Furthermore, alkane C–H oxidation reactions find major interest in current organic synthesis.^{7,8} Particularly interesting are C–H oxidation processes mediated by iron-based species that occur with retention of the configuration at the hydroxylated carbon. Stereospecific hydroxylations find ample precedent in iron oxygenases, cytochrome P-450 being a paradigmatic case.³ However, they are difficult to reproduce with synthetic complexes because the combination of oxidants with iron compounds very easily results in the formation of Fenton-like free diffusing radical processes.^{8–14} The preparation of non-heme Fe^{IV}(O) complexes during the past decade has represented a major step forward, reproducing the chemistry taking place at non-heme iron-dependent oxygenases, and has

prompted the investigation of their reactivity in alkane C–H oxidation.^{15,16}

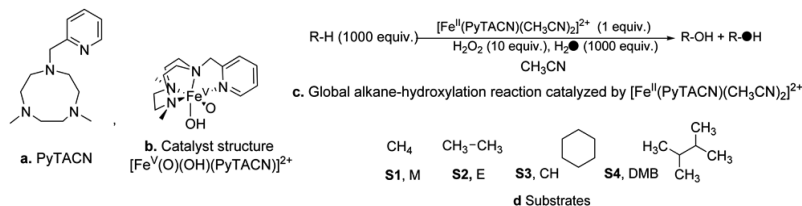
Non-heme Fe^V(O) species have been shown to be capable of breaking the strong C–H bond of alkanes via a hydrogen atom transfer (HAT) reaction.^{17,18} Close investigation of the non-enzymatic reactions shows that long-lived carbon-centered radicals are produced after the initial HAT.^{19,20} Thus, these reactions fundamentally depart from stereoretentive processes. In parallel studies, a series of iron complexes containing aminopyridine ligands have been shown capable of mediating stereospecific C–H hydroxylation reactions upon reaction with hydrogen peroxide, and therefore their mechanism of action does not involve generation of free diffusing radicals.^{9–11,21}

Among the non-heme iron complexes that are catalytically active in AHPs we can mention the perferyl [Fe^V(O)(OH)(PyTACN)]²⁺ (PyTACN = 1-(2'-pyridylmethyl)-4,7-dimethyl-1,4,7-triazacyclononane) species, that is formed upon reaction of

Received: March 18, 2015

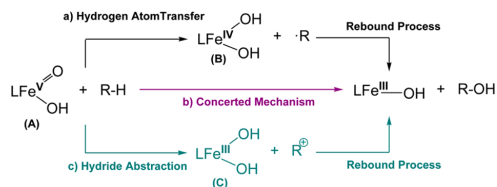
Published: August 19, 2015

Scheme 1. Ligand (a), Catalyst (b), and Substrates (d) Used in This Study, and Global Alkane Hydroxylation Reaction Catalyzed by the Studied Catalyst (c)



the [Fe^{II}(CF₃SO₃)₂(PyTACN)] catalyst with excess of H₂O₂ in acetonitrile (Scheme 1a–c). The capability of ferryl complexes to catalyze AHPs has been proven experimentally and computationally.^{22–24} This reaction occurs with stereoretention at the hydroxylated carbon site, indicating that long-lived carbon centered radicals or cations are not involved. Other complexes studied in the literature that have also been proposed to involve Fe^V(O) species include: [Fe^V(O)(OH)(L)]²⁺ (where L = TPA (TPA = tris(2-pyridylmethyl)amine) and related),^{21,25} [Fe^V(O)(L)]⁺ (where L = dpqa (dpqa = 2-[bis(pyridin-2-ylmethyl)amino-*N*-quinolin-8-yl-acetamidate]),²⁶ and [Fe^V(O)-(TAML)]⁻ (TAML = tetraamido macrocyclic ligand) and related.^{27–29} However, the reaction mechanisms for alkane oxidation processes catalyzed by Fe^V(O) complexes presented in literature show important differences among them, whose origin is not completely understood.^{23,25,29,30} In all cases reaction of the Fe^V(O) (A) species with an alkane starts with a HAT from the C–H bond by the iron-oxo group and then several different hypothetical pathways are proposed (Scheme 2). The most

Scheme 2. Proposed Mechanisms for Alkane Hydroxylation via Fe^V(O)(OH)(L) Catalysts



accepted one is the “rebound mechanism” where the HAT forms an alkyl radical intermediate (R[•]) that interacts with a bishydroxo Fe^{IV}(OH)₂ species (B) that leads to the final hydroxylated products (path a in Scheme 2). This rebound mechanism for alkane hydroxylation catalyzed by non-heme Fe^V(O) species was proposed in previous density functional theory (DFT) studies as, for instance, in a work of methane and acetonitrile hydroxylation by [Fe^V(O)(OH)(TPA)]²⁺.²⁵

A second proposed mechanism involves direct formation of the hydroxylated products through a concerted highly asynchronous mechanism (path b in Scheme 2). The transition state in this single step process is given by the HAT, which is followed by the C–O bond formation without the generation of any intermediate. For instance, this asynchronous concerted mechanism was proposed for the cyclohexane hydroxylation catalyzed by [Fe^V(O)(OH)(L)]²⁺ (L = tetradentate bispidine ligand)³² and by [Fe^V(O)(OH)(PyTACN)]²⁺.²³ Finally, in the present work we show (*vide infra*) that a third pathway where a hydride transfer process leads to a cationic alkyl intermediate

(R⁺) and a bishydroxo Fe^{III}(OH)₂(L) unit (C) cannot be *a priori* discarded. Transfer of one of the hydroxide ligands to R⁺ would afford the final hydroxylated product (path c in Scheme 2). This third option is similar to the proposed mechanism for the cyclohexane chlorination by [Fe^V(O)(Cl)(TPA)]²⁺.³⁰ Therefore, depending on the substrate, catalysts, and method of calculation, several authors arrived at different conclusions about the operative mechanism in AHPs (Scheme 2). A fourth possible mechanism where the substrate radical formed via HAT dissociates and reacts with a second oxo-iron compound to give the corresponding hydroxylated product is also described in literature. This dissociative mechanism has been proposed for the hydroxylation of alkanes catalyzed by [Fe^{IV}(O)(BnTPEN)]²⁺,³¹ [Fe^{IV}(O)(N4Py)]²⁺³¹ and [Fe^V(O)(TAML)]²⁺,^{28,29}

and in these three cases this mechanism is supported by theoretical and experimental evidence. Furthermore, Gupta and co-workers suggested that the oxidation of cyclohexane catalyzed by their synthesized biuret-substituted TAML ligand Fe^VO compound may proceed by either a rebound mechanism, a dissociative mechanism or a combination of both.²⁸ Then, in principle, it is plausible to propose that dissociation of the substrate radical could be competitive with or preferable to the rebound pathway. However, for the particular case of the [Fe^V(O)(OH)(PyTACN)]²⁺ compound, all experimental evidences conclusively discard the dissociation mechanism (see below), and thus it has not been studied here.

The main goal of this work is to gain insight into the reaction mechanism of AHPs studying by hydroxylation of methane, ethane, cyclohexane, and 2,3-dimethylbutane (2,3-DMB) catalyzed by the [Fe^V(O)(OH)(PyTACN)]²⁺ complex (Scheme 1). The studied alkanes were chosen because they bear different types of C–H bonds (methane, primary, secondary, tertiary). Our aim is to investigate whether hydroxylation of C–H bonds of different nature proceeds or not through different reaction pathways. A second goal is to analyze how solvent affects the reaction mechanism of AHPs. To this end, we performed calculations (i) at gas phase, (ii) at gas phase including single-point energy corrections for dispersion and acetonitrile solvent effects, and (iii) in acetonitrile solution (see Computational Details section for more details). The final goal of this study is to identify the key steps of the AHP mechanism to get a better understanding of these reactions that ultimately should help the design of more efficient catalysts.

II. COMPUTATIONAL DETAILS

All values presented in this computational study have been obtained with the Gaussian 09 software package³³ using the spin-unrestricted UB3LYP^{34,35} hybrid DFT functional in conjunction with the SDD basis set and the associated effective core potential (ECP) for Fe³⁶ and the 6-311G(d,p) basis set for the rest of the atoms. All geometry optimizations were performed without symmetry constraints. Analytical Hessians were

computed to determine the nature of stationary points (one and zero imaginary frequencies for transition states and minima, respectively). Furthermore, the connectivity between stationary points was unambiguously established by intrinsic reaction path calculations.

All final reported energy values were systematically corrected after geometry optimization by removing spin-contamination using the following expressions:^{39,40}

$$E_{\text{spin-corr}} = \frac{E_S - a \cdot E_{(S+1)}}{1 - a} \quad (1)$$

$$a = \frac{\langle S_S^2 \rangle - S \cdot (S + 1)}{\langle S_{(S+1)}^2 \rangle - S \cdot (S + 1)} \quad (2)$$

where E_S and $\langle S_S^2 \rangle$ are the UB3LYP/6-311G(d,p)~SDD electronic energy and square total spin angular momentum of the S spin state obtained by means of an unrestricted calculation. $E_{(S+1)}$ and $\langle S_{(S+1)}^2 \rangle$ are the electronic energy and square total spin angular momentum obtained for the $(S+1)$ spin state computed with the same level of theory and at the geometry of the S spin state. $E_{\text{spin-corr}}$ is the spin-corrected electronic energy.

From this general level of theory, three different computational methodologies were used. First, we calculated relative gas-phase Gibbs energy values (ΔG_g°) including spin-corrected UB3LYP/6-311G(d,p)~SDD electronic energies ($E_{\text{spin-corr}}^g$), together with thermal and entropy corrections at 298.15 K obtained from frequency calculations (G_{corr}^g) (eq 3). Second, we obtained relative Gibbs energies ($\Delta G_{g+\text{corr}}^g$) that included relative gas-phase Gibbs energy values plus single-point Gibbs solvation energies in acetonitrile solution ($G_{\text{solv-corr}}^g$) and dispersion corrections (E_{disp}^g) (eq 4). Dispersion effects were calculated using the Grimme DFT-D2 method,⁴¹ whereas solvation effects were computed using the Polarizable Continuum Model–SMD method developed by Truhlar and co-workers, which is based on the quantum mechanical charge density of the solute molecule interacting with a continuum description of the solvent.⁴² The solvent contribution was obtained as the difference between the electronic energy at gas phase and in solution both computed with the B3LYP method and the 6-31G(d) basis set, the basis set used to parametrize the SMD method. All calculated solvation Gibbs energies use a standard state of an ideal gas at a gas-phase concentration of 1 mol/L dissolved as an ideal dilute solution at a liquid-phase concentration of 1 mol/L. The change of conventional 1 atm standard state for gas-phase calculations to a standard-state gas-phase concentration of 1 M requires the introduction of a concentration-change term of 1.89 kcal/mol at 298.15 K, $\Delta G^{o/\#}$. Finally, in the third computational methodology used (ΔG_{solv}), the effect of the acetonitrile solution and the D2 dispersion corrections were taken into account during geometry optimization processes at the UB3LYP/6-311G(d,p)~SDD level of theory ($E_{\text{spin-corr}}^{\text{solv}} + E_{\text{disp}}^{\text{solv}} + G_{\text{solv-corr}}^{\text{solv}}$), instead of being added through single-point energy calculations at the gas-phase optimized geometries (eq 5). Then, following the approach suggested by Cramer et al., Gibbs energy corrections at 298.15 K obtained from frequency calculations at the solvent-phase optimized geometries ($G_{\text{corr}}^{\text{solv}}$) were added.⁴³ We can summarize the energy contributions included in each approach as follows:

$$G_g = E_{\text{spin-corr}}^g + G_{\text{corr}}^g \quad (3)$$

$$G_{g+\text{corr}} = E_{\text{spin-corr}}^g + E_{\text{disp}}^g + G_{\text{solv-corr}}^g + G_{\text{corr}}^g + \Delta G^{o/\#} \quad (4)$$

$$G_{\text{solv}} = E_{\text{spin-corr}}^{\text{solv}} + E_{\text{disp}}^{\text{solv}} + G_{\text{solv-corr}}^{\text{solv}} + G_{\text{corr}}^{\text{solv}} + \Delta G^{o/\#} \quad (5)$$

Unless otherwise noted, energies discussed in this work were obtained using eq 5. In the Supporting Information (SI), we provide tables with energies obtained using eqs 3 and 4.

The rigorous accurate computational study of electron-transfer (ET) processes in solvent requires expensive multiconfigurational calculations in order to describe electronic states properly. Moreover, the search of the ET barrier in solution, at UB3LYP/SMD level of theory, did not yield a good description of the barrier. UB3LYP/SMD led to abrupt

changes in the potential energy surfaces instead of a smooth description of the ET potential energy profile even when the more flexible IEFFPCM model was used.⁴⁴ In this work, to compute the ET barriers, we used the widely accepted classical Marcus formalism.^{45,46} The Marcus theory uses the Gibbs energy of the redox reaction ($\Delta G^\circ = \Delta G_{\text{prod}} - \Delta G_{\text{react}}$) and the reorganization energy (λ) to calculate the ET Gibbs energy barrier (ΔG^*) through

$$\Delta G^* = \frac{(\Delta G^\circ + \lambda)^2}{4\lambda} \quad (6)$$

The reorganization energy (λ) is the energy change due to the whole chemical system (the complex and the surrounding solvent molecules) rearrangement. It splits into inner-sphere reorganization energies, λ_{is} and outer-sphere reorganization energies, λ_{os} ($\lambda = \lambda_{\text{is}} + \lambda_{\text{os}}$). λ_{is} is the relaxation energies for the complex, while λ_{os} accounts for the required energy to reorganize solvent distribution surrounding the complex. λ_{is} has the precursor contribution, $\lambda_{\text{is}1}$, and the products contribution, $\lambda_{\text{is}2}$ ($\lambda_{\text{is}} = \lambda_{\text{is}1} + \lambda_{\text{is}2}$). $\lambda_{\text{is}1}$ is the difference between the energy of products in their ground state at the precursors geometry, $E(\text{Prod})_{\text{PRE}}$, and the energy of products at their ground state optimized geometry, $E(\text{Prod})_{\text{OPT}}$ (eq 7). Similarly, $\lambda_{\text{is}2}$ is the difference between the energy of precursors in their ground state at the products geometry, $E(\text{Pre})_{\text{PROD}}$, and the energy of precursors at their ground state optimized geometry, $E(\text{Pre})_{\text{OPT}}$ (eq 8) (see Figure 1).

$$\lambda_{\text{is}1} = E(\text{Prod})_{\text{PRE}} - E(\text{Prod})_{\text{OPT}} \quad (7)$$

$$\lambda_{\text{is}2} = E(\text{Pre})_{\text{PROD}} - E(\text{Pre})_{\text{OPT}} \quad (8)$$

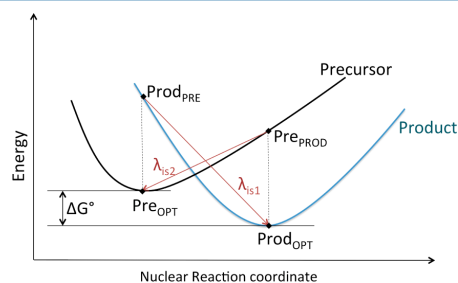


Figure 1. Schematic illustration of the procedure used for the calculation of inner-sphere reorganization energies (λ_{is}).

Meanwhile, the λ_{os} for continuum solvent models is given by

$$\lambda_{\text{os}} = (\Delta q)^2 \left(\frac{1}{2r_1} + \frac{1}{2r_2} - \frac{1}{R} \right) \left(\frac{1}{D_{\text{op}}} - \frac{1}{\epsilon_s} \right) \quad (9)$$

where Δq is the charge transferred, r_1 and r_2 are the effective radii of the precursor molecules, R is the effective radius of the whole precursor complex, and ϵ_s and D_{op} are the static and high-frequency (optical) dielectric constants of the solvent. Radii are expressed in angstroms and, in our case, the charge transferred is equal to 1, and ϵ_s and D_{op} for acetonitrile are 35.688 and 1.801, respectively. The final λ_{os} value is given in eV.

The self-interaction error (SIE) intrinsic in density-functional theory has also been taken into account. SIE in DFT is the consequence of the fact that the residual self-repulsion in the Coulombic term of the energy functional is not totally canceled by the exchange part of the functional.^{47,48} The SIE artificially stabilizes delocalized states, since delocalization reduces the self-repulsion.⁴⁹ Siegbahn et al. proposed a simple approach to measure the magnitude of the SIE effects in systems composed of a catalytic transition metal complex and a substrate molecule.⁵⁰ Their approach is based on the comparison of electronic spin density and energy of *a priori* two quasi-equivalent DFT structures: (i) the localized states of the catalyst and substrate at infinite distance

Table 1. Relative Gibbs Energies (ΔG_{soliv} in kcal/mol) for Radical and Cation Iron-Bishydroxo Catalyst Intermediates for Different Spin Multiplicities

UB3LYP-D2-SMD			substrates / ΔG_{soliv} (kcal/mol)				
S	electronic configuration		methane	ethane	cyclohexane	2,3-DMB	
	iron	substrate					
1/2	I_{cat}	C 	R ⁺ 	- ^a	9.66	10.38	- ^a
	I_{rad}	B 	R [*] 	0.00	8.86	23.28	- ^a
3/2	I_{cat}	C 	R ⁺ 	- ^a	9.34	9.52	10.52
	I_{rad}	B 	R [*] 	1.12	9.75	22.70	34.55
5/2	I_{cat}	C 	R ⁺ 	- ^a	0.00	0.00	0.00
	I_{rad}	B 	R [*] 	6.55	- ^a	- ^a	- ^a

^aWe were unable to optimize the intermediate in this particular electronic configuration. Key symbols: B = Fe^{IV}(OH)₂; R^{*} = radical substrate; I_{rad} = B/R^{*}; C = Fe^{III}(OH)₂; R⁺ = cationic substrate; I_{cat} = C/R⁺.

Table 2. Relative Gibbs Energies (ΔG_{soliv} in kcal/mol) for Several Radical and Cation Iron-Bishydroxo Catalyst Electronic Configurations, Evaluated Considering Catalyst and Substrate Separated at Infinite Distance^a

UB3LYP-D2-SMD			substrates / ΔG_{soliv} (kcal/mol)				
S	iron configuration	substrate configuration	methane	ethane	cyclohexane	2,3-DMB	
1/2	I_{cat}	C 	R ⁺ 	26.65 (26.65)	10.37 (0.00)	10.37 (0.00)	10.37 (0.00)
	I_{rad}	B 	R [*] 	11.85 (11.85)	25.02 (14.64)	37.81 (27.43)	48.89 (38.51)
3/2	I_{cat}	C 	R ⁺ 	26.61 (26.61)	10.34 (0.00)	10.34 (0.00)	10.34 (0.00)
	I_{rad}	B 	R [*] 	0.00 (0.00)	13.16 (2.83)	25.95 (15.62)	37.03 (26.70)
5/2	I_{cat}	C 	R ⁺ 	16.27 (10.61)	0.00 (0.00)	0.00 (0.00)	0.00 (0.00)
	I_{rad}	B 	R [*] 	5.66 (0.00)	18.82 (18.82)	31.61 (31.61)	42.70 (42.70)

^aValues in parentheses correspond to Gibbs energy differences within the same multiplicity species. Key symbols: B = Fe^{IV}(OH)₂; R^{*} = radical substrate; I_{rad} = B/R^{*}; C = Fe^{III}(OH)₂; R⁺ = cationic substrate; I_{cat} = C/R⁺.

obtained from two different calculations, and (ii) the states obtained from a single calculation of the catalyst and substrate separated by a very long distance (e.g., 60 Å). The only difference between both types of calculations should be the small Coulomb interaction between the catalyst and the substrate at 60 Å. If the latter DFT calculation leads to different electronic spin density and lower energy than the former (after

removing the effect of the Coulomb interaction), the DFT calculation of such catalyst–substrate complex suffers SIE effects. On the contrary, if both calculations lead to the same electronic spin density and energy, there is no evidence of SIE effects on the catalyst–substrate complex. In this paper we have used this approach to measure the possible SIE effects of the compounds studied here (see SI for more details).

The AHP may involve different spin states. In our work, we have analyzed the doublet, quartet, and sextuplet potential energy surfaces (PESs). Superscripts in the labels of the different species along the reaction coordinate refer to their spin multiplicity; 2, 4, and 6 stand for doublet, quartet, and sextuplet, respectively. The relative spin state energies of UB3LYP/6-311G(d,p)~SDD structures have been checked at UOPBE/6-311G(d,p)~SDD level of theory (see Tables S4 and S5). Previous validation studies have shown the validity of the OPBE functional for the spin-state splittings of iron complexes.^{51–54} The comparison between UB3LYP and UOPBE spin ground states indicates that same qualitative pictures are obtained with the two functionals. The same conclusion was drawn by de Visser et al. when comparing the spin state splittings obtained using the UB3LYP, UBLYP, UB3PW91, and TPSS functionals.⁵⁵ For this reason, we will focus on the UB3LYP results only.

For the cases where the energy surfaces of two spin multiplicities were close in energy and the obtained spin crossing was reliable, the minimum energy crossing points (MECPs) were optimized and evaluated using Gaussian 09 together with the code developed by Harvey et al.⁵⁶

III. RESULTS AND DISCUSSION

1. Electronic Structure and Stability of the Iron-Bishydroxo Intermediate (B or C) Formed after C–H Bond Breakage. The main difference between all pathways suggested in Scheme 2 lies on the stability and the electronic structure of the intermediate species that are formed after substrate C–H breakage by the $\text{Fe}^{\text{V}}(\text{O})(\text{OH})$ species (A): B/R* (I_{rad}) or C/R* (I_{cat}). As explained above the examples reported in the literature suggest either (i) a highly asynchronous concerted mechanism for alkane hydroxylation (path b in Scheme 2) without the existence of an intermediate or (ii) the rebound mechanism through a R*/B intermediate (path a in Scheme 2). Nevertheless, in this work several R*/C intermediates have been optimized using different theoretical models. Furthermore, in most of the cases they are even thermodynamically more stable than their I_{rad} counterparts. These results suggest that the third pathway, labeled as path c in Scheme 2, may be also possible.

Table 1 summarizes the relative ΔG_{solv} stabilities of I_{rad} and I_{cat} intermediates at the three different spin states studied and for all analyzed substrates, namely, methane, ethane, cyclohexane, and 2,3-DMB. For each total spin state and iron oxidation state, only the most stable electronic configuration has been studied. The results show that the relative stability of methane intermediates is clearly different from that of other substrates. Most stable methane intermediates have the R*/B electronic structure for each of the three spin multiplicities studied. Indeed the methyl cation/C form could not be optimized. On the contrary, for all other substrates, the most stable iron-bishydroxo structure is R*/C. The $\text{I}_{\text{rad}} - \text{I}_{\text{cat}}$ energy difference linearly correlates with the ionization energies (IE) of the substrate (see Figures S9 and S10), which can be used to predict the relative stability of the two intermediates. Obviously, the correlation is even better if the IE of substrates are replaced by the IE of the alkyl radicals (see Figure S8 and below for further discussion).

Table 2 lists the relative ΔG_{solv} stabilities of I_{rad} and I_{cat} intermediates when considering the substrate and the catalyst separated by an infinite distance. Thus, it presents the relative Gibbs energies of all possible combinations between the radical with $S = 1/2$ (cationic with $S = 0$) substrate and the $S = 0, S = 1$, and $S = 2$ spin states of the B species ($S = 1/2, S = 3/2$, and $S = 5/2$ spin states of the C species). Only the most stable I_{rad} combinations shown in Table 2 were optimized as I_{rad} intermediates (Table 1). In agreement with the results in Table 1, the data presented in Table 2 indicates that while methane has an I_{rad} form as the lowest energy state, for all other

substrates the I_{cat} represents the lowest energy structure. The simple model used in Table 2 does not take into account the coupling between the substrate and the iron species. However, the approximate values of Table 2 are useful to offer an explanation on the relative Gibbs energies for the different intermediates at the different spin states. For instance, the results of Table 2 for methane point out that for $S = 1/2$ the lowest-lying electronic state corresponds to the antiferromagnetic coupling of the methyl radical and the $S = 1$ B species, whereas the methyl radical/ $S = 0$ B or methyl cation/ $S = 1/2$ C electronic states are more than 10 kcal/mol higher in energy.

Tables 1 and 2 show that for I_{cat} species the most stable multiplicity is always sextuplet, while for I_{rad} intermediates the lowest-lying energy structures involve always a $S = 1$ B moiety. For the latter, energies between antiferromagnetic and ferromagnetic equivalent species have always close values indicating a weak spin coupling between the unpaired electrons of the two fragments (see I_{rad} species with total spin equals to $S = 1/2$ and $S = 3/2$ in Table 1). With the exception of methane, the most stable intermediate is I_{cat} in sextuplet multiplicity, due in part to the extra stability given by the half-filled d shell of the iron center. On the contrary, geometry optimization of the sextuplet radical states, which are given by a ferromagnetic coupling between R* and the $S = 2$ B catalyst, yields directly to alcohol products without the presence of a stable intermediate. Furthermore, results of Table 2 indicate that the doublet and quadruplet I_{rad} are for all the substrates more stable than the sextuplet.

As a general trend, I_{cat} stabilization with respect to its I_{rad} counterpart ($\Delta C_{\text{solv}}^{\text{I}_{\text{rad}}} - \Delta C_{\text{solv}}^{\text{I}_{\text{cat}}}$) increases when the number of carbons attached to the carbon that suffers the HAT increases (see Table 2). Thus, the sextuplet cationic ethyl, cyclohexyl, and 2,3-DMB/B intermediates are, respectively, 13.2, 26.0, and 37.0 kcal/mol more stable than the lowest energy I_{rad} intermediates, while for methane, I_{rad} is favored over cationic methyl/B by 16.3 kcal/mol. This can be easily predicted just from the ionization energy of R* (IE_{subst}) and the electron affinity of the B moiety (EA_{cat}) (see Tables S1 and S2). For all the studied substrates but methane the ET process is thermodynamically favorable in solution (i.e., $\text{IE}_{\text{subst}} - \text{EA}_{\text{cat}} < 0$).

In summary, the results obtained analyzing all possible electronic states of the intermediates indicate that the new proposed mechanism c of Scheme 2 could be the most favorable for C–H oxidation at primary, secondary, or tertiary carbon atoms.

2. Mechanistic Study of the Alkane Hydroxylation Process (AHP). *2.a. Hydrogen Atom Transfer (HAT) Process.* $[\text{Fe}^{\text{V}}(\text{O})(\text{OH})(\text{PyTACN})]^{2+}$ has been proposed as the active species in alkane^{22–24} and water^{57–59} oxidation. Moreover, its generation and its reaction with olefins has been proved by variable-temperature mass spectroscopy and DFT calculations.⁶⁰ The *cis* relative disposition of the oxo and hydroxo ligands gives two possible isomeric forms for $[\text{Fe}^{\text{V}}(\text{O})(\text{OH})(\text{PyTACN})]^{2+}$. The $[\text{Fe}^{\text{V}}(\text{O})(\text{OH})(\text{PyTACN})]^{2+}$ isomeric form that has the oxo group *trans* to a N–CH₃ moiety of the PyTACN ligand is the most stable one,²³ and consequently in the present mechanistic study it is assumed as the initial active species, A. To identify the key steps for the AHP, in this section we study the first step of the process, that is, the HAT process for all the studied substrates in acetonitrile solution (see Scheme 2).

An alternative to the HAT for the first step of the mechanism is a long-range electron transfer from the substrate to the high-valent $[\text{Fe}^{\text{V}}(\text{O})(\text{OH})(\text{PyTACN})]^{2+}$. This ET first step mecha-

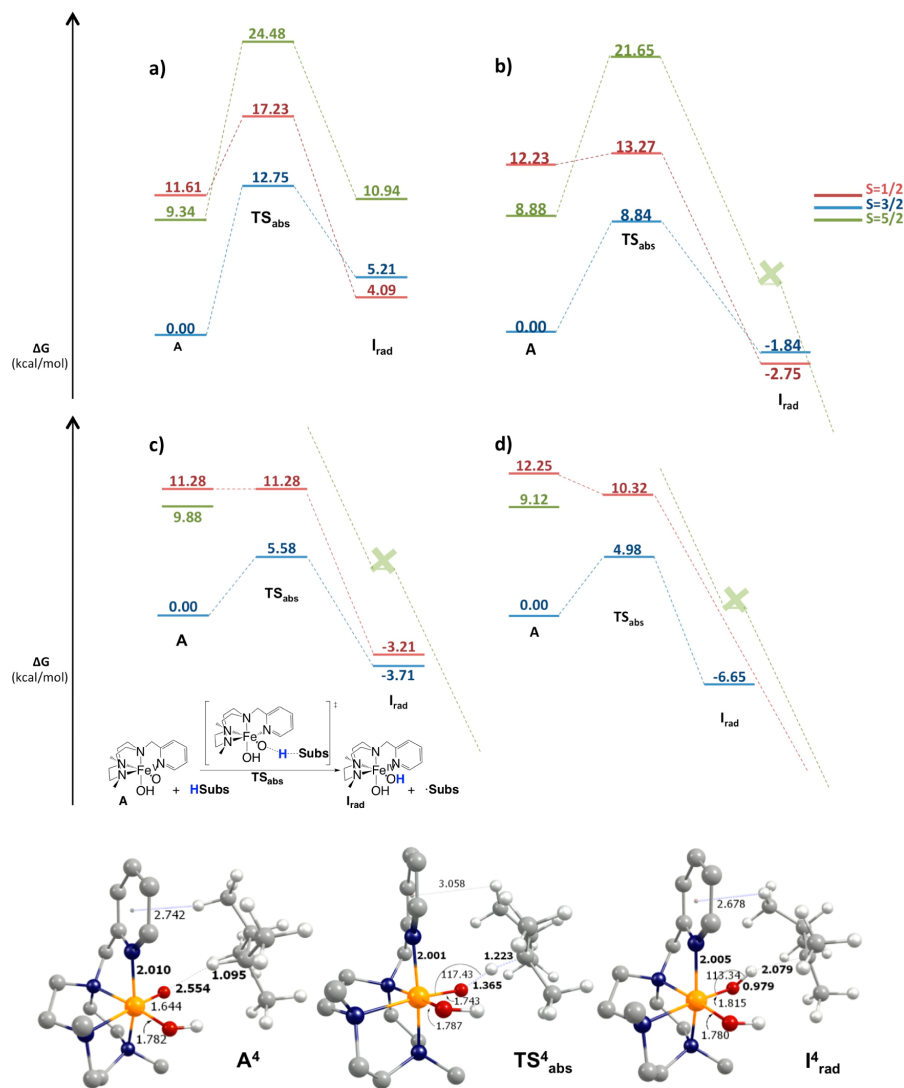


Figure 2. (Top) Gibbs energy profiles in solution (ΔG_{solv}) of the HAT step for (a) methane, (b) ethane, (c) cyclohexane, and (d) 2,3-DMB (kcal/mol). Red, blue, and green profiles correspond to doublet, quartet, and sextuplet multiplicities, respectively. (Bottom) Structures of the HAT process for 2,3-DMB substrate in the ground state ($S = 3/2$). Selected distances and angles are indicated in angstroms (Å) and in degrees (deg), respectively. C atoms are represented in gray, N in blue, O in red, Fe in orange, and H in white. Hydrogen atoms of the PyTACN ligand have been omitted for clarity.

nism was computationally determined by de Visser et al. as the most viable for $[\text{Fe}(\text{O})(\text{BQEN})(\text{NCCH}_3)]^{3+}$ (BQEN = *N,N'*-dimethyl-*N,N'*-bis(8-quinolyl)ethane-1,2-diamine), an iron(IV)-oxo ligand cation radical which has an extremely large electron affinity.⁶¹ The same charge transfer first step mechanism was also proposed on the basis of computational studies for Cpd I of P450⁶² and non-heme iron(IV)-tosylimido species.⁶³ However, for $[\text{Fe}^{\text{V}}(\text{O})(\text{OH})(\text{PyTACN})]^{2+}$ the ET is always far more endothermic than the HAT barrier, so that the ET mechanism can be clearly ruled out (see Tables S7 and S8).

The Gibbs energy profiles for the HAT step of the four studied substrates are presented in Figure 2. The ground state of the initial active $\text{Fe}^{\text{V}}(\text{O})(\text{OH})$ species (A^4) and HAT transition states (TS_{abs}^4) are quartet spin states for all substrates, while $S = 1/2$ and $S = 5/2$ excited spin states are, at least, 4.5 kcal/mol higher in energy. The first excited state of $\text{Fe}^{\text{V}}(\text{O})(\text{OH})$ species is the sextuplet state and the second has a doublet spin state configuration. However, the opposite is true for the TS of the hydrogen abstraction. The inclusion of spin contamination, thermal, and entropy corrections have a key effect on the relative energy of the different spin states of the intermediates and

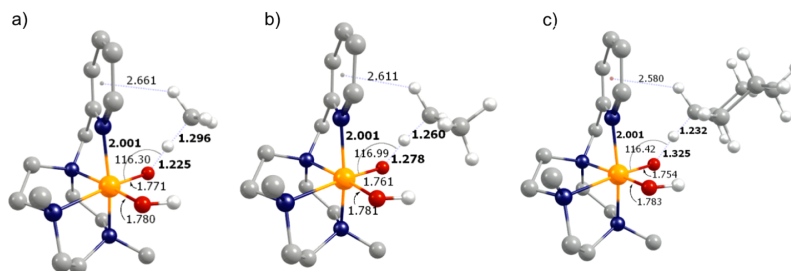
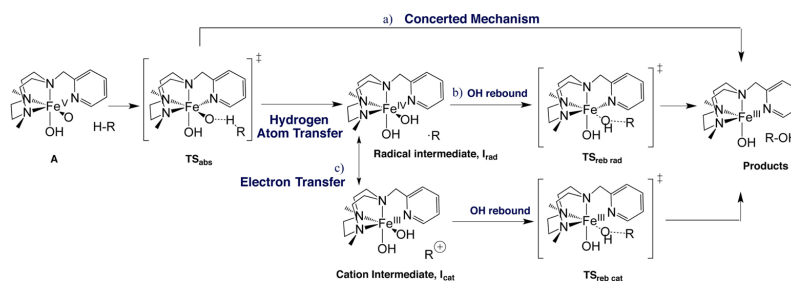


Figure 3. TS_{abs} structures in solution at $S = 3/2$ for (a) methane, (b) ethane, and (c) cyclohexane, TS_{abs}^4 . Distances in Å and angles in degrees. C atoms are represented in gray, N in blue, O in red, Fe in orange, and H in white. Hydrogen atoms of the PyTACN ligand have been omitted for clarity.

Scheme 3. Three Proposed Mechanisms for Alkane Hydroxylation Processes Catalyzed by $[\text{Fe}^{\text{V}}(\text{O})(\text{OH})(\text{PyTACN})]^{2+}$



transition states species (see Table S4). For cyclohexane, the calculated kinetic isotopic effect (KIE) for TS_{abs}^4 using the classical transition state theory expressions is 4.9, in very good agreement with the experimental KIE = 4.3.²³

Spin population analysis of A^2 and A^4 reveals two unpaired electrons on the iron and one unpaired electron on the oxo ligand antiferromagnetically or ferromagnetically coupled, respectively (see Table S3). The presence of this antiferromagnetic coupling translates into an important spin contamination correction in the unrestricted calculation of A^2 . The electronic distribution for A^6 is clearly different and shows three unpaired electrons on iron, a partial unpaired electron on the oxo ligand and almost an unpaired electron centered on the nitrogen atom of the pyridine group.

Our results show that HAT Gibbs energy barriers (ΔG^\ddagger) decrease when the number of carbon atoms bound to the C–H group that suffers the hydrogen abstraction increases. The same trend is found for the Gibbs reaction energies (ΔG_{reac}). $\Delta G_{\text{A} \rightarrow \text{I}_{\text{rad}}}$ becomes more exergonic when the number of carbons bound to the C that suffers hydrogen abstraction increases. Then, whereas the HAT step for methane is endergonic (4.1 kcal/mol), for ethane, cyclohexane, and 2,3-DMB, the HAT process is exergonic by -2.8 , -3.7 , and -6.7 kcal/mol, respectively. And in agreement with the Bell–Evans–Polanyi principle, the hydrogen abstraction Gibbs energy barrier evolves from 12.8 kcal/mol for methane to 8.8, 5.6, and 5.0 kcal/mol for ethane, cyclohexane, and 2,3-DMB, respectively. Moreover, the HAT Gibbs energy barriers (ΔG^\ddagger) also occur with the strength of the broken C–H bond: the highest ΔG^\ddagger for the strongest C–H bond of methane, and then a lower ΔG^\ddagger for ethane, cyclohexane, and 2,3-DMB, respectively. The binding dissociation energy of the C–H bond is in part determined by the free radical stability that follows the order methyl < primary < secondary < tertiary.⁶⁴

As it was previously shown by de Visser et al.,^{65–67} the HAT energy barriers of the different substrates correlates linearly with the C–H bond dissociation energy ($\text{BDE}_{\text{C-H}}$) of the substrate abstracted hydrogen (see Figures S6 and S7). Furthermore, the HAT energy barriers also show a good linear correlation with IEs of the substrates (see Figure S5). The larger the IE, the higher the HAT barrier.

In addition, our calculations also show a clear relation between the HAT energy barrier and the TS_{abs} geometric parameters (see Figure 3 and Table S5). The longer (shorter) the C–H (O–H) bond distance in the TS_{abs} , the higher the HAT Gibbs energy barrier, thus suggesting a “late” transition state for higher barriers, in agreement with the predictions of the Hammond postulate. Hence, methane has the largest C–H distance and the shortest H–O distance for TS_{abs} structures (late transition state), whereas 2,3-DMB has the shortest C–H distance and the largest H–O distance among the different TS_{abs} structures. The HAT barrier shows very good linear correlations with respect to the O–H bond distance and C–H bond distance of the TS_{abs} structures (see Figures S1 and S2). Furthermore, as it is shown in Figures S3 and S4, the HAT barriers also correlate with the imaginary frequencies and the spin density of the C bonded to the abstracted hydrogen of the TS_{abs} . The HAT barrier increases when the absolute values of the imaginary frequency and C spin density increase. A high value of the C spin density indicates a late HAT transition state.

TS_{abs} structures present a Fe–O–H angle of 108 – 117° for all studied multiplicities and substrates (see Figure 3). Thus, following Solomon and Neese terminology,^{68,69} the reaction proceeds via a π -channel with an orientation of the substrate that enhances the orbital overlap without increasing too much the Pauli repulsion. Although we have also searched the linear σ -channel HAT transition state for the quadruplet and sextuplet

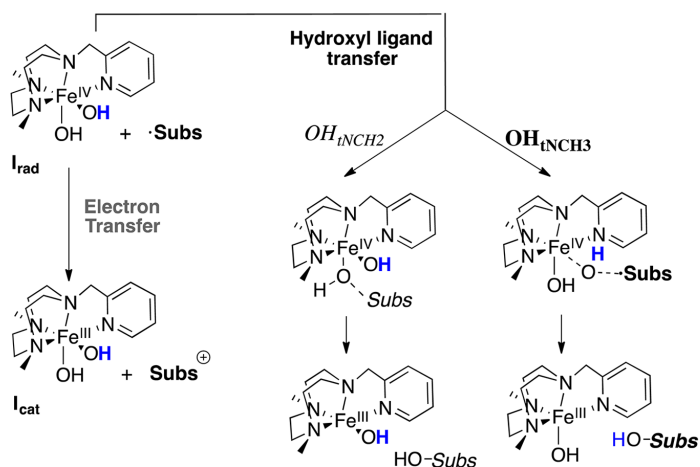
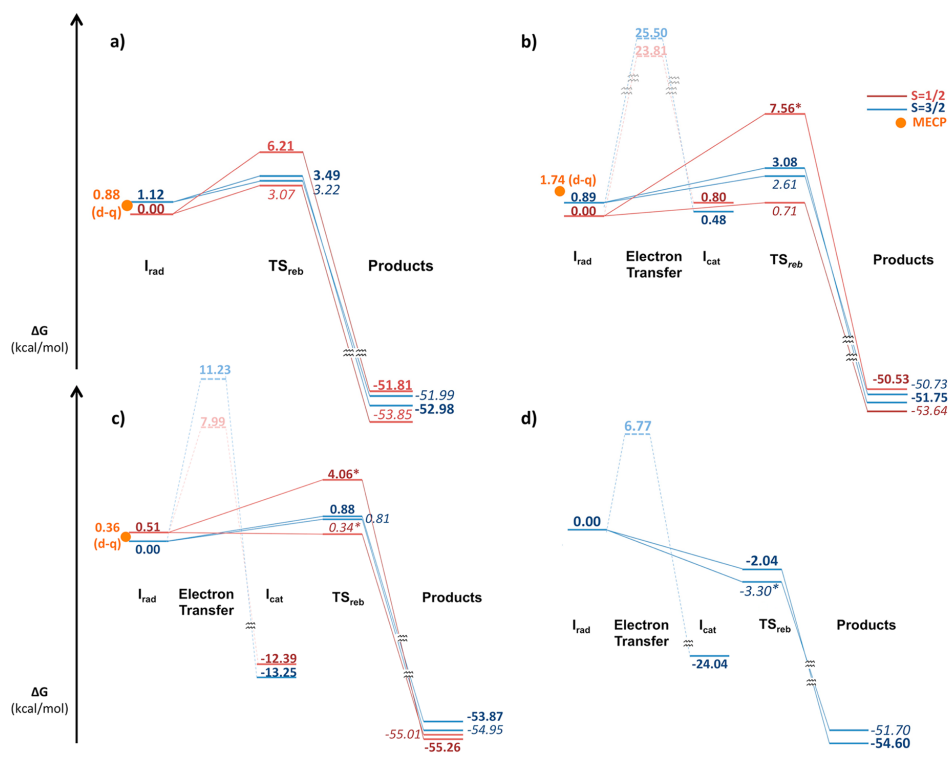


Figure 4. (Top) Gibbs energy profiles (in kcal/mol) in acetonitrile solution (ΔG_{solv}) of the ET and the hydroxyl ligand transfer for (a) methane, (b) ethane, (c) cyclohexane, and (d) 2,3-DMB catalyzed by $[\text{Fe}^{\text{IV}}(\text{OH})(\text{OH})(\text{PyTACN})]^{2+}$. Red profiles correspond to doublet and blue ones to quartet multiplicity states. Values in *italics* represent the $\text{OH}_{\text{INCH}_2}$ ligand transfer, and **bold** values represent the $\text{OH}_{\text{INCH}_3}$ ligand transfer. The values marked with an * are approximated upper bound solutions obtained by scanning the C–O bond in linear transits from I_{rad} to products. (Bottom) Reaction mechanisms analyzed in the Gibbs energy profiles.

states, all optimizations lead to the angular π -channel for the TS of the hydrogen abstraction. This scenario is in contrast with HAT reactions by $S = 1 \text{ Fe}^{\text{IV}}\text{O}$ complexes, that can occur both via

σ - and π -paths.⁷⁰ The presence of a CH/π interaction⁷¹ between all substrates and the pyridine ring of $[\text{Fe}^{\text{V}}(\text{O})(\text{OH})-$

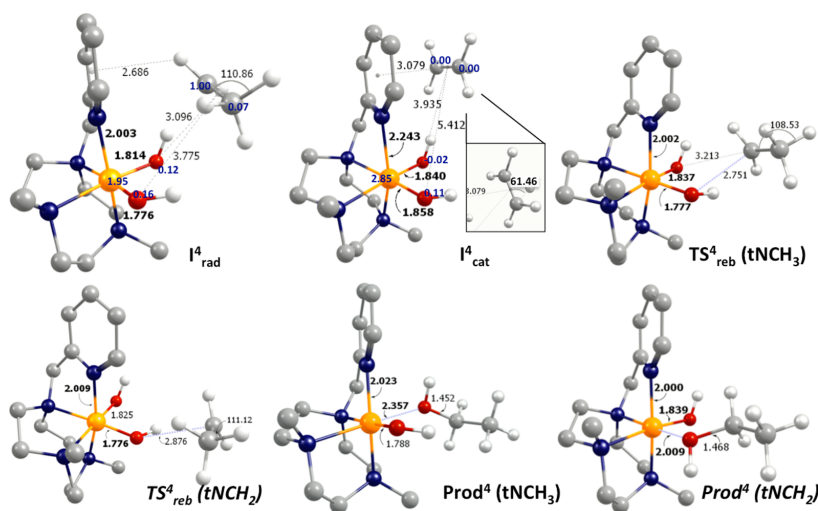


Figure 5. Structures involved in the ET and the hydroxyl ligand transfer processes for ethane. Selected distances and angles are indicated in angstroms (Å) and in degrees (deg), respectively. Selected spin densities (in electrons) are given in blue. C atoms are represented in gray, N in blue, O in red, Fe in orange, and H in white. Hydrogen atoms of the PyTACN ligand have been omitted for clarity.

(PyTACN)]²⁺ complex favors the substrate orientation that triggers the π -channel for the hydrogen abstraction processes.

Intrinsic reaction coordinate (IRC) calculations were done for TS_{abs} in order to ensure connection with the active species A and the next intermediate (I_{rad} or I_{cat}). The IRC calculations show that TS_{abs}^4 always leads to an I_{rad} intermediate (see Figure 2). Thus, in acetonitrile solution, the studied hydroxylation reactions at the $S = 3/2$ ground state are stepwise because the HAT does not lead directly to products, but instead an I_{rad} intermediate is found. However, for $S = 5/2$ state of ethane, cyclohexane, and 2,3-DMB and the $S = 1/2$ state for 2,3-DMB, TS_{abs} directly connects with the final products. Thus, for these excited states, the mechanism can be defined as a highly asynchronous concerted process. Although for all the substrates but methane I_{cat} is more stable than I_{rad} , our calculations show that the first step of the mechanism is always hydrogen abstraction instead of a hydride abstraction. Thereby, IRC calculations discard path *c* suggested in Scheme 2. To achieve the more stable I_{cat} , an ET process through a second step would be necessary, and then the proposed mechanisms for AHP for $[\text{Fe}^{\text{V}}(\text{O})(\text{OH})-(\text{PyTACN})]^{2+}$ could be rewritten as shown in Scheme 3.

2.b. Electron Transfer versus Rebound (Hydroxyl Ligand Transfer). As explained in the previous section, the ground state TS_{abs}^4 always leads to I_{rad} . Nevertheless, after the HAT step, I_{rad} can evolve to the alcohol product through a hydroxyl radical transfer (rebound step path b in Scheme 3) or can be followed by an ET step to I_{cat} (path c in Scheme 3). In this section the competition between the OH radical rebound process and the ET step is evaluated.

The ET step has been studied for the two most stable multiplicities of I_{rad} of ethane and cyclohexane, that is quadruplet and doublet multiplicities. For 2,3-DMB, only quadruplet I_{rad} has been found. For methane I_{cat} is less stable than I_{rad} and the ET was discarded. Marcus theory (see Computational Details) has been used to analyze the kinetics of the ET processes. The kinetics of the hydroxyl radical rebound step was determined by optimizing the corresponding TS. Gibbs energy profiles of the

ET and OH-rebound pathways are shown in Figure 4, and the corresponding structures for the ethane case are depicted in Figure 5.

For A and TS_{abs} , the $S = 3/2$ spin state is the ground state for all substrates. But for I_{rad} , whereas the quadruplet is still the ground state for cyclohexane and 2,3-DMB, for methane and ethane the ground state is $S = 1/2$. The doublet–quadruplet (d-q) minimum-energy crossing point (MECP) for methane, ethane, and cyclohexane I_{rad} intermediates is clearly lower in energy than the quadruplet barriers for the ET and OH-rebound. However, the major change between the doublet and quadruplet spin density is located in the substrate carbon radical, and then the d-q spin-crossing is likely to be not allowed due to the small spin-coupling term of the dipole moment of the transition integral. Nevertheless, we have studied the ET and OH-rebound on doublet and quadruplet multiplicities. Moreover, the TSs for the hydroxyl rebound in the two –OH groups of the $[\text{Fe}^{\text{IV}}(\text{OH})_2(\text{PyTACN})]^{2+}$ structure have also been studied. OH groups are labeled as $\text{OH}_{\text{tNCH}_2}$ and $\text{OH}_{\text{tNCH}_3}$. $\text{OH}_{\text{tNCH}_2}$ is the OH that has an $\text{N}-(\text{CH}_2)_3-$ group in *trans* (and it is the initial oxo group), whereas $\text{OH}_{\text{tNCH}_3}$ has an $\text{N}-(\text{CH}_2)_2(\text{CH}_3)-$ group in *trans*.

In Figure 4b–d, the ET processes are represented in pale dashed lines, while the two different possible OH-rebounds are represented in bold and italics. For all substrates, Figure 4 clearly shows that the OH-rebound is kinetically more favorable than the ET. For ethane, OH-rebound barriers are between 1.7 and 2.2 kcal/mol, while ET activation energies range from 23.8 to 25.5 kcal/mol. It is worth noting that the C_2H_5^+ moiety in I_{cat} has the H^+ bridge C_{2v} conformation, which is the most stable for the free ethyl cation at the B3LYP and CCSD levels of theory (see Figure 5).⁷² For cyclohexane, OH-rebound barriers are in the interval from 0.8 to 0.9 kcal/mol, while ET activation energies are between 8.0 and 11.2 kcal/mol. Finally, 2,3-DMB has a barrierless OH-rebound while the ET process has an energetic cost of 6.8 kcal/mol.

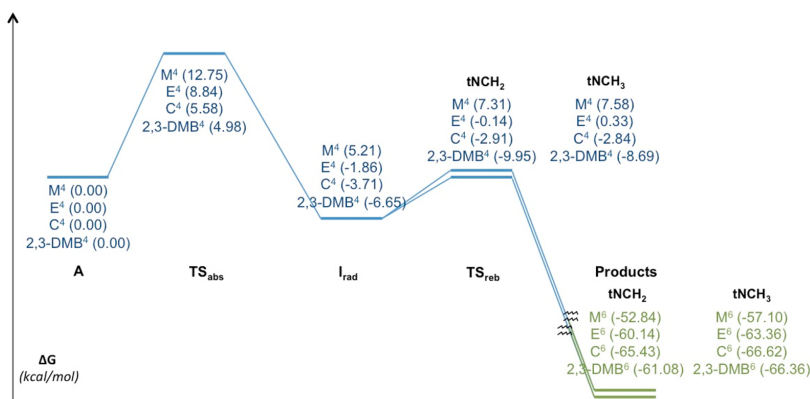


Figure 6. Gibbs energy (in kcal/mol) profiles for methane (M), ethane (E), cyclohexane (C), and 2,3-dimethylbutane (2,3-DMB) hydroxylation processes. Only the ground state for each substrate and structure is represented. Blue accounts for quartet and green for sextuplet ground states.

It has been experimentally proved on the basis of isotopic labeling and product analyses that the radical is short living and does not diffuse freely in the alkane hydroxylation reaction catalyzed by the $[\text{Fe}^{\text{V}}(\text{O})(\text{OH})(\text{PyTACN})]^{2+}$ complex.^{22–24} Therefore, in this paper the dissociation mechanism has not been studied.

To summarize, ET and rebound Gibbs energy barriers share the same behavior: they decrease when the number of C atoms bonded to the radical carbon increases. Indeed both processes account for a $1e^-$ reduction from Fe^{IV} to Fe^{III} and an oxidation of the substrate. The ET is a pure electron transfer, whereas the rebound process entails oxygenation of the substrate to form an alcohol. Thus, in terms of the formal oxidation state of the iron center both reactions formally account for a similar process and share the same behavior (i.e., the barriers decrease from methane to 2,3-DMB), being the barriers for the rebound always lower than the ET barriers.

2.c. The Complete Alkane Hydroxylation Mechanism. From the results obtained in the two previous subsections it can be concluded that (i) AHP always goes through the general rebound mechanism (path b in Scheme 2) and (ii) I_{rad} is never an intermediate of the AHP mechanism. The ground state profiles for methane, ethane, cyclohexane, and 2,3-DMB hydroxylation are represented in Figure 6. The ground state of the active initial species, $\text{Fe}^{\text{V}}(\text{O})(\text{OH})$, is always the quartet and the hydrogen abstraction also goes through this multiplicity (which has three unpaired electrons on the catalyst). The Gibbs energy profiles clearly show that the hydrogen abstraction process is the TOF-determining transition state (TDTS).⁷³ I_{rad} $S = 1/2$ and $S = 3/2$ states have similar Gibbs energies for all studied substrates since they have the same electron distribution (three electrons on the catalyst, two in the iron d shell, and one in the oxo moiety) with weak coupling with the substrate (ferromagnetic or antiferromagnetic). Then, I_{rad} ground-state multiplicity varies between $S = 1/2$ and $S = 3/2$ depending on the substrate (doublet for methane and ethane and quartet for cyclohexane and 2,3-DMB) (see Figure 5).

The OH radical rebound (TS_{reb}) has been evaluated for doublet and quartet multiplicities for both isomeric positions despite the d-q spin crossing is likely to be not allowed (see above). The rebound with the OH *trans* to NCH_2 is always the most favorable one and its ground state is again doublet for

methane and ethane and quartet for cyclohexane and DMB, as for I_{rad} (see Figure 5). For quartet spin state, the rebound with the hydroxyl *trans* to NCH_3 is less than 1 kcal/mol higher in energy than the rebound with the OH *trans* to the NCH_2 moiety. Thus, the calculations show that the rebound with the OH *trans* to NCH_2 moiety is the most favorable one, although these results should be taken with some caution since energy differences between both rebounds are within the limits of precision of the used DFT approach. The final products with the alcohol formed fall down to sextuplet states.

3. Comparison between Gas-Phase and Solvent-Phase Mechanisms. As previously mentioned in the introduction, computational studies of the reaction mechanism for alkane oxidation processes catalyzed by $\text{Fe}^{\text{V}}\text{O}$ do not present a clearly established pathway for many substrates and catalysts. DFT equilibrium geometries of the intermediates and transition states of the proposed mechanisms are usually optimized at gas phase. In some cases, the solvent-phase corrections are included through single-point solvent-phase corrections. Here we will show that the single-point calculations approach to include the solvent-phase effects is not always a good method to determine the reaction mechanism in solution and that the solvent effects should also be included during the optimization of the equilibrium geometries. In the first part of this paper, depending on the substrate two different trends for the relative stability of the I_{cat} and I_{rad} intermediates have been observed in solution. While for methane the I_{rad} structure is the most stable, for all the other alkane substrates I_{cat} is the most stable form. To assess the reliability of the different approaches given by eqs 3–5 (i.e., G_{g} , $G_{\text{g}+\text{corr}}$, and G_{sol}) to describe AHP properly, one substrate of each group (methane and cyclohexane) has been studied computationally with the three methodologies.

We have also studied the electronic structure and stability of the iron-bishydroxo intermediates for methane and cyclohexane at gas phase (G_{g}) and at gas phase including single-point dispersion and acetonitrile solvent corrections ($G_{\text{g}+\text{corr}}$). The gas-phase Gibbs energy of all possible combinations between the radical (cationic) substrate and all possible multiplicities of the catalyst at infinite distance are listed in Tables S6 and S7. Comparison of these gas-phase (Table S6) and solvent-phase (Table 2) values show that the acetonitrile solution stabilizes I_{rad} over the most stable I_{cat} . The larger solvent stabilization of I_{rad} as

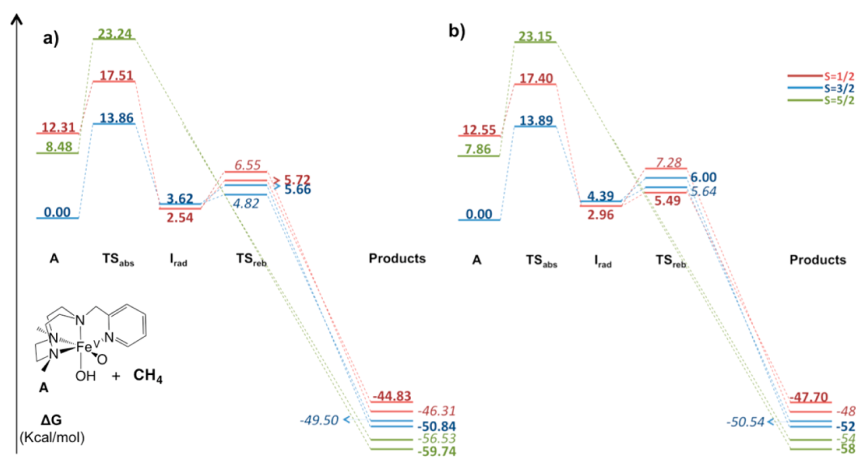


Figure 7. Gibbs energy profile in kcal/mol for the AHP of methane at gas phase (G_g) (a) and at gas phase including the dispersion and solvent corrections (G_{g+corr}) (b). Values in *italics* represent the OH_{INCH_3} ligand transfer, and **bold** values represent the OH_{INCH_3} ligand transfer.

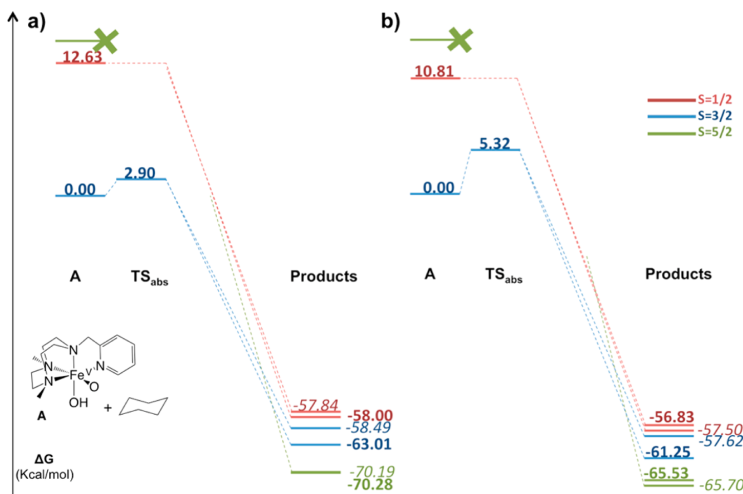


Figure 8. Gibbs energy profiles in kcal/mol for the AHP of cyclohexane at gas phase (a) and at gas phase including dispersion and solvent corrections (b). Values in *italics* represent products where the alcohol group comes from the OH_{INCH_3} .

compared to I_{cat} is caused by the localization of the +2 positive charge on the catalyst in the former intermediate. The solvent relative stabilization of I_{rad} as compared to I_{cat} increases when the size of the substrate increases. However, the latter effect is smaller than the stabilization of I_{cat} due to the reduction of IE_{subst} when the size of the substrate increases. As it is well-known, the general stability of simple alkyl carbocations follows the trend tertiary > secondary > primary > methyl.⁷⁴ Finally, we want to note that when the single-point energy corrections for dispersion and solvent effects are added to the gas-phase values, the values obtained lead to the same conclusions than the results obtained in solution (see Table S7).

The effect of the coupling between the substrate and the catalyst has also been studied considering the whole intermediate (substrate + catalyst) (see Table S8). Again, gas-phase and

solvent-phase results give the same general trends. However, a few key differences between solvent- and gas-phase intermediates appear here. In the gas phase, unlike in solution, there are no stable I_{cat} (I_{rad}) intermediates for methane (cyclohexane). For these electronic states, optimizations at gas phase lead directly to the alcohol products without finding any stable intermediate. The observed differences already seem to indicate that (i) gas-phase and solution reaction mechanisms can be different for a given substrate and (ii) for two different substrates, the reaction mechanisms can differ even if they are computed in the same phase (gas or solution). This may explain the diversity of alkane hydroxylation reaction mechanisms found in the literature.^{23,25,29,30} For this reason, we studied the gas-phase hydroxylation mechanisms of methane and cyclohexane and we compared them with those obtained in solution.

For methane substrate, the AHP Gibbs energy profile obtained at gas phase (Figure 7) is very similar to the one obtained in solution (Figures 2 and 4) with the exception of the sextuplet multiplicity state, for which the intermediate I_{rad} cannot be optimized at gas phase. Thus, although the $G_{\text{g+corr}}$ approach introduces only part of the solvent effects, for the methane case, $G_{\text{g+corr}}$ methodology gives a good semiquantitative description of the solvent-phase profile.

For cyclohexane, differences between G_{g} , $G_{\text{g+corr}}$, and G_{solv} profiles are qualitatively far more important than for methane. As it has already been mentioned, I_{rad} for cyclohexane at gas phase is not a stable minimum, and after the hydrogen abstraction the process yields directly to products (compare Figure 8 with Figures 2 and 4). The cationic intermediates I_{cat} , which are stable minima at gas phase, are not part of the mechanism reaction pathway. Thus, the different stabilization of the intermediates in gas phase and solvent clearly affects the reaction mechanism derived from Gibbs energy profiles. Whereas in solution the cyclohexane hydroxylation by $[\text{Fe}^{\text{V}}(\text{O})(\text{OH})(\text{PyTACN})]^{2+}$ catalyst follows a HAT + rebound stepwise mechanism, at gas phase the cyclohexane hydroxylation mechanism is concerted and highly asynchronous. Nevertheless, in both cases, the TDTS is given by the HAT transition state. In this case, on the contrary to methane hydroxylation, $G_{\text{g+corr}}$ approach turns to be an unreliable method to determine the solvent-phase mechanism.

Another difference between cyclohexane hydroxylation Gibbs energy profiles at gas phase and in solution is that, while at gas phase the $S = 3/2$ products are more stable than $S = 1/2$ products, the opposite is true in solution. Also here $G_{\text{g+corr}}$ approach fails in describing the relative stability of these excited spin states in solution.

Finally, let us mention that in a recent DFT modeling of the C–H abstraction catalyzed by the non-heme $[\text{Fe}^{\text{IV}}(\text{O})(\text{N4Py})]^{2+}$ compound, Shaik et al. showed that for this system the effects of the self-interaction error in DFT lead to an incorrect description of the hydroxylation mechanism.⁷⁵ Using the approach given by Siegbahn,⁵⁰ we have computed the SIE of all optimized radical intermediates, I_{rad} , and cationic intermediates, I_{cat} . Our check covers all substrates and more stable spin states for both gas- and solution-phase optimized structures. None of our optimized structures suffers significant SIE effects (see Tables S13–S18). Nevertheless, Shaik and co-workers' paper and our work are perfectly complementary to describe how to achieve a proper description of the alkane hydroxylation mechanism by means of DFT. In the former case, a $\text{Fe}^{\text{IV}}\text{O}$ species is studied and removing the effects of the SIE is essential. Instead, in our work case, hydroxylation is mediated by a Fe^{VO} species, and SIE has no role. But in both works the utilization of gas-phase optimized structures is strongly discouraged.

IV. CONCLUSIONS

In this work, we have investigated with DFT methods the stereospecific hydroxylation of a series of alkanes (methane, ethane, cyclohexane, and 2,3-dimethylbutane) that occurs in the presence of $[\text{Fe}^{\text{II}}(\text{CH}_3\text{CN})_2(\text{PyTACN})]^{2+}$ species treated with excess H_2O_2 in acetonitrile. Our computational results support the proposal that the mechanism for alkane hydroxylation processes takes place through high-valent $[\text{Fe}^{\text{V}}(\text{O})(\text{OH})(\text{PyTACN})]^{2+}$ species. Furthermore, we have determined the key effects of the substrate and solvent in the hydroxylation mechanism. In acetonitrile solution, a stepwise mechanism that starts with a hydrogen atom transfer and follows with a hydroxyl radical rebound is determined for methane, ethane, cyclohexane,

and 2,3-DMB. The same mechanism is valid for the gas-phase methane hydroxylation. On the contrary, gas-phase cyclohexane hydroxylation evolves through a concerted and highly asynchronous mechanism. Namely, gas-phase I_{rad} intermediates are not stabilized, and the initial HAT yields directly the alcohol products. The differences between acetonitrile solution and gas-phase cyclohexane mechanisms can be attributed to the important stabilization by the acetonitrile solvent of I_{rad} intermediate that has a 2+ charge in the catalyst and is neutral in the R^\bullet moiety.

I_{cat} structures are thermodynamically more stable than I_{rad} intermediates for ethane, cyclohexane, and 2,3-DMB. However, IRC calculations and Marcus theory prove that the I_{cat} species are not involved in the hydroxylation mechanism. Although the ET barriers of the evolution of I_{rad} to I_{cat} are smaller than 26 kcal/mol, OH radical rebound barriers for I_{rad} are always far lower. Thus, after the hydrogen abstraction, the iron-bishydroxo intermediate goes to the alcohol products instead of evolving via an ET process. For methane, I_{rad} structures are more stable than I_{cat} ones, and then the ET process can be ruled out. The kinetics of the HAT step is always energetically more demanding than for the rebound step, the former being the rate-determining step.

In a previous work we showed that, for the non-heme iron catalyst studied in this paper, ^{18}O -labeling experiments gave an equal incorporation of oxygen from water and from peroxide in the final cyclohexanol products.²³ Taking into account that the mechanism in acetonitrile solvent is stepwise, in order to explain these labeling results, the activation barriers of both the HAT and the rebound steps should be very similar for the two *cis* active sites. In our previous work, some of us showed that this condition is fulfilled for the HAT step. The results presented here for cyclohexane substrate show that the hydroxyl rebounds barriers for the two –OH groups are nearly identical ($\Delta\Delta G^\ddagger$ of the hydroxyl ligand transfer between the two –OH groups of cyclohexane is less than 0.1 kcal/mol). Thus, the DFT profile for the hydroxylation of cyclohexane catalyzed by $[\text{Fe}^{\text{V}}(\text{O})(\text{OH})(\text{PyTACN})]^{2+}$ presented here is in agreement with the labeling results measured in our previous study. Furthermore, the clarification of the hydroxylation mechanism in acetonitrile solvent as stepwise is also key for the complete rationalization of the experimental ^{18}O incorporation yields that points to the conclusion that the incorporation of oxygen comes only (or mostly) from water or from the peroxide. In this case, both the HAT and the rebound steps should favor one of the two *cis* labile positions of $[\text{Fe}^{\text{V}}(\text{O})(\text{OH})(\text{PyTACN})]^{2+}$.

Finally, the calculation of minimum-energy crossing points between doublet and quartet potential energy surfaces for methane, ethane, and cyclohexane shows that the two-state reactivity does not play a key role in the HAT step. For I_{rad} , the MECP studies show that the energetic cost of crossing from the quadruplet state to the doublet state is always lower than the energy needed to surmount the barriers of the rebound processes. However, the changes between the I_{rad}^2 and I_{rad}^4 spin densities occur in the radical carbon of the substrate, which implies a low spin–orbit coupling term for the spin-crossing transition integral. Therefore, the rebound process evolves always through the $S = 3/2$ spin state potential energy surface since the spin crossing is likely to be not allowed. For the 2,3-DMB hydroxylation, only the quartet state plays a role, since the doublet Gibbs energy profile mechanism, which is concerted, is always much higher in energy.

■ ASSOCIATED CONTENT

■ Supporting Information

The Supporting Information is available free of charge on the ACS Publications website at DOI: 10.1021/acs.inorgchem.5b00583.

Ionization energies of the radical substrates; electron affinities of the B moiety; Mulliken spin population values of A_x complexes; UOPBE energy values for different spin states; energy values for gas phase and gas phase including the dispersion and solvent corrections for all the possible combinations between the radical (cationic) substrate and all possible multiplicities of the catalyst at infinite distance and also considering the optimized intermediate; and xyz coordinates for all the structures (PDF)

■ AUTHOR INFORMATION

Corresponding Authors

*E-mail: miquel.sola@udg.edu.

*E-mail: miquel.costas@udg.edu.

*E-mail: josepm.luis@udg.edu.

Notes

The authors declare no competing financial interest.

■ ACKNOWLEDGMENTS

This work has been supported by Ministerio de Economía y Competitividad of Spain (Projects CTQ2014-54306-P, CTQ2014-52525-P, and CTQ2012-37420-C02-01, Ramón y Cajal contract to A.C., and grant No. BES-2012-052801 to V.P.), Generalitat de Catalunya (project numbers 2014SGR931, 2014SGR862, Xarxa de Referència en Química Teòrica i Computacional, and ICREA Academia prizes for M.S. and M.C.), the European Commission (ERC-2009-StG-239910 to M.C. and FP7-PEOPLE-2011-CIG-303522 to A.C.), and European Fund for Regional Development (FEDER grant UNGI10-4E-801).

■ REFERENCES

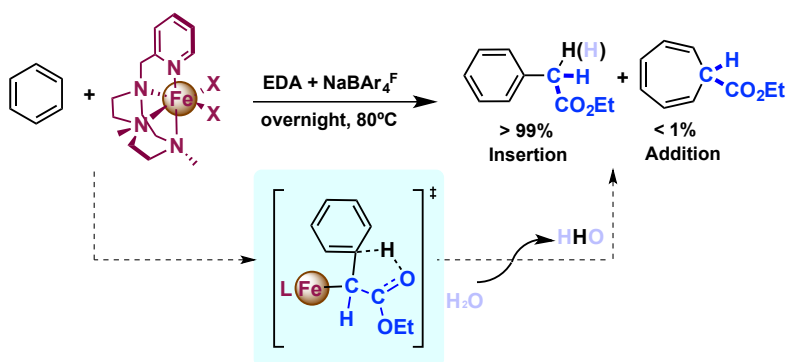
- Company, A.; Gómez, L.; Costas, M. In *Alkane C-H Activation by Single-Site Metal Catalysis*; Perez, P. J., Ed.; Springer: Dordrecht, 2013; pp 143–228.
- Newhouse, T.; Baran, P. S. *Angew. Chem., Int. Ed.* **2011**, *50*, 3362–3374.
- Ortiz De Montellano, P. R. *Chem. Rev.* **2010**, *110*, 932–948.
- Kovaleva, E. G.; Lipscomb, J. D. *Nat. Chem. Biol.* **2008**, *4*, 186–193.
- Costas, M.; Mehn, M. P.; Jensen, M. P.; Que, L., Jr. *Chem. Rev.* **2004**, *104*, 939–986.
- Guengerich, F. P.; Munro, A. W. *J. Biol. Chem.* **2013**, *288*, 17065–17073.
- White, M. C. *Science* **2012**, *335*, 807–809.
- Costas, M. *Coord. Chem. Rev.* **2011**, *255*, 2912–2932.
- Que, L., Jr.; Tolman, W. B. *Nature* **2008**, *455*, 333–340.
- Codola, Z.; Lloret-Fillol, J.; Costas, M. *Progress in Inorganic Chemistry*; John Wiley & Sons, Inc.: Hoboken, New Jersey, 2014; Vol. 59, p 447.
- Bryliakov, K. P.; Talsi, E. P. *Coord. Chem. Rev.* **2014**, *276*, 73–96.
- Ensing, B.; Buda, F.; Blöchl, P.; Baerends, E. J. *Angew. Chem., Int. Ed.* **2001**, *40*, 2893–2895.
- Buda, F.; Ensing, B.; Gribnau, M. C.; Baerends, E. J. *Chem. - Eur. J.* **2001**, *7*, 2775–2783.
- Ensing, B.; Buda, F.; Baerends, E. J. *J. Phys. Chem. A* **2003**, *107*, 5722–5731.
- McDonald, A. R.; Que, L., Jr. *Coord. Chem. Rev.* **2013**, *257*, 414–428.
- Nam, W.; Lee, Y.-M.; Fukuzumi, S. *Acc. Chem. Res.* **2014**, *47*, 1146–1154.
- Kleespies, S. T.; Oloo, W. N.; Mukherjee, A.; Que, L., Jr. *Inorg. Chem.* **2015**, *54*, 5053–5064.
- Krebs, C.; Galonić Fujimori, D.; Walsh, C. T.; Bollinger, J. M. *Acc. Chem. Res.* **2007**, *40*, 484–492.
- De Visser, S. P. *J. Am. Chem. Soc.* **2006**, *128*, 9813–9824.
- Hirao, H.; Kumar, D.; Que, L., Jr.; Shaik, S. *J. Am. Chem. Soc.* **2006**, *128*, 8590–8606.
- Chen, K.; Que, L., Jr. *J. Am. Chem. Soc.* **2001**, *123*, 6327–6337.
- Company, A.; Gómez, L.; Güell, M.; Ribas, X.; Luis, J. M.; Que, L., Jr.; Costas, M. *J. Am. Chem. Soc.* **2007**, *129*, 15766–15767.
- Prat, L.; Company, A.; Postils, V.; Ribas, X.; Que, L., Jr.; Luis, J. M.; Costas, M. *Chem. - Eur. J.* **2013**, *19*, 6724–6738.
- Company, A.; Gómez, L.; Fontrodon, X.; Ribas, X.; Costas, M. *Chem. - Eur. J.* **2008**, *14*, 5727–5731.
- Bassan, A.; Blomberg, M. R. A.; Siegbahn, P. E. M.; Que, L., Jr. *Chem. - Eur. J.* **2005**, *11*, 692–705.
- Hitomi, Y.; Arakawa, K.; Funabiki, T.; Kodera, M. *Angew. Chem., Int. Ed.* **2012**, *51*, 3448–3452.
- Tiago de Oliveira, F.; Chanda, A.; Banerjee, D.; Shan, X.; Mondal, S.; Que, L., Jr.; Bominaar, E. L.; Münck, E.; Collins, T. J. *Science* **2007**, *315*, 835–838.
- Ghosh, M.; Singh, K. K.; Panda, C.; Weitz, A.; Hendrich, M. P.; Collins, T. J.; Dhar, B. B.; Gupta, S. S. *J. Am. Chem. Soc.* **2014**, *136*, 9524–9527.
- Kwon, E.; Cho, K.-B.; Hong, S.; Nam, W. *Chem. Commun.* **2014**, *50*, 5572–5575.
- Noack, H.; Siegbahn, P. E. M. *J. Biol. Inorg. Chem.* **2007**, *12*, 1151–1162.
- Cho, K. B.; Wu, X.; Lee, Y. M.; Kwon, Y. H.; Shaik, S.; Nam, W. *J. Am. Chem. Soc.* **2012**, *134*, 20222–20225.
- Comba, P.; Maurer, M.; Vadivelu, P. *J. Phys. Chem. A* **2008**, *112*, 13028–13036.
- Frisch, M. J.; Trucks, G. W.; Schlegel, H. B.; Scuseria, G. E.; Robb, M. A.; Cheeseman, J. R.; Scalmani, G.; Barone, V.; Mennucci, B.; Petersson, G. A.; Nakatsuji, H.; Caricato, M.; Li, X.; Hratchian, H. P.; Izmaylov, A. F.; Bloino, J.; Zheng, G.; Sonnenberg, J. L.; Hada, M.; Ehara, M.; Toyota, K.; Fukuda, R.; Hasegawa, J.; Ishida, M.; Nakajima, T.; Honda, Y.; Kitao, O.; Nakai, H.; Vreven, T.; Jr.; Peralta, J. E.; Ogliaro, F.; Bearpark, M.; Heyd, J. J.; Brothers, E.; Kudin, K. N.; Staroverov, V. N.; Kobayashi, R.; Normand, J.; Raghavachari, K.; Rendell, A.; Burant, J. C.; Iyengar, S. S.; Tomasi, J.; Cossi, M.; Rega, N.; Millam, J. M.; Klene, M.; Knox, J. E.; Cross, J. B.; Bakken, V.; Adamo, C.; Jaramillo, J.; Gomperts, R.; Stratmann, R. E.; Yazyev, O.; Austin, A. J.; Cammi, R.; Pomelli, C.; Ochterski, J. W.; Martin, R. L.; Morokuma, K.; Zakrzewski, V. G.; Voth, G. A.; Salvador, P.; Dannenberg, J. J.; Dapprich, S.; Daniels, A. D.; Farkas, Foresman, J. B.; Ortiz, J. V.; Cioslowski, J.; Fox, D. J. *Gaussian 09*, Revision A.02; Gaussian Inc.: Wallingford, CT, 2009.
- Becke, A. J. *Chem. Phys.* **1993**, *98*, 5648–5652.
- Lee, C.; Yang, W.; Parr, R. G. *Phys. Rev. B: Condens. Matter Mater. Phys.* **1988**, *37*, 785–789.
- Dolg, M.; Wedig, U.; Stoll, H.; Preuss, H. *J. Chem. Phys.* **1987**, *86*, 866–872.
- Hratchian, H. P.; Schlegel, H. B. *J. Chem. Theory Comput.* **2005**, *1*, 61–69.
- Hratchian, H. P.; Schlegel, H. B. *J. Chem. Phys.* **2004**, *120*, 9918–9924.
- Yamaguchi, K.; Jensen, F.; Dorigo, A.; Houk, K. N. *Chem. Phys. Lett.* **1988**, *149*, 537–542.
- Wittbrodt, J. M.; Schlegel, H. B. *J. Chem. Phys.* **1996**, *105*, 6574–6577.
- Grimme, S. *J. Comput. Chem.* **2006**, *27*, 1787–1799.
- Marenich, A. V.; Cramer, C. J.; Truhlar, D. G. *J. Phys. Chem. B* **2009**, *113*, 6378–6396.
- Ribeiro, R. F.; Marenich, A. V.; Cramer, C. J.; Truhlar, D. G. *J. Phys. Chem. B* **2011**, *115*, 14556–14562.
- Scholes, G. D.; Curutchet, C.; Mennucci, B.; Cammi, R.; Tomasi, J. *J. Phys. Chem. B* **2007**, *111*, 6978–6982.

- (45) *Advances in Chemical Physics*; Prigogine, I., Rice, S. A., Eds.; John Wiley & Sons, Inc.: Hoboken, NJ, USA, 1999; Vol. 106.
- (46) Marcus, R. A. *J. Chem. Phys.* **1956**, *24*, 966–978.
- (47) Perdew, J. P.; Zunger, A. *Phys. Rev. B: Condens. Matter Mater. Phys.* **1981**, *23*, 5048–5079.
- (48) Zhang, Y.; Yang, W. *J. Chem. Phys.* **1998**, *109*, 2604–2608.
- (49) Lundberg, M.; Siegbahn, P. E. M. *J. Chem. Phys.* **2005**, *122*, 224103.
- (50) Johansson, A. J.; Blomberg, M. R. A.; Siegbahn, P. E. M. *J. Chem. Phys.* **2008**, *129*, 154301.
- (51) Swart, M.; Groenhof, A. R.; Ehlers, A. W.; Lammertsma, K. J. *Phys. Chem. A* **2004**, *108*, 5479–5483.
- (52) Swart, M. *J. Chem. Theory Comput.* **2008**, *4*, 2057–2066.
- (53) Güell, M.; Solà, M.; Swart, M. *Polyhedron* **2010**, *29*, 84–93.
- (54) Radoń, M. *J. Chem. Theory Comput.* **2014**, *10*, 2306–2321.
- (55) Ji, L.; Faponle, A. S.; Quesne, M. G.; Sainna, M. A.; Zhang, J.; Franke, A.; Kumar, D.; van Eldik, R.; Liu, W.; de Visser, S. P. *Chem. - Eur. J.* **2015**, *21*, 9083–9092.
- (56) Harvey, J. N.; Aschi, M.; Schwarz, H.; Koch, W. *Theor. Chem. Acc.* **1998**, *99*, 95–99.
- (57) Acuña-Parés, F.; Codolà, Z.; Costas, M.; Luis, J. M.; Lloret-Fillol, J. *Chem. - Eur. J.* **2014**, *20*, 5696–5707.
- (58) Acuña-Parés, F.; Costas, M.; Luis, J. M.; Lloret-Fillol, J. *Inorg. Chem.* **2014**, *53*, 5474–5485.
- (59) Codolà, Z.; Garcia-Bosch, I.; Acuña-Parés, F.; Prat, I.; Luis, J. M.; Costas, M.; Lloret-Fillol, J. *Chem. - Eur. J.* **2013**, *19*, 8042–8047.
- (60) Prat, I.; Mathieson, J. S.; Güell, M.; Ribas, X.; Luis, J. M.; Cronin, L.; Costas, M. *Nat. Chem.* **2011**, *3*, 788–793.
- (61) Karamzadeh, B.; Singh, D.; Nam, W.; Kumar, D.; de Visser, S. P. *Phys. Chem. Chem. Phys.* **2014**, *16*, 22611–22622.
- (62) De Visser, S. P.; Tan, L. S. *J. Am. Chem. Soc.* **2008**, *130*, 12961–12974.
- (63) Kumar, S.; Faponle, A. S.; Barman, P.; Vardhaman, A. K.; Sastri, C. V.; Kumar, D.; de Visser, S. P. *J. Am. Chem. Soc.* **2014**, *136*, 17102–17115.
- (64) Zavitsas, A. A. *J. Org. Chem.* **2008**, *73*, 9022–9026.
- (65) De Visser, S. P. *J. Am. Chem. Soc.* **2010**, *132*, 1087–1097.
- (66) Kumar, D.; Karamzadeh, B.; Sastry, G. N.; de Visser, S. P. *J. Am. Chem. Soc.* **2010**, *132*, 7656–7667.
- (67) Kumar, D.; Latifi, R.; Kumar, S.; Rybak-Akimova, E. V.; Sainna, M. A.; de Visser, S. P. *Inorg. Chem.* **2013**, *52*, 7968–7979.
- (68) Ye, S.; Geng, C.-Y.; Shaik, S.; Neese, F. *Phys. Chem. Chem. Phys.* **2013**, *15*, 8017–8030.
- (69) Decker, A.; Rohde, J.-U.; Klinker, E. J.; Wong, S. D.; Que, L., Jr.; Solomon, E. I. *J. Am. Chem. Soc.* **2007**, *129*, 15983–15996.
- (70) Sahu, S.; Widger, L. R.; Quesne, M. G.; De Visser, S. P.; Matsumura, H.; Moënne-Loccoz, P.; Siegler, M. A.; Goldberg, D. P. *J. Am. Chem. Soc.* **2013**, *135*, 10590–10593.
- (71) Tsuzuki, S. *Annu. Rep. Prog. Chem., Sect. C: Phys. Chem.* **2012**, *108*, 69–95.
- (72) Alamiddine, Z.; Humbel, S. *Front. Chem.* **2014**, *1*, 37.
- (73) Kozuch, S.; Shaik, S. *Acc. Chem. Res.* **2011**, *44*, 101–110.
- (74) Houle, F. A.; Beauchamp, J. L. *J. Am. Chem. Soc.* **1979**, *101*, 4067–4074.
- (75) Janardanan, D.; Usharani, D.; Chen, H.; Shaik, S. *J. Phys. Chem. Lett.* **2011**, *2*, 2610–2617.

NOTE ADDED AFTER ASAP PUBLICATION

After this paper was published ASAP August 19, 2015, Figure 4 was replaced. The corrected version was reposted August 24, 2015.

4.2 The Mechanism of the Selective Fe-Catalyzed Arene Carbon-Hydrogen Bond Functionalization



Postils, V.; Rodríguez, M.; Sabenya, G.; Conde, A.; Díaz-Requejo, M.M.; Pérez, P.J.; Costas, M.; Solà, M.; Luis, J.M. **The Mechanism of the Selective Fe-Catalyzed Arene Carbon-Hydrogen Bond Functionalization**, *ACS Catal.* Just Accepted Manuscript. DOI: 10.1021/acscatal.7b03935.

Reproduced with permission from:

Postils, V.; Rodríguez, M.; Sabenya, G.; Conde, A.; Díaz-Requejo, M.M.; Pérez, P.J.; Costas, M.; Solà, M.; Luis, J.M. The Mechanism of the Selective Fe-Catalyzed Arene Carbon-Hydrogen Bond Functionalization. ACS Catal. 2018, 8(5), 4313-4322

<http://dx.doi.org/10.1021/acscatal.7b03935>

Copyright © 2018 American Chemical Society

The Mechanism of the Selective Fe-Catalyzed Arene Carbon-Hydrogen Bond Functionalization

Verònica Postils,^{†,‡} Mònica Rodríguez,^{†,‡} Gerard Sabenya,[†] Ana Conde,[§] M. Mar Díaz-Requejo,^{§,*} Pedro J. Pérez,^{§,*} Miquel Costas,^{†,*} Miquel Solà,^{†,*} and Josep M. Luis^{†,*}

[†]Institut de Química Computacional i Catàlisi (IQCC) and Departament de Química, Universitat de Girona, Campus Montilivi, 17071, Girona, Spain

[§]Laboratorio de Catálisis Homogénea, Unidad Asociada al CSIC, CIQSO-Centro de Investigación en Química Sostenible and Departamento de Química, Universidad de Huelva, 21007 Huelva, Spain

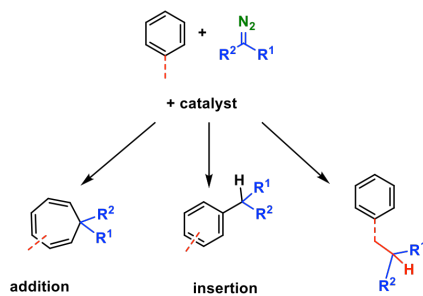
ABSTRACT: The complete chemoselective functionalization of aromatic C(sp²)-H bonds of benzene and alkyl-benzenes by carbene insertion from ethyl diazoacetate was unknown until the recent discovery of an iron-based catalytic system toward such transformation. A Fe(II) complex bearing the pytacn ligand (pytacn=L1=1-(2-pyridylmethyl)-4,7-dimethyl-1,4,7-triazacyclononane) transferred the CHCO₂Et unit exclusively to the C(sp²)-H bond. The cycloheptatriene compound commonly observed through Buchner reaction or, when employing alkyl-benzenes, the corresponding derivatives from C(sp³)-H functionalization are not formed. We herein present a combined experimental and computational mechanistic study to explain this exceptional selectivity. Our computational study reveals that the key step is the formation of an enol-like substrate, which is the precursor of the final insertion products. Experimental evidences based on substrate probes and isotopic labelling experiments in favor of this mechanistic interpretation are provided.

KEYWORDS carbene transfer iron catalysis C-H activation C(sp²)-H functionalization DFT calculations

INTRODUCTION

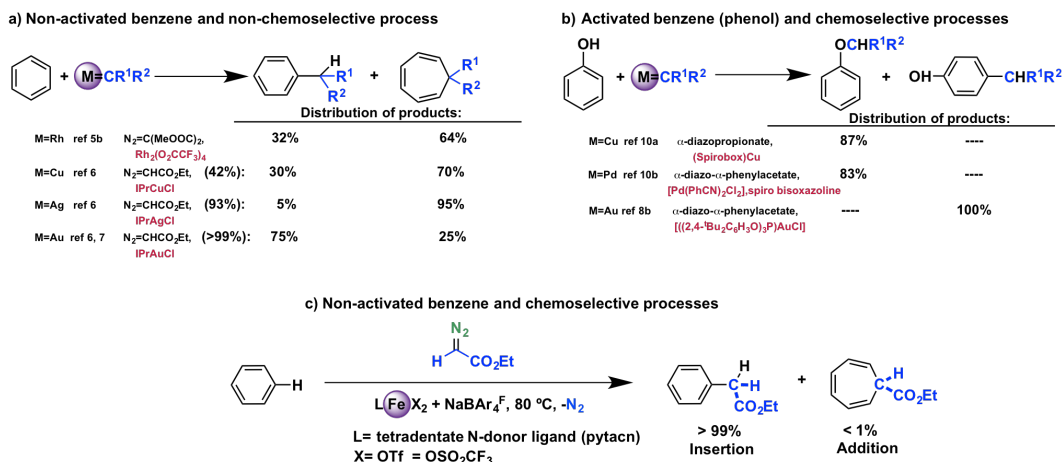
The metal-catalyzed carbene transfer from a diazo reagent to C-H bonds constitutes a strategy that is gaining interest in the last decade.¹ Both C(sp²)-H and C(sp³)-H bonds can be modified by this methodology, albeit when working with benzene derivatives the issue of selectivity emerges as a serious drawback. This is the consequence of a series of competing reactions that may occur, as shown in Scheme 1. The addition of the carbene unit to a C=C bond of the arene leads to a norcaradiene intermediate that spontaneously converts into the cycloheptatriene derivative, the addition product. This is the

Scheme 1. Possible products in the metal catalyzed alkyl-benzene functionalization by carbene insertion



so-called Buchner reaction, known in a thermal manner since the XIX century,² and in the rhodium-catalyzed version after the work by Noels and co-workers.³ The second transformation is that of the neat *insertion*⁴ of the carbene unit in the C(sp²)-H bond of the arene, a less frequent transformation. To date the functionalization of benzene and other non-substituted arenes by this methodology based on metal-carbene intermediates, generated from diazo reagents, has been achieved using several metals (Scheme 2) such as rhodium,⁵ or coinage metals.^{6,7} In all these cases, a mixture of products is obtained due to the existence of aforementioned competing reactions (Scheme 1). Until recently, the best selectivity for insertion as opposed to addition products is ca 3:1 (Scheme 2a), and was obtained with a gold-based catalyst.⁷ A chemoselective insertion of the carbene group in aromatic C(sp²)-H bonds can be achieved with the use of electron-rich benzene derivatives such as phenol or anisole (Scheme 2b). The addition of these π -electron-donating groups (-OH, -OCH₃) to benzene enhances the nucleophilic reactivity of the aromatic carbons and favors insertion products. The use of electron-deficient phosphite ligands increases the electrophilic character of the carbene moiety in gold catalysts, enabling selective insertion in electron-rich arenes. Finally, the existence of alkyl-substituents⁹ or other X-H groups (X = O, N)¹⁰ in the substrate may lead to their functionalization, also upon insertion of the carbene group. These substrate functionalization reactions competing also with the non-productive metal-catalyzed coupling of two carbene units.¹¹

Scheme 2. Functionalization of arenes by metal-carbene catalysts.



a) Precedents in the catalytic functionalization of benzene by metal-carbene transfer. Non-chemoselective processes. **b)** Precedents in the functionalization of activated benzenes (phenol) by metal-carbene transfer. Chemoselective processes. **c)** Reaction of this study. First example of a chemoselective functionalization of benzene.

Recently, we reported the first example for a chemoselective functionalization of non-activated aryl C(sp²)-H bonds with the use of the commercially available ethyl diazoacetate (EDA) and iron- or manganese-based catalysts.¹² Fe^{II} and Mn^{II} complexes bearing the tetradentate pytacn ligand (pytacn = L1 = 1-(2-pyridylmethyl)-4,7-dimethyl-1,4,7-triazacyclononane) lead to >99% formation of insertion products and no formation of cycloheptatriene derivatives (Scheme 2c). Fumarate and maleate products, resulting from coupling of two carbene units, were also practically absent. This work also expanded to first-row transition metal catalysts the direct functionalization of non-activated aryl C(sp²)-H bonds by metal-carbene transfer from ethyl diazoacetate. Interestingly, the presence of substituents in a series of alkyl-aromatic substrates did not affect the selectivity of the reaction, since the alkylic C-H bonds remained unreacted, only the aryl C-H bonds being functionalized. In view of the novelty of this transformation in terms of the exceptional selectivity, we have performed a combined experimental and theoretical study that has led to the understanding of the mechanistic details of the functionalization of C-H bond of benzene, which may serve in the design of novel generations of catalysts with improved efficiency and chemoselectivity.

RESULTS AND DISCUSSION

Experimental analyses

Effect of the catalyst architecture in the catalytic activity. Initially we studied the potential ability of iron complexes to catalyze the reaction of ethyl diazoacetate (EDA) and benzene (Scheme 2c and Table 1). Reactions were performed at 80°C during 12h in a 1:1 mixture of benzene and CH₂Cl₂

under N₂, and were initiated by the addition of 20 equiv of EDA to a solution of 5 mol% of the catalyst and NaBAR₄^F (2-8 equiv). Reactions provided insertion (**I**) and addition (**A**) products, and the yields and relative amount of both products were dependent on the catalyst. The typology of the catalysts studied in our previous work was mainly focused in tetradentate aminopyridine ligand (Scheme 3), which have proven to form iron complexes particularly active in oxygen atom transfer reactions (L1 and L7 constitute prototypical examples).¹³ In the current work, this collection has been extended with the use of iron complexes bearing sterically encumbered tridentate (L10) and tetradentate (L9) ligands based in pyrazole rings, that have been found particularly active in other carbene transfer reactions with first row transition metals.¹⁴ This analysis reinforces [FeX₂(L1)] (where X = Cl or OTf) as a particularly efficient (entries 1 and 2, up to 86% of EDA was converted into products) and chemoselective catalysts towards the insertion product (>99%). Modifications in the electron donating properties of the pyridine (entries 3-6), and in the denticity of the ligand (entries 7 and 9) led to lower product yields. Particularly noticeable was the observation that complex [Fe(OTf)(L8)](OTf), bearing a pentadentate ligand, was inactive (entry 9), strongly suggesting that the presence of two labile sites at the first coordination sphere of the iron center is necessary for activity. Complexes based in pyrazolyl donors, i.e. [Fe(OTf)₂(L9)] and [Fe(OTf)(L10)], are active (entries 10 and 11) but provide roughly 1:1 mixtures of insertion and addition products.

On the basis of the previous observations, [Fe(OTf)₂(L1)] was taken as the catalyst of choice to test other carbene sources, that led to limited success (entries 12 and 13). Unlike EDA, which provides insertion products in good yield and selectivity, the use of phenyldiazoacetate or its 4-bromo de-

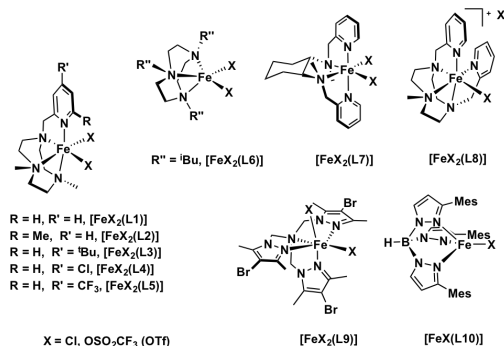
rivative resulted instead in a slight preference towards the expansion product in moderate (41-51%) yields.

Table 1. Catalytic behavior of different $[\text{FeX}_2(\text{L})]$ complexes in the reaction of benzene and ethyl diazoacetate.^a

Entry	L	X	Yield ^b	%:1:A ^{c,d}	Ref
1	L1	Cl	86	>99:1	12
2	L1	OTf	83	>99:1	12
3	L2	OTf	77	>99:1	12
4	L3	OTf	47	>99:1	12
5	L4	OTf	85	>99:1	12
6	L5	OTf	18	>99:1	12
7	L6	OTf	67	>99:1	12
8	L7	OTf	70	>99:1	12
9	L8	OTf	n.r	...	12
10	L9	Cl	57	42:58	This work
11	L10 ^e	Cl	55	53:47	This work
12	L1	OTf	41	45:55 ^f	This work
13	L1	OTf	51	40:60 ^g	This work

^aReactions carried out at 80°C with 0.005 mmol of catalyst, 8 equiv of $\text{NaBAR}_4^{\text{F}}$ and 20 equiv of ethyl diazoacetate in 1.5 mL of benzene + 1.5 mL of CH_2Cl_2 . Reaction time: 12 h. ^bInitial EDA converted into insertion (*I*) + addition (*A*) products. Determined by GC; some ethyl glycolate from adventitious water was detected as byproduct. ^cDetermined by NMR. ^dThe acid-catalyzed conversion of *A* into *I* has been discarded on the basis of blank experiment: see Supporting Information. ^e $\text{FeX}[\text{L}10]$ complex ^fPhenyldiazoacetate was used as carbene source instead of EDA. ^g4-Br-phenyldiazoacetate was used as carbene source instead of EDA.

Scheme 3. Complexes employed as catalyst precursors in the screening shown in Table 1.



Considering that 2-8 equivalents of $\text{NaBAR}_4^{\text{F}}$ are necessary for efficient activity, we investigated the iron species that are

formed when this salt reacts with $[\text{Fe}(\text{OTf})_2(\text{L}1)]$. Diiron complex $[\text{Fe}_2(\mu^2\text{-OTf})_2(\text{L}1)_2](\text{BAR}_4^{\text{F}})_2$ was prepared by reaction of $[\text{Fe}(\text{OTf})_2(\text{L}1)]$ with 1-4 equiv. of $\text{NaBAR}_4^{\text{F}}$, and it was crystallographically characterized. An ORTEP diagram of the diiron complex is shown in Figure 1, and compared with that of $[\text{Fe}(\text{OTf})_2(\text{L}1)]$.¹⁵ Iron centers in both complexes are coordinatively saturated. They have distorted octahedral coordination geometry, with four sites occupied by the L1 ligand and the two remaining sites fulfilled by oxygen atoms of the triflate ligands, which are terminally coordinated in the mononuclear complex and bridging in the dinuclear case.

When $[\text{Fe}_2(\mu^2\text{-OTf})_2(\text{L}1)_2](\text{BAR}_4^{\text{F}})_2$ complex was tested under standard reaction conditions, but in the absence of additional $\text{NaBAR}_4^{\text{F}}$, it was catalytically inactive. However, when the same reaction was conducted in the presence of 4 equiv. of $\text{NaBAR}_4^{\text{F}}$, the insertion product was obtained as the only product in 80% yield. These observations strongly suggest that detachment of the first triflate anion from $[\text{Fe}(\text{OTf})_2(\text{L}1)]$ does not lead to an active catalyst, and instead removal of the two anionic ligands, generating two vacant sites at the iron coordination sphere, are most likely needed for EDA activation. Unfortunately, iron species resulting from elimination of the second triflate ligand could not be isolated, and the paramagnetic nature of the iron species makes ¹H-NMR ineffective to probe its formation in solution. However, prominent ions at $m/z = 152.1$ with isotopic patterns characteristic of $[\text{Fe}(\text{L}1)]^{2+}$ could be observed in the ESI-MS spectra of $[\text{Fe}(\text{OTf})_2(\text{L}1)]$, suggesting that tetracoordinate dicationic species are viable intermediates.

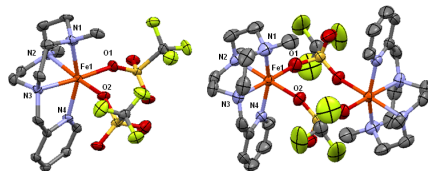


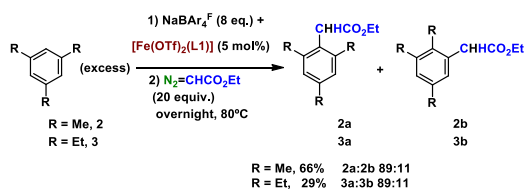
Figure 1. ORTEP diagram of the single crystal X-ray structure for $[\text{Fe}(\text{OTf})_2(\text{L}1)]$ (left) and $[\text{Fe}_2(\mu^2\text{-OTf})_2(\text{L}1)_2](\text{BAR}_4^{\text{F}})_2$ (right). 15 50% ellipsoid probability, H atoms have been omitted for clarity. $[\text{Fe}(\text{OTf})_2(\text{L}1)]$ selected distances (Å): Fe1-N1: 2.231, Fe1-N2: 2.251, Fe1-N3: 2.205, Fe1-N4: 2.165, Fe1-O1: 2.055, Fe1-O2: 2.165. $[\text{Fe}_2(\mu^2\text{-OTf})_2(\text{L}1)_2](\text{BAR}_4^{\text{F}})_2$ selected distances (Å): Fe1-N1: 2.200, Fe1-N2: 2.210, Fe1-N3: 2.187, Fe1-N4: 2.142, Fe1-O1: 2.060, Fe1-O2: 2.189.

The results collected in this section reveal that $[\text{Fe}(\text{OTf})_2(\text{L}1)]$ is a particularly efficient and chemoselective catalyst for the formal carbene insertion from EDA into the C-H bonds of benzene, reinforcing the findings of the preliminary communication.¹² It is worth noting that the scope of this catalytic system with a series of substituted benzenes showed the complete selectivity toward arene C-H bonds in the presence of alkyl C-H sites of the substituents. The presence of two labile coordination sites appears to be necessary for efficient catalysis.

Mechanistic considerations from product analysis. Our previous contribution included¹² a Hammett analysis of the carbene transfer reaction, determined by means of competitive

functionalization of pairs of monosubstituted arenes, which provided $\rho = -2.75 \pm 0.37$, indicative of an electrophilic functionalization of the arene. Furthermore, an inverse intermolecular KIE = 0.95 was determined, consistent with a change in the hybridization from sp^2 to sp^3 in the arene functionalization step. These parameters strongly suggest that the functionalization of the arene occurs via an electrophilic aromatic substitution, a proposal that is in good concordance with the *o*:*m*:*p* ratios observed in the functionalization of monosubstituted benzenes. We have now collected additional pieces of information *en route* to mechanism elucidation.

Scheme 4. Alkyl migrations in the functionalization of 1,3,5-trialkylsubstituted arenes.



Alkyl group migrations. Functionalization of mesitylene (2) and 1,3,5-triethylbenzene (3) under standard reaction conditions (Scheme 4) provides the ethyl esters **2a** and **3a** as major products resulting from a formal insertion at arene C-H bond. However, inspection of the reaction crude NMR spectra reveals the formation of a minor product **2b** and **3b**, respectively (~11%) resulting from alkyl migration.

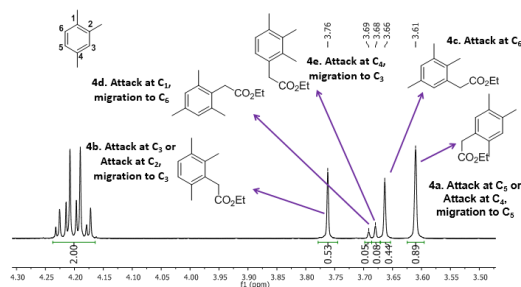
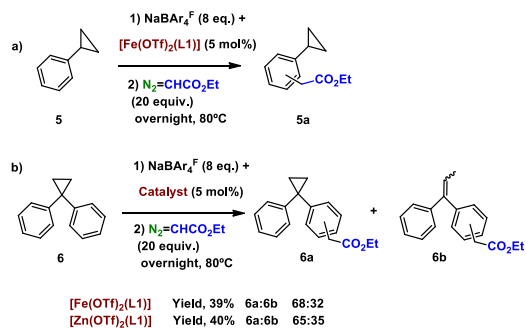


Figure 2. $^1\text{H-NMR}$ spectrum (CDCl₃, 400MHz, 300K) of the EDA insertion products obtained in the functionalization of **4** with $[\text{Fe}(\text{OTf})_2(\text{L}1)]$. The origin of the different products is indicated in each case.

Alkyl migrations are best evidenced by performing the functionalization of 1,2,4-trimethylbenzene (**4**) under standard reaction conditions (Figure 2). The reaction produced three major (**4a**, **4b** and **4c**) and two minor (**4d** and **4e**) products. Major products originate from formal carbene insertion in C-H bonds at C₅, C₃ and C₆, respectively, while minor products are indicative of insertions accompanied by alkyl migrations. **4d** can be explained based on an initial attack at C₁, followed by methyl migration to C₆, while **4e** indicates initial attack on C₄ followed by methyl migration to C₃. Of these, **4a** appears

as the major product, presumably because: i) C₅ and C₆ are sterically less congested than C₃; and ii) C₅ is preferentially activated towards an electrophilic attack because it is in *para* position with respect to the methyl group at C₂. We note that **4a** and **4b** may be also partially originating from reactions where methyl migration takes place (see Figure 2).

Scheme 5. Carbene insertion into radical-clock substrate probes.



Radical clock substrate probes. An experiment of this type was provided in our previous report, where we described that the functionalization of cyclopropylbenzene (**5**) with $[\text{Fe}(\text{OTf})_2(\text{L}1)]$ proceeds without ring opening (Scheme 5a). This experiment suggested that radical intermediates were not formed, or alternatively they must have very short lifetimes, incompatible with radical rearrangements. To further substantiate this point, an ultrafast radical probe (**6**, Scheme 5b) was subjected to standard reaction conditions, employing the same catalysts. The reaction produced not-rearranged cyclopropyl product **6a**, and rearranged product **6b** in a 68:32 ratio, with a combined 39% yield. This observation may initially suggest that the reaction proceeds via short living carbocationic or radical intermediates. Most remarkably, an almost identical ratio (65:35) and yield (40%) was obtained when $[\text{Zn}(\text{OTf})_2(\text{L}1)]$ was used as catalyst (see Supporting Information), suggesting that carbocationic and not radical rearrangements are involved.¹⁶

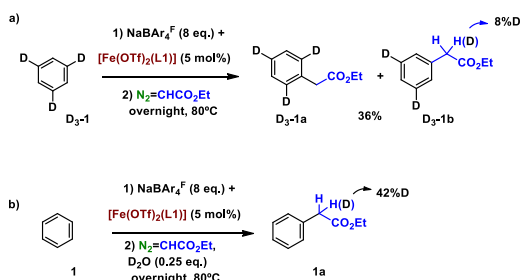
These results demonstrate that the reaction mechanism for carbene insertion must accommodate reaction intermediates susceptible to engage alkyl arene migrations and carbocationic rearrangements. Indeed, we notice that migrations may be also indicative of carbocationic intermediates.

Isotopic labelling analyses. Isotopic labelling analyses has revealed valuable mechanistic details in order to validate the computational analysis that follows. Under standard reaction conditions, formal carbene transfer to 1,3,5- D_3 -benzene **D₃-1** yields **D₃-1a**, resulting from formal carbene insertion into an arene C-H bond, and **D₃-1b**, where insertion has occurred at the C-D bond (Scheme 6a). The ratio of insertion vs. expansion is higher than 99%, indicating that the deuteration of benzene does not change the chemoselectivity of the catalysis. Interestingly, partially D atom ends up forming the benzylic C-D bond in the **D₃-1b** product. A 8% of the D is incorporated in the product, with the remaining corresponding to the fully

hydrogenated benzylic position, suggesting the possibility of the incorporation of protons from an external source. The ratio between the two mentioned products is 49.3:50.7 (extracted from relative integration of the aromatic signals), which translates into an intramolecular kinetic isotope effect, KIE = 0.97, in agreement with the intermolecular KIE previously determined from the competitive functionalization of benzene and D₆-benzene. Noticeable, products resulting from deuterium migration in the aromatic ring, analogous to those observed from alkyl groups, are not observed.

Finally, when the functionalization of benzene was conducted in the presence of D₂O (0.25 equiv.), 42% of the corresponding benzylic ester product **1a** contains a benzylic C-D group (Scheme 6b). Control experiments showed that the benzylic C-H bonds in **1a** do not exchange the hydrogen atoms with D₂O. Consequently, these experiments indicate that the carbene transfer reaction involves species that could exchange an H atom with D₂O. The involvement of adventitious water in these transformations with gold-catalysts has been recently proposed.⁶

Scheme 6. Isotopic labelling analysis.



The above reactivity implies that the mechanism of carbene insertion must accommodate a path that enables the transfer of an arene hydrogen atom to the benzylic position, and partial exchange of a benzylic C-H bond with external water molecules.

Computational analyses

Generation of the carbene moiety. It is widely accepted that the most feasible reaction of metal catalysts with EDA proceeds via N₂ loss to form a metal-carbene species.¹⁷ We have studied the mechanism of this reaction for [Fe(OTf)₂(L1)], taking into account the singlet, triplet, and quintet spin states. "Since the experimental data shows that the diiron complex [Fe₂(μ²-OTf)₂(L1)₂]²⁺ does not participate in the activation of EDA, it was not considered in the computational analyses" All structures were optimized and characterized at the UB3LYP-D3BJ/6-31G(d)/SMD(CH₂Cl₂) level of theory. Then, the electronic energies were improved performing single point calculations at the UB3LYP-D3BJ/cc-pVTZ/SMD(50%Bz,50%CH₂Cl₂) level (SI contains full details on computational calculations).

Based on the previously described experimental data, which suggests that the two triflate ligands are removed in the catalytically active species, two possible [(L)Fe-(EDA)]²⁺ adducts have been characterized depending on which atom of EDA

interacts with the iron (Figure 3). The carbonyl O-bound adduct **A** is the most stable form, while the carbon-bound adduct **A'** is 14.2 kcal/mol higher in energy. Then, the most stable adduct is given by the interaction between the iron and the most nucleophilic atom of EDA. The nitrogen-bound adduct has not been characterized as a stable minimum, as opposite to other metal catalysts interacting with EDA.¹⁸ For [Fe(L1)]²⁺ and all EDA-bound adducts, the most stable spin state is the quintet (see Figure S1 for more details).

Only the **A'** adduct is able to evolve, via N₂ elimination, towards the formation of the Fe-carbene moiety. The relative instability of **A'** with respect to **A** leads to a global energy barrier of 29.5 kcal/mol for the overall reaction (Figure 3). Although an energy barrier of 29.5 kcal/mol is not affordable at room temperature, it can be overcome from ca. 80°C, which is the experimental working temperature. High-energy barriers for carbene formation were also found for the formation of iron and cobalt porphyrin carbenes.¹⁹ This, along with the fact that the formation of the iron-carbene is the rate-determining step of the overall reaction of benzene functionalization, prevents the accumulation and experimental characterization of the putative iron-carbene or any other intermediate. Thus, the computational study becomes necessary for a proper mechanistic description.

Once the transition state (TS) for the S=2 carbene formation (TS_{A'-C@N2}) is surmounted, a spin crossing takes place and triplet becomes the most stable spin state for the adduct between the Fe-carbene and N₂ (**C@N₂**). Finally, the loss of the N₂ moiety is favorable and the global carbene formation process (**A** to **C**) is endergonic by 4.9 kcal/mol. A quasi-equivalent **C@N₂** isomer is obtained if EDA is coordinated to the labile position perpendicular to the pyridyl ring instead of the parallel one (see Figure S2).

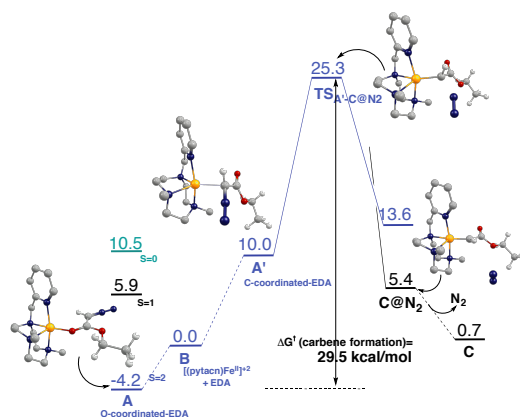


Figure 3. Gibbs energy profile, ΔG , (kcal·mol⁻¹) of the metal-carbene bond formation. Blue, black and green profiles correspond to quintet, triplet and singlet multiplicities, respectively. Hydrogen atoms of L1 ligand have been omitted for clarity (C: grey, N: blue, O: red, Fe: yellow, H: white).

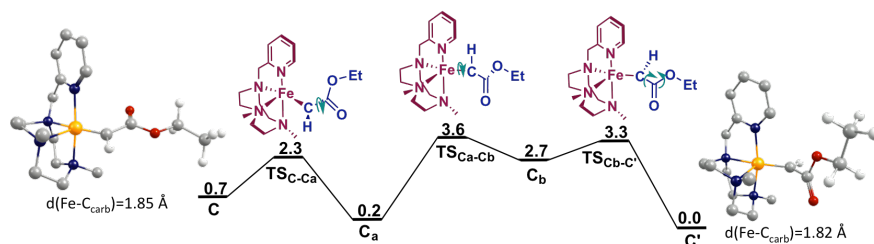


Figure 4. Gibbs energy profile, ΔG (kcal·mol⁻¹) of the C-to-C' conformational change at the triplet spin state. For C and C' intermediates, the Fe-C bond distance is given in Å. Hydrogen atoms of the L1 ligand have been omitted for clarity (C: grey, N: blue, O: red, Fe: yellow, H: white).

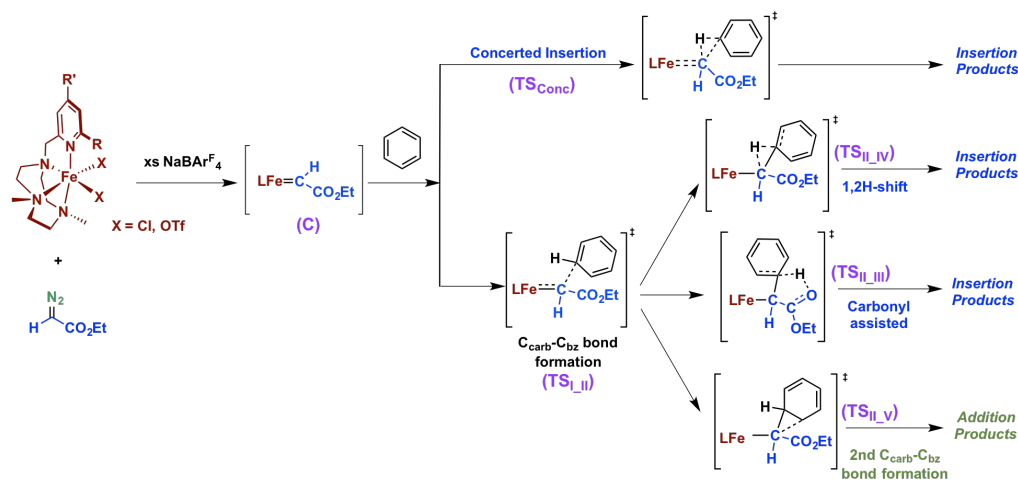
The metal center in the iron-carbene species (C) displays distorted octahedral coordination geometry, with one free-coordination site and five occupied-coordination sites taken by the tetradentate ligand and the carbene. The Fe-C_{carbene} distance in C is 1.85 Å (Figure 4). Iron-carbene bond lengths are sensitive to the electronic nature and chemical environments of the carbene and iron ligands.²⁰ The DFT analyses of the spin densities, frontier molecular orbitals (MOs), natural bond orbitals (NBO),²¹ and the effective oxidation states (efFOS)²² suggest that the electronic nature of Fe-carbene C is described as a Fe(III) and a formal radical alkyl substituent (see Supporting Information for details). An equivalent electronic structure was reported by Shaik et al. for an iron porphyrin carbene complex.^{17b}

Iron-carbene C is not the Fe-carbene conformer that presents the lowest barrier to react with benzene. Among all the conformers analyzed, the C' conformer was found to be the most suitable for the approach of benzene to the C_{carb} and to facilitate further benzene functionalization reactions. The main difference between C and C' is the position of the carbene tail (see Figure 4). While in the C conformer the carbonyl group is pointing towards the free-coordination site of the catalyst, in the C' conformer the tail of the carbene is bent towards the equatorial-NCH₃ group of the ligand. Although in the C conformer the carbonyl oxygen of the carbene tail is pointing toward the free-coordination site of iron, on the basis of non-covalent interaction (NCI)²³ and NBO analysis, a bonding interaction between the carbonyl oxygen of the carbene tail and the iron atom is discarded (see Figure S6). Fur-

thermore, NCI analyses evidence that the C' conformer presents a less crowded environment than C for C_{carb} (see section 3.2 in SI for the detailed NCI analysis). Therefore, on the contrary to C, C' has enough vacant space to allow: i) the approach of benzene in front of the free-coordination site of the iron; and ii) the movement of the carbene hydrogen required for the interaction between benzene and C_{carb} (see Figure S7). Thus, the comparison between C and C' also shows the essential role of the free-coordination site of the Fe-carbene in the functionalization of benzene, which agrees with the experimental need to add more than 2 equivalents of NaBAR₄^F for the reaction to proceed. The excess of NaBAR₄^F ensures the formation of the initial dicationic species [Fe(L1)]²⁺ with two free coordination sites (complex B, Figure 3), required for the formation of the metal-carbene.

The detailed pathway from C to C' has been computationally studied and it is shown in Figure 4. The evolution contains several low-energy transition states connecting intermediates of similar energy that match up to three consecutive σ -bond rotations²⁴ of: i) the bond of C_{carb} with the carbonyl carbon (TS_{C-C_a}), ii) the bond of C_{carb} with the iron (TS_{C_a-C_b}), and iii) again the bond of C_{carb} with the carbonyl carbon (TS_{C_b-C'}). TS_{C_a-C_b} has the highest energy barrier of the conformational evolution, which is only 3.4 kcal/mol. The Fe-C_{carb} bond rotation and its low energy barrier are consistent with the existence of a very weak Fe-C_{carb} π -interaction. Apart from the key differences pointed above, conformers C and C' have similar geometric and electronic structures (see SI for details).

Scheme 7. Plausible pathways for the formation of insertion and addition products



Mechanistic insights in benzene functionalization I. Concerted insertion versus stepwise mechanisms. Our study of the first step of the reaction between the iron-carbene and benzene has taken into account two different possible pathways: an stepwise mechanism and a concerted one (see Scheme 7 and Figure 5). In the former, the attack of the aromatic benzene C(sp²) to C_{carb} (**TS_{I,II}**) leads to an intermediate with a C_{carb}-C_{bz} bond (**II**). The intermediate **II** can evolve through three different pathways to the possible final products, i.e. the insertion and expansion products (see next section). In the concerted mechanism, the attack of the aromatic benzene C(sp²) to C_{carb} (**TS_{Conc}**) directly gives insertion products. Both pathways have been described in the literature on mechanisms of C-H bond insertion by metal-carbenes.²⁵ The singlet, triplet, and quintuplet spin states were considered in the calculation of the Gibbs energy profile. Besides the study of the reaction of **C'** with benzene that yields the adduct **I**, it has also been considered the reaction of benzene with a bidentate carbene isomer (**I**^{k2}), which is 1.2 kcal/mol less stable than **I**. The **I**^{k2} isomer with a singlet ground state can be understood as an evolution of carbene **C**, where the carbonyl oxygen is bonded to iron through its sixth-coordination site. A global picture of the results is represented in Figure 5.

The most favorable mechanism for the initial step of the functionalization of benzene is the C_{carb}-C_{bz} bond formation from monodentate **C'** to yield **II** through **TS_{I,II}**, which is, at least, 8.5 kcal/mol lower in energy than any other studied pathway. This step has a global energy barrier of only 17.3 kcal/mol whereas the same reaction mechanism for the bidentate carbene has an energy barrier of 25.9 kcal/mol (**TS**^{k2}_{I,II}). Therefore, we discard any role of isomer **I**^{k2} in the functionalization of benzene (see Figures S10, S12, and S13 in the SI for geometry and electronic details of **TS_{I,II}** and **TS**^{k2}_{I,II}).

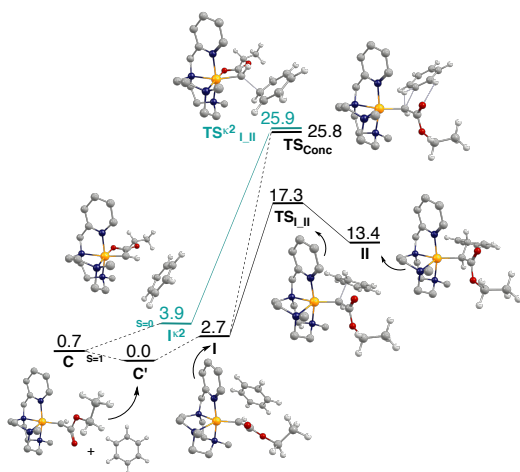


Figure 5. Comparative Gibbs energy profile, ΔG , ($\text{kcal}\cdot\text{mol}^{-1}$) of the first steps of the studied reactions between benzene and the iron-carbene. Black and green profiles correspond to triplet and singlet multiplicities, respectively. Hydrogen atoms of the L1

ligand have been omitted for clarity (C: grey, N: blue, O: red, Fe: yellow, H: white).

For the concerted mechanism, a high-energy barrier of 25.8 kcal/mol (**TS_{Conc}**) at the triplet spin ground state is found. Thus, the concerted mechanism is also discarded. In agreement with our results, the fact that metal-carbenes do not perform a concerted C_{substrate}-H bond insertion for aromatic substrates contrary to alkane substrates has been also recently reported for gold-carbenes.^{8a} The same conclusion can also be obtained comparing the mechanistic literature of the reactions of Au, Cu, Ag or Rh carbenes with alkanes²⁶ and with aromatic compounds.^{6a,25b}

DFT analysis of the electronic structure of intermediate **II** suggests a cyclohexadienyl radical character intermediate (see Table S7). However, several pieces of experimental evidences point towards this reaction proceeding via an electrophilic attack of the carbene on the aromatic ring, generating a Wheland type intermediate. On one hand, o:m:p ratios and Hammett parameters are consistent with this scenario. On the other hand, the inverted KIE effect is in good agreement with a sp² to sp³ change in hybridization in the arene functionalization step. Furthermore, the cationic nature of the intermediate is well supported by the observation of alkyl migration products, and by the carbocationic rearrangement product obtained in the functionalization of the ultrafast radical probe **6**. The degree of reorganization of this substrate is identical to that measured with the red-ox inactive [Zn(OTf)₂(L1)] catalyst, providing strong argumentation against a radical electronic structure of **II**. The radical electronic structure of ³**II** predicted by DFT calculations could be due to the particular strong spin contamination of the wavefunction of intermediate ³**II** (i.e. $\langle S^2 \rangle = 3.1$). Nevertheless, it is important to remark here that we have used the Yamaguchi correction²⁷ to remove the spin-contamination error of the computed Gibbs energies used to determine the most favorable mechanism (see Computational Details and Section 6 in the SI). Several conformers for all the reaction pathways and S=0, S=1, and S=2 spin states were examined. Figure 5 just shows the most important results and the complete data is shown in Figure S11 and Tables S4, S5 and S6. Emphasis had been placed on a proper description of the energy barrier and spin splitting of the C_{carb}-C_{bz} bond formation (³**TS_{I,II}** and ⁵**TS_{I,II}**). Thus, although the precise electronic structure of intermediate ³**II** is not exactly described by our methodology, additional calculations (*vide infra*) indicate that the Gibbs barrier of the transformation of **I** to **II** through ³**TS_{I,II}** is properly estimated.

It has to be mentioned here that ⁵**TS_{I,II}** is found to be 7.8 kcal/mol lower in energy than ³**TS_{I,II}**. However, we have not taken into account ⁵**TS_{I,II}** in our mechanism for the reasons that follow. It is known that B3LYP is not a good functional to describe the correlation energy changes of reactions where the number of unpaired electrons of the metal-carbon bond changes.²⁸ Furthermore, B3LYP tends to overstabilize the high-spin states.²⁹ A study of homolytic Fe-, Co-, and Ni-C bond dissociation energies in tetra-pyrrole-like systems shows that the use of pure DFT methods with Becke's exchange functionals (BP86, BLYP or BPW91) are a better alternative than B3LYP to describe the metal-C bond breaking.²⁸ Thus, we have optimized **I** and **TS_{I,II}** for the triplet and quintet spin

states using B3LYP, B3LYP*, OPBE, M06-L, BP86, BLYP, and BPW91 functionals and 6-31G(d), 6-311+G(d,p) and Def2-SVP basis sets (see Table S5 and S6 in the SI for details). The results obtained with the literature-recommended functionals for this step^a of the mechanism (i.e. BP86, BLYP and BPW91) are similar among them and indicate that the triplet state is the spin ground state for both **I** and **TS_{I,II}**. Besides, the three recommended functionals lead to similar ³**TS_{I,II}** energy barriers. Thus, according to these results, we do not consider the spin-crossing from ³**TS_{I,II}** to ⁵**TS_{I,II}**. However, we keep B3LYP as the reference functional because hybrid methods like B3LYP are more reliable functionals to study the other steps of the mechanism that involve formation and breaking of bonds between H, C, and O atoms.³⁰ For consistency, we have chosen the same functional, B3LYP, to present the results for all the steps of the mechanism.

Mechanistic Insights in the benzene functionalization II. Insertion versus Expansion mechanisms. In this section the mechanism that determines the complete selective insertion of -C(H)CO₂Et into benzene C-H bonds with no formation of cycloheptatriene byproducts is addressed. Figure 6 presents all the possible different mechanisms we found that connect intermediate **II** with insertion or addition products.

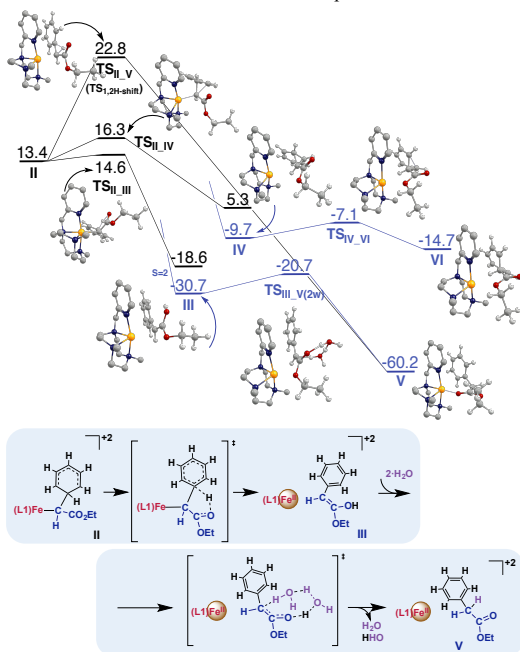


Figure 6. Comparative Gibbs energy profile, ΔG , ($\text{kcal}\cdot\text{mol}^{-1}$) of the formation of addition (**VI**) and insertion (**V**) products from **II**. Black and blue profiles correspond to triplet and quintet multiplicities, respectively. Hydrogen atoms of the L1 ligand have been omitted for clarity (C: grey, N: blue, O: red, Fe: yellow, H: white). The inset below the energy profile details the reaction mechanism to obtain insertion products through the formation of the enol intermediate.

Two different pathways connect **II** with insertion products: i) the classical direct hydrogen migration between the two carbons that form the $\text{C}_{\text{carb}}\text{-C}_{\text{bz}}$ bond (i.e. from C_{bz} to C_{carb}), the called [1,2]-H shift reaction (**TS_{II,V}**); and ii) a hydrogen abstraction reaction of the same hydrogen by the carbonyl oxygen of the native EDA (**TS_{II,III}**). The latter mechanism, named carbonyl assisted insertion, generates an enol intermediate that, to finally yield the insertion product, should subsequently evolve to the ester form. On the other hand, we only found one possible reaction that connects **II** with addition products. The addition pathway implies the formation of a second $\text{C}_{\text{carb}}\text{-C}_{\text{bz}}$ bond with an adjacent carbon of the phenyl (**TS_{II,IV}**). This TS does not directly give the addition product, but a norcaradiene, which can evolve to the final cycloheptatriene addition product (**VI**) through a thermally allowed electrocyclic disrotatory ring opening.

As it is shown in Figure 6, among the three different pathways that start at **II**, the formation of the enol is the lowest energy barrier process (**TS_{II,III}**). The enol formation from **II** is strongly exergonic. Then, the next and last transition state of this pathway, the enol-to-ester transformation barrier, takes place at far lower Gibbs energy barriers. Thus, the most favorable mechanism from **II** is the formation of the enol intermediate that leads to the final insertion of -C(H)CO₂Et into benzene C-H bond. The abstraction of the hydrogen bonded to the phenylic carbon that forms the $\text{C}_{\text{carb}}\text{-C}_{\text{bz}}$ bond by one carbonyl oxygen has also been reported as the most favorable mechanism for the C-H functionalization of arenes by Au and Ag carbene catalysts,^{6,Error! Bookmark not defined.} and in the functionalization of N-H bonds by Fe porphyrin carbene species.^{19b}

The enol formation process has a small energy barrier of 1.2 kcal/mol. Although the enol product formed still remains close to iron (the $\text{Fe}\cdots\text{C}$ distance is 2.28 Å), there is not a formal bond between them and iron is described as an $\text{Fe}^{2+}(d^6)$. The enol intermediate structure **III** that involves a high spin d^6 iron with four unpaired electrons, ⁵**III**, is energetically more favorable than ³**III** by 12.1 kcal/mol. Thus, a spin crossing takes places at this stage and the global process (**II** to **III**) becomes highly exoergic (44.1 kcal/mol) because the benzyl group recovers the aromatic character.

The formation of the norcaradiene, the addition-product precursor, through **TS_{II,IV}** and the direct formation of the insertion product through the classical hydrogen migration from the phenylic carbon to the benzylic carbon, **TS_{II,V}**, involve energy barriers of 2.9 and 9.4 kcal/mol, respectively. Thus, both **TS_{II,IV}** and **TS_{II,V}** have higher energies than **TS_{II,III}**, which implies that these other two reactions will hardly take place. This result nicely agrees and explains the experimental data, which show that our Fe catalyst presents a clear selectivity for the generation of insertion products. It is worth noticing that, in electronic energy terms, the enol formation barrier is higher than the norcaradiene formation barrier. Then, entropy has a key effect favoring **TS_{II,III}** over **TS_{II,IV}** due to the loose five-membered ring structure of **TS_{II,III}** (see Table S8). When EDA is replaced by 4-Br-phenyldiazoacetate (entry 13 of Table 1), DFT barriers show that the chemoselectivity for the formation of insertion products decreases (see Table S11), in

nice agreement with the experimental data and the reduction of the carbonyl group basicity of **II**.

Both the norcaradiene-formation transition state and the [1,2]-H shift transition state imply the rearrangement reaction and the dissociation of the products formed. In **TS_{II-IV}**, besides the substrate formation, norcaradiene decoordinates from the catalyst (Fe \cdots C_{carb} distance of **IV** is 3.30Å); and, in **TS_{II-V}**, along with the substrate formation and decoordination (Fe \cdots C_{carb} distance of **V** is 3.62Å), the formation of a new adduct between Fe and the oxygen atom of the carbonyl group of insertion products occurs (Fe \cdots O_{carb} distance of **V** is 1.97Å). Despite the Fe \cdots O_{carb} interaction in **IV** and **V** products, iron recovers its Fe²⁺(d⁶) electronic configuration and, since the high spin state is the most stable spin case for [Fe(L1)]²⁺(d⁶), a spin crossing from ³IV(³V) to ⁵IV(⁵V) arises.

The final steps from the norcaradiene intermediate, ⁵IV, to addition products, ⁵VI, or from the enol intermediate, ⁵III, to insertion products, ⁵V, imply low energy barriers. The ring-expansion reaction that gives the final cycloheptatriene product from norcaradiene intermediate involves a 2.6 kcal/mol energy barrier, ⁵TS_{IV-VI}. On the other hand, the enol-ester tautomerism involves a 10.0 kcal/mol energy barrier when it is assisted by two water molecules, ⁵TS_{III-V}. It is interesting to note that the water is essential to decrease the value of ⁵TS_{III-V}, since the equivalent transition state Gibbs energy barrier without water has a value of ca. 46.6 kcal/mol (see Table S9 in the SI). Although water was not added in our experiments, the presence of adventitious water molecules was experimentally detected by the formation of certain amount of ethyl glycolate products.¹²

Most importantly, it must be noted that this mechanism accounts for the results on the isotopic labelling experiments; in first place, the hydrogen atom at the C-H bond that suffers the attack of the carbene moiety can end up at the benzylic position of the product. In addition, the intermediacy of the enol provides a path for the incorporation of hydrogen atoms from water in the final product.

CONCLUSIONS

The mechanism of the recently discovered iron-catalyzed selective functionalization of benzene upon carbene insertion from ethyl diazoacetate has been elucidated. The catalyst precursor [Fe(OTf)₂(L1)] originates an electrophilic iron carbene intermediate that attacks the arene rendering a Wheland type intermediate that can engage in cationic rearrangements. Experimental data supports an electrophilic aromatic substitution behavior. A complementary computational analysis has demonstrated that the exquisite chemoselectivity towards the insertion product is rooted in the evolution of this intermediate via a facile hydrogen atom transfer from the arene to the carbonyl moiety of the carbene, forming an enol intermediate. DFT calculations show that the entropy is the driving force that induces the chemoselectivity of this catalyst for aryl C-H insertion. Isotopic labelling analyses also provide credibility to this mechanism. Overall, the current study provides a mechanistic basis for understanding the unique chemoselectivity exhibited by this type of iron catalysts in carbene transfer reactions.

ASSOCIATED CONTENT

Supporting Information

Experimental procedures and DFT calculations are provided as a single pdf file. Cartesian coordinates of all computed structures are given in a separate text file in xyz format. The Supporting Information is available free of charge on the ACS Publications website.

AUTHOR INFORMATION

Corresponding Authors

josepm.luis@udg.edu; miquel.sola@udg.edu; miquel.costas@udg.edu; perez@dqcm.uhu.es; mmdiaz@dqcm.uhu.es.

Present Addresses

† Institut de Química Computacional i Catàlisi (IQCC) and Departament de Química, Universitat de Girona, Campus Montilivi, 17003 Girona (Spain).

§ Laboratorio de Catálisis Homogénea, Unidad Asociada al CSIC, CIQSO-Centro de Investigación en Química Sostenible and Departamento de Química, Universidad de Huelva, Campus de El Carmen s/n, 21007 Huelva (Spain).

Author Contributions

‡ These authors equally contributed to this work.

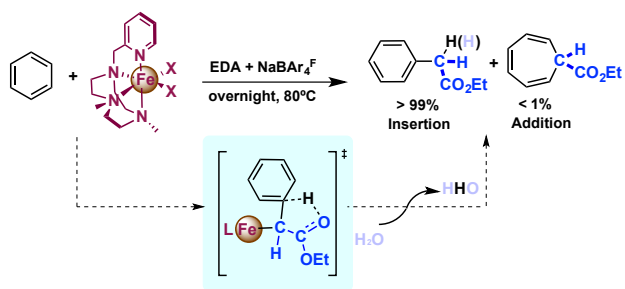
Funding Sources

Support for this work was provided by the MINECO (CTQ2014-62234-EXP, CTQ2014-52769-C3-R-1, CTQ2014-54306-P, CTQ2014-52525-P, and Grant BES-2012-052801 to V.P.), the Junta de Andalucía (P10-FQM-06292) and the Generalitat de Catalunya (Project 2014SGR264, Xarxa de Referència en Química Teòrica i Computacional, ICREA Academia prizes 2013 to M.C. and 2014 to M.S.). The EU under the FEDER grant UNGI10-4E-801 (European Fund for Regional Development) has also funded this research.

REFERENCES

- (1) (a) Cheng, Q.-Q.; Doyle, M. P. *Adv. Organomet. Chem.* **2016**, *66*, 1-31. (b) Thumar, N. J.; Wei, Q. H.; Hu, W. H. *Adv. Organomet. Chem.* **2016**, *66*, 33-91; (c) Caballero, A.; Díaz-Requejo, M. M.; Fructos, M. R.; Olmos, A.; Urbano, J.; Pérez, P. *J. Dalton Trans.* **2015**, *44*, 20295-20307; (d) Fructos, M. R.; Díaz-Requejo, M. M.; Pérez, P. *J. Chem Commun* **2016**, *52*, 7326-7335.
- (2) Buchner, E.; Curtius, T. *Berichte der Dtsch. Chem. Gesellschaft* **1885**, *18*, 2371-2377.
- (3) Anciaux, A. J.; Demonceau, A.; Noels, A. F.; Hubert, A. J.; Warin, R.; Teyssie, P. H. *J. Org. Chem.* **1981**, *46*, 873-876.
- (4) Given that the product obtained corresponds with that in which the carbene group has been inserted into the C-H bond, we refer to this as the insertion product. However, the mechanism of this transformation does not necessarily takes place by an insertion step.
- (5) (a) Rosenfeld, M. J.; Shankar, B. K. R.; Shechter, H. *J. Org. Chem.* **1988**, *53*, 2699-2705. (b) Yang, M.; Webb, T. R.; Livant, P. *J. Org. Chem.* **2001**, *66*, 4945-4949.

- (6) Fructos, M. R.; Besora, M.; Braga, A. A. C.; Díaz-Requejo, M. M.; Maseras, F.; Pérez, P. *J. Organometallics* **2017**, *36*, 172–179.
- (7) (a) Fructos, M. R.; Belderrain, T. R.; de Frémont, P.; Scott, N. M.; Nolan, S. P.; Díaz-Requejo, M. M.; Pérez, P. *J. Angew. Chem. Int. Ed.* **2005**, *44*, 5284–5288. (b) Rivilla, I.; Gómez-Emeterio, B. P.; Fructos, M. R.; Díaz-Requejo, M. M.; Pérez, P. *J. Organometallics* **2011**, *30*, 2855–2860.
- (8) (a) Liu, Y.; Yu, Z.; Luo, Z.-L.; Zhang, J. Z.; Liu, L.; Xia, F. *J. Phys. Chem. A* **2016**, *120*, 1925–1932. (b) Yu, Z.; Ma, B.; Chen, M.; Wu, H.-H.; Liu, L.; Zhang, J. *J. Am. Chem. Soc.* **2014**, *136*, 6904–6907. (c) Xi, Y.; Su, Y.; Yu, Z.; Dong, B.; McClain, E. J.; Lan, Y.; Shi, X. *Angew. Chem. Int. Ed.* **2014**, *53*, 9817–9821.
- (9) (a) Callot, H. J.; Metz, F. *Nov. J. Chem.* **1985**, *9*, 167–171. (b) Davies, H. M. L.; Jin, Q. *Tetrahedron Asymmetry* **2003**, *14*, 941–949. (c) Davies, H. M. L.; Jin, Q.; Ren, P.; Kovalevsky, A. Y. *J. Org. Chem.* **2002**, *67*, 4165–4169. (d) Morilla, M. E.; Díaz-Requejo, M. M.; Belderrain, T. R.; Nicasio, M. C.; Trofimenko, S.; Pérez, P. *J. Organometallics* **2004**, *23*, 293–295.
- (10) (a) Osako, T.; Panicakul, D.; Uozumi, Y. *Org. Lett.* **2012**, *14*, 194–197. (b) Chen, C.; Zhu, S.-F.; Liu, B.; Wang, L.-X.; Zhou, Q.-L. *J. Am. Chem. Soc.* **2007**, *129*, 12616–12617. (c) Xie, X.-L.; Zhu, S.-F.; Guo, J.-X.; Cai, Y.; Zhou, Q.-L. *Angew. Chem. Int. Ed.* **2014**, *53*, 2978–2981. (d) Miura, T.; Zhao, Z.; Murakami, M. *Angew. Chem. Int. Ed.* **2017**, *56*, 16645–16649.
- (11) Rivilla, I.; Sameera, W. M. C.; Alvarez, E.; Díaz-Requejo, M. M.; Maseras, F.; Pérez, P. *J. Dalton Trans.* **2013**, *42*, 4132–4138.
- (12) Conde, A.; Sabenya, G.; Rodríguez, M.; Postils, V.; Luis, J. M.; Díaz-Requejo, M. M.; Costas, M.; Pérez, P. *J. Angew. Chem.* **2016**, *128*, 6640–6644.
- (13) Codolà, Z.; Lloret-Fillol, J.; Costas, M. *Prog. Inorg. Chem.* **2014**, *59*, 447–532.
- (14) (a) For trispyrazolylborate ligands see reference 1c. (b) For trispyrazolylamines see: Haldón, E.; Álvarez, E.; Nicasio, M. C.; Pérez, P. *J. Chem. Commun.*, **2014**, *50*, 8978–8981.
- (15) Company, A.; Gómez, L.; Güell, M.; Ribas, X.; Luis, J. M.; Que, L., Jr; Costas, M. *J. Am. Chem. Soc.* **2007**, *129*, 15766–15767.
- (16) Kulkarni, N. V.; Dash, C.; Jayaratna, N. B.; Ridlen, S. G.; Khani, S. K.; Das, A.; Kou, S.; Yousufuddin, M.; Cundari, T. R.; Dias, H. V. R. *Inorg. Chem.* **2015**, *54*, 11043–11045.
- (17) (a) Doyle, M. P.; Duffy, R.; Ratnikov, M.; Zhou, L. *Chem. Rev.* **2010**, *110*, 704–724. (b) Doyle, M. P.; McKervey, M. A.; Ye, T. *Modern Catalytic Methods for Organic Synthesis with Diazo Compounds*; Wiley: New York, 1998. (c) Davies, H. M. L.; Dick, A. R. *Top. Curr. Chem.* **2009**, *292*, 303–345. (d) Davies, H. M. L.; Manning, J. R. *Nature* **2008**, *451*, 417–424.
- (18) (a) Dzik, W. I.; Xu, X.; Zhang, X. P.; Reek, J. N. H.; de Bruin, B. *J. Am. Chem. Soc.* **2010**, *132*, 10891–10902. (b) Pereira, A.; Champouret, Y.; Martin, C.; Álvarez, E.; Etienne, E.; Belderrain, T. R.; Pérez, P. *J. Chem. Eur. J.* **2015**, *21*, 9769–9775.
- (19) (a) Khade, R. L.; Zhang, Y. *J. Am. Chem. Soc.* **2015**, *137*, 7560–7563. (b) Sharon, D. A.; Mallick, D.; Wang, B.; Shaik, S. *J. Am. Chem. Soc.* **2016**, *138*, 9597–9610.
- (20) (a) Liu, Y.; Xu, W.; Zhang, J.; Fuller, W.; Schulz, C. E.; Li, J. *J. Am. Chem. Soc.* **2017**, *139*, 5023–5026. (b) Khade, R. L.; Fan, W.; Ling, Y.; Yang, L.; Oldfield, E.; Zhang, Y. *Angew. Chem. Int. Ed.* **2014**, *53*, 7574–7578. (c) Li, Y.; Huang, J.-S.; Zhou, Z.-Y.; Che, C.-M.; You, X.-Z. *J. Am. Chem. Soc.* **2002**, *124*, 13185–13193.
- (21) Weinhold, F.; Landis, C. R. *Valency and bonding: a natural bond orbital donor-acceptor perspective*; Cambridge University Press: Cambridge, U.K., **2005**.
- (22) (a) Ramos-Cordoba, E.; Postils, V.; Salvador, P. *J. Chem. Theory Comput.* **2015**, *11*, 1501–1508. (b) Skara, G.; Gimferrer, M.; De Prof, F.; Salvador, P.; Pinter, B. *Inorg. Chem.* **2016**, *55*, 2185–2199.
- (23) Johnson, E. R.; Keinan, S.; Mori-Sánchez, P.; Contreras-García, J.; Cohen, A. J.; Yang, W. *J. Am. Chem. Soc.*, **2010**, *132*, 6498–6506.
- (24) Luga, N.; Fernández, I.; Brousses, R.; Valyaev, D. A.; Lavigne, G.; Ustynyuk, N. A.; Antipin, M. Y.; Ustynyuk, N. A. *Dalton Trans.* **2013**, *42*, 898–901.
- (25) (a) Padwa, A.; Austin, D. J.; Price, A. T.; Semones, M. A.; Doyle, M. P.; Protopopova, M. N.; Winchester, W. R.; Tran, A. *J. Am. Chem. Soc.* **1993**, *115*, 8669–8680. (b) Liu, Y.; Yu, Z.; Zhang, J. Z.; Liu, L.; Xia, F.; Zhang, J. *Chem. Sci.* **2016**, *7*, 1988–1995.
- (26) (a) Braga, A. A. C.; Maseras, F.; Urbano, J.; Caballero, A.; Díaz-Requejo, M. M.; Pérez, P. *J. Organometallics* **2006**, *25*, 5292–5300. (b) Nakamura, E.; Yoshikai, N.; Yamanaka, M. *J. Am. Chem. Soc.* **2002**, *124*, 7181–7192. (b) Bouloutakis-Arapinis, M.; Gandon, V.; Prost, E.; Micouin, L.; Lecourt, T. *Adv. Synth. Catal.* **2014**, *356*, 2493–2505.
- (27) (a) Yamaguchi, K.; Jensen, F.; Dorigo, A.; Houk, K. N. *Chem. Phys. Lett.* **1988**, *149*, 537–542. (b) Wittbrodt, J. M.; Schlegel, H. B. *J. Chem. Phys.* **1996**, *105*, 6574–6577.
- (28) (a) Jensen, K. P.; Ryde, U. *J. Phys. Chem. A* **2003**, *107*, 7539–7545. (b) Kuta, J.; Patchkovskii, S.; Zgierski, M. Z.; Kozłowski, P. M. *J. Comput. Chem.* **2006**, *27*, 1429–1437. (c) Qi, X.-J.; Li, Z.; Fu, Y.; Guo, Q.-X.; Liu, L. *Organometallics* **2008**, *27*, 2688–2698.
- (29) (a) Swart, M.; Groenhof, A. R.; Ehlers, A. W.; Lammertsma, K. *J. Phys. Chem. A* **2004**, *108*, 5479–5483. (b) Güell, M.; Solà, M.; Swart, M. *Polyhedron* **2010**, *29*, 84–93.
- (30) (a) Cohen, A. J.; Mori-Sánchez, P.; Yang, W. *Chem. Rev.* **2012**, *112*, 289–320. (b) Mangiatordi, G. F.; Brémond, E.; Adamo, C. *J. Chem. Theory Comput.* **2012**, *8*, 3082–3088.



Chapter 5

Computational determination of OSs

5.1 Reaching the new IUPAC definition of oxidation state by computational techniques

Postils, V.; Delgado-Alonso, C.; Luis, J.M.; Salvador, P. **Reaching the new IUPAC definition of oxidation state by computational techniques**, submitted to *Angew. Chem. Int. Ed.*

Embargoed until publication date

Postils, V.; Delgado-Alonso, C.; Luis, J.M.; Salvador, P. Reaching the new IUPAC definition of oxidation state by computational techniques. Manuscript submitted for publication

Abstract

Are quantum chemistry methods up to the challenge to match with the definition of oxidation state? The term has been recently revised by the IUPAC, providing a more general and unambiguous definition based upon the ionic approximation (IA). In spite of this, there are a number of caveats and unanswered questions when it comes to the practical application of the IA. Our comprehensive study using the so-called effective oxidation state (EOS) analysis reveals that the chemical environment of the atoms is quintessential, and determines the direction of the electron count beyond their intrinsic electronegativities. The EOS approach successfully predicts the OS of most of the analyzed chemical systems *without* any special input, including difficult and controversial cases, as it is shown here for high oxidation states transition metal (TM) complexes, Lewis acid-base and π -adducts, noninnocent ligands or TM carbenes. The fundamental role of the local spin state of the π -system in π -adducts and its effect upon the oxidation state of the metal center has been recognized here for the first time. The limitation of the current principles of the IA have been further illustrated with transition metal carbene complexes, for which the EOS method performs well. The IA supported on Allen's electronegativity could be essentially utilized without exceptions by considering the principle of identifying subsystems of enhanced stability (SES) within the molecular system prior to its application. An alternative beyond general rules and principles is to fully rely on quantum mechanical approaches such as EOS analysis.

Chapter 6

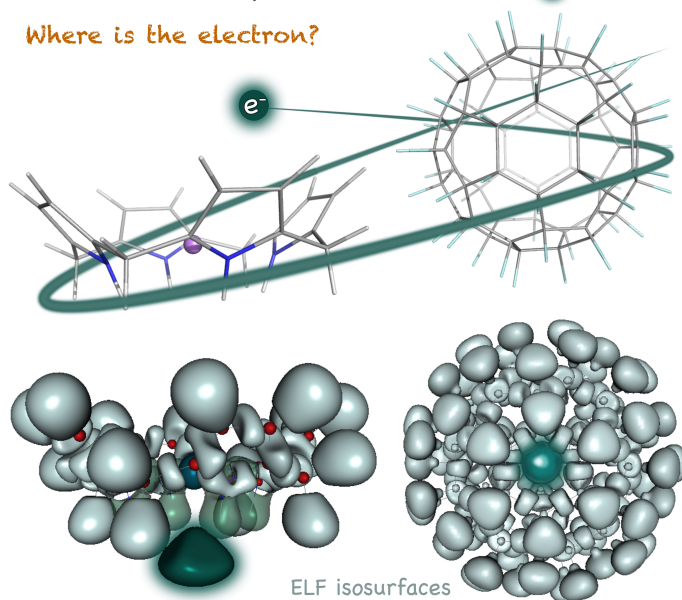
Theoretical characterization of molecular electrides

6.1 On the existence and characterization of molecular electrifies

Molecular Electrides

Ionic Compounds: [Molecule · e⁻]

Where is the electron?



Postils, V.; Garcia-Borràs, M.; Solà, M.; Luis, J.M.; Matito, E. **On the existence and characterization of molecular electrifies.** *Chem. Commun.* **2015**, 51, 4865-4868. DOI: 10.1039/c5cc00215j.

Reproduced with permission from:

Postils, V.; Garcia-Borras, M.; Sola, M.; Luis, J.M.; Matito, E. On the existence and characterization of molecular electrides. Chem. Commun. 2015, 51, 4865-4868.

<http://dx.doi.org/10.1039/c5cc00215j>

Copyright © 2015 Royal Society of Chemistry

Cite this: *Chem. Commun.*, 2015, 51, 4865Received 9th January 2015,
Accepted 12th February 2015

DOI: 10.1039/c5cc00215j

www.rsc.org/chemcomm

On the existence and characterization of molecular electrides†

Verònica Postils, Marc Garcia-Borràs, Miquel Solà, Josep M. Luis* and Eduard Matito*

Electrides are ionic compounds thus far appearing in the solid state, where the anionic part is constituted by isolated electrons. We herein provide an unambiguous computational means to distinguish electrides from similar species, proving the existence of some electrides in the gas phase. We also put forward a recipe to design new electrides.

Electrides are among the most intriguing species lately discovered. These ionic compounds, postulated and synthesized by J. L. Dye,^{1–4} have electrons occupying the anionic positions of solid compounds. They eluded room temperature stability until the group of Hosono produced $[\text{Ca}_{24}\text{Al}_{28}\text{O}_{68}]4\text{e}^-$, the first stable electride.^{5,6} Thereupon, these compounds have found a plethora of applications,^{7–10} ranging from an electron emitter¹¹ to a reversible H_2 storage device.¹² Perhaps the most fascinating realization of an electride is the transformation of mayenite, a component of alumina cement, first into an electride and then into an electric conductor.^{7,13} Despite many attempts just ten electrides have been synthesized,^{4,5,9} only three of them being stable at room temperature. The density of the free electrons in electrides is not large enough to be located in the X-ray of the crystal structure and its experimental characterization can only be achieved from indirect evidence.^{14–16} Thus far, only a few studies attempted the analysis of the electronic structure of these compounds and none featured the possibility of electrides beyond the solid lattice, where the electron is hosted in an empty cavity.^{17,18} Different computational techniques were used to characterize electrides, but none presented a tool to unambiguously differentiate electrides from other similar species. For instance, electrides were shown to exhibit large nonlinear optical properties (NLOPs),^{19–21} and have non-nuclear attractors (NNAs) of the electron density^{9,18} and even electron localization function (ELF) basins.^{9,22} However, other molecules show these properties without the

presence of an isolated electron. This work has a twofold purpose: to show that *molecular electrides* can exist and to provide a means to characterize and distinguish them from other similar species, thus contributing to the design of new electrides. Finally, we will analyze whether electride's structure truly consists of an isolated electron or it is actually just a formal picture to represent these molecules.

We will address seven molecules that have been previously labeled as electrides and can be classified into three different groups: (i) *push electrides*, where electron donor groups push the electrons away from an alkali metal: tetracyanoquinodimethane (TCNQ) derivatives TCNQLi₂ and TCNQNa₂,²³ Li@calix[4]pyrrole^{20,24} and Li··NCH₂²⁵; (ii) *pull electrides*, where electron withdrawing groups pull the electrons away from an alkali metal: Li@B₁₀H₁₄ (ref. 26) and Li··HCN,²⁵ and (iii) *non-alkali electrides*, where the electride structure holds an extra electron without the presence of a nearby alkali metal: e-@C₆₀F₆₀.²¹ All these molecules show large NLOPs,¹⁹ delocalized diffuse excess electrons on high-lying occupied orbitals and, therefore, they were previously characterized as electrides.^{20,21,23,25,26} To study these compounds, *ab initio* calculations at the B3LYP level with split-valence double-zeta basis sets augmented with polarization and diffuse functions have been performed in conjunction with quantum theory of atoms in molecules (QTAIM)²⁷ and ELF analyses²⁸ (see ESI† for details).^{29–33} All the molecules presented in this work show ionization potentials above 3.82 eV (ESI†). The characterization of an electride will be performed using three different criteria that are consistent with the presence of an isolated electron: the existence of a NNA, an ELF basin, and negative values of the Laplacian of the electron density ($\nabla^2\rho$). NNAs are maxima of the electron density at points distinct from nuclear positions; ELF basins are molecular regions with highly localized electrons; and $\nabla^2\rho$ basins were proposed as physical bases for the valence-shell electron-pair repulsion (VSEPR) model.²⁷ Some of these criteria have been used in the past to characterize electrides,^{9,18,22} but the occurrence of only one criterion is not a sufficient condition to assess the presence of an electride. Indeed, NNAs and negative values of the Laplacian are found in species such as C₂H₂,³⁴ ELF basins are usually present in valence

Institut de Química Computacional i Catàlisi (IQCC), and Departament de Química, Univ. Girona, Campus de Montilivi s/n, Girona, Spain. E-mail: josepm.luis@udg.edu, ematito@gmail.com; Tel: +34 972 418 357

† Electronic supplementary information (ESI) available: Full analysis of the molecules, computational details and methodology validation. See DOI: 10.1039/c5cc00215j

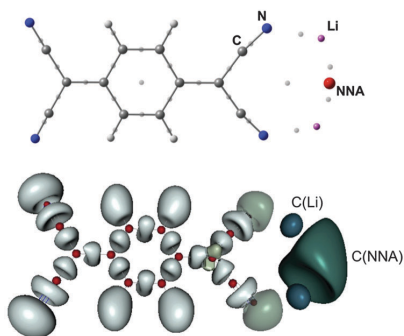


Fig. 1 QTAIM topological analysis (top) and ELF = 0.75 (bottom) representations of TCNQLi₂.

regions of molecules such as HCN, while systems like polydiacetylene show large NLOPs. None of these molecules is an electrider and, therefore, none of the mentioned criteria by itself is valid to unambiguously characterize an electrider. Yet electrideres usually show some of these properties.^{9,18} Do electrideres need to fulfill all these criteria or only a small subset of them?

The first molecules subjected to analysis are TCNQLi₂ and TCNQNa₂. These molecules contain the TCNQ moiety, which acts as an electron acceptor in a number of charge-transfer complexes. The two alkali metals are close to the nitrogen lone pairs that push electron density from the metals, giving rise to an isolated electron hold by the electrostatic forces exerted by two positively-charged metals (see Fig. 1). The QTAIM analysis of TCNQLi₂ shows a NNA between both Li core basins with a negative value of $\nabla^2\rho$. There are 0.7 electrons in the NNA basin (68% of them completely localized in this region) and an ELF basin between the metals with 0.89 electrons. These data clearly indicate the presence of an isolated electron between the lithium atoms. This situation is reminiscent of Li₂, where a NNA is also located in the center of the bond, there is an ELF basin and the molecule exhibits a large second hyperpolarizability.^{35,36} In this sense, TCNQLi₂ could be regarded as a molecular realization of Li₂, which is a strong electrophile and, therefore, difficult to handle. TCNQNa₂ analysis provides a similar picture. These results are confirmed by more accurate calculations at the MP2 and CISD levels of theory. The details of these calculations and the analogous analysis of the TCNQNa₂ species are included in the ESI.†

Li@calix[4]pyrrole (Fig. 2) possesses a cup-shaped structure with a lithium atom lying in the narrowest region of the cup. The lone pairs of the nitrogen atoms of the pyrrole rings push the electron

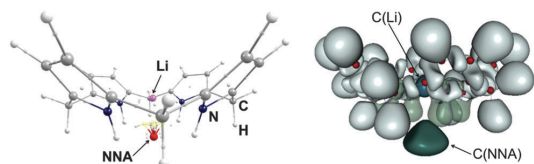


Fig. 2 QTAIM topological analysis (left) and ELF = 0.75 (right) representations of Li@calix[4]pyrrole.

away from the alkali metal, leading to an electrider-like structure. This picture is corroborated by the finding of a NNA and an ELF basin below the lithium region, where there is also a negative Laplacian value. However, the electron numbers of these basins (0.17 e and 0.51 e, respectively) are not fully consistent with the formal electrider structure of almost one electron isolated from the rest of the molecules. Furthermore, the electron density on this region is quite delocalized, with only 0.02 and 0.34 electrons localized in the NNA region and the ELF basins, respectively.

Li@B₁₀H₁₄ is formed by a nido boron hydride cluster with a lithium atom on top of the open cavity (see Fig. 3). The mechanism to hold the alkali metal is the complete opposite of that used for previous molecules. The electron-deficient decaborane cluster exerts an attractive force on the electron density of the lithium that pulls the electron away from the alkali and holds it encapsulated in the box. This picture suggests that a NNA and an ELF basin should be located in the center of the cage but none is found. The analysis of the Laplacian of the electron density does not reveal any important contributions either. Therefore, we cannot characterize this molecule as an electrider despite the large values of the first hyperpolarizabilities reported.²⁶ The latter is due to the highly delocalized nature of this molecule, which has up to 36% of its electron density delocalized, including the four uppermost hydrogen atoms of the cluster that delocalize 0.5 e between them or towards the lithium atom.

Hydrogen cyanide can interact with a lithium atom from both ends of the molecule to give Li···HCN and Li···NCH (see Fig. 4). The latter was suggested as a push-electrider, where the lone pair of nitrogen atoms plays the usual role in pushing electrons away from lithium, generating an isolated electron at one extreme of the molecule.²⁵ Li···HCN was also predicted to have an electrider-like structure, but as a result of the opposite mechanism: the internal polarization of hydrogen cyanide induces a partial positive charge over the hydrogen atom that can withdraw electron charge from lithium, giving rise to an isolated electron between HCN and the alkali metal. The QTAIM analysis does not reveal any NNA for either species but the ELF analysis found valence basins in the proximity of lithium. However, these basins remain so close to lithium that they can be barely considered anything else than the lithium valence itself. The examination of the Laplacian of the electron density leads to the same conclusions drawn from the ELF study. Therefore, the analyses describe these molecules as lithium atoms perturbed by

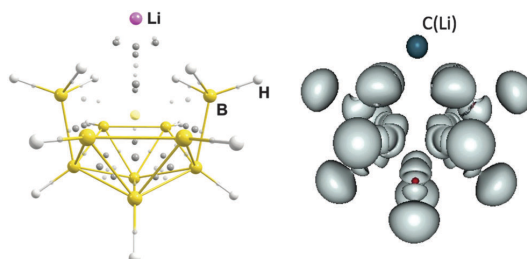


Fig. 3 QTAIM topological analysis (left) and ELF = 0.75 (right) representations of Li@B₁₀H₁₄.

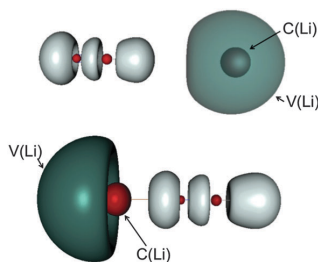


Fig. 4 ELF = 0.75 representations of Li...HCN (top) and Li...NCH (bottom) molecules.

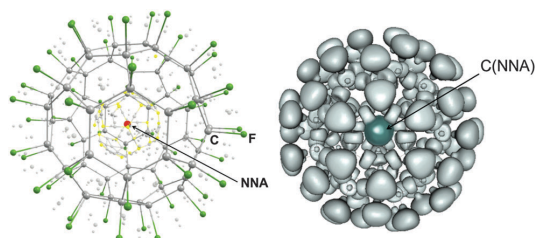


Fig. 5 QTAIM topological analysis (left) and ELF = 0.75 (right) representations of $e^-@C_{60}F_{60}$.

the presence of hydrogen cyanide, a picture that by no means is consistent with an electride as it was previously suggested.²⁵

Finally, we will analyze the only *non-alkali electride* reported,²¹ which is not constructed by pulling or pushing electrons from alkali metals. $e^-@C_{60}F_{60}$ (Fig. 5) consists of a $C_{60}F_{60}$ cage with sufficient interior attractive potential to host an electron inside. We have performed additional calculations to assess the validity of this statement (ESI†). The topological analysis shows a NNA in the center of the cage and the corresponding ELF basin. These basins accommodate 0.19 electrons. The electronic structure of $C_{60}F_{60}^-$ is consistent with an electride-like molecule but it cannot be considered a formal one-electron electride. The analysis of the Laplacian of the electron density corroborates this hypothesis, giving negative values in the center of the cage. These results have been reproduced with different basis sets, ruling out the possibility of a basis set artifact (ESI†).

The results reported in this communication support the existence of gas-phase molecular electrides, thus extending the possibility of this species beyond the lattice. Only TCNQ-based molecules can be presented as *formal electrides*, with almost one electron isolated. Pyrrole-calixarenes and polarized hollow structures have also electronic features consistent with electrides, but their NNA basins contain far less than one electron. Thus these chemical systems may also be classified as electride-like molecules and are candidates to design new electrides. Table 1 summarizes these findings and reveals the criteria to identify electrides.

All the molecules studied in this manuscript were previously considered to be electrides on the basis of large NLOPs and

Table 1 Summary of the criteria used to characterize electrides in this study

	NLOP	NNA	$\nabla^2\rho$	ELF	Electride
TCNQLi ₂	✓	✓	✓	✓	✓
TCNQNa ₂	✓	✓	✓	✓	✓
Li@calix[4]pyrrole	✓	✓	✓	✓	✓
Li@B ₁₀ H ₁₄	✓	×	×	×	×
$e^-@C_{60}F_{60}$	✓	✓	✓	✓	✓
Li...HCN	✓	×	✓ ^a	✓ ^a	×
HCN...Li	✓	×	✓ ^a	✓ ^a	×
Li ₂	✓	✓ ^a	✓ ^a	✓ ^a	✓
C ₂ H ₂	×	✓ ^a	✓ ^a	✓ ^a	×

^a These molecules show NNA, $\nabla^2\rho$ or ELF basins in the close vicinity of an atom and, therefore, the isolated nature of the electron is dubious.

frontier orbitals with large density values in the vicinity of the position where one would expect the isolated electron of the electrides. However, we have shown here that some of them are actually not electrides. The presence of a NNA, an ELF basin or negative values of the Laplacian of the electron density are necessary conditions to assert the existence of an isolated electron. Nevertheless, molecules such as C₂H₂, with a NNA or the ELF basin close to an atomic position, put forward that these conditions might not be always sufficient to assess the presence of an electride. In this respect, large NLOPs can be used together with the latter conditions to confirm the true electride nature of a given species.

NNA is not a frequent feature of molecular densities. Therefore, one could design an electride by prompting the occurrence of a NNA using the data of Pendás and coworkers,³⁴ who analyzed the range of diatomic distances at which several dimers show a NNA. The TCNQ actually plays a role in stabilizing Li₂ and Na₂ molecules at a favorable distance where the NNA appears. We hope that our results will motivate further research on this fascinating species and the development of new electrides with compelling applications.

This research has been funded by the EU under the Marie Curie Career Integration grant PCI09-GA-2011-294240 (E.M.), the Spanish MINECO Europa Excelencia project CTQ2013-41236-ERC (E.M.), the Spanish MICINN Project No. CTQ2011-23156/BQU the FEDER grant UNGI08-4E-003 (European Fund for Regional Development), the Generalitat de Catalunya (project number 2014SGR931, Xarxa de Referència en Química Teòrica i Computacional, and ICREA 2014 prize to M.S.) and the predoctoral fellowships AP2010-2517 (M.G.-B.) and BES-2012-052801 (V.P.). Excellent service by the Centre de Serveis Científics i Acadèmics de Catalunya (CESCA) is gratefully acknowledged.

References

- J. L. Dye, *Science*, 1990, **247**, 663–668.
- J. L. Dye and M. G. DeBacker, *Annu. Rev. Phys. Chem.*, 1987, **38**, 271–299.
- J. L. Dye, *Science*, 2003, **301**, 607–608.
- J. L. Dye, *Acc. Chem. Res.*, 2009, **42**, 1564–1572.
- S. Matsuishi, Y. Toda, M. Miyakawa, K. Hayashi, T. Kamiya, M. Hirano and I. Tanaka and H. Hosono, *Science*, 2003, **301**, 626–629.
- Y. Toda, Y. Kubota, M. Hirano, H. Hirayama and H. Hosono, *ACS Nano*, 2011, **5**, 1907–1914.

- 7 S. W. Kim, T. Shimoyama and H. Hosono, *Science*, 2011, **333**, 71–74.
- 8 H. Buchhammagari, Y. Toda, M. Hirano, H. Hosono, D. Takeuchi and K. Osakada, *Org. Lett.*, 2007, **9**, 4287–4289.
- 9 K. Lee, S. W. Kim, Y. Toda, S. Matsuishi and H. Hosono, *Nature*, 2013, **494**, 336–340.
- 10 H. Yanagi, T. Kuroda, K.-B. Kim, Y. Toda, T. Kamiya and H. Hosono, *J. Mater. Chem.*, 2012, **22**, 4278–4281.
- 11 Y. Toda, H. Yanagi, E. Ikenaga, J. J. Kim, M. Kobata, S. Ueda, T. Kamiya, M. Hirano, K. Kobayashi and H. Hosono, *Adv. Mater.*, 2007, **19**, 3564–3569.
- 12 M. Kitano, Y. Inoue, Y. Yamazaki, F. Hayashi, S. Kanbara, S. Matsuishi, T. Yokoyama, S.-W. Kim, M. Hara and H. Hosono, *Nat. Chem.*, 2012, **4**, 934–940.
- 13 P. P. Edwards, *Science*, 2011, **333**, 49–50.
- 14 J. L. Dye, *Nature*, 1993, **365**, 10–11.
- 15 D. J. Singh, H. Krakauer, C. Haas and W. E. Pickett, *Nature*, 1993, **365**, 39–42.
- 16 J. L. Dye, *Inorg. Chem.*, 1997, **36**, 3816–3826.
- 17 M.-S. Miao and R. Hoffmann, *Acc. Chem. Res.*, 2014, **47**, 1311–1317.
- 18 S. G. Dale, A. Otero-de-la Roza and E. R. Johnson, *Phys. Chem. Chem. Phys.*, 2014, **16**, 14584–14593.
- 19 M. García-Borràs, M. Solà, J. M. Luis and B. Kirtman, *J. Chem. Theory Comput.*, 2012, **8**, 2688–2697.
- 20 W. Chen, Z.-R. Li, D. Wu, Y. Li, C.-C. Sun and F. L. Gu, *J. Am. Chem. Soc.*, 2005, **127**, 10977–10981.
- 21 Y.-F. Wang, Z.-R. Li, D. Wu, C.-C. Sun and F.-L. Gu, *J. Comput. Chem.*, 2010, **31**, 195–203.
- 22 M. Marqués, G. J. Ackland, L. F. Lundegaard, G. Stinton, R. J. Nelmes, M. I. McMahon and J. Contreras-García, *Phys. Rev. Lett.*, 2009, **103**, 115501.
- 23 Z.-J. Li, F.-F. Wang, Z.-R. Li, H.-L. Xu, X.-R. Huang, D. Wu, W. Chen, G.-T. Yu, F. L. Gu and Y. Aoki, *Phys. Chem. Chem. Phys.*, 2009, **11**, 402–408.
- 24 W. Chen, Z.-R. Li, D. Wu, Y. Li, C.-C. Sun, F. L. Gu and Y. Aoki, *J. Am. Chem. Soc.*, 2006, **128**, 1072–1073.
- 25 W. Chen, Z.-R. Li, D. Wu, R.-Y. Li and C.-C. Sun, *J. Phys. Chem. B*, 2005, **109**, 601–608.
- 26 S. Muhammad, H. Xu, Y. Liao, Y. Kan and Z. Su, *J. Am. Chem. Soc.*, 2009, **131**, 11833–11840.
- 27 R. F. W. Bader, *Atoms in Molecules: A Quantum Theory*, Oxford Univ. Press, Oxford, 1990.
- 28 A. D. Becke and K. E. Edgecombe, *J. Chem. Phys.*, 1990, **92**, 5397–5403.
- 29 E. Matito, M. Solà, P. Salvador and M. Duran, *Faraday Discuss.*, 2007, **135**, 325–345.
- 30 T. A. Keith, *AIMAll (Version 14.11.23)*, TK Gristmill Software, Overland Park KS, USA, 2014, (aim.tkgristmill.com).
- 31 E. Matito, *ESI-3D: Electron Sharing Indices Program for 3D Molecular Space Partitioning*, Institute of Computational chemistry and Catalysis, University of Girona, Catalonia, Spain, 2014.
- 32 S. Noury, X. Krokidis, F. Fuster and B. Silvi, *TopMoD package*, 1997.
- 33 E. Matito, M. Duran and M. Solà, *J. Chem. Phys.*, 2005, **122**, 014109.
- 34 A. M. Pendás, M. A. Blanco, A. Costales, P. M. Sánchez and V. Luaña, *Phys. Rev. Lett.*, 1999, **83**, 1930–1933.
- 35 C. Gatti, P. Fantucci and G. Pacchioni, *Theor. Chem. Acc.*, 1987, **72**, 433–458.
- 36 J. Cioslowski, *J. Phys. Chem.*, 1990, **94**, 5496–5498.

Chapter 7

Results and Discussion

In this chapter, the main achievements of this thesis are briefly discussed. The reading of the articles reported in previous chapters is recommended since in this summary just the most interesting aspects of each study are highlighted.

As already stated in the introduction, and following F. Jensen quote about what chemistry is, the studies carried out during this thesis can be divided into three different blocks: transformation, properties, and construction of molecules. Thus, this chapter is also divided in the corresponding sections. In the first section (*transformation of molecules*), the main achievements obtained from studies about the functionalization of C-H bonds of hydrocarbons through iron catalysts are summed up (matches with [chapter 4](#)). In the second section (*properties of molecules*), the improvements in the theoretical characterization of oxidation states proved by the critical assessment of the performance of the EOS method are specified (matches with [chapter 5](#)). Finally, in the third section (*construction of molecules*), the main goals reached within the description of the electron distribution feature in challenging molecules, *i.e.* electriles, are emphasized (matches with [chapter 6](#)).

7.1 Functionalization of C-H bonds of hydrocarbons by iron catalysts

Both reactivity studies addressed in this thesis deal with iron catalysts, specifically with the [(PyTACN)FeX₂] catalyst (where X=Cl or OTf) and its activated forms.

Without doubt, the majority of the studies in organometallic catalysis are based on precious metals such as palladium, rhodium, iridium, and ruthenium. However, due to the limited availability of these metals as well as their high price³³⁵ and, sometimes, significant toxicity, there is an interest to search for more economical and environmentally friendly alternatives. In this respect, homogeneous catalysis with iron complexes offers a highly attractive option. Despite homogeneous iron catalysis has already a long history, a look into the common chemical databases shows that this field has become a central research area only in the last decades, in agreement with the exponential rise in the number of publications after the turn of the millennium.^{336–339} The publications reported in Chapter 4 of this thesis are in line with this current scenario.

The highlighted results reported below belong to two different iron-catalyst reactivities: i) the highly studied hydroxylation of alkanes by means of iron-oxo catalysts (subsection 7.1.1); and ii) the just recently reported chemoselective carbene-insertion reaction into aromatic C-H bonds by iron-carbene catalysts (subsection 7.1.2).

7.1.1 Effects of the substrate and solvent in the alkane hydroxylation mechanism. The nonheme [(PyTACN)Fe^V]²⁺ complex case study.

This subsection is based on the contents of the manuscript by Postils *et al.* *Inorg. Chem.* **2015**, 54, 8223-8236, which can be found in section 4.1 of this thesis (ref. 104).

The widely accepted mechanism of alkane hydroxylation processes (AHPs) catalyzed by biomimetic Fe(IV)=O and Fe(V)=O catalysts is the already described Groves' or rebound mechanism (see Figure 1.11). However, among computational studies in literature, several reaction mechanisms that differ among them can be found, the origin of their variability is not completely understood.^{107,340–342} Figure 7.1 summarizes all reaction mechanisms for AHPs postulated in literature, together with other reaction paths that we studied in ref. 104.

The classical rebound mechanism, depicted by the central path in Figure 7.1, consists in an initial hydrogen atom transfer (HAT) reaction that forms an alkyl radical intermediate which further reacts with one hydroxyl group of the catalyst to form the final hydroxylated products. Figure 7.1 also shows other proposed mechanisms, such as the direct formation of the hydroxylated products by a concerted highly asynchronous mechanism where the HAT transition state is the sole barrier (above reaction path), or a cationic mechanism, where an initial **hydride** abstraction leads to a cationic alkyl intermediate, which will undergo the final

7.1 FUNCTIONALIZATION OF C-H BONDS BY IRON CATALYSTS

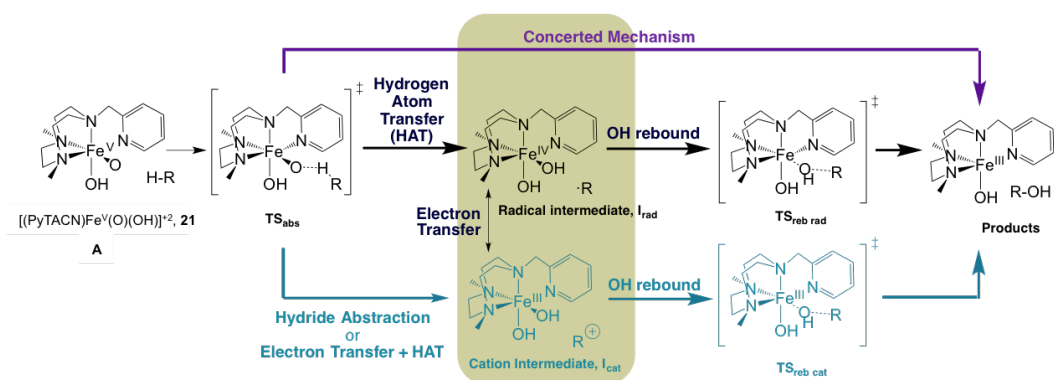


Figure 7.1: Postulated reaction mechanisms for AHPs. Catalyst **21**, represented in the scheme, is the one studied in this thesis.

hydroxyl rebound to form hydroxylated products. All possible electron transfer (ET) processes that have been taken into account in ref. 104 are also represented.

It is worth highlighting that the main difference between all pathways suggested in the previous scheme lies on the stability and the electronic structure of the intermediate species (I_{rad} vs. I_{cat} vs. \emptyset). Thus, the study of this iron-bishydroxyl + alkyl intermediate was the starting point to clarify substrate effects into the mechanism.

Computational insights of the substrate effect into the mechanism of alkane hydroxylation

Table 7.1 includes the main results regarding intermediate stability in solvent. We studied four substrates with different types of carbon atoms, namely, methane, ethane (primary carbon atoms), cyclohexane (secondary carbon atoms), and 2,3-dimethylbutane (2,3-DMB) (tertiary carbon atoms); and we also considered all the possible multiplicities.

S=	electronic configuration		ΔG_{solv} (kcal/mol)			
	iron	substrate	methane	ethane	cyclohexane	2,3-DMB
1/2	I_{cat} C		---	9.66	10.38	---
	I_{rad} B		0.00	8.86	23.28	---
3/2	I_{cat} C		---	9.34	9.52	10.52
	I_{rad} B		1.12	9.75	22.7	34.55
5/2	I_{cat} C		---	0.00	0.00	0.00
	I_{rad} B		6.55	---	---	---

Table 7.1: Relative Gibbs Energies (ΔG_{solv} , in kcal/mol) for radical and cation iron-bishydroxo intermediates.

Table 7.1 clearly shows two different trends: while the most stable methyl intermediates have radical electronic structures, the most stable intermediates

of the other analyzed substrates share cationic configurations. Moreover, stable cationic structures were not localized on methyl intermediates and, regarding the other substrates, stable radical intermediates were not localized on some spin states. When a given intermediate form was not located, its geometry optimization always directly yielded to the formation of the alcohol products.

Based on previous thermodynamic data (Table 7.1), none of the postulated reaction mechanisms for AHPs reported in Figure 7.1 could be completely ruled out, despite some mechanisms could really be discarded by some spin states (*e.g.* stepwise mechanism with a radical intermediate by $S=5$ spin states for ethane, cyclohexane, and 2,3-DMB). Thus, kinetic studies to clarify the reactivity were mandatory.

Kinetic studies exhibited that, for all substrates, the energy demand of an initial HAT was lower than the energetic cost of the ET between the substrate and the catalyst **21** (*i.e.*, the HAT process is favored over the hydride abstraction or the electron transfer previous the HAT process). Intrinsic reaction coordinate (IRC) calculations showed that HAT reactions led to a radical intermediate for all substrates in the ground spin state (quartet). These mechanistic results are consistent with the fact that radical intermediates of the quartet spin state were characterized for all the substrates. Thus, despite the differences between the thermodynamic stability of the iron-bishydroxo + alkyl intermediates of the analyzed substrates, they share the same reactivity for the initial step of the AHP. However, the thermodynamic stability of the intermediate that is formed, does really affect the energy barrier of the HAT process, and trends and correlations can be established. For example:

- The energy barriers of the HAT process follow the Bell-Evans-Polanyi principle. Thus, the differences in the activation free energy of the HAT reaction (ΔG_{HAT}^\ddagger) between substrates are proportional to the differences of their reaction free energy: $\Delta G_{A \rightarrow Irad}$, in this instance. Then, the stability of \mathbf{I}_{rad} versus **A** influences the energy barrier of the HAT process, which is the TOF-determining transition state (TDTS)^{343,344} of the hydroxylation mechanism.
- The Gibbs energy barrier of the HAT reaction (ΔG_{HAT}^\ddagger) also concurs with the strength of the broken C-H bond. This correlates with the fact that the highest ΔG_{HAT}^\ddagger was found for methane, which has the strongest C-H bond, and then lower free energy barriers were found following the order ethane > cyclohexane > 2,3-DMB.
- In turn, binding dissociation energies of C-H bonds are also in part determined by the free radical (or cationic) stability of their alkyl form, that follows the order methyl < primary carbon < secondary carbon < tertiary carbon.
- Furthermore, the stability of radical or cationic alkyl forms also show a good correlation with the ionization energy of the substrates, which, consequently, also shows a good linear trend with the HAT energy barriers.

To complete the assessment of the substrate effects on the alkane hydroxylation mechanism mediated by iron-oxo catalysts, the formation of the final hydroxylated products from the radical intermediate was also studied. Again,

7.1 FUNCTIONALIZATION OF C-H BONDS BY IRON CATALYSTS

taking into account \mathbf{I}_{rad} and \mathbf{I}_{cat} stabilities reported in Table 7.1, we considered two reactions: the direct hydroxyl rebound and an electron transfer process from \mathbf{I}_{rad} to \mathbf{I}_{cat} before the OH rebound.

Similar results were obtained for all substrates: the ET process, analyzed with the use of Marcus theory,^{317–319} was discarded because the OH rebound is always kinetically more favorable than the ET.

For the rebound study, we took into account two spin multiplicities (doublet and quartet) and the hydroxyl rebound with the two *cis* hydroxyls of the catalyst ($t\text{NCH}_2$ and $t\text{NCH}_3$). Sextuplet multiplicity was not studied in this step according to the results obtained in the HAT reaction. Regarding the doublet-quartet spin crossing at \mathbf{I}_{rad} intermediates, despite the minimum-energy crossing point (MECP) was always clearly lower in energy than the energy needed to surmount the barriers of the OH rebound process, the changes between the \mathbf{I}_{rad}^2 and \mathbf{I}_{rad}^4 spin densities occur in the radical carbon of the substrate, which implies a low spin-orbit coupling term for the spin-crossing transition integral that forbids the transition. Thus, the spin crossing is not possible and the hydroxyl rebound will take place at the quartet multiplicity. Regarding the hydroxyl rebound of the two *cis* ligands, the energy differences between both rebounds are within the limits of precision of the used DFT approach and the results should be taken with some caution (Figure 7.2).

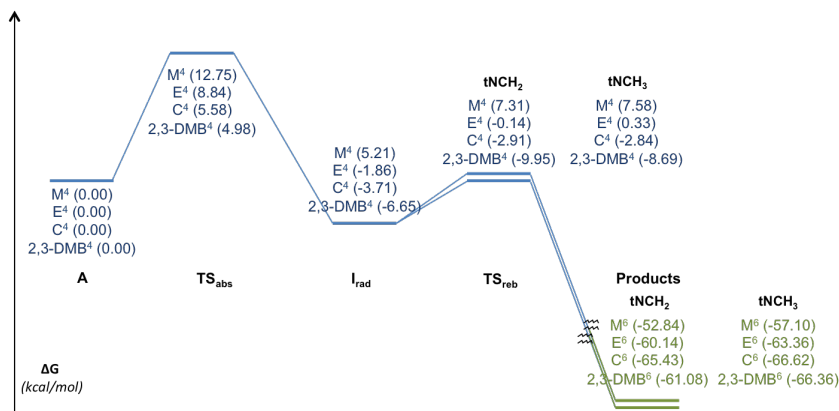


Figure 7.2: Gibbs energy profile (in kcal/mol) of the alkane hydroxylation process for the different analyzed substrates by 21. Only the ground state for each substrate and reaction intermediate of the mechanism is represented. Blue accounts for quartet and green for sextuplet spin states. M refers to methane results, E to ethane, C to cyclohexane, and 2,3-DMB to 2,3-dimethylbutane. $t\text{NCH}_2$ and $t\text{NCH}_3$ refer to the two *cis* hydroxyls of the catalyst, which are placed in trans to a NCH_2 group and a NCH_3 group, respectively.

In this first part of the study, focused in substrate effects on the mechanism of AHPs, the analysis concludes that, in solvent phase, despite general trends and correlations are found between the energy barriers of the mechanism and the substrates, the general mechanism is not affected by them. This is clearly represented in Figure 7.2, which shows the Gibbs energy profile of the AHP for the different analyzed substrates, only depicting the spin ground state for each substrate and reaction intermediate of the mechanism. Figure 7.2 reveals that

substrates just lead to free energy changes in the barriers and intermediates of the mechanism.

Comparison between the Gas-Phase and the Solvent-Phase mechanism of alkane hydroxylation

In the second part of the study, the solvent effect on the mechanism of AHPs was analyzed. The data obtained in the previous section of the study (using a solvent-phase model, G_{solv}) was compared with the computational results obtained using a gas-phase model (G_g) and a gas-phase model considering the solvent effect as a single-point correction added at a later stage (G_{g+corr}).

We considered all the reaction mechanisms summarized in Figure 7.1, keeping in mind that the main difference between them is the stability of the intermediate species. At this point, we used the knowledge gained in the previous section to simplify the case studies. We have already seen that the different substrates followed two main trends regarding intermediate stability (*i.e.* the most stable intermediate forms of methyl intermediates in solvent phase have radical electronic structures, while the most stable intermediate forms of the other substrates in solvent phase have cationic electronic structures); thus, in this section, just one substrate of each group (*i.e.* methane and cyclohexane) were studied.

S=	electronic configuration				ΔG_g (kcal/mol)		ΔG_{g+corr} (kcal/mol)	
		iron		substrate	methane	cyclohexane	methane	cyclohexane
1/2	I_{cat}	C		R^+	---	14.07	---	10.22
	I_{rad}	B		$R\cdot$	0.00	---	0.00	---
3/2	I_{cat}	C		R^+	---	11.63	---	9.55
	I_{rad}	B		$R\cdot$	1.43	---	1.08	---
5/2	I_{cat}	C		R^+	---	0.00	---	0.00
	I_{rad}	B		$R\cdot$	20.7*	---	---	---

Table 7.2: Relative Gibbs Energies at gas-phase (ΔG_g) and at gas-phase including single-point dispersion and acetonitrile solvent corrections (ΔG_{g+corr}) (kcal/mol) for radical and cation iron-bishydroxo catalyst intermediates. * ΔE_{elec} value.

Table 7.2 reports the main results regarding intermediate stability obtained at the G_g and G_{g+corr} levels of theory. If we compare these results with the ones reported in Table 7.1, a key difference appears: at gas phase, unlike in solution, there are no stable I_{rad} intermediates for cyclohexane. For these electronic states, optimizations at gas phase lead directly to the alcohol products. Gas-phase and solvent-phase calculations agree in the description of the ground states for the iron-bishydroxo + alkyl intermediates. However, the fact that the different levels of theory differ in the description of the excited states for cyclohexane (at gas phase radical intermediates are not stable minima) will obviously affect the mechanism of its AHP, because in solvent the alkane hydroxylation mechanism of cyclohexane evolved through the radical intermediate. The larger stabilization of I_{rad} versus I_{cat} in solvent, when it is compared with gas-phase results, comes

7.1 FUNCTIONALIZATION OF C-H BONDS BY IRON CATALYSTS

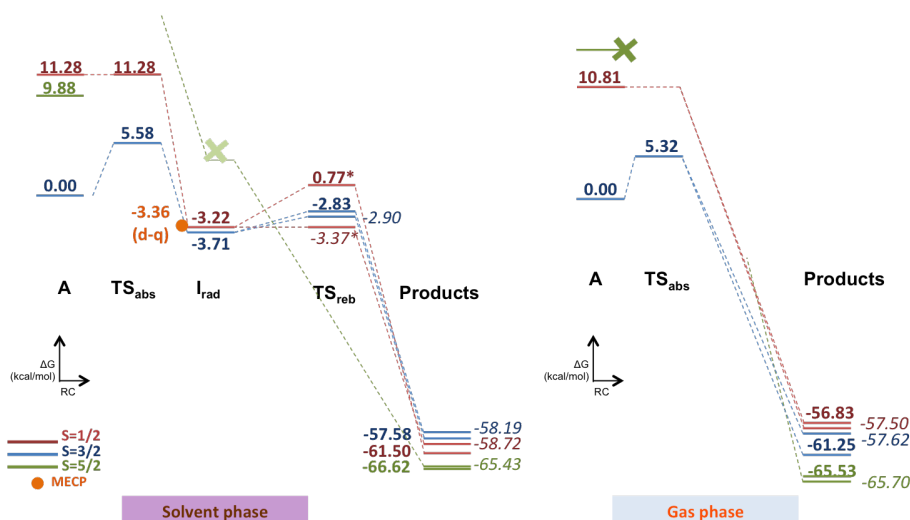


Figure 7.3: Gibbs energy profiles (in kcal/mol) of the alkane hydroxylation process for cyclohexane at solvent phase (left-hand-side profile), and at gas phase including single-point dispersion and solvent corrections (right-hand-side profile). Values in *italics* represent the OH_{tNCH_2} ligand transfer and values in **bold** represent the OH_{tNCH_3} ligand transfer. The values marked with an * are approximated upper bound values obtained by scanning the C-O bond distance in linear transits from I_{rad} to products.

because solvent phases stabilize the concentration of charges more easily than gas phase. Particularly, I_{rad} intermediates present a +2 charge in the catalyst and a neutral alkyl radical moiety, whereas I_{cat} intermediates present a +1 charge in the catalyst and a +1 charge in the cationic alkyl. The former is more easily stabilized by solvent phase than by gas phase. On the contrary, gas-phase favors the electronic state with the positive charge split between the catalyst and the alkyl moiety.^a

Figure 7.3 offers a comparison between the Gibbs energy profiles of the cyclohexane hydroxylation mechanism in solvent and at gas phase. Indeed, it shows how the AHP evolves under different mechanisms in both situations; namely, at gas phase the hydroxylation process evolves through a concerted and highly asynchronous mechanism while in solvent the mechanism is stepwise, with an initial HAT followed by an OH rebound process.

The changes in the reaction mechanism of AHPs identified in this study can help to rationalize the high variability in alkane hydroxylation mechanisms reported in literature.

^a It is important to mention that in some situations when the system is affected by self-interaction error (SIE), electron delocalized states are overstabilized and the use of a solvent model is not enough to properly describe experimental conditions and the proper mechanism. In this project, SIE effects were ruled out. However, in this sense, Shaik and co-workers published a perfectly complementary paper that describes how to achieve a proper description of the alkane hydroxylation mechanism by means of DFT when SIE is present.⁹⁷

7.1.2 Elucidating the reaction mechanism of the chemoselective carbene-insertion reaction into C-H bonds by iron-carbene catalysts.

This subsection is based on the contents of the manuscript by Postils *et al.* *The mechanism of the selective Fe-Catalyzed Arene Carbon-Hydrogen Bond Functionalization*, submitted. The manuscript is reported in [section 4.2](#) of this thesis.

As noted in the introduction, together with our experimental collaborators, we published the first experimental study where the **chemoselective** insertion of carbenes into C(sp²)-H bonds of non-activated benzene was observed. Moreover, this achievement was reached by using Fe and Mn catalysts, which extended the chemoselective reactivity of carbenes to first-row TM for the first time.¹⁴⁰

The peculiarity and the chemical relevance of the reactivity reported in that study motivated the computational research presented in [section 4.2](#) of this thesis, focused on obtaining a deep understanding of the reaction mechanism of the process. Furthermore, one of the catalysts that presents chemoselective reactivity by the carbene insertion into C(sp²)-H bonds in that study is precisely the same we have just seen, [(PyTACN)Fe^V]²⁺. Thus, we considered that achieving the complete description of its reaction mechanism by the carbene insertion process would be interesting since it would give further insights into its C-H bond oxidative reactivity. Hereunder, the main achievements of the computational study of [section 4.2](#) are reported. I will summarize the insights into the reaction mechanism we spotted in the article in two blocks. The first one will address the carbene formation; and the second one will address the mechanism of the reaction between the carbene and benzene.

Generation of the carbene moiety

In agreement with experimental evidences, the carbene formation was computationally studied considering the [(PyTACN)Fe^V]²⁺ species, without the two labile triflate or chloride ligands coordinated to the iron atom unlike the steady-state catalyst **32** ([Figure 1.30](#)). [Figure 7.4](#) reports the minimum-Gibbs energy profile of the carbene-formation reaction and exhibits the main features of it.

The global energy barrier of the carbene formation reaction is 29.5 kcal/mol. This high barrier, which is not affordable at room temperature, explains the experimental need for working at 80 °C. Moreover, as it is shown in the [paper](#), it is the highest energy barrier of the overall reaction of benzene functionalization, and, consequently, the rate-determining step (RDS) of the process. Being the RDS prevents the accumulation of iron-carbene species when they are formed, which underlines the need for computational studies in order to obtain a proper mechanistic description.

The origin of the high energy barrier for the carbene formation is also exhibited in [Figure 7.4](#): the formation of non-reactive but more stable adducts between the catalyst and ethyl diazoacetate (EDA) (*e.g.*, adduct **A**) than the reactive one (*i.e.*, adduct **A'**).

Another interesting feature of this section of the mechanistic study is the electronic nature of the **C** Fe-carbene (and its isomers - see the correspondin

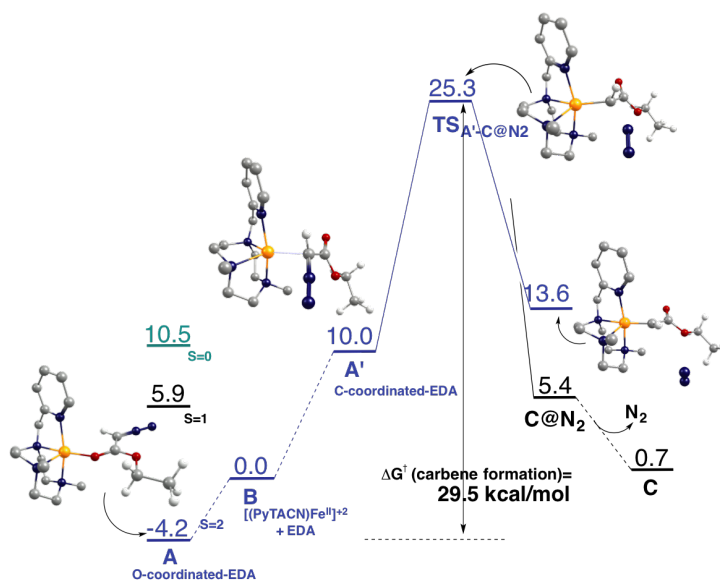


Figure 7.4: Gibbs energy profiles, ΔG , (kcal/mol) of the metal-carbene bond formation. The reactive adduct between the catalyst and EDA, **A'**, originates the iron-carbene compound through the release of N_2 . Blue, black and green profiles correspond to quintet, triplet and singlet multiplicities, respectively. Hydrogen atoms of the PyTACN ligand have been omitted for clarity (C:grey, N:blue, O:red, Fe:yellow, and H:white).

Annex). **C** is computationally described as an Fe(III) and a formal radical alkyl carbene, being the first nonheme iron radical carbene described up to date. In the Supporting Information of the main manuscript, the DFT description of **C** as a radical alkyl is analyzed. This is closely related with the need to use a broken-symmetry approach to achieve accurate electronic descriptions of iron systems. For **C**, the different symmetry and polarization of α and β occupied MOs of the system resulted in a different bonding pattern for α and β electrons, which caused the final Fe(III) + radical alkyl carbene configuration.

Before moving on to the next section about the reaction mechanism between the carbene and benzene, it is worthwhile to note that the Fe-carbene species **C** is not the conformer that presents the lowest barrier to react with benzene and, therefore, it is not the conformer considered in the next section. Several iron-carbene conformers were analyzed and the so-called conformer **C'** (see section 4.2) was found to be the most suitable one for the functionalization of benzene. From this conformational analysis, the essential role of the two free *cis*-coordination sites of the catalyst can be inferred: the most active conformer is the most suitable one for the approximation of benzene to C_{carb} . Thus, the two free *cis*-coordination sites are essential to leave enough space to allow the formation of the C-C bond between the carbene and the benzene.

Reaction mechanism of the benzene functionalization by iron-carbenes

As mentioned in the introduction, the first reaction step between the carbene moiety and the benzene substrate is the formation of an intermediate with a

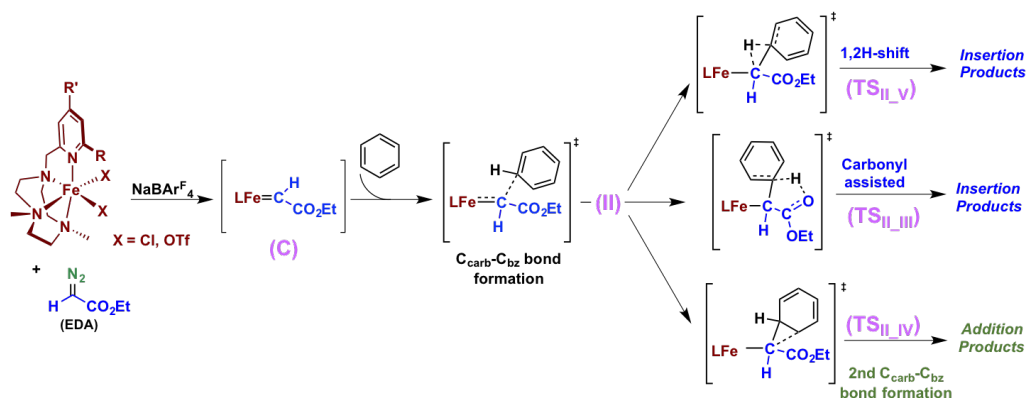


Figure 7.5: Studied pathways for the formation of insertion and addition products.

C_{carb}-C_{bz} bond, **II** (according section 4.2 nomenclature). Following the typical reactivity of C(sp²)-H bonds with carbenes, and, unlike the usual concerted mechanism between C(sp³)-H bonds and carbenes, we observed the formation of this intermediate via an initial electrophilic addition of the carbene carbon to the aromatic C-H bond. Therefore, the overall benzene functionalization process follows a stepwise mechanism.

From that intermediate **II**, different pathways were analyzed in order to rationalize the experimental preference for the formation of insertion products over the formation of addition products. Figure 7.5 summarizes them. Specifically, two different pathways to insertion products and one pathway to addition products were investigated. Regarding the formation of insertion products, we analyzed the classical mechanism that involves the direct hydrogen migration between the two carbons that form the C_{carb}-C_{bz} bond, the so-called [1,2]H - shift mechanism, and an alternative mechanism that involves a hydrogen abstraction reaction of the same hydrogen by the carbonyl oxygen of the native EDA (see Figure 7.5). This latter mechanism, named carbonyl assisted insertion, generates an enol intermediate that should subsequently evolve to the ester form to finally yield the insertion product. Before starting the writing process of our manuscript, an article reporting this last mechanism for the chemoselective carbene insertion into C-H bonds of phenol by a gold-carbene catalyst was published.¹⁵⁹ Regarding the formation of addition products, the classical mechanism that involves a second C_{carb}-C_{bz} bond with an adjacent carbon of the phenyl was analyzed. This process leads to the formation of a norcaradiene intermediate, which can evolve to the final cycloheptatriene addition products through a thermally allowed electrocyclic ring opening.

Figure 7.6 compares the energetic barriers of the three analyzed pathways from **II** to products. As it can be seen, the formation of the enol intermediate is the lowest energy barrier process (TS_{II_III}) and the one through the mechanism will evolve. However, it is needed to be stressed that, in electronic energy terms, the enol formation barrier is higher than the norcaradiene formation barrier (TS_{II_IV}). Thus, entropy has a key effect favoring TS_{II_III} over TS_{II_IV} and, in general, the achieved chemoselective formation of insertion products.

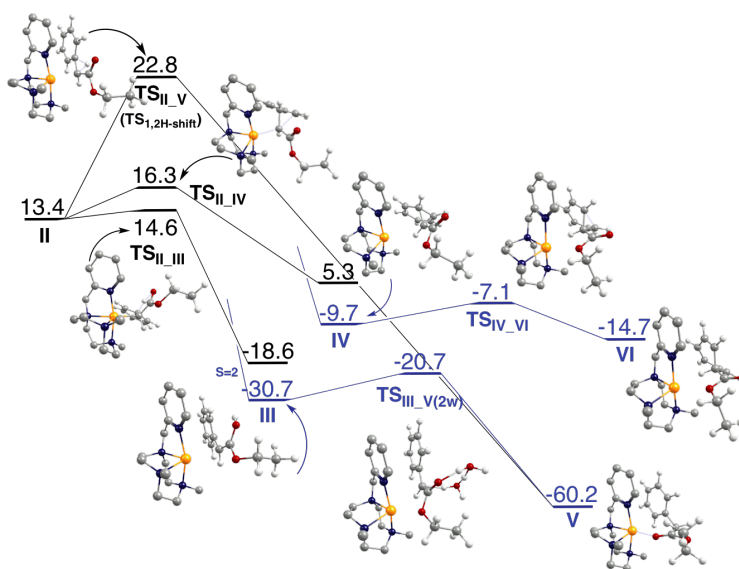


Figure 7.6: Comparative Gibbs energy profile, ΔG , (kcal/mol) of the formation of addition (VI) and insertion (V) products from II. Black and blue profiles correspond to triplet and quintet multiplicities, respectively. Hydrogen atoms of the PyTACN ligand have been omitted for clarity (C:grey, N:blue, O:red, Fe:yellow, and H:white).

The formation of the enol intermediate structure (III in Figure 7.6) is a strongly exergonic process. Nevertheless, in order to establish that the final insertion products can be formed from III, the energy barrier of the enol-ester tautomerism has to be studied. Figure 7.6 also shows that the tautomerism has an energy barrier of only 10.0 kcal/mol that can be easily overcome when it is assisted by two water molecules. However, if water molecules are not considered, the equivalent Gibbs energy barrier has a value of ca. 46.6 kcal/mol. Thus, the computational study also revealed that the presence of water molecules (even adventitious) was a necessary condition to obtain the chemoselective insertion products. Despite water was not added in our initial experimental work, the presence of adventitious water molecules was experimentally detected by the formation of certain amount of ethyl glycolate products.¹⁴⁰ Moreover, in the manuscript presented in section 4.2, the substrate probes and the isotopic labelling analysis reported also provide experimental evidences that reinforce the involvement of water molecules in the mechanism.

7.2 Theoretical characterization of the oxidation state property by effective oxidation state (EOS) analysis

This section is based on the contents of the manuscript by Postils *et al.* *Reaching the new IUPAC definition of oxidation state by computational techniques*, submitted. The manuscript is reported in [chapter 5](#) of this thesis.

In this new section, the results of the [chapter 5](#) of this thesis, which refer to the theoretical characterization of a molecular property (*i.e.*, the oxidation state) are discussed. Specifically, the knowledge acquired on the applicability of the effective oxidation state (EOS) method is summarized below. The oxidation state is a chemical concept of utmost relevance in chemistry. In reaction mechanisms of organometallic catalysis, for example, it is an intrinsic descriptor and the complete fingerprint of the chemical reaction is not complete until the determination of the OSs of the species involved. Thus, taking advantage of the recent development in our group of the new EOS tool for the determination of oxidation states,²³⁷ we decided to perform a benchmark study of the applicability of the method.

The article presented in the fifth chapter falls within the end of the lack of a general definition of the oxidation state term, since IUPAC organization recently set a formal OS definition as well as practical algorithms to its determination.^{173,175,345} Although the OS property is intrinsically related to the physical electron distribution around atoms, in IUPAC reports the role of quantum-chemical calculations for OS assignment is still tiptoed across. In this thesis we wanted to enhance the suitability of the theoretical determination of OSs by proving the applicability of the EOS method. Moreover, the study also highlights that the theoretical determination of OS can provide new insights and consistent answers to unsettled cases that result from ambiguities and caveats of the new OS definition.

Taking into account the new IUPAC's definition of OS ([subsection 1.3.1](#)), two main caveats have to be considered. The first one is related to the need to define an initial Lewis structure, *i.e.*, the need to define *bonds*, whose electrons will be assigned to their most electronegative atom. The second caveat is indeed related to the use of fix EN values to decide on the distribution of these electrons. When the chemical bond is affected by the whole molecular constitution, as in reversible or dative bonds, fix EN values may not agree with their electron distribution. For these particular bonds, special considerations have to be taken into account in order to obtain the correct OS. Despite these warnings have already been commented in IUPAC reports, [chapter 5](#) shows that the use of the EOS method retrieves a proper OS definition directly, without any special consideration.

The need to define an initial Lewis structure may be a handicap in the definition of OSs of organometallic compounds when they present non-innocent ligands or ligands that may coordinate according several hapticities, such as aromatic rings or conjugated chains that may present resonance structures. In these situations, drawing their Lewis formula requires extra information about bond orders

7.2 THEORETICAL CHARACTERIZATION OF OXIDATION STATES

from diffraction and spectral data, and the final assignation of the OS of the TM center is often ascertained from spectral and magnetic measurements.

For non-innocent ligands, EOS analysis gets back a proper OS definition in the 100% of studied situations, while for haptocomplexes, the agreement is >90% (see [Table 7.3](#)). The reason of the good performance of EOS method in these situations is that neither the geometry nor EOS construction scheme require the previous definition of chemical bonds. The geometry is just defined by *xyz* coordinates and the EOS construction scheme, as it was explained in the introduction, works with effective atomic orbitals (effAOs) (or effective fragment orbitals), which are natural-type orbitals centered at atoms (fragments) without any electron sharing between them. EOS analyses do not provide the bonding pattern of the system. EOS analyses provide the OSs of the system by describing it as a formal pure ionic system through orbitals centered and confined in atomic (fragment) regions. Therefore, as it is shown in the [chapter 5](#), the EOS method fails badly in nearly pure covalent systems such those essentially formed by homonuclear bonds ([Table 7.3](#)).

Systems with reversible or dative bonds may also deserve special attention when we intend to apply the new OS definition by IUPAC. An specific situation that is already commented in IUPAC reports is when the bonding pattern takes place between a Lewis acid (LA) and a Lewis base (LB) ligand, and the LA (acceptor) is more electronegative than the LB (donor). In these situations, the general use of electronegativities for the division of the electron bonds leads to incorrect OSs. According the EN, the electrons of the LA-LB adduct would be assigned to the LA ligand; however, according the Lewis theory (formation of a dative bond) and the reversibility of the adduct, the LA ligand does not keep the bond pair, *i.e. there is no change in the oxidation number of any atoms*.³⁴⁶ In this sense, the handicap of the OS assignation in the reversibly-bonded Lewis-acidic electronegative ligands was introduced in IUPAC reports.

The study of the different bonding modes of the SO₂ ligand illustrates the influence of the nature of the chemical bond in OSs, as well as the fact that the simple use of EN values is not enough to define them. [Figure 7.7](#) summarizes the results of the study on the SO₂ ligand we addressed in Chapter 5. There are represented the three experimentally identified bonding modes of the SO₂ ligands in mononuclear complexes. From left to right, the SO₂ ligand is bound as a L-type ligand, as a Z-type ligand, and as a π -complex ligand. In each situation, the TM-SO₂ bond is different. As a L-type ligand, the sulfur atom acts as a LB (sigma donor); thus, both electrons that form the dative bond are provided by the ligand. In this situation, since S is more electronegative than Rh, the IA retrieves a good description of the electron-pair assignation and the OSs. When SO₂ ligand acts as a π -complex, the bonding is mainly a π interaction where SO₂ (specifically an SO unit), again, acts as a LB (pi donor) because the metal is a better π -acceptor than σ -acceptor. In this second situation, as one would expect, the IA retrieves again a good description of the OSs. However, when SO₂ acts as a Z-type ligand, the sulfur atom is the LA (sigma acceptor) and the electrons that form the sigma dative covalent bond are provided by the metal, which is the LB. This last described situation provides a typical example of a reversible-

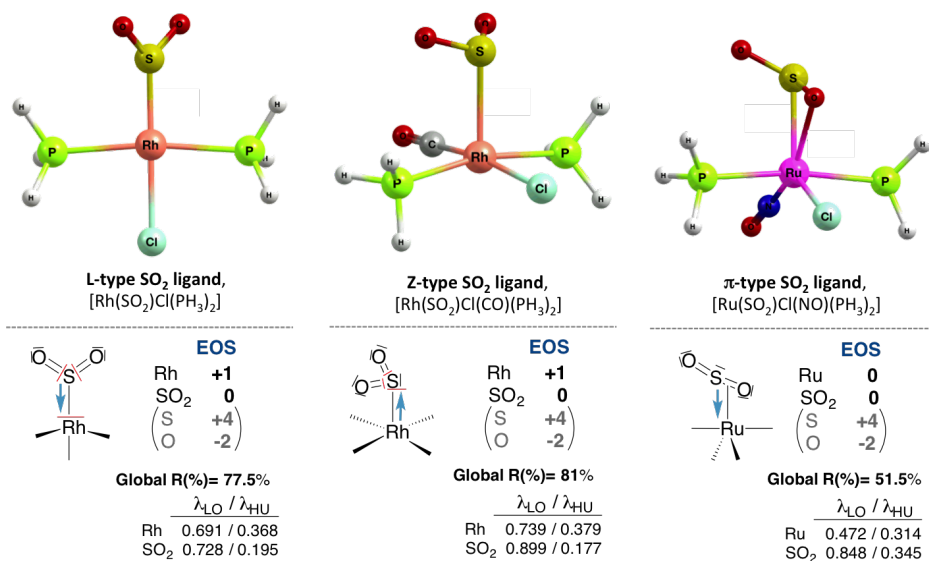


Figure 7.7: Examples of three types of sulfur bonding in SO₂ ligands. From left to right, the SO₂ ligand is bound as a L-type ligand, as a Z-type ligand, and as a π -complex ligand. Below, schematic representations of their Lewis formulas and EOS results are shown. In the Lewis formulas, blue arrows reveal the origin of the electrons that form the dative M-SO₂ bonds; red lines illustrate the proper assignments of electrons that retrieve the OSs. The occupation number of the *frontier* eff-AOs, namely, the last occupied, λ_{LO} , and the first unoccupied, λ_{HU} , of the metal and the SO₂ ligand are reported.

bonded Lewis-acid electronegative ligand. Thus, the general IA criteria, which assigns the electrons of the TM-SO₂ bond to S, fails, and an exception to the general rule should be applied. However, without additional data like atomic coordinates, it is difficult to assert the bonding mode of the SO₂ ligand in advance and, therefore, errors can occur in the OS assignment. As Figure 7.7 also shows, EOS analyses naturally yield the expected OS of the SO₂ ligand (and its atoms) and the metal, no matter the bonding pattern and without any external guidance.

Organometallic compounds that hold carbene ligands constitute another situation where the coordination pattern should deserve special attention in order to determine the OS. Although no reference about carbenes is provided in IUPAC reports, if we apply the IA criteria to different standard carbene-type compounds, we can already note that the IA criteria is not able to distinguish between Schrock-type and Fischer-type carbenes. Figure 7.8 reminds us the different bonding patterns of Fischer- and Schrock-type carbenes, and how their *method of deconstruction* determines the final assignment of the OS.

In general, C atoms are more electronegative than TMs. Thus, taking into account the EN criteria of the IA, the four electrons of the metal-carbene double bond will be assigned to the C atom, providing partial OS_(carbene) = -2 and partial OS_(TM) = +2. In fact, OSs of Schrock-type carbene complexes agree with this description (see *methods of deconstruction* in Figure 7.8), since their bonding is described as two covalent bonds (one σ and one π) between a triplet carbene and a triplet metal fragment, and both bonds are polarized toward the carbon

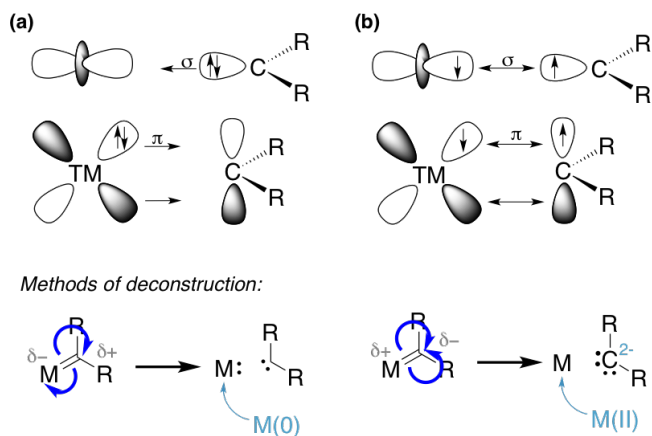


Figure 7.8: Above, schematic representation of the dominant orbital interactions in: (a) Fischer-type carbene complexes and (b) Schrock-type carbene complexes. Below, their respective methods of deconstruction are schematically represented.

atom. Schrock carbenes are also named alkylidenes because they have no donor-acceptor interactions between the metal and the carbene fragment. Conversely, the bonding of Fischer-type carbenes comes from a different pattern. The dominant bonding interactions arise from: i) a σ donating bond from the singlet carbene to the metal, and ii) a π back-donating bond from the metal to the carbene ligand. Thus, the bond with π character of Fischer-type carbenes also follows the pattern of a reversible-bonded Lewis-acid electronegative ligand (*i.e.*, it is polarized toward the TM), although the bond with σ character does not (*i.e.*, it is polarized toward the carbon atom). In this sense, the deconstruction method of each bond of the metal-carbene double bond is different (Figure 7.8) and, certainly, it is a situation not covered by IUPAC reports at all, which precludes a proper OS assignment. In our study, we applied the EOS method to fifteen organometallic compounds that held carbene ligands with different bonding patterns (*i.e.*, Schrock-, Fischer-, and radical-type carbenes). All the analyses retrieve the expected OS value, according the carbene nature, prior literature or evidences.

In short, the article reported in chapter 5 captures the applicability of the EOS method to determine OSs. It shows that EOS method presents a general excellent performance, determining the expected OSs with high agreement with experimental evidences or prior literature. The only exception are high covalent systems where a ionic definition to retrieve OSs is meaningless (Table 7.3). Moreover, the article proves that in those situations that result in ambiguities and caveats of the IA approach, the EOS method is very helpful because it naturally yields the expected OS without any external guidance.

As a final point, I would like to briefly discuss the results obtained from the EOS analyses on haptocomplexes. As pointed out above, the need to define an initial Lewis structure may be a handicap in the definition of OSs of organometallic compounds that hold aromatic rings or conjugated chains because they may be coordinated according different hapticities. Moreover, as admitted

	Agreement (%) [*]
General Examples	90 %
Homonuclear bonds and Clusters	47 %
High Oxidation States	89 %
Non-Innocent Ligand	100 %
Lewis acid-base Adducts	91 %
π -adducts	84 %
Carbenes	93 %

Table 7.3: Summary of the agreement between the OSs predicted by EOS analyses and *the ones reported in Karen’s reports^{173,175,345} or prior literature.

by Karen,^{173,175} in spite of having defined and determined the Lewis structure, the final OS of the π system is indeed governed by aromaticity. Aromaticity acts as the driving force to set the bonding pattern that finally will determine the OS.

Our analyses on OSs of sets of haptocomplexes allowed us, not only to corroborate that aromaticity acts as a driven force, but also to refine and improve the argument. For example, we observed that when the π system presents a local triplet spin state, regardless the global spin state of the organometallic compound, the ionic charge that the ligand will present agrees with Baird’s rule of aromaticity for triplet states. Thus, we conclude that the local spin state of the π system has to be also considered to predict proper OSs and that the OS assignment is not always straightforward. Moreover, we also observed that for bent π systems, their ionic character (and therefore the final OS) is better explained if conjugated delocalized segments are analyzed separately, rather than looking at the whole system. However, in these situations, the stabilization of each segment constitutes a lower (less dominant) driving force than the stabilization of the whole π systems via aromaticity, and the final OS is less predictable. So, along with demonstrating that EOS method works perfectly on the determination of OS, our study also shows that EOS method may also be useful to rationalize and shed some light on the behavior of the OS property.

7.3 Electron distribution in molecular electrides

This section is based on the contents of the manuscript by Postils *et al.* *Chem. Commun.* **2015**, 51, 4865-4868, which can be found in [chapter 6](#) of this thesis (ref. 261).

In this last section of the chapter, the results presented in [chapter 6](#) are briefly commented. This chapter contains the computational study of this thesis focused on the construction of molecules, specifically on how the electronic structure of an intriguing molecules, *i.e.* electrides, is organized. It is precisely because of the intriguing electronic structure of electrides that the oxidation state assignments of such molecules, for example, can not be done by classical formalisms. However, in [chapter 6](#) we went a step further and, instead of *just* quantifying the oxidation state property, we focused on the description of the whole electronic structure and electron distribution.

By definition, electrides are ionic species where isolated electrons constitute the anionic part.³⁴⁷ Although the existence and the electronic structure of electrides in the solid lattice had been already studied in a few attempts when we published our article^{250,252,256,348} and have been further explored since then,^{253,254,269,270,349,350} the study presented here is the unique published work that features the possibility of electrides beyond the solid lattice by the resolution of their electronic structure in gas phase. In this project, besides the characterization of molecular electrides, a criterion to differentiate electrides from other similar species was also provided.

The molecules selected to conduct the study had been previously tagged as electrides because they show large nonlinear optical properties (NLOPs) and delocalized diffuse excess electrons on high-lying occupied orbitals. However, the isolated-electron character required for being tagged as electrides had not previously been confirmed. Thus, in this project we performed the characterization of their electronic structure using three different criteria: the existence of a non-nuclear attractor (NNA), an electron localization function (ELF) basin, and negative values of the Laplacian of the electron density (see [subsection 2.3.1](#) for the theoretical background). Then, the electride nature is determined by the presence of these three features in specific non-atomic regions where the isolated electron is expected to be held.

[Table 7.4](#) summarizes the results obtained in the study by the aforementioned criteria and it also reports the final conclusions about the electride nature of the analyzed molecules. It can be observed that the results support the existence of gas-phase molecular electrides. Specifically, the Li@calix[4]pyrrole, the e-@C₆₀F₆₀, and the TCNQ-based molecules are characterized as electrides. All these chemical systems fulfill the three criteria used to characterize electrides. In this sense, we established that the presence of a NNA and an ELF basin or negative values of the Laplacian of the electron density are necessary conditions to assert the existence of an isolated electron and the electride nature.

Among the molecules identified as electrides, by quantifying the electron density confined in the ELF basin of the isolated electron and in the NNA basin, two

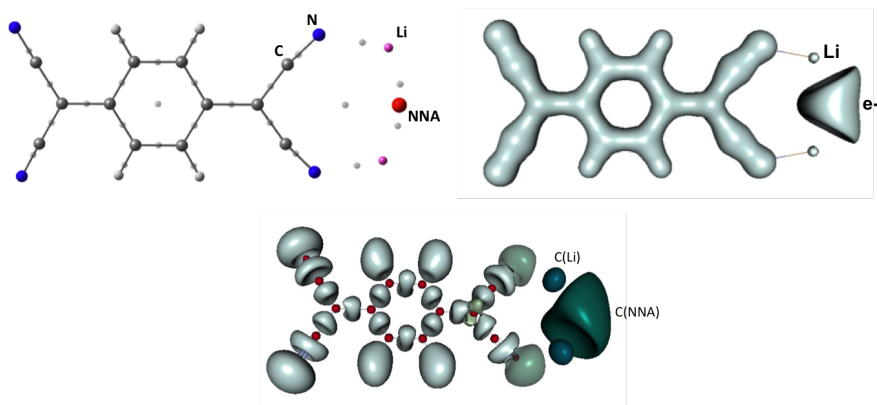


Figure 7.9: QTAIM topological analysis (top left), $\nabla^2\rho=-0.001$ (top right) and $\text{ELF}=0.75$ (bottom) representations of TCNQLi_2 .

different scenarios are observed. On the one hand, TCNQ-based molecules that, with almost one electron integrated in the abovementioned basins, can be presented as *formal electriles*. On the other hand, $\text{Li@calix[4]pyrrole}$ and $e\text{-@C}_{60}\text{F}_{60}$ that, containing far less than one electron integrated in the abovementioned basins, may just be classified as *electrile-like* molecules. Figure 7.9 presents the QTAIM topological analysis, ELF and $\nabla^2\rho$ representations of TCNQLi_2 .

It is important to note that there are chemical systems that have NNAs, $\nabla^2\rho$ or ELF basins and they are not electriles. Therefore, the presence of these features should be properly analyzed before assigning the tag of electrile to the studied system. For example, $\text{Li}\cdots\text{HCN}$ and $\text{Li}\cdots\text{NCH}$ molecules present independent ELF and $\nabla^2\rho$ basins in the proximity of lithium. However, these basins remain so close to lithium that they can be barely considered anything else than the polarized lithium valence itself. We also suggested that large NLOPs can be used, together with the three latter conditions related to the electronic structure, to confirm the true electrile nature of the given species.

	NLOP	NNA	$\nabla^2\rho$	ELF	Electrile?
TCNQLi_2	✓	✓	✓	✓	✓
TCNQNa_2	✓	✓	✓	✓	✓
$\text{Li@calix[4]pyrrole}$	✓	✓	✓	✓	✓
$\text{Li@B}_{10}\text{H}_{14}$	✓	×	×	×	×
$e\text{-@C}_{60}\text{F}_{60}$	✓	✓	✓	✓	✓
$\text{Li}\cdots\text{HCN}$	✓	×	$\sqrt{^a}$	$\sqrt{^a}$	×
$\text{HCN}\cdots\text{Li}$	✓	×	$\sqrt{^a}$	$\sqrt{^a}$	×
<i>Control molecules</i>					
Li_2	✓	✓	✓	✓	✓
C_2H_2	×	$\sqrt{^a}$	$\sqrt{^a}$	$\sqrt{^a}$	×

Table 7.4: Summary of the criteria used to characterize electriles in this study.

^a These molecules show NNA, $\nabla^2\rho$ or ELF basins in the close vicinity of an atom and, therefore, the isolated nature of the electron is dubious.

7.3 ELECTRON DISTRIBUTION IN MOLECULAR ELECTRIDES

Finally, besides tidying up the proper identification of molecular electriles by setting the criteria for their identification, we also put forward a recipe to design new electriles based on the occurrence of NNA, which is not at all a frequent feature of molecular densities. In this sense, we suggested the use of the data of Pendás and coworkers,²⁶² who analyzed the range of diatomic distances at which several dimers show a NNA. We were inspired by TCNQ-based molecules, where TCNQ moiety actually plays a role in stabilizing Li_2 and Na_2 molecules at a favorable distance where the NNA appears.

Chapter 8

Conclusions

The main conclusions of this thesis are collected in this chapter, and organized in three main groups.

Functionalization of C-H bonds of hydrocarbons by the [(PyTACN)Fe^V] catalyst

First:

The effects of the substrate and solvent in the alkane hydroxylation mechanism catalyzed by an Fe(V)=O catalyst, [(PyTACN)Fe^VO], have been studied. Substrate effects were studied in solvent and taking into account hydrocarbons that hold different types of carbon atoms (*i.e.*, methane and hydrocarbons with primary, secondary, and tertiary carbon atoms). It was found that, despite correlation between the energy barriers of the C-H breaking and the substrate nature can be drawn, the general mechanism of the alkane hydroxylation process (AHP) is not affected by changing the substrate. Thus, for all hydrocarbons, the alkane hydroxylation process in solvent follows the classical Groves' or rebound mechanism. The first step of the rebound mechanism consists in an hydrogen atom transfer (HAT) reaction that forms an alkyl radical intermediate, which further reacts with one hydroxyl group of the catalyst to form the final hydroxyl products.

When we move from solvent phase to gas phase in order to study the solvent effect on the AHP, we observed key changes in the reaction mechanism. On the contrary to solvent-phase, the gas-phase alkyl radical intermediates of hydrocarbons are not stable minima, except for methane. Therefore, the stepwise mechanism via the radical intermediate is precluded except for the methane substrate. In turn, in gas phase these substrates evolve through a concerted and highly asynchronous mechanism where the HAT reaction leads directly to the final hydroxyl products. The non-stabilization of radical intermediates at gas phase is explained by the fact that gas phase does not favor the concentration of charges (*i.e.*, the +2 charge the radical intermediate presents on the catalysts is not stabilized). On the contrary, gas phase stabilizes the charge splitting of the cationic intermediates (*i.e.*, +1 charge on the catalyst and +1 charge on the substrate).

The changes in the reaction mechanism of AHPs identified and analyzed in

detail in our systematic study can help to rationalize the high variability in alkane hydroxylation mechanisms reported in literature.

Second:

The [(PyTACN)Fe^V] catalyst is within the first examples of iron catalysts that are able to catalyze the chemoselective carbene insertion into C(sp²)-H bonds of non-activated arenes. In this thesis, the reaction mechanism of such reactivity has been computationally rationalized. The carbene formation from EDA (the carbene precursor) is the rate-determining step of the process, with a barrier high enough to explain the experimental need of working at 80 °C, which hinders the direct experimental detection of the intermediates of the reaction mechanism. The electronic nature of the formed Fe-carbene is computationally described as an Fe(III) and a formal radical alkyl carbene, which is the first nonheme iron radical carbene described up to date.

Moreover, the surprising unprecedented chemoselective reactivity is explained by a novel mechanism. From the intermediate form, where an initial C_{carb}-C_{bz} bond is already assembled, the formation of the final insertion products evolves through a hydrogen abstraction reaction of the hydrogen of the C_{carb} atom that is already forming the C_{carb}-C_{bz} bond by the carbonyl oxygen of the native EDA. At this stage, an enol intermediate is formed. The final insertion products are achieved after an enol-ester tautomerism, where the hydrogen of the enol moves to its final position (C_{carb}) and the ester is recovered. This process is assisted by water molecules.

Theoretical characterization of oxidation states

Third:

We have shown that the effective oxidation state (EOS) method efficiently retrieves the oxidation states of many kinds of organometallic catalysts (from catalysts that bear non-innocent ligands, to TM systems with formally very high OS, passing through systems with reversible or dative bonds). Thus, the EOS method presents a general excellent performance in determining the expected OSs of different kind of systems with high agreement with experimental evidences or prior literature.

One of the main strengths of the EOS method is that is not based on the identification of bonding patterns. EOS analyses provide the OSs of the systems by describing the system as a formal pure ionic entity through orbitals centered and confined in atomic (fragment) regions without electron sharing between them. In this way, EOS analyses are able to get back the proper OS in situations where the application of the generic definition of OS of IUPAC based on Allen electronegativities is not conclusive. For instance, the EOS method is successful when there are non-innocent ligands or ligands with aromatic rings or conjugated chains that may present resonance structures).

Another main strength of the EOS method is that, by construction, it retrieves the influence of the whole chemical environment of the system in the assignation of OSs. In this sense, EOS method identifies if the fragments we have defined are subsystems of enhanced stability, and, in line with this, the method establishes the final OSs without any external guidance. This is especially useful when the existence of dative bonds can bias the final OSs of the system.

Finally, the EOS method not only reaches by computational techniques the new IUPAC's definition of OS, but also extends the identification of OSs to other systems that cannot be properly addressed by IUPAC's definition. For example, we have shown how EOS method correctly retrieves different OSs by carbene ligands, discerning between Schrock-, Fisher-, and radical-type carbenes. Moreover, we have also shown that the EOS results of aromatic ligands are in complete agreement with the OS assignation considering the proper aromaticity rule in each situation in accordance with the local spin state of the ligand (*i.e.*, Baird or Hückel rule).

The results of the EOS analysis only disagree with the expected results for molecules of main-group elements exhibiting homonuclear bonds. This is mainly because the case of a homonuclear bond is the worst-case scenario for methods (like EOS) that seek to recover the ionic character of molecules in line with the foundations of the OS property.

Electron distribution in molecular electrides

Fourth:

The proper characterization of molecules as molecular electrides requires the identification of the isolated-electron character, which can be accomplished by means of electron distribution analyses. As we demonstrated, for the first time, the presence of a non-nuclear attractor (NNA) and an ELF basin or negative values of the Laplacian of the electron density are necessary conditions to assert the existence of an isolated electron and, consequently, the electride nature. Moreover, large values of nonlinear optical properties (NLOPs) can be used, together with the three latter conditions, to confirm the true electride nature of the given species; especially when the presence of the electronic indicators (*i.e.*, the NNA, the ELF or the $\nabla^2\rho$ basin) is close to atoms. By quantifying the electron density confined in the ELF and in the NNA basin, *formal electrides* and *electride-like* molecules can be discerned. The formers present almost one electron integrated in the abovementioned basins, while the latters contain far less than one electron integrated in them.

The occurrence of NNAs, which is not a frequent feature in molecules at all, can be used as a criterion to design new electrides.

Chapter 9

Bibliography

Bibliography

- [1] Rahimi, N.; Karimzadeh, R. *Applied Catalysis A: General* **2011**, *398*, 1–17.
- [2] Bellussi, G.; Pollesel, P. *Studies in Surface Science and Catalysis* **2005**, *158*, 1201–1212.
- [3] Labinger, J. A.; Bercaw, J. E. *Nature* **2002**, *417*, 507–514.
- [4] Sattler, J. J. H. B.; Ruiz-Martinez, J.; Santillan-Jimenez, E.; Weckhuyssen, B. M. *Chemical Reviews* **2014**, *114*, 10613–10653.
- [5] Godula, K.; Sames, D. *Science* **2006**, *312*, 67–72.
- [6] Fenton, H. J. H. *J. Chem. Soc., Trans.* **1894**, *65*, 899–910.
- [7] Kharasch, M. S.; Isbell, H. S. *Journal of the American Chemical Society* **1931**, *53*, 3053–3059.
- [8] Kleiman, J. P.; Dubeck, M. *Journal of the American Chemical Society* **1963**, *85*, 1544–1545.
- [9] Chatt, J.; Davidson, J. M. *Journal of the Chemical Society (Resumed)* **1965**, 843.
- [10] van Helden, R.; Verberg, G. *Recueil des Travaux Chimiques des Pays-Bas* **1965**, *84*, 1263–1273.
- [11] Fujiwara, Y.; Moritani, I.; Danno, S.; Asano, R.; Teranishi, S. *Journal of the American Chemical Society* **1969**, *91*, 7166–7169.
- [12] Garnett, J. L.; Hodges, R. J. *Journal of the American Chemical Society* **1967**, *89*, 4546–4547.
- [13] Gol'dshleger, N. F.; Tyabin, M. B.; Shilov, A. E.; Shteinman, A. A. *Russian Journal of Physical Chemistry A* **1969**, *43*, 2174.
- [14] Shilov, A. E.; Shul'pin, G. B. *Chemical reviews* **1997**, *97*, 2879–2932.
- [15] Garnett, J.; Long, M.; Peterson, K. *Australian Journal of Chemistry* **1974**, *27*, 1823–1825.
- [16] Rudakov, E.; Zamashchikov, V.; Belyayeva, N.; Rudakova, R. *Russian Journal of Physical Chemistry A* **1973**, *47*, 2732.
- [17] Gol'dshleger, N.; Es'kova, V.; Shilov, A.; Shteinman, A. *Russian Journal of Physical Chemistry A* **1972**, *46*, 1353.
- [18] Tretakov, V.; Arzamaskova, L.; Ermakov, Y. I. *I. Kinet. Katal* **1974**, *15*, 538.
- [19] Cooper, T. A.; Waters, W. A. *Journal of the Chemical Society B: Physical Organic* **1967**, 687.
- [20] Hanotier, J.; Camerman, P.; Hanotier-Bridoux, M.; De Radzitzky, P. *Journal of the Chemical Society, Perkin Transactions 2* **1972**, 2247.
- [21] Diaz-Requejo, M. M.; Perez, P. J. *Chemical Reviews* **2008**, *108*, 3379–3394.
- [22] Arakawa, H. et al. *Chemical reviews* **2001**, *101*, 953–996.
- [23] Milas, N. A.; Sussman, S. *Journal of the American Chemical Society* **1936**,

CHAPTER 9: BIBLIOGRAPHY

- 58, 1302–1304.
- [24] Mortreux, A.; Delgrange, J.; Blanchard, M.; Lubochinsky, B. *Journal of Molecular Catalysis* **1977**, *2*, 73–82.
- [25] Ziegler, K.; Holzkamp, E.; Breil, H.; Martin, H. *Angewandte Chemie* **1955**, *67*, 426–426.
- [26] Smidt, J.; Hafner, W.; Jira, R.; Sedlmeier, J.; Sieber, R.; Rüttinger, R.; Kojer, H. *Angewandte Chemie* **1959**, *71*, 176–182.
- [27] Smidt, J.; Sedlmeier, J.; Hafner, W.; Sieber, R.; Sabel, A.; Jira, R. *Angewandte Chemie International Edition in English* **1962**, *1*, 80–88.
- [28] Hérisson, P. J.-L.; Chauvin, Y. *Die Makromolekulare Chemie* **1971**, *141*, 161–176.
- [29] Fischer, E. O.; Maasböl, A. *Angewandte Chemie International Edition in English* **1964**, *3*, 580–581.
- [30] Heck, R. F.; Nolley, J. P. *The Journal of Organic Chemistry* **1972**, *37*, 2320–2322.
- [31] King, A. O.; Okukado, N.; Negishi, E.-i. *Journal of the Chemical Society, Chemical Communications* **1977**, 683–684.
- [32] Miyaura, N.; Yamada, K.; Suzuki, A. *Tetrahedron Letters* **1979**, *20*, 3437–3440.
- [33] Chirik, P.; Morris, R. *Accounts of Chemical Research* **2015**, *48*, 2495–2495.
- [34] Holland, P. L. *Accounts of Chemical Research* **2015**, *48*, 1696–1702.
- [35] Winter, M. J. *Journal of Chemical Education* **2011**, *88*, 1507–1510.
- [36] Brunning, A. Endangered Elements. <https://www.acs.org/content/acs/en/greenchemistry/research-innovation/research-topics/endangered-elements.html>.
- [37] Shul'pin, G. B. *Catalysts* **2016**, *6*, 50.
- [38] Shilov, A. E.; Shul'pin, G. B. *Activation and Catalytic Reactions of Saturated Hydrocarbons in the Presence of Metal Complexes*; Catalysis by Metal Complexes; Kluwer Academic Publishers: Dordrecht, 2002; Vol. 21; pp 1–551.
- [39] Barton, D. H. R.; Gastiger, M. J.; Motherwell, W. B. *Journal of the Chemical Society, Chemical Communications* **1983**, *0*, 41.
- [40] Barton, D. H. R.; Doller, D. *Accounts of Chemical Research* **1992**, *25*, 504–512.
- [41] Periana, R. A.; Taube, D. J.; Gamble, S.; Taube, H.; Satoh, T.; Fujii, H. *Science* **1998**, *280*, 560–4.
- [42] Mason, H. S.; Fowlks, W. L.; Peterson, E. *Journal of the American Chemical Society* **1955**, *77*, 2914–2915.
- [43] Hayaishi, O.; Katagiri, M.; Rothberg, S. *Journal of the American Chemical Society* **1955**, *77*, 5450–5451.
- [44] van Beilen, J. B.; Funhoff, E. G. *Current Opinion in Biotechnology* **2005**, *16*, 308–314.
- [45] Nam, W. *Accounts of Chemical Research* **2007**, *40*, 522–531.
- [46] Meunier, B.; de Visser, S. P.; Shaik, S. *Chemical Reviews* **2004**, *104*, 3947–3980.
- [47] Denisov, I. G.; Makris, T. M.; Sligar, S. G.; Schlichting, I. *Chemical Reviews* **2005**, *105*, 2253–2278.
- [48] Shaik, S.; Cohen, S.; Wang, Y.; Chen, H.; Kumar, D.; Thiel, W. *Chemical Reviews* **2010**, *110*, 949–1017.

CHAPTER 9: BIBLIOGRAPHY

- [49] Ortiz de Montellano, P. R. *Chemical Reviews* **2010**, *110*, 932–948.
- [50] Ortiz de Montellano, P. R. In *Cytochrome P450 : structure, mechanism, and biochemistry*, 4th ed.; Ortiz de Montellano, P. R., Ed.; Springer International Publishing: New York, 2015; p 912.
- [51] Archakov, A. I.; Bachmanova, G. I. *Cytochrome P-450 and active oxygen*; Taylor & Francis, 1990; p 339.
- [52] Fertinger, C.; Hessenauer-Ilicheva, N.; Franke, A.; vanEldik, R. *Chemistry - A European Journal* **2009**, *15*, 13435–13440.
- [53] Franke, A.; Fertinger, C.; vanEldik, R. *Angewandte Chemie International Edition* **2008**, *47*, 5238–5242.
- [54] Jeong, Y. J.; Kang, Y.; Han, A.-R.; Lee, Y.-M.; Kotani, H.; Fukuzumi, S.; Nam, W. *Angewandte Chemie International Edition* **2008**, *47*, 7321–7324.
- [55] Li, X.-X.; Postils, V.; Sun, W.; Faponle, A. S.; Solà, M.; Wang, Y.; Nam, W.; de Visser, S. P. *Chemistry - A European Journal* **2017**, *23*, 6406–6418.
- [56] Groves, J. T.; McClusky, G. A. *Journal of the American Chemical Society* **1976**, *98*, 859–861.
- [57] van Beilen, J. B.; Panke, S.; Lucchini, S.; Franchini, A. G.; Röthlisberger, M.; Witholt, B. *Microbiology* **2001**, *147*, 1621–1630.
- [58] Smits, T. H.; Witholt, B.; van Beilen, J. B. *Antonie van Leeuwenhoek* **2003**, *84*, 193–200.
- [59] Austin, R. N.; Groves, J. T. *Metallomics* **2011**, *3*, 775–787.
- [60] Rojo, F. *Journal of bacteriology* **2005**, *187*, 19–22.
- [61] Lee, S.-K.; Nesheim, J. C.; Lipscomb, J. D. *The Journal of biological chemistry* **1993**, *268*, 21569–21577.
- [62] Shu, L.; Nesheim, J. C.; Kauffmann, K.; Münck, E.; Lipscomb, J. D.; Que, L. *Science* **1997**, *275*, 515–518.
- [63] Banerjee, R.; Proshlyakov, Y.; Lipscomb, J. D.; Proshlyakov, D. A. *Nature* **2015**, *518*, 431–434.
- [64] Ray, K.; Pfaff, F. F.; Wang, B.; Nam, W. *Journal of the American Chemical Society* **2014**, *136*, 13942–13958.
- [65] Gagnon, N.; Tolman, W. B. *Accounts of chemical research* **2015**, *48*, 2126–2131.
- [66] Solomon, E. I.; Heppner, D. E.; Johnston, E. M.; Ginsbach, J. W.; Cirera, J.; Qayyum, M.; Kieber-Emmons, M. T.; Kjaergaard, C. H.; Hadt, R. G.; Tian, L. *Chemical Reviews* **2014**, *114*, 3659–3853.
- [67] Bauer, I.; Knölker, H.-J. *Chemical Reviews* **2015**, *115*, 3170–3387.
- [68] Che, C.-M.; Lo, V. K.-Y.; Zhou, C.-Y.; Huang, J.-S. *Chemical Society Reviews* **2011**, *40*, 1950–1975.
- [69] Hohenberger, J.; Ray, K.; Meyer, K. *Nature Communications* **2012**, *3*, 720.
- [70] Groves, J. T.; Haushalter, R. C.; Nakamura, M.; Nemo, T. E.; Evans, B. J. *Journal of the American Chemical Society* **1981**, *103*, 2884–2886.
- [71] Fujii, H. *Coordination Chemistry Reviews* **2002**, *226*, 51–60.
- [72] Jung, C. *Biochimica et Biophysica Acta (BBA) - Proteins and Proteomics* **2011**, *1814*, 46–57.
- [73] Groves, J. T. *Journal of Inorganic Biochemistry* **2006**, *100*, 434–447.
- [74] Nam, W. *Accounts of Chemical Research* **2007**, *40*, 465–465.
- [75] Kang, Y.; Chen, H.; Jeong, Y. J.; Lai, W.; Bae, E. H.; Shaik, S.; Nam, W. *Chemistry - A European Journal* **2009**, *15*, 10039–10046.

CHAPTER 9: BIBLIOGRAPHY

- [76] Grapperhaus, C. A.; Mienert, B.; Bill, E.; Weyhermüller, T.; Wieghardt, K. *Inorganic Chemistry* **2000**, *39*, 5306–5317.
- [77] Rohde, J.-U.; In, J.-H.; Lim, M. H.; Brennessel, W. W.; Bukowski, M. R.; Stubna, A.; Münck, E.; Nam, W.; Que, L. *Science* **2003**, *299*, 1037–1039.
- [78] Klinker, E. J.; Kaizer, J.; Brennessel, W. W.; Woodrum, N. L.; Cramer, C. J.; Que, L. *Angewandte Chemie International Edition* **2005**, *44*, 3690–3694.
- [79] Kaizer, J.; Klinker, E. J.; Oh, N. Y.; Rohde, J.-U.; Song, W. J.; Stubna, A.; Kim, J.; Münck, E.; Nam, W.; Que, L. *Journal of the American Chemical Society* **2003**, *126*, 472–473.
- [80] Kleespies, S. T.; Oloo, W. N.; Mukherjee, A.; Que, L. *Inorganic Chemistry* **2015**, *54*, 5053–5064.
- [81] Comba, P.; Wunderlich, S. *Chemistry - A European Journal* **2010**, *16*, 7293–7299.
- [82] Wang, D.; Ray, K.; Collins, M. J.; Farquhar, E. R.; Frisch, J. R.; Gómez, L.; Jackson, T. A.; Kerscher, M.; Waleska, A.; Comba, P.; Costas, M.; Que, L. *Chem. Sci.* **2013**, *4*, 282–291.
- [83] Biswas, A. N.; Puri, M.; Meier, K. K.; Oloo, W. N.; Rohde, G. T.; Bominaar, E. L.; Münck, E.; Que, L. *Journal of the American Chemical Society* **2015**, *137*, 2428–2431.
- [84] Janardanan, D.; Wang, Y.; Schyman, P.; Que, L.; Shaik, S. *Angewandte Chemie International Edition* **2010**, *49*, 3342–3345.
- [85] de Visser, S. P. *Journal of the American Chemical Society* **2006**, *128*, 9813–9824.
- [86] Solomon, E. I.; Wong, S. D.; Liu, L. V.; Decker, A.; Chow, M. S. *Current Opinion in Chemical Biology* **2009**, *13*, 99–113.
- [87] Wong, S. D.; Bell, C. B.; Liu, L. V.; Kwak, Y.; England, J.; Alp, E. E.; Zhao, J.; Que, L.; Solomon, E. I. *Angewandte Chemie International Edition* **2011**, *50*, 3215–3218.
- [88] Srnec, M.; Wong, S. D.; Solomon, E. I. *Dalton Trans.* **2014**, *43*, 17567–17577.
- [89] Hirao, H.; Que, L.; Nam, W.; Shaik, S. *Chemistry - A European Journal* **2008**, *14*, 1740–1756.
- [90] Seo, M. S.; Kim, N. H.; Cho, K.-B.; So, J. E.; Park, S. K.; Clémancey, M.; Garcia-Serres, R.; Latour, J.-M.; Shaik, S.; Nam, W. *Chemical Science* **2011**, *2*, 1039–1045.
- [91] Geng, C.; Ye, S.; Neese, F. *Dalton Transactions* **2014**, *43*, 6079–6086.
- [92] Bordwell, F. G.; Cheng, J.; Ji, G. Z.; Satish, A. V.; Zhang, X. *Journal of the American Chemical Society* **1991**, *113*, 9790–9795.
- [93] Mayer, J. M. *Accounts of Chemical Research* **1998**, *31*, 441–450.
- [94] Prat, I.; Mathieson, J. S.; Güell, M.; Ribas, X.; Luis, J. M.; Cronin, L.; Costas, M. *Nature chemistry* **2011**, *3*, 788–93.
- [95] Engelmann, X.; Monte-Pérez, I.; Ray, K. *Angewandte Chemie International Edition* **2016**, *55*, 7632–7649.
- [96] Ye, S.; Geng, C.-Y.; Shaik, S.; Neese, F. *Physical Chemistry Chemical Physics* **2013**, *15*, 8017–8030.
- [97] Janardanan, D.; Usharani, D.; Chen, H.; Shaik, S. *The Journal of Physical Chemistry Letters* **2011**, *2*, 2610–2617.
- [98] Evans, M. G.; Polanyi, M. *Transactions of the Faraday Society* **1936**, *32*,

CHAPTER 9: BIBLIOGRAPHY

- 1333–1360.
- [99] Evans, M. G.; Polanyi, M. *Transactions of the Faraday Society* **1938**, *34*, 11–24.
- [100] Hirao, H.; Kumar, D.; Que, L.; Shaik, S. *Journal of the American Chemical Society* **2006**, *128*, 8590–606.
- [101] Ye, S.; Geng, C.-Y.; Shaik, S.; Neese, F. *Physical chemistry chemical physics : PCCP* **2013**, *15*, 8017–8030.
- [102] Decker, A.; Rohde, J.-U.; Klinker, E. J.; Wong, S. D.; Que, L.; Solomon, E. I. *Journal of the American Chemical Society* **2007**, *129*, 15983–96.
- [103] Geng, C.; Ye, S.; Neese, F. *Angewandte Chemie International Edition* **2010**, *49*, 5717–5720.
- [104] Postils, V.; Company, A.; Solà, M.; Costas, M.; Luis, J. M. *Inorganic chemistry* **2015**, *54*, 8223–36.
- [105] Klinker, E. J. High-valent Iron Compounds Supported by Pentadentate Ligands. Ph.D. thesis, University of Minnesota, 2005.
- [106] Cho, K. B.; Wu, X.; Lee, Y. M.; Kwon, Y. H.; Shaik, S.; Nam, W. *Journal of the American Chemical Society* **2012**, *134*, 20222–20225.
- [107] Kwon, E.; Cho, K.-B.; Hong, S.; Nam, W. *Chemical communications (Cambridge, England)* **2014**, *50*, 5572–5.
- [108] Doyle, M. P.; McKervey, M. A.; Ye, T. *Modern catalytic methods for organic synthesis with diazo compounds : from cyclopropanes to ylides*; Wiley: New York, 1998; p 652.
- [109] Davies, H. M. L.; Manning, J. R. *Nature* **2008**, *451*, 417–424.
- [110] Liu, Z.; Wang, J. *The Journal of Organic Chemistry* **2013**, *78*, 10024–10030.
- [111] Xia, Y.; Liu, Z.; Feng, S.; Zhang, Y.; Wang, J. *The Journal of Organic Chemistry* **2015**, *80*, 223–236.
- [112] Doyle, M. P.; Duffy, R.; Ratnikov, M.; Zhou, L. *Chemical Reviews* **2010**, *110*, 704–724.
- [113] Cheng, Q.; Doyle, M. P. In *Advances in organometallic chemistry*. 66, 1st ed.; Pérez, P. J., Ed.; Zoe Kruze: Oxford, 2016; Chapter One, p 396.
- [114] Scott, L. T.; DeCicco, G. J. *Journal of the American Chemical Society* **1974**, *96*, 322–323.
- [115] Wulfman, D. S.; McDaniel, R. S.; Peace, B. W. *Tetrahedron* **1976**, *32*, 1241–1249.
- [116] Kennedy, M.; McKervey, M. A.; Maguire, A. R.; Roos, G. H. P. *J. Chem. Soc., Chem. Commun.* **1990**, *0*, 361–362.
- [117] Davies, H. M. L.; Bruzinski, P. R.; Lake, D. H.; Kong, N.; Fall, M. J. *Journal of the American Chemical Society* **1996**, *118*, 6897–6907.
- [118] Watanabe, N.; Ogawa, T.; Ohtake, Y.; Ikegami, S.; Hashimoto, S.-i. *Synlett* **1996**, 85–86.
- [119] Espino, C. G.; Fiori, K. W.; Kim, M.; Bois, J. D. *Journal of the American Chemical Society* **2004**, *126*, 15378–15379.
- [120] Wenkert, E.; Davis, L. L.; Mylari, B. L.; Solomon, M. F.; Da Silva, R. R.; Shulman, S.; Warnet, R. J.; Ceccherelli, P.; Curini, M.; Pellicciari, R. *The Journal of Organic Chemistry* **1982**, *47*, 3242–3247.
- [121] Padwa, A.; Austin, D. J.; Price, A. T.; Semones, M. A.; Doyle, M. P.; Protopopova, M. N.; Winchester, W. R.; Tran, A. *Journal of the American*

CHAPTER 9: BIBLIOGRAPHY

- Chemical Society* **1993**, *115*, 8669–8680.
- [122] Doyle, M. P.; Kalinin, A. V.; Ene, D. G. *Journal of the American Chemical Society* **1996**, *118*, 8837–8846.
- [123] Doyle, M. P.; Dyatkin, A. B.; Protopopova, M. N.; Yang, C. I.; Miertschin, C. S.; Winchester, W. R.; Simonsen, S. H.; Lynch, V.; Ghosh, R. *Recueil des Travaux Chimiques des Pays-Bas* **2010**, *114*, 163–170.
- [124] Díaz-Requejo, M. M.; Belderraín, T. R.; Nicasio, M. C.; Trofimenko, S.; Pérez, P. J. *Journal of the American Chemical Society* **2002**, *124*, 896–897.
- [125] Dias, H. V. R.; Lu, H.-L.; Kim, H.-J.; Polach, S. A.; Goh, T. K. H. H.; Browning, R. G.; Lovely, C. J. *Organometallics* **2002**, *21*, 1466–1473.
- [126] Dias, H. V. R.; Wang, Z.; Jin, W. *Inorganic Chemistry* **1997**, *36*, 6205–6215.
- [127] Davies, H. M. L.; Stafford, D. G.; Hansen, T. *Organic Letters* **1999**, *1*, 233–236.
- [128] Müller, P.; Tohill, S. *Tetrahedron* **2000**, *56*, 1725–1731.
- [129] Davies, H. M. L.; Hansen, T.; Hopper, D. W.; Panaro, S. A. *Journal of the American Chemical Society* **1999**, *121*, 6509–6510.
- [130] Davies, H. M. L.; Beckwith, R. E. J.; Antoulinakis, E. G.; Jin, Q. *The Journal of organic chemistry* **2003**, *68*, 6126–6132.
- [131] Davies, H. M.; Gregg, T. M. *Tetrahedron Letters* **2002**, *43*, 4951–4953.
- [132] Davies, H. M.; Walji, A. M.; Townsend, R. J. *Tetrahedron Letters* **2002**, *43*, 4981–4983.
- [133] Rosenfeld, M. J.; Shankar, B. K. R.; Shechter, H. *The Journal of Organic Chemistry* **1988**, *53*, 2699–2705.
- [134] Yang, M.; Webb, T. R.; Livant, P. *The Journal of organic chemistry* **2001**, *66*, 4945–4949.
- [135] Fructos, M. R.; de Frémont, P.; Nolan, S. P.; Díaz-Requejo, M. M.; Pérez, P. J. *Organometallics* **2006**, *25*, 2237–2241.
- [136] Fructos, M. R.; Belderrain, T. R.; de Frémont, P.; Scott, N. M.; Nolan, S. P.; Díaz-Requejo, M. M.; Pérez, P. J. *Angewandte Chemie International Edition* **2005**, *44*, 5284–5288.
- [137] Rivilla, I.; Gomez-Emeterio, B. P.; Fructos, M. R.; Diaz-Requejo, M. M.; Perez, P. J. *Organometallics* **2011**, *30*, 2855–2860.
- [138] Delgado-Rebollo, M.; Beltrán, Á.; Prieto, A.; Mar Díaz-Requejo, M.; Echavarren, A. M.; Pérez, P. J. *European Journal of Inorganic Chemistry* **2012**, *2012*, 1380–1386.
- [139] Fructos, M. R.; Besora, M.; Braga, A. A. C.; Díaz-Requejo, M. M.; Maseras, F.; Pérez, P. J. *Organometallics* **2017**, *36*, 172–179.
- [140] Conde, A.; Sabenya, G.; Rodríguez, M.; Postils, V.; Luis, J. M.; Díaz-Requejo, M. M.; Costas, M.; Pérez, P. J. *Angewandte Chemie International Edition* **2016**, *55*, 6530–6534.
- [141] Yu, Z.; Ma, B.; Chen, M.; Wu, H.-H.; Liu, L.; Zhang, J. *Journal of the American Chemical Society* **2014**, *136*, 6904–6907.
- [142] Xi, Y.; Su, Y.; Yu, Z.; Dong, B.; McClain, E. J.; Lan, Y.; Shi, X. *Angewandte Chemie International Edition* **2014**, *53*, 9817–9821.
- [143] Osako, T.; Panichakul, D.; Uozumi, Y. *Organic Letters* **2012**, *14*, 194–197.
- [144] Chen, C.; Zhu, S.-F.; Liu, B.; Wang, L.-X.; Zhou,; Zhou, Q.-L. *Journal of*

CHAPTER 9: BIBLIOGRAPHY

- the American Chemical Society* **2007**, *129*, 12616–12617.
- [145] Xie, X.-L.; Zhu, S.-F.; Guo, J.-X.; Cai, Y.; Zhou, Q.-L. *Angewandte Chemie International Edition* **2014**, *53*, 2978–2981.
- [146] Li, Y.; Huang, J.-S.; Zhou, Z.-Y.; Che, C.-M.; You, X.-Z. *Journal of the American Chemical Society* **2002**, *124*, 13185–13193.
- [147] Dzik, W. I.; Xu, X.; Zhang, X. P.; Reek, J. N. H.; de Bruin, B. *Journal of the American Chemical Society* **2010**, *132*, 10891–10902.
- [148] Dzik, W. I.; Zhang, X. P.; de Bruin, B. *Inorganic Chemistry* **2011**, *50*, 9896–9903.
- [149] Khade, R. L.; Zhang, Y. *Journal of the American Chemical Society* **2015**, *137*, 7560–7563.
- [150] Khade, R. L.; Fan, W.; Ling, Y.; Yang, L.; Oldfield, E.; Zhang, Y. *Angewandte Chemie International Edition* **2014**, *53*, 7574–7578.
- [151] Sharon, D. A.; Mallick, D.; Wang, B.; Shaik, S. *Journal of the American Chemical Society* **2016**, *138*, 9597–9610.
- [152] Liu, Y.; Xu, W.; Zhang, J.; Fuller, W.; Schulz, C. E.; Li, J. *Journal of the American Chemical Society* **2017**, *139*, 5023–5026.
- [153] Das, B. G.; Chirila, A.; Tromp, M.; Reek, J. N. H.; de Bruin, B. *Journal of the American Chemical Society* **2016**, *138*, 8968–8975.
- [154] Renata, H.; Wang, Z. J.; Kitto, R. Z.; Arnold, F. H. *Catalysis Science and Technology* **2014**, *4*, 3640–3643.
- [155] Coelho, P. S.; Brustad, E. M.; Kannan, A.; Arnold, F. H. *Science* **2013**, *339*, 307–310.
- [156] Liu, Y.; Yu, Z.; Luo, Z.; Zhang, J. Z.; Liu, L.; Xia, F. *The Journal of Physical Chemistry A* **2016**, *120*, 1925–1932.
- [157] Nakamura, E.; Yoshikai, N.; Yamanaka, M. *Journal of the American Chemical Society* **2002**, *124*, 7181–7192.
- [158] Braga, A. A.; Maseras, F.; Urbano, J.; Caballero, A.; Díaz-Requejo, M. M.; Pérez, P. J. *Organometallics* **2006**, *25*, 5292–5300.
- [159] Liu, Y.; Yu, Z.; Zhang, J. Z.; Liu, L.; Xia, F.; Zhang, J. *Chemical Science* **2016**, *7*, 1988–1995.
- [160] Mendeleev, D. I. *Principles of Chemistry*; 1870.
- [161] Meyer, J. L. *Justus Liebigs Annalen der Chemie* **1870**, *Supp. 7*, 354–364.
- [162] Wöhler, F. *Grundriss der Chemie: unorganische Chemie*, 3rd ed.; Duncker und Humblot: Berlin, 1835; p 187.
- [163] Latimer, W. M. *The Oxidation States of the Elements and Their Potentials in Aqueous Solutions*, 2nd ed.; Prentice-Hall, Incorporated: New York, 1938; p 352.
- [164] Jørgensen, C. K. *Oxidation Numbers and Oxidation States*; Springer-Verlag: New York, 1969.
- [165] Hegedus, L. S. *Transition Metals in the Synthesis of Complex Organic Molecules*, 2nd ed.; University Science Books: Sausalito, California, 1999; p 337.
- [166] IUPAC. Compendium of Chemical Terminology. 1997; <http://goldbook.iupac.org>.
- [167] IUPAC. Oxidation State. 1990; <https://www.iupac.org/goldbook/004365.pdf>.
- [168] Jansen, M.; Wedig, U. *Angewandte Chemie International Edition* **2008**, *47*, 10026–10029.

CHAPTER 9: BIBLIOGRAPHY

- [169] Altun, A.; Shaik, S.; Thiel, W. *Journal of the American Chemical Society* **2007**, *129*, 8978–8987.
- [170] Ogliaro, F.; de Visser, S. P.; Groves, J. T.; Shaik, S. *Angewandte Chemie International Edition* **2001**, *40*, 2874–2878.
- [171] Steinborn, D. *Journal of Chemical Education* **2004**, *81*, 1148–1154.
- [172] Loock, H.-P. *Journal of Chemical Education* **2011**, *88*, 282–283.
- [173] Karen, P.; Mcardle, P.; Takats, J. *Pure and Applied Chemistry* **2014**, *86*, 1017–1081.
- [174] IUPAC, Oxidation State. 2017; <http://goldbook.iupac.org/004365.html>.
- [175] Karen, P. *Angewandte Chemie International Edition* **2015**, *54*, 4716–4726.
- [176] Kaupp, M.; von Schnering, H. G. *Angewandte Chemie International Edition* **1995**, *34*, 986–986.
- [177] Allen, L. C. *Journal of the American Chemical Society* **1989**, *111*, 9003–9014.
- [178] Mann, J. B.; Meek, T. L.; Allen, L. C. *Journal of the American Chemical Society* **2000**, *122*, 2780–2783.
- [179] Mann, J. B.; Meek, T. L.; Knight, E. T.; Capitani, J. F.; Allen, L. C. *Journal of the American Chemical Society* **2000**, *122*, 5132–5137.
- [180] Pritchard, H. O.; Skinner, H. A. *Chemical Reviews* **1955**, *55*, 745–786.
- [181] Sen, K. D.; Alonso, J. A.; Jørgensen, C. K.; Balbas, L. C.; Bartolotti, L. J.; Bergmann, D.; Bohm, M. C.; Galvan, M.; Gazquez, J. L.; Hinze, J.; Mortier, W. J.; Mullay, J.; Schmidt, P. C.; Vela, A. M. In *Electronegativity. Structure and bonding (Book 66)*; Jorgensen, C. K., Sen, K. D., Eds.; Springer Berlin: Heidelberg, 1987; p 198.
- [182] Bergmann, D.; Hinze, J. *Angewandte Chemie International Edition* **1996**, *35*, 150–163.
- [183] Usón, R.; Forniés, J.; Espinet, P.; Fortuño, C.; Tomas, M.; Welch, A. J. *J. Chem. Soc., Dalton Trans.* **1988**, *0*, 3005–3009.
- [184] Sircoglou, M.; Bontemps, S.; Mercy, M.; Saffon, N.; Takahashi, M.; Bouhadir, G.; Maron, L.; Bourissou, D. *Angewandte Chemie International Edition* **2007**, *46*, 8583–8586.
- [185] Moret, M.-E.; Peters, J. C. *Angewandte Chemie International Edition* **2011**, *50*, 2063–2067.
- [186] Cundari, T. R.; Gordon, M. S. *Journal of the American Chemical Society* **1991**, *113*, 5231–5243.
- [187] Vyboishchikov, S. F.; Frenking, G. *Chemistry - A European Journal* **1998**, *4*, 1428–1438.
- [188] Cases, M.; Frenking, G.; Duran, M.; Solà, M. *Organometallics* **2002**, *21*, 4182–4191.
- [189] Frenking, G.; Solà, M.; Vyboishchikov, S. F. *Journal of Organometallic Chemistry* **2005**, *690*, 6178–6204.
- [190] Dapprich, S.; Frenking, G. *The Journal of Physical Chemistry* **1995**, *99*, 9352–9362.
- [191] Hodgson, D. J.; Payne, N. C.; McGinnety, J. A.; Pearson, R. G.; Ibers, J. A. *Journal of the American Chemical Society* **1968**, *90*, 4486–4488.
- [192] Pierpont, C. G.; Eisenberg, R. *Inorganic Chemistry* **1972**, *11*, 1088–1094.
- [193] Bieseimer, F.; Müller, U.; Massa, W. *Zeitschrift für anorganische und allgemeine Chemie* **2002**, *628*, 1933–1934.

CHAPTER 9: BIBLIOGRAPHY

- [194] Hammerl, A.; Klapötke, T. M.; Schwerdtfeger, P. *Chemistry - A European Journal* **2003**, *9*, 5511–5519.
- [195] Menconi, G.; Kaltsoyannis, N. *Organometallics* **2005**, *24*, 1189–1197.
- [196] Zeinstra, J.; De Boer, J. *Journal of Organometallic Chemistry* **1973**, *54*, 207–211.
- [197] Jørgensen, C. K. *Zeitschrift für anorganische und allgemeine Chemie* **1986**, *540*, 91–105.
- [198] Palenik, G. J. *Inorganic chemistry* **1997**, *36*, 3394–3397.
- [199] Wood, R. M.; Palenik, G. J. *Inorganic chemistry* **1998**, *37*, 4149–4151.
- [200] Sit, P. H.-L.; Car, R.; Cohen, M. H.; Selloni, A. *Inorganic Chemistry* **2011**, *50*, 10259–10267.
- [201] Mulliken, R. S. *The Journal of Chemical Physics* **1955**, *23*, 1833–1840.
- [202] Löwdin, P. *The Journal of Chemical Physics* **1950**, *18*, 365–375.
- [203] Reed, A. E.; Curtiss, L. A.; Weinhold, F. *Chemical Reviews* **1988**, *88*, 899–926.
- [204] Bayly, C. I.; Cieplak, P.; Cornell, W.; Kollman, P. A. *The Journal of Physical Chemistry* **1993**, *97*, 10269–10280.
- [205] Gabrieli, A.; Sant, M.; Demontis, P.; Suffritti, G. B. *Journal of Chemical Theory and Computation* **2015**, *11*, 3829–3843.
- [206] Campana, C.; Mussard, B.; Woo, T. K. *Journal of Chemical Theory and Computation* **2009**, *5*, 2866–2878.
- [207] Chen, D.-L.; Stern, A. C.; Space, B.; Johnson, J. K. *The Journal of Physical Chemistry A* **2010**, *114*, 10225–10233.
- [208] Resta, R. *Nature* **2008**, *453*, 735.
- [209] Raebiger, H.; Lany, S.; Zunger, A. *Nature* **2008**, *453*, 763–766.
- [210] Aullón, G.; Alvarez, S. *Theoretical Chemistry Accounts* **2009**, *123*, 67–73.
- [211] Koch, D.; Manzhos, S. *The Journal of Physical Chemistry Letters* **2017**, *8*, 1593–1598.
- [212] Ivanic, J.; Atchity, G. J.; Ruedenberg, K. *Theoretical Chemistry Accounts* **2008**, *120*, 281–294.
- [213] Sit, P. H.-L.; Zipoli, F.; Chen, J.; Car, R.; Cohen, M. H.; Selloni, A. *Chemistry - A European Journal* **2011**, *17*, 12136–12143.
- [214] Vidossich, P.; Lledós, A. *Dalton Transactions* **2014**, *43*, 11145.
- [215] Löwdin, P.-O.; Slater, J. C. In *Quantum theory of atoms, molecules, and the solid state.*; Per-Olov Löwdin, Ed.; Academic Press: New York, 1966; p 641.
- [216] Marzari, N.; Vanderbilt, D. *Physical Review B* **1997**, *56*, 12847–12865.
- [217] Thom, A. J. W.; Sundstrom, E. J.; Head-Gordon, M. *Physical Chemistry Chemical Physics* **2009**, *11*, 11297–11304.
- [218] Edmiston, C.; Ruedenberg, K. *Reviews of Modern Physics* **1963**, *35*, 457–464.
- [219] Yamaguchi, K.; Yamanaka, S.; Isobe, H.; Shoji, M.; Koisumi, K.; Kitagawa, Y.; Kawakami, T.; Okumura, M. *Polyhedron* **2007**, *26*, 2216–2224.
- [220] Knizia, G. *Journal of Chemical Theory and Computation* **2013**, *9*, 4834–4843.
- [221] Ramos-Cordoba, E.; Postils, V.; Salvador, P. *Journal of Chemical Theory and Computation* **2015**, *11*, 1501–1508.
- [222] Mayer, I. *The Journal of Physical Chemistry* **1996**, *100*, 6249–6257.
- [223] Jensen, F. *Introduction to computational chemistry*, second ed ed.; John

CHAPTER 9: BIBLIOGRAPHY

- Wiley & Sons, Inc.: Hoboken, NJ, USA, 2007; p 599.
- [224] von Niessen, W. *The Journal of Chemical Physics* **1972**, *56*, 4290–4297.
- [225] Foster, J.; Boys, S. *Reviews of Modern Physics* **1960**, *32*, 300–302.
- [226] Bader, R. F. W. *Atoms in molecules : a quantum theory*, first edit ed.; Clarendon Press: New York, 1990; p 438.
- [227] Gadre, S. R.; Shirsat, R. N. *Electrostatics of atoms and molecules*, 1st ed.; Universities Press: Hyderabad, India, 2000; p 134.
- [228] Becke, A. D.; Edgecombe, K. E. *The Journal of Chemical Physics* **1990**, *92*, 5397–5403.
- [229] Morokuma, K. *The Journal of Chemical Physics* **1971**, *55*, 1236–1244.
- [230] Ziegler, T.; Rauk, A. *Theoretica Chimica Acta* **1977**, *46*, 1–10.
- [231] Francisco, E.; Pendás, A. M.; Blanco, M. A. *Journal of Chemical Theory and Computation* **2006**, *2*, 90–102.
- [232] Salvador, P.; Duran, M.; Mayer, I. *The Journal of Chemical Physics* **2001**, *115*, 1153–1157.
- [233] Poater, J.; Fradera, X.; Duran, M.; Solà, M. *Chemistry - A European Journal* **2003**, *9*, 400–406.
- [234] Heyndrickx, W.; Salvador, P.; Bultinck, P.; Solà, M.; Matito, E. *Journal of Computational Chemistry* **2011**, *32*, 386–395.
- [235] Williams, D. In *The Magnetic Properties of Matter*; American Elsevier,, Ed.; 1966; p Chap. 4.7.
- [236] Le Fevre, R. J. W. *Dipole Moments: Their Measurement and Application in Chemistry*, third edit ed.; Methuen & Co.: London, 1953; p 140.
- [237] Ramos-Cordoba, E.; Postils, V.; Salvador, P. *Journal of Chemical Theory and Computation* **2015**, *11*, 1501–1508.
- [238] Ellaboudy, A.; Dye, J. L.; Smith, P. B. *Journal of the American Chemical Society* **1983**, *105*, 6490–6491.
- [239] Dye, J. L. *Accounts of chemical research* **2009**, *42*, 1564–1572.
- [240] Matsuishi, S.; Toda, Y.; Miyakawa, M.; Hayashi, K.; Kamiya, T.; Hirano, M.; Tanaka, I.; Hosono, H. *Science (New York, N.Y.)* **2003**, *301*, 626–9.
- [241] Redko, M. Y.; Jackson, J. E.; Huang, R. H.; Dye, J. L. *Journal of the American Chemical Society* **2005**, *127*, 12416–12422.
- [242] Toda, Y.; Yanagi, H.; Ikenaga, E.; Kim, J.; Kobata, M.; Ueda, S.; Kamiya, T.; Hirano, M.; Kobayashi, K.; Hosono, H. *Advanced Materials* **2007**, *19*, 3564–3569.
- [243] Toda, Y.; Matsuishi, S.; Hayashi, K.; Ueda, K.; Kamiya, T.; Hirano, M.; Hosono, H. *Advanced Materials* **2004**, *16*, 685–689.
- [244] Yanagi, H.; Kim, K.-B.; Koizumi, I.; Kikuchi, M.; Hiramatsu, H.; Miyakawa, M.; Kamiya, T.; Hirano, M.; Hosono, H. *The Journal of Physical Chemistry C* **2009**, *113*, 18379–18384.
- [245] Toda, Y.; Hirayama, H.; Kuganathan, N.; Torrisi, A.; Sushko, P. V.; Hosono, H. *Nature Communications* **2013**, *4*, 2378.
- [246] Kitano, M.; Inoue, Y.; Yamazaki, Y.; Hayashi, F.; Kanbara, S.; Matsuishi, S.; Yokoyama, T.; Kim, S.-W.; Hara, M.; Hosono, H. *Nature chemistry* **2012**, *4*, 934–40.
- [247] Kitano, M.; Inoue, Y.; Yamazaki, Y.; Hayashi, F.; Kanbara, S.; Matsuishi, S.; Yokoyama, T.; Kim, S.-W.; Hara, M.; Hosono, H. *Nature Chemistry* **2012**, *4*, 934–940.

CHAPTER 9: BIBLIOGRAPHY

- [248] Chen, W.; Li, Z.-R.; Wu, D.; Li, Y.; Sun, C.-C.; Gu, F. L. *Journal of the American Chemical Society* **2005**, *127*, 10977–10981.
- [249] Li, Z.-J.; Wang, F.-F.; Li, Z.-R.; Xu, H.-L.; Huang, X.-R.; Wu, D.; Chen, W.; Yu, G.-T.; Gu, F. L.; Aoki, Y. *Physical Chemistry Chemical Physics* **2009**, *11*, 402–408.
- [250] Lee, K.; Kim, S. W.; Toda, Y.; Matsuishi, S.; Hosono, H. *Nature* **2013**, *494*, 336–40.
- [251] Chen, G.; Bai, Y.; Li, H.; Li, Y.; Wang, Z.; Ni, Q.; Liu, L.; Wu, F.; Yao, Y.; Wu, C. *ACS Applied Materials & Interfaces* **2017**, *9*, 6666–6669.
- [252] Zhang, X.; Xiao, Z.; Lei, H.; Toda, Y.; Matsuishi, S.; Kamiya, T.; Ueda, S.; Hosono, H. *Chemistry of Materials* **2014**, *26*, 6638–6643.
- [253] Lu, Y.; Li, J.; Tada, T.; Toda, Y.; Ueda, S.; Yokoyama, T.; Kitano, M.; Hosono, H. *Journal of the American Chemical Society* **2016**, *138*, 3970–3973.
- [254] Mizoguchi, H.; Okunaka, M.; Kitano, M.; Matsuishi, S.; Yokoyama, T.; Hosono, H. *Inorganic Chemistry* **2016**, *55*, 8833–8838.
- [255] Postils, V. *Revista de Societat Catalana de Química* **2015**, *14*, 83–90.
- [256] Toda, Y.; Kubota, Y.; Hirano, M.; Hirayama, H.; Hosono, H. *ACS nano* **2011**, *5*, 1907–14.
- [257] McCracken, J.; Shin, D. H.; Dye, J. L. *Applied Magnetic Resonance* **1992**, *3*, 305–316.
- [258] Kuchenmeister, M. E.; Dye, J. L. *Journal of the American Chemical Society* **1989**, *111*, 935–938.
- [259] Oh, J. S.; Kang, C.-J.; Kim, Y. J.; Sinn, S.; Han, M.; Chang, Y. J.; Park, B.-G.; Kim, S. W.; Min, B. I.; Kim, H.-D.; Noh, T. W. *Journal of the American Chemical Society* **2016**, *138*, 2496–9.
- [260] Bader, R. F. W. *Chemical Reviews* **1991**, *91*, 893–928.
- [261] Postils, V.; Garcia-Borràs, M.; Solà, M.; Luis, J. M.; Matito, E. *Chemical communications* **2015**, *51*, 4865–4868.
- [262] Pendás, A. M.; Blanco, M. A.; Costales, A.; Sánchez, P. M.; Luaña, V. *Physical Review Letters* **1999**, *83*, 1930–1933.
- [263] Silvi, B.; Savin, A. *Nature* **1994**, *371*, 683–686.
- [264] Johnson, E. R.; Keinan, S.; Mori-Sanchez, P.; Contreras-Garcia, J.; Cohen, A. J.; Yang, W. *Journal of the American Chemical Society* **2010**, *132*, 6498–6506.
- [265] Dale, S. G.; Johnson, E. R. *Physical Chemistry Chemical Physics* **2016**, *18*, 27326–27335.
- [266] Kumar, A.; Gadre, S. R. *Physical Chemistry Chemical Physics* **2015**, *17*, 15030–15035.
- [267] Kumar, A.; Gadre, S. R.; Mohan, N.; Suresh, C. H. *The Journal of Physical Chemistry A* **2014**, *118*, 526–532.
- [268] Dale, S. G.; Johnson, E. R. *Physical Chemistry Chemical Physics* **2017**, *19*, 12816–12825.
- [269] Inoshita, T.; Jeong, S.; Hamada, N.; Hosono, H. *Physical Review X* **2014**, *4*, 031023.
- [270] Zhang, Y.; Xiao, Z.; Kamiya, T.; Hosono, H. *The Journal of Physical Chemistry Letters* **2015**, *6*, 4966–4971.
- [271] Pickard, C. J.; Needs, R. J. *Physical Review Letters* **2009**, *102*, 146401.
- [272] Ma, Y.; Eremets, M.; Oganov, A. R.; Xie, Y.; Trojan, I.; Medvedev, S.;

CHAPTER 9: BIBLIOGRAPHY

- Lyakhov, A. O.; Valle, M.; Prakapenka, V. *Nature* **2009**, *458*, 182–185.
- [273] Pickard, C. J.; Needs, R. J. *Nature Materials* **2010**, *9*, 624–627.
- [274] Li, P.; Gao, G.; Wang, Y.; Ma, Y. *The Journal of Physical Chemistry C* **2010**, *114*, 21745–21749.
- [275] Miao, M.-S.; Hoffmann, R. *Accounts of Chemical Research* **2014**, *47*, 1311–1317.
- [276] Miao, M.-s.; Hoffmann, R. *Journal of the American Chemical Society* **2015**, *137*, 3631–3637.
- [277] Garcia-Borràs, M.; Solà, M.; Luis, J. M.; Kirtman, B. *Journal of Chemical Theory and Computation* **2012**, *8*, 2688–2697.
- [278] Wang, Y.-F.; Li, Z.-R.; Wu, D.; Sun, C.-C.; Gu, F.-L. *Journal of Computational Chemistry* **2010**, *31*, 195–203.
- [279] Dale, S. G.; Otero-de-la Roza, A.; Johnson, E. R. *Physical Chemistry Chemical Physics* **2014**, *16*, 14584–14593.
- [280] Marqués, M.; Ackland, G. J.; Lundegaard, L. F.; Stinton, G.; Nemes, R. J.; McMahon, M. I.; Contreras-García, J. *Physical Review Letters* **2009**, *103*, 115501.
- [281] Neese, F. *Coordination Chemistry Reviews* **2009**, *253*, 526–563.
- [282] Neese, F. *JBIC Journal of Biological Inorganic Chemistry* **2006**, *11*, 702–711.
- [283] Ghosh, A. *JBIC Journal of Biological Inorganic Chemistry* **2006**, *11*, 712–724.
- [284] Noodleman, L.; Han, W.-G. *JBIC Journal of Biological Inorganic Chemistry* **2006**, *11*, 674–694.
- [285] Siegbahn, P. E. M. In *Advances in Chemical Physics: New Methods in Computational Quantum Mechanics*; Prigogine, I., Rice, S. A., Eds.; John Wiley & Sons, Inc.: Hoboken, NJ, USA, 1996; Chapter 93, pp 333–387.
- [286] Riplinger, C.; Sandhoefer, B.; Hansen, A.; Neese, F. *The Journal of Chemical Physics* **2013**, *139*, 134101–134113.
- [287] Wang, Y. A.; Govind, N.; Carter, E. A. *Physical Review B* **1999**, *60*, 16350–16358.
- [288] Iyengar, S. S.; Ernzerhof, M.; Maximoff, S. N.; Scuseria, G. E. *Physical Review A* **2001**, *63*, 052508.
- [289] Kohn, W.; Sham, L. J. *Physical Review* **1965**, *140*.
- [290] Car, R. *Nature Chemistry* **2016**, *8*, 820–821.
- [291] Perdew, J. P.; Ruzsinszky, A.; Tao, J.; Staroverov, V. N.; Scuseria, G. E.; Csonka, G. I. *The Journal of Chemical Physics* **2005**, *123*, 062201.
- [292] Siegbahn, P. E. M. *JBIC Journal of Biological Inorganic Chemistry* **2006**, *11*, 695–701.
- [293] Vydrov, O. A.; Scuseria, G. E. *The Journal of Chemical Physics* **2005**, *122*, 184107.
- [294] Fouqueau, A.; Mer, S.; Casida, M. E.; Lawson Daku, L. M.; Hauser, A.; Mineva, T.; Neese, F. *The Journal of Chemical Physics* **2004**, *120*, 9473–9486.
- [295] Fouqueau, A.; Casida, M. E.; Lawson Daku, L. M.; Hauser, A.; Neese, F. *The Journal of Chemical Physics* **2005**, *122*, 044110.
- [296] Poater, J.; Solà, M.; Rimola, A.; Rodríguez-Santiago, L.; Sodupe, M. *The Journal of Physical Chemistry A* **2004**, *108*, 6072–6078.
- [297] Guell, M.; Luis, J. M.; Rodríguez-Santiago, L.; Sodupe, M.; Sola, M. *The*

CHAPTER 9: BIBLIOGRAPHY

- Journal of Physical Chemistry A* **2009**, *113*, 1308–1317.
- [298] Grimme, S. *Wiley Interdisciplinary Reviews: Computational Molecular Science* **2011**, *1*, 211–228.
- [299] Grimme, S.; Antony, J.; Ehrlich, S.; Krieg, H. *The Journal of Chemical Physics* **2010**, *132*, 154104.
- [300] Grimme, S.; Ehrlich, S.; Goerigk, L. *Journal of Computational Chemistry* **2011**, *32*, 1456–1465.
- [301] Jurecka, P.; Cerný, J.; Hobza, P.; Salahub, D. R. *Journal of Computational Chemistry* **2007**, *28*, 555–569.
- [302] Neugebauer, J.; Hess, B. A. *The Journal of Chemical Physics* **2003**, *118*, 7215.
- [303] Becke, A. *J. Chem. Phys.* **1993**, *98*, 5648–5652.
- [304] Lee, C.; Yang, W.; Parr, R. G. *Physical Review B* **1988**, *37*, 785–789.
- [305] Schultz, N. E.; Zhao, Y.; Truhlar, D. G. *The Journal of Physical Chemistry A* **2005**, *109*, 11127–11143.
- [306] Koch, W.; Holthausen, M. C. *A Chemist's Guide to Density Functional Theory*, second ed. ed.; Wiley-VCH Verlag GmbH: Weinheim, FRG, 2001.
- [307] Curtiss, L. A.; Raghavachari, K.; Redfern, P. C.; Pople, J. A. *The Journal of Chemical Physics* **1997**, *106*, 1063–1079.
- [308] Curtiss, L. A.; Raghavachari, K.; Redfern, P. C.; Pople, J. A. *The Journal of Chemical Physics* **2000**, *112*, 7374–7383.
- [309] Bassan, A.; Blomberg, M. R.; Borowski, T.; Siegbahn, P. E. *Journal of Inorganic Biochemistry* **2006**, *100*, 727–743.
- [310] Jensen, K. P.; Ryde, U. *The Journal of Physical Chemistry A* **2003**, *107*, 7539–7545.
- [311] Ghosh, A.; Vangberg, T.; Gonzalez, E.; Taylor, P. *Journal of Porphyrins and Phthalocyanines* **2001**, *05*, 345–356.
- [312] Ghosh, A.; Gonzalez, E. *Israel Journal of Chemistry* **2000**, *40*, 1–8.
- [313] De Angelis, F.; Jin, N.; Car, R.; Groves, J. T. *Inorganic chemistry* **2006**, *45*, 4268–4276.
- [314] Swart, M.; Groenhof, A. R.; Ehlers, A. W.; Lammertsma, K. *The Journal of Physical Chemistry A* **2004**, *108*, 5479–5483.
- [315] Solà, M.; Mestres, J.; Carbó, R.; Duran, M. *The Journal of Chemical Physics* **1996**, *104*, 636–647.
- [316] Cramer, C. J. *Essentials of computational chemistry: theories and models*, second ed. ed.; John Wiley & Sons: Chichester, West Sussex, England, 2004; p 596.
- [317] Prigogine, I., Rice, S. A., Eds. *Advances in Chemical Physics*; John Wiley & Sons, Inc.: Hoboken, NJ, USA, 1999; Vol. 106.
- [318] Marcus, R. A. *The Journal of Chemical Physics* **1956**, *24*, 966–78.
- [319] Marcus, R. A. *The Journal of Chemical Physics* **1965**, *43*, 679–701.
- [320] Johansson, A. J.; Blomberg, M. R. A.; Siegbahn, P. E. M. *The Journal of chemical physics* **2008**, *129*, 154301.
- [321] Yamaguchi, K.; Jensen, F.; Dorigo, A.; Houk, K. *Chemical Physics Letters* **1988**, *149*, 537–542.
- [322] Wittbrodt, J. M.; Schlegel, H. B. *JOURNAL OF CHEMICAL PHYSICS* **1996**, *105*, 6574–6577.
- [323] Soda, T.; Kitagawa, Y.; Onishi, T.; Takano, Y.; Shigeta, Y.; Nagao, H.; Yoshioka, Y.; Yamaguchi, K. *Chemical Physics Letters* **2000**, *319*, 223–230.

CHAPTER 9: BIBLIOGRAPHY

- [324] Noodleman, L.; Peng, C.; Case, D.; Mouesca, J.-M. *Coordination Chemistry Reviews* **1995**, *144*, 199–244.
- [325] Lewis, G. N. *Journal of the American Chemical Society* **1916**, *38*, 762–785.
- [326] Hirshfeld, F. L. *Theoretica Chimica Acta* **1977**, *44*, 129–138.
- [327] Bultinck, P.; Van Alsenoy, C.; Ayers, P. W.; Carbó-Dorca, R. *The Journal of Chemical Physics* **2007**, *126*, 144111.
- [328] Becke, A. D. *The Journal of Chemical Physics* **1988**, *88*, 2547–2553.
- [329] Salvador, P.; Ramos-Cordoba, E. *The Journal of Chemical Physics* **2013**, *139*, 071103.
- [330] Slater, J. C. *The Journal of Chemical Physics* **1964**, *41*, 3199–3204.
- [331] Mayer, I.; Salvador, P. *Chemical Physics Letters* **2004**, *383*, 368–375.
- [332] Matito, E.; Solà, M.; Salvador, P.; Duran, M. *Faraday Discussions* **2007**, *135*, 325–345.
- [333] Cioslowski, J. In *Many-electron densities and reduced density matrices*, 1st ed.; Cioslowski, J., Ed.; Springer US: New York, 2000; p 301.
- [334] Mayer, I. *Canadian Journal of Chemistry* **1996**, *74*, 939–942.
- [335] Johnson Matthey - Precious Metals Management. <http://www.platinum.matthey.com>.
- [336] Enthaler, S.; Junge, K.; Beller, M. *Angewandte Chemie International Edition* **2008**, *47*, 3317–3321.
- [337] Junge, K.; Schröder, K.; Beller, M. *Chemical Communications* **2011**, *47*, 4849–4859.
- [338] Fürstner, A. *ACS Central Science* **2016**, *2*, 778–789.
- [339] Shang, R.; Iliés, L.; Nakamura, E. *Chemical Reviews* **2017**, *117*, 9086–9139.
- [340] Prat, I.; Company, A.; Postils, V.; Ribas, X.; Que, L.; Luis, J. M.; Costas, M. *Chemistry European Journal* **2013**, *19*, 6724–6738.
- [341] Bassan, A.; Blomberg, M. R. A.; Siegbahn, P. E. M.; Que, L. *Chemistry European Journal* **2005**, *11*, 692–705.
- [342] Noack, H.; Siegbahn, P. E. M. *Journal of biological inorganic chemistry : JBIC : a publication of the Society of Biological Inorganic Chemistry* **2007**, *12*, 1151–62.
- [343] Kozuch, S.; Shaik, S. *The Journal of Physical Chemistry A* **2008**, *112*, 6032–6041.
- [344] Kozuch, S.; Shaik, S. *Accounts of chemical research* **2011**, *44*, 101–10.
- [345] Karen, P.; Mcardle, P.; Takats, J. *Pure and Applied Chemistry* **2016**, *88*, 831–839.
- [346] Lewis, G. N. In *Valence and The Structure of Atoms and Molecules*; American Chemical Society, Ed.; The Chemical Catalog Company, Inc.: New York, USA, 1923; p 172.
- [347] Dye, J. L. *Science (New York, N.Y.)* **2003**, *301*, 607–8.
- [348] Sushko, P. V.; Shluger, A. L.; Hirano, M.; Hosono, H. *Journal of the American Chemical Society* **2007**, *129*, 942–951.
- [349] Dale, S. G.; Otero-de-la Roza, A.; Johnson, E. R. *Physical chemistry chemical physics* **2014**, *16*, 14584–14593.
- [350] Zhao, S.; Kan, E.; Li, Z. *Wiley Interdisciplinary Reviews: Computational Molecular Science* **2016**, *6*, 430–440.

Annex

Supporting Information Section 4.1

Supporting Information

Computational Insight into the Alkane- Hydroxylation Mechanism by Non-Heme Fe(PyTACN) Iron Complexes. Effect of the Substrate and Solvent

Verònica Postils, Anna Company, Miquel Solà, Miquel Costas* and Josep M. Luis**

Institut de Química Computacional i Catàlisi (IQCC) and Departament de Química,
Universitat de Girona, Campus de Montilivi, 17071 Girona, Catalonia, Spain.

Contents

IONIZATION ENERGIES AND ELECTRON AFFINITIES.	3
MULLIKEN SPIN POPULATIONS.	4
UOPBE ENERGY VALUES.	5
MAGNITUDE OF THE SPIN CONTAMINATION	6
ANALYSIS OF THE ELECTRON TRANSFER IN THE INITIAL COMPOUND A.....	7
ANALYSIS OF THE IRON-BISHYDROXO INTERMEDIATES' STABILITY.....	8
CORRELATIONS of:	
TS Energy Barriers of the H-Abstraction	12
Icat-Irad energy differences	16
SELF-INTERACTION ERROR (SIE) ANALYSES.....	18

Ionization Energies and Electron Affinities

	G_g (kcal/mol)	G_{g+corr} (kcal/mol)	G_{solv} (kcal/mol)	
EA	Fe(IV) m1 → Fe(III) m2	-243.85	-159.79	-130.68
	Fe(IV) m3 → Fe(III) m4	-234.55	-115.17	-118.86
	Fe(IV) m5 → Fe(III) m6	-247.97	-134.15	-134.86
	Global Fe(IV) m3 → Fe(III) m6	-245.04	-130.18	-129.20
IE	Methyl	228.85	145.12	145.47
	Ethyl	190.35	116.20	116.04
	Cyclohexyl	162.24	103.79	103.25
	DMB	151.68	93.59	92.17

Table S1. Gibbs Energy values at gas-phase (G_g), at gas-phase including the dispersion and solvent corrections (G_{g+corr}), and at solvent (acetonitrile) (G_{solv}) for the ionization energies (IE) of the radical substrates and for the electron affinities (EA) of the $Fe^{IV}(OH)_2$ moiety at different multiplicities.

	G_g (kcal/mol)			
	Radical → Cation			
	Methyl	Ethyl	Cyclohexyl	DMB
m2	-15.01	-53.51	-81.61	-92.17
m4	-5.70	-44.20	-72.31	-82.87
m6	-19.12	-57.62	-85.73	-96.29
Global	-16.20	-54.70	-82.80	-93.36
	G_{g+corr} (kcal/mol)			
m2	-14.67	-43.59	-56.00	-66.19
m4	29.95	1.02	-11.38	-21.58
m6	10.97	-17.95	-30.36	-40.55
Global	14.94	-13.98	-26.39	-36.58
	G_{solv} (kcal/mol)			
m2	14.79	-14.64	-27.43	-38.51
m4	26.61	-2.83	-15.62	-26.70
m6	10.61	-18.82	-31.61	-42.70
Global	16.27	-13.16	-25.95	-37.03

Table S2. Energy differences between the IE of the deprotonated substrates and the EA of the $Fe^{IV}(OH)_2$ moiety at different catalyst multiplicities. Negative values account for a favorable substrate oxidation (cationic forms), while positive values indicate that deprotonated substrate oxidation is not favorable and they keep the radical form. Values in kcal/mol and for gas-phase (G_g), gas-phase including the dispersion and solvent corrections (G_{g+corr}), and solvent (G_{solv}) computational methodologies.

Mulliken Spin Populations

		Fe	O (oxo)	O (hydroxyl)	N (trans to pyridine)
Methane	A^{2a}	1.899	-0.868	0.1845	NS
	A⁴	2.054	0.914	0.1771	NS
	A⁶	3.182	0.591	0.0983	0.800
Ethane	A^{2a}	1.885	-0.862	0.188	NS
	A⁴	2.031	0.927	0.180	NS
	A⁶	3.168	0.603	0.097	0.799
Cyclohexane	A^{2a}	1.880	-0.858	0.189	NS
	A⁴	2.026	0.927	0.181	NS
	A⁶	3.167	0.605	0.096	0.799
2,3-DMB	A^{2a}	1.885	-0.860	0.187	NS
	A⁴	2.044	0.920	0.178	NS
	A⁶	3.187	0.592	0.096	0.801

NS=Not

Significant value.

∴ S=1/2 monoradicaloid energies have been evaluated and they are always higher in energy than triradicaloid structures.

Table S3. Mulliken spin population analysis of **A** structures.

UOPBE Energy values

		ΔE_{elec} (UOPBE)	ΔE_{elec} (UB3LYP)
A	m2	19.45	9.16
	m4	0.00	0.00
	m6	23.27	14.02
TS _{abs}	m2	7.04	2.68
	m4	0.00	0.00

Table S4. Ethane relative electronic energies obtained with single point calculations at UOPBE/6-311G(d,p)~SDD + SMD level of theory for the corresponding UB3LYP geometries.

		Methyl		Ethyl		Cyclohexyl		DMB	
		ΔE_{elec} (UOPBE)	ΔE_{elec} (UB3LYP)						
I _{rad}	m2	0.00	0.00	0.21	0.00	0.00	0.32		
	m4	1.95	0.61	0.00	1.55	0.54	0.00	0.00	0.00
	m6	8.51	9.62						
I _{cat}	m2			10.90	5.17	8.61	3.76		
	m4			9.29	7.94	8.47	7.97	9.53	8.18
	m6			0.00	0.00	0.00	0.00	0.00	0.00

Table S5. I_{rad} and I_{cat} relative Electronic Energies obtained with **single point calculations** at UOPBE/6-311G(d,p)~SDD + SMD level of theory for the corresponding UB3LYP geometries.

Magnitude of the SPIN Contamination

	A^2		TS_{abs}^2		I_{rad}^2		$TS_{reb_NCH2}^2$		$TS_{reb_NCH3}^2$	
	$\langle \widehat{S}_s^2 \rangle$	ΔE								
Methane (solv.)	1.815	3.39	1.799	1.14	1.736	-1.01	1.576	-1.33	1.610	-0.37
Ethane (solv.)	1.813	3.43	1.796	1.42	1.688	-1.18	1.459	-1.12	1.769	0.06
Cyclohexane (solv.)	1.812	3.45	1.800	1.84	1.801	0.10			1.786	0.09
2,3-DMB (solv.)	1.814	3.43	1.770	1.71						
Methane (gas)	1.812	3.42	1.757	0.95	1.723	-0.95	1.768	0.04	1.758	-0.30

Table S6. Value of the square of the total spin angular momentum operator, $\langle \widehat{S}_s^2 \rangle$, obtained for cases with spin contamination and the amount of energy corrected calculated as: $\Delta E = (E_{spin}^{corr} - E)$ in kcal·mol⁻¹. E_{ref} refers to the original electronic energy obtained for the calculation and E_{spin,corr} refers to the final reported energy value obtained applying eq. 1 of the manuscript.

Analysis of the electron transfer in the initial compound A

		G_{solv} (kcal/mol)
EA	Fe(V) m2 \rightarrow Fe(IV) m1	-135.60
	Fe(V) m4 \rightarrow Fe(IV) m3	-126.66
	Fe(V) m6 \rightarrow Fe(IV) m5	-140.57
	Global Fe(V) m4 \rightarrow Fe(III) m5	-132.17
IE	Methane	202.42
	Ethane	197.29
	Cyclohexane	159.84
	2,3-DMB	155.87

Table S7. Gibbs energy values at solvent (acetonitrile) (G_{solv}) for the ionization energies (IE) of the alkane substrates and for the electron affinities (EA) of the $\text{Fe}^{\text{v}}(\text{O})(\text{OH})$ catalyst at different multiplicities.

	G_{golv} (kcal/mol)			
	Alkane \rightarrow Radical alkane			
	Methane	Ethane	Cyclohexane	2,3-DMB
m2	66.82	75.75	61.85	70.25
m4	61.70	70.63	56.72	65.13
m6	24.25	33.18	19.27	27.67
Global	20.28	29.21	15.30	23.70

Table S8. Energy differences between the IE of the substrates and the EA of the $\text{Fe}^{\text{v}}(\text{O})(\text{OH})$ catalyst at different catalyst multiplicities. Negative values account for a favorable substrate oxidation (radical forms), while positive values indicate that substrate oxidation is not favorable and they keep the neutral form. Values in kcal/mol and at solvent (G_{solv}).

Analysis of the Iron-bishydroxo intermediates' stability

At gas-phase

UB3LYP/6-311G(d,p)-SDD				Substrates / ΔG_g (kcal/mol)			
S	Catalyst Configuration	Substrate Configuration	Methyl	Ethyl	Cyclohexyl	2,3-DMB	
1/2	Fe ^{III}			15.65 (0.00)	15.65 (0.00)	15.65 (0.00)	16.65 (0.00)
	Fe ^{IV}			30.66 (15.01)	69.16 (53.51)	97.26 (81.61)	107.82 (92.17)
	Fe ^{IV}			16.20 (0.54)	54.70 (39.05)	82.80 (67.15)	93.36 (77.71)
3/2	Fe ^{III}			10.49 (0.00)	10.49 (0.00)	10.49 (0.00)	10.49 (0.00)
	Fe ^{IV}			16.20 (5.70)	54.70 (44.20)	82.80 (72.31)	93.36 (82.87)
	Fe ^{IV}			19.12 (8.63)	57.62 (47.13)	85.73 (75.24)	96.29 (85.79)
5/2	Fe ^{III}			0.00 (0.00)	0.00 (0.00)	0.00 (0.00)	0.00 (0.00)
	Fe ^{IV}			19.12 (19.12)	57.62 (57.62)	85.73 (85.73)	96.29 (96.29)

Table S9. Relative Gibbs energies (ΔG_g) in kcal/mol for radical and cation iron-bishydroxo catalysts electronic configurations evaluated considering catalyst and substrate separated at infinite distances. Values in parenthesis correspond to Gibbs energy differences within the same multiplicity species.

At gas-phase including single-point dispersion and acetonitrile solvent corrections

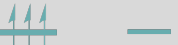
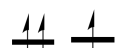
UB3LYP/6-311G(d,p)-SDD		Substrates / ΔG_{g+corr} (kcal/mol)				
S	Catalyst Configuration	Substrate Configuration	Methyl	Ethyl	Cyclohexyl	2,3-DMB
1/2	Fe ^{III}		27.14 (27.14)	12.20 (0.00)	12.20 (0.00)	12.20 (0.00)
	Fe ^{IV}		41.81 (41.81)	55.79 (43.59)	68.20 (56.00)	78.40 (66.19)
	Fe ^{IV}		0.00 (0.00)	13.98 (1.78)	26.39 (14.18)	36.58 (24.38)
3/2	Fe ^{III}		29.95 (29.95)	15.01 (1.02)	15.01 (0.00)	15.01 (0.00)
	Fe ^{IV}		0.00 (0.00)	13.98 (0.00)	26.39 (11.38)	36.58 (21.58)
	Fe ^{IV}		3.97 (3.97)	17.95 (3.97)	30.36 (15.35)	40.55 (25.55)
5/2	Fe ^{III}		14.94 (10.97)	0.00 (0.00)	0.00 (0.00)	0.00 (0.00)
	Fe ^{IV}		3.97 (0.00)	17.95 (17.95)	30.36 (30.36)	40.55 (40.55)

Table S10. Relative Gibbs energies (ΔG_{g+corr}) in kcal/mol for radical and cation iron-bishydroxo catalysts electronic configurations evaluated considering catalyst and substrate separated at infinite distances. Values in parenthesis correspond to Gibbs energy differences within the same multiplicity species.

For the intermediates evaluated as an adduct

UB3LYP/6-311G(d,p)~SDD		Substrates / ΔG_g (kcal/mol)		Substrates / ΔG_{g+corr} (kcal/mol)	
S	Electronic Configuration Iron Substrate	Methane	Cyclohexane	Methane	Cyclohexane
1/2	Fe ^{III} 	- ^a	14.07	- ^a	10.22
	Fe ^{IV} 	0.00	- ^a	0.00	- ^a
3/2	Fe ^{III} 	- ^a	11.63	- ^a	9.55
	Fe ^{IV} 	1.43	- ^a	1.08	- ^a
5/2	Fe ^{III} 	- ^a	0.00	- ^a	0.00
	Fe ^{IV} 	20.70^b	- ^a	- ^a	- ^a

^a We were unable to optimize the intermediate in this particular electronic structure. ^b ΔE_{inc} value.

Table S11. Relative Gibbs Energies at gas-phase (ΔG_g) and at gas-phase including single-point dispersion and acetonitrile solvent corrections (ΔG_{g+corr}) (kcal/mol) for radical and cation iron-bishydroxo intermediates for different spin multiplicities.

Radical stability against dissociation

It is widely accepted that when continuum solvation models are applied to calculate the solvation free energy of reactions that imply a change in the molecularity (i. e. association and dissociation reactions), the solvation entropy may be greatly overestimated.¹⁻³ There exist many published works where this overestimation of the solvation entropy has been reported and treated.⁴⁻⁹

The majority of approaches to compute the Gibbs energy of dissociation reactions in solution consider that most of the changes between gas-phase and solution free energies are due to the entropic term. Then, the Gibbs energy in solution can be computed through the following general expression:

$$\Delta G_{(sol)} = \Delta G_{(gas)} + \Delta G^{O/*} - \lambda T \Delta S_{(gas)}$$

The $\lambda T \Delta S_{(gas)}$ term determines the reduction of the gas-phase dissociation reaction entropy when the reaction takes place at solution. It has been proposed several approaches to compute $\lambda T \Delta S_{(gas)}$.¹⁰⁻¹² Here we have used the method proposed by Wertz based on the empirical correlation between solvent $S_{(m)}$ and $S_{(g)}$.¹⁰ Wertz method was derived from the experimental evidence that different small molecules lose the same fraction of their entropy upon going from the gas phase into solution. Then, despite differences in the solute-solvent interactions, the entropy of solution is a fairly constant fraction of the gaseous-phase entropy, which only depends on the solvent physical constants.^{10,13}

The fraction of entropy that is lost in going from gas to liquid is given by :

$$\alpha = \frac{S_{liq}^o - (S_{gas}^o + R \ln(\frac{V_{m,liq}}{V_{m,gas}}))}{(S_{gas}^o + R \ln(\frac{V_{m,liq}}{V_{m,gas}}))} \quad .^{13}$$

Where S_{liq}^o and S_{gas}^o are the standard molar entropy of the solvent at liquid and gas phases, $V_{m,liq}$ is the molar volume of the solvent at liquid-phase and $V_{m,gas}$ is the ideal gas molar volume of the solvent. Then, using Wertz approach, the expression used to compute the $\lambda S_{(gas)}$ term is:

$$\lambda S_{(gas)} = \alpha \left(S_{(gas)} + R \ln \left(\frac{V_{m,liq}}{V_{m,gas}} \right) \right).$$

The right-hand term inside the parenthesis accounts for changes in molar volume.

For acetonitrile, which is the solvent considered in this paper, at 298.15K, S_{liq}^o is 149.62 J/molK and S_{gas}^o is 245.48 J/molK,¹⁴ $V_{m,liq}$ is 0.052 l. and $V_{m,gas}$ is 24.45 l. Then, the quantitative expression obtained for acetonitrile is: $S_{int} = -0.23(S_{int} - 12.22)$ (cal/molK).

$\Delta G_{(sol)} = \Delta G_{(gas)} - \lambda T \Delta S_{(gas)}$ (kcal/mol)	Methyl	Ethyl	Cyclohexyl	2,3-DMB
I_{int}^1	0.00	0.00	0.00	0.00
I_{int}^2	-1.42	-3.82	-2.09	---
Dissociated: $Fe^{IV}(OH)_2 \cdots \cdots R\cdot$	0.87	-2.81	3.92	1.67

Table S12. Gibbs energy ($\Delta G_{(sol)}$) stabilization of radical intermediates against dissociation in acetonitrile solution. Energies are given in kcal/mol. Dissociated intermediates have been evaluated considering the catalyst form ($Fe^{IV}(OH)_2$) and the radical deprotonated substrate at infinite distance.

- (1) Leung, B. O.; Reid, D. L.; Armstrong, D. A.; Rauk, A. *J. Phys. Chem. A* **2004**, *108*, 2720–2725.
- (2) Wolfe, S.; Kim, C.-K.; Yang, K.; Weinberg, N.; Shi, Z. *J. Am. Chem. Soc.* **1995**, *117*, 4240–4260.
- (3) Wolfe, S.; Shi, Z.; Yang, K.; Ro, S.; Weinberg, N.; Kim, C.-K. *Can. J. Chem.* **1998**, *76*, 114–124.
- (4) Voutchkova, A. M.; Feliz, M.; Clot, E.; Eisenstein, O.; Crabtree, R. H. *J. Am. Chem. Soc.* **2007**, *129*, 12834–12846.
- (5) Solans-Monfort, X.; Pleixats, R.; Sodupe, M. *Chem. - A Eur. J.* **2010**, *16*, 7331–7343.
- (6) Liu, W.-G.; Sbergaeva, A. V.; Nielsen, R. J.; Goddard, W. A.; Vedernikov, A. N. *J. Am. Chem. Soc.* **2014**, *136*, 2335–2341.
- (7) Kuznetsov, M. L.; Teixeira, F. A.; Bokach, N. A.; Pombeiro, A. J. L.; Shul'pin, G. B. *J. Catal.* **2014**, *313*, 135–148.
- (8) Chakraborty, B.; Bhunya, S.; Paul, A.; Paine, T. K. *Inorg. Chem.* **2014**, *53*, 4899–4912.
- (9) Adão, P.; Barroso, S.; Carvalho, M. F. N. N.; Teixeira, C. M.; Kuznetsov, M. L.; Pessoa, J. C. *Dalt. Trans.* **2015**, *44*, 1612–1626.
- (10) Wertz, D. H. *J. Am. Chem. Soc.* **1980**, *102*, 5316–5322.
- (11) Gallicchio, E.; Kubo, M. M.; Levy, R. M. *J. Phys. Chem. B* **2000**, *104*, 6271–6285.
- (12) Schmid, R. *Monatshefte fuer Chemie/Chemical Mon.* **2001**, *132*, 1295–1326.
- (13) Cooper, J.; Ziegler, T. *Inorg. Chem.* **2002**, *41*, 6614–6622.
- (14) Putnam, W. E.; McEachern, D. M.; Kilpatrick, J. E. *J. Chem. Phys.* **1965**, *42*, 749.

Correlations of:

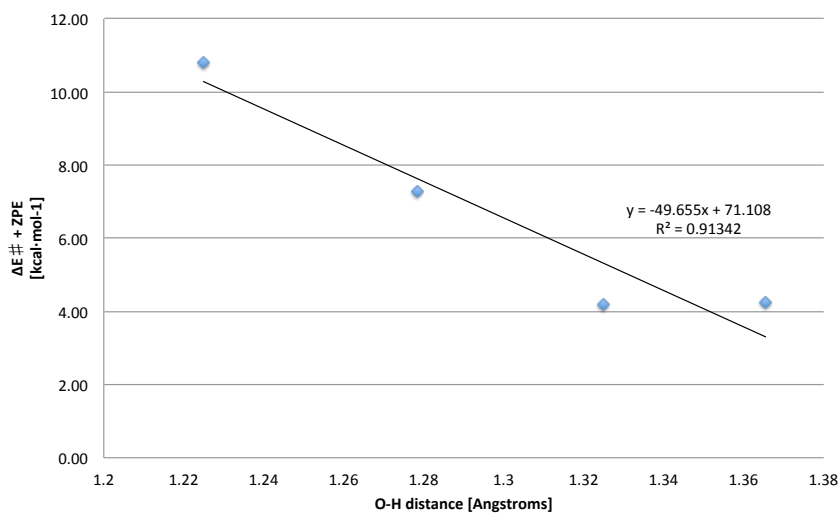
TS Energy Barriers of the H-Abstraction

Figure S1. Correlation of the HAT energy barrier ($\Delta E^\ddagger + ZPE$) with respect to the transition state's O··H distance of the new formed bond.

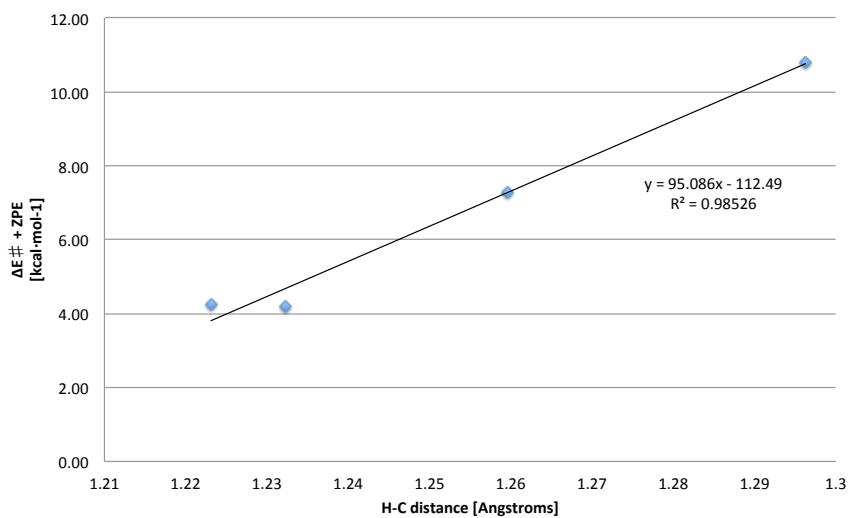


Figure S2. Correlation of the HAT energy barrier ($\Delta E^\ddagger + ZPE$) with respect to the transition state's C··H distance of the substrate cleaved bond.

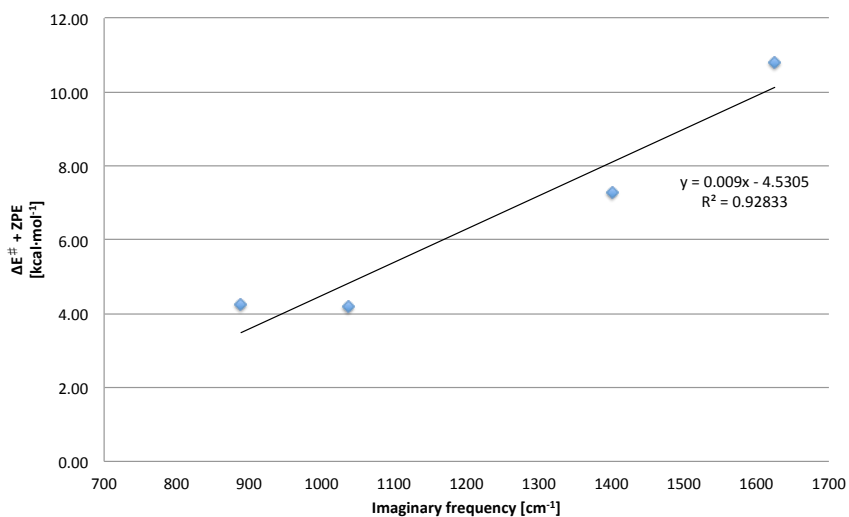


Figure S3. Correlation of the HAT energy barrier ($\Delta E^\ddagger + \text{ZPE}$) with respect to the transition state's imaginary frequency.

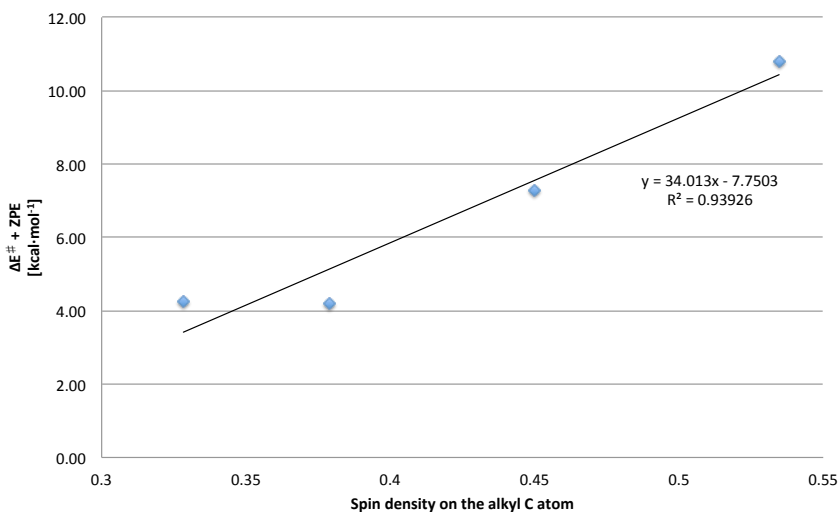


Figure S4. Correlation of the HAT energy barrier ($\Delta E^\ddagger + \text{ZPE}$) with respect to the spin density (radical character) of the C bonded to the abstracted hydrogen on the transition state.

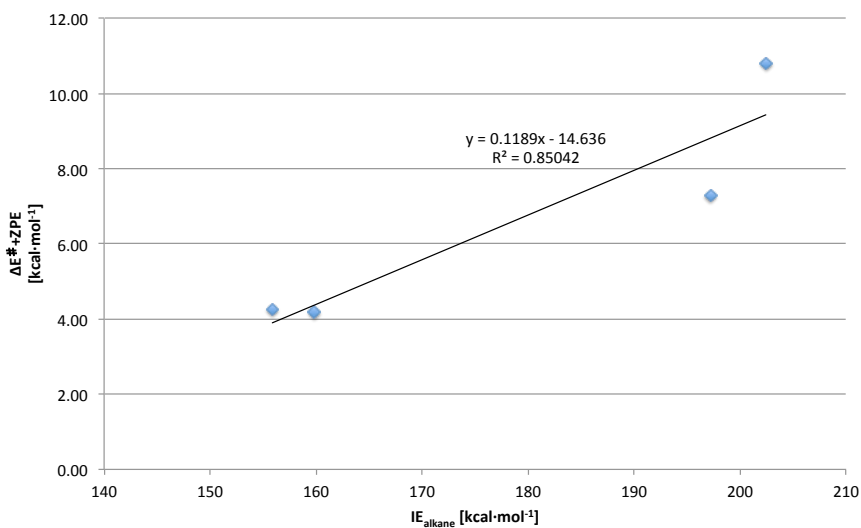


Figure S5. Correlation of the height of the HAT energy barrier ($\Delta E^\ddagger + \text{ZPE}$) with respect to the IE of the substrate.

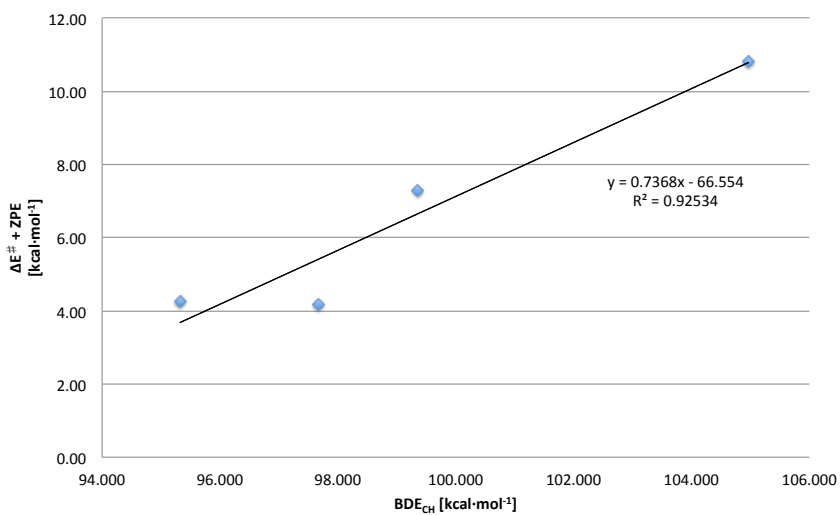


Figure S6. Correlation of the HAT energy barrier ($\Delta E^\ddagger + \text{ZPE}$) with the BDE_{CH} of substrates.

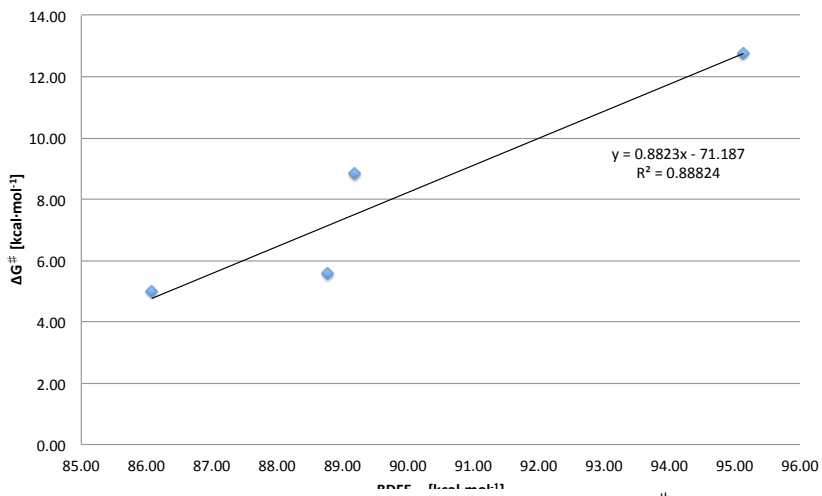


Figure S7. Correlation of the HAT free energy barrier (ΔG^\ddagger) with the C-H bond dissociation free energy of substrates ($BDFE_{C-H}$).

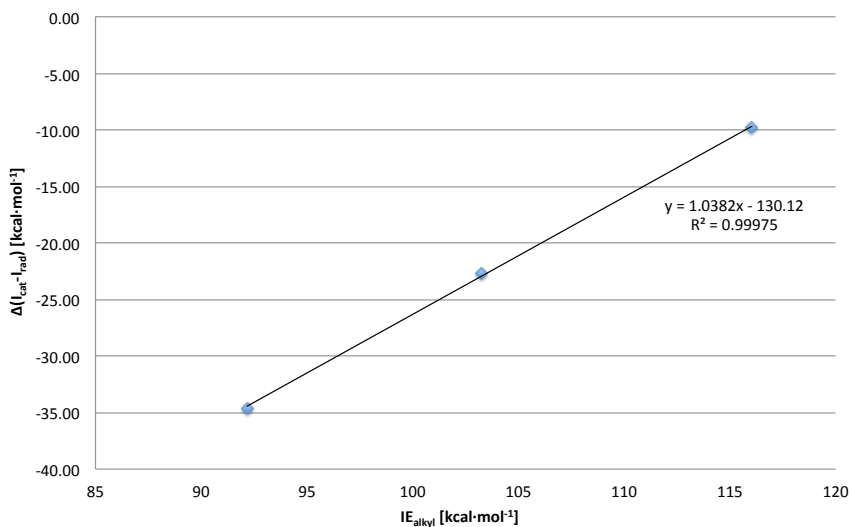
I_{cat}-I_{rad} energy difference

Figure S8. Correlation of the I_{cat}-I_{rad} energy difference with the IE of the radical alkyl. [Only ethyl, cyclohexyl and 2,3-dimethanebutyl data are included because the I_{cat} is not optimized for the methyl substrate.]

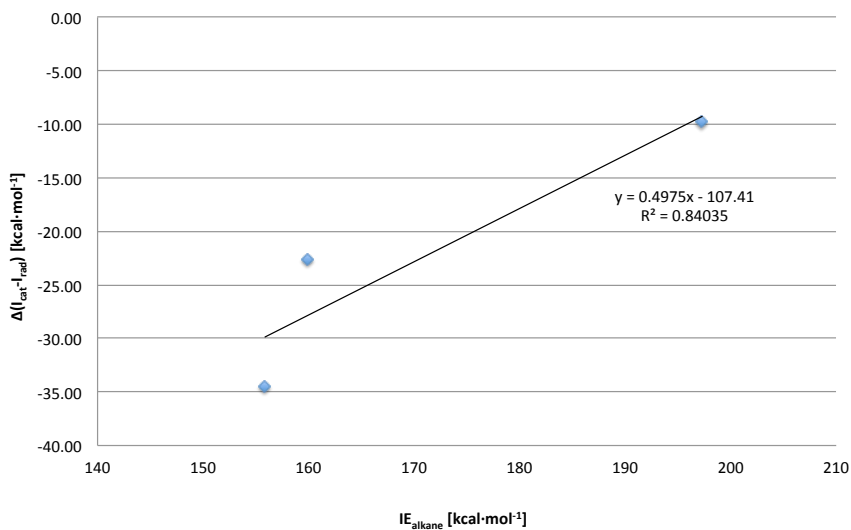


Figure S9. Correlation of the I_{cat}-I_{rad} energy difference with the IE of the substrate. [Only ethyl, cyclohexyl and 2,3-dimethanebutyl correlations are evaluated because the I_{cat} is not detected for the methyl substrate.]

SUPPORTING INFORMATION SECTION 4.1

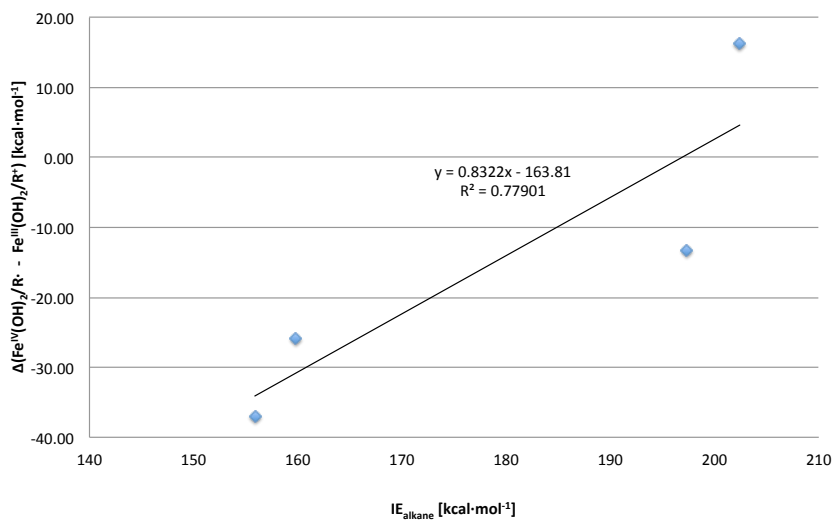


Figure S10. Stabilization of the cation intermediate ($\text{Fe}^{\text{V}}(\text{OH})_2/\text{R}\cdot$) versus the radical intermediate ($\text{Fe}^{\text{III}}(\text{OH})_2/\text{R}\cdot$) with respect to the IE of the alkane substrate. The global cationic and radical intermediate energies have been calculated considering the catalyst and the alkyl substrate at infinite distance.

Self-Interaction Error (SIE) Analyses

Acetonitrile Solution

The self-interaction error (SIE) effect in the energy of the compounds is evaluated calculating the delocalization error at 60Å accordingly to:

$$\Delta E_{deloc(60\text{Å})} = E(Fe_{complex} - Alkyl)_{60\text{Å}} - E(Fe_{complex}) - E(Alkyl) - \frac{1}{4\pi\epsilon} \frac{Q_1 Q_2}{r},$$

Where $E(Fe_{complex} - Alkyl)_{60\text{Å}}$ is the energy of the Fe complex and the alkyl separated by 60 Å, $E(Fe_{complex})$ is the energy of the isolated Fe complex, $E(Alkyl)$ is the energy of the isolated alkyl, and $\frac{1}{4\pi\epsilon} \frac{Q_1 Q_2}{r}$ is the Coulomb interaction in the localized state at $r=60\text{Å}$. The Coulomb repulsion between two plus charges at gas-phase ($\epsilon_s = 1$) at 60Å is 5.53 kcal/mol. The Coulomb repulsion considered between two plus charges at acetonitrile solution ($\epsilon_s = 37.5$) at 60Å is 0.15 kcal/mol.

Iron complex	Q _{tot}	S _{tot}	Mulliken Spin Densities			Ŝ ²	E _{electronic} (a.u.)	E _{rel.}
			Fe	O (trans NCH ₂)	O (trans NCH ₂)			
[Fe ^{iv} (OH) ₂ (PyTACN)] ²⁺	+2	0	0.00	0.00	0.00	0.00	-1042.605618	22.60
[Fe ^{iv} (OH) ₂ (PyTACN)] ²⁺	+2	1	1.96	0.07	0.16	2.06	-1042.641636	0.00
[Fe ^{iv} (OH) ₂ (PyTACN)] ²⁺	+2	2	3.55	0.13	0.15	6.13	-1042.626859	9.27
[Fe ⁱⁱⁱ (OH) ₂ (PyTACN)] ⁺	+1	1/2	1.00	0.02	0.04	0.78	-1042.828693	-117.38
[Fe ⁱⁱⁱ (OH) ₂ (PyTACN)] ⁺	+1	3/2	2.83	0.02	0.04	3.81	-1042.824940	-115.03
[Fe ⁱⁱⁱ (OH) ₂ (PyTACN)] ⁺	+1	5/2	4.15	0.24	0.25	8.76	-1042.837298	-122.78

Table S13. Absolute (a.u.) and relative (kcal/mol) electronic energies of the [Fe^(x)(OH)₂(PyTACN)]ⁿ catalysts ((x,n) being (IV,2) or (III,1)) obtained taking into account the effect of the acetonitrile solution and the D2 dispersion during the optimization ($E_{elec}^{solv} + E_{disp}^{solv}$). Mulliken spin densities of iron and oxygen atoms are also indicated. Q_{tot} and S_{tot} denote the total charge and total electronic spin angular momentum of the system.

Alkyl	Q _{tot}	S _{tot}	Mulliken Spin Densities		Ŝ ²	E _{electronic} (a.u.)
			C _{alkyl}			
·CH ₃	0	2	1.14		0.75	-39.852819
·CH ₂ CH ₃	0	2	1.08		0.75	-79.187314
·CH ₂	0	2	1.02		0.75	-235.300359
·C(CH ₃) ₂ CH(CH ₃) ₂	0	2	0.95		0.75	-236.513442
CH ₂ ·	+1	1	0.00		0.00	-39.623821
CH ₂ CH ₂ ·	+1	1	0.00		0.00	-79.006025
C·H ₂	+1	1	0.00		0.00	-235.138494
C(CH ₃) ₂ CH(CH ₃) ₂ ·	+1	1	0.00		0.00	-236.369177

Table S14. Absolute electronic energies (a.u.) of the alkyl substrates studied in this project obtained taking into account the effect of the acetonitrile solution and the D2 dispersion during the optimization ($E_{elec}^{solv} + E_{disp}^{solv}$). Mulliken spin densities of alkyl carbons are also indicated. Q_{tot} and S_{tot} denote the total charge and total electronic spin angular momentum of the system.

¹ Johansson, A. J.; Blomberg, M. R. A.; Siegbahn, P. E. M. *J. Chem. Phys.* **2008**, *129*, 154301.

SUPPORTING INFORMATION SECTION 4.1

System	IE+AE	S _{tot}	Mulliken Spin Densities					ξ ²	SIE (ΔE _{delocal})
			Fe	O (trans NCH)	O (trans NCH)	C _{alkyl}	Alkyl _{chain}		
Localized reference state [+2,0]									
Fe ^{IV} (OH) ₂ $\xrightarrow{60\text{\AA}}$ ·CH ₂ CH ₃	-2.79	1/2	1.95	0.07	0.17	-1.08	-1.00	0.96	0.82
	-2.83	3/2	1.95	0.08	0.16	1.08	1.00	3.75	0.25
Fe ^{IV} (OH) ₂ $\xrightarrow{60\text{\AA}}$ ·C ₆ H ₁₁	-15.58	1/2	1.95	0.08	0.16	-1.01	-1.00	0.96	0.77
	-15.62	3/2	1.95	0.08	0.16	1.01	1.00	3.75	0.80
Fe ^{IV} (OH) ₂ $\xrightarrow{60\text{\AA}}$ ·C(CH ₃) ₂ CH(CH ₃) ₂	-26.70	3/2	1.97	0.07	0.15	0.95	1.00	3.75	0.83
Localized reference state [+1,+1]									
Fe ^{III} (OH) ₂ $\xrightarrow{60\text{\AA}}$ CH ₂ CH ₃ ⁺	2.79	1/2	1.01	0.02	0.04	0.00	0.00	0.75	0.17
	2.83	3/2	2.85	-0.03	0.11	0.00	0.00	3.75	0.95
	18.82	5/2	4.16	0.24	0.25	0.00	0.00	8.75	0.52
Fe ^{III} (OH) ₂ $\xrightarrow{60\text{\AA}}$ C ₆ H ₁₁ ⁺	15.58	1/2	0.97	0.05	0.05	0.00	0.00	0.75	1.17
	15.62	3/2	2.85	-0.03	0.11	0.00	0.00	3.75	0.96
	31.61	5/2	4.15	0.24	0.25	0.00	0.00	8.75	0.27
Fe ^{III} (OH) ₂ $\xrightarrow{60\text{\AA}}$ C(CH ₃) ₂ CH(CH ₃) ₂ ⁺	26.70	3/2	2.85	-0.02	0.11	0.00	0.00	3.75	1.58
	42.70	5/2	4.16	0.24	0.24	0.00	0.00	8.75	0.43

Table S15. Evaluation of the SIE at 60Å of the Fe^{III}(OH)₂/R· (I_{ox}) and Fe^{IV}(OH)₂/R· (I_{red}) intermediate species for ethane, cyclohexane and 2,3-dimethylbutane substrates taking into account the effect of the **acetonitrile solution** and the D2 dispersion during the optimization ($E_{elec}^{solv} + E_{disp}^{solv}$). Mulliken spin densities of iron, oxygens, the alkyl carbon atom and the whole alkyl substrate are also specified. The IE+AE term at G_{orb} energies is indicated for each system. Negative values of the IE+AE reflect that the reduction of the oxidized specie is favorable instead of the current situation. Positive values of the IE+AE term reflect the energy cost of the reduction of the current oxidized specie. All energies are given in kcal/mol.

No SIE is found neither for radical or cationic intermediates at acetonitrile solution. Slightly positive values of the delocalization error are found instead of negative or zero values. This is mainly due to two factors. First, the spin contamination of the independent Fe_{complex} species has not been corrected (see Table S9), which cause an extra stabilization of the infinite distance separate species respect to the ones separated 60Å. Second, single-point calculations of the 60Å-separated species are done taking into account the Fe_{complex} and alkyl geometries of the I_{ox} and I_{red} minima, which are not the most stable geometries at 60Å.

Gas-phase

Iron complex	Q _{tot}	S _{tot}	Mulliken Spin Densities			ξ ²	E _{electronic} (a.u.)	E _{rel}
			Fe	O (trans NCH)	O (trans NCH)			
[Fe ^v (OH) ₂ (PyTACN)] ⁺	+2	0	0.04	-0.03	-0.03	1.04	-1042.249775	13.97
[Fe ^v (OH)(PyTACN)] ⁺	+2	1	1.43	0.08	0.17	2.06	-1042.272033	0.00
[Fe ^v (OH) ₂ (PyTACN)] ⁺	+2	2	3.52	0.14	0.14	6.13	-1042.261444	6.64
[Fe ^{iv} (OH) ₂ (PyTACN)] ⁺	+1	1/2	1.00	0.02	0.04	0.79	-1042.635780	-228.26
[Fe ^{iv} (OH)(PyTACN)] ⁺	+1	3/2	2.83	0.03	0.04	3.81	-1042.637386	-229.26
[Fe ⁱⁱⁱ (OH) ₂ (PyTACN)] ⁺	+1	5/2	4.13	0.27	0.28	8.76	-1042.653487	-239.37

Table S16. Absolute (a.u.) and relative (kcal/mol) electronic energies of the [Fe^x(OH)_n(PyTACN)]^m catalysts ((x,n) being (IV,2) or (III,1)) obtained at **gas-phase** (E_{elec}^g). Mulliken spin densities of iron and oxygen atoms are also indicated. Q_{tot} and S_{tot} denote the total charge and total electronic spin angular momentum of the system.

Alkyl	Q _{tot}	S _{tot}	Mulliken Spin Densities		ξ ²	E _{electronic} (a.u.)
			C _{alkyl}	C _{alkyl}		
·C ₆ H ₁₁	0	2	1.02	0.75	0.75	-235.277295
C ₆ H ₁₁ ⁺	+1	1	0.00	0.00	0.00	-235.021145

Table S17. Absolute (a.u.) electronic energies of the cyclohexyl substrates studied at **gas-phase** (E_{elec}^g). Mulliken spin densities of the alkyl carbon are also indicated. Q_{tot} and S_{tot} denote the total charge and total electronic spin angular momentum of the system.

System	IE+AE	S _{tot}	Mulliken Spin Densities				ξ ²	SIE (ΔE _{deloc(alkyl)})
			Fe	O (trans NCH)	O (trans NCH)	C _{alkyl}		
Fe ^{iv} (OH) ₂ $\xrightarrow{60\text{\AA}}$ ·C ₆ H ₁₁	-67.15	1/2	1.93	0.08	0.17	-1.02	-1.00	0.96
	-72.31	3/2	1.94	0.08	0.17	1.02	1.00	0.07
	-85.73	5/2	3.52	0.14	0.14	1.02	1.00	-0.02
Fe ⁱⁱⁱ (OH) ₂ $\xrightarrow{60\text{\AA}}$ C ₆ H ₁₁ ⁺	67.15	1/2	1.00	0.02	0.04	0.00	0.00	0.75
	72.31	3/2	2.83	0.03	0.04	0.00	0.00	3.75
	85.75	5/2	4.13	0.27	0.28	0.00	0.00	8.75

Table S18. Evaluation of the SIE at 60Å of the Feⁱⁱⁱ(OH)₂/R[·] (I_{red}) and Fe^{iv}(OH)₂/R[·] (I_{ox}) intermediate species for the cyclohexane substrate at **gas-phase** (E_{elec}^g). Mulliken spin densities of iron, the oxygens, the alkyl carbon atom and the whole cyclohexyl substrate are also specified. The IE+AE term at G_s energies is given for each system. Negative values reflect that the reduction of the oxidized specie is favorable instead of the current situation. Positive values of the IE+AE term reflect the energy cost of the reduction of the current oxidized specie. All energies are given in kcal/mol.

SIE is not found at the gas-phase case. In this study, the Fe_{electronic} and alkyl geometries of the 60Å-separated species are the same as the separate species geometries. These geometries are more close to the optimized geometries and remove the positive values of the delocalization error.

Supporting Information Section 4.2

Supporting Information

Mechanism of the Selective Fe-catalyzed Arene Carbon-Hydrogen Bond Functionalization

Verònica Postils,[†] Mònica Rodríguez,[†] Gerard Sabenya,[†] Ana Conde,[§] M.Mar Díaz-Requejo,^{§,*} Pedro J. Pérez,^{§,*} Miquel Costas,^{†,*} Miquel Solà,^{†,*} and Josep M. Luis^{†,*}

[†] Institut de Química Computacional i Catàlisi (IQCC) and Departament de Química, Universitat de Girona, Campus Montilivi, 17071 Girona (Spain).

[§] Laboratorio de Catálisis Homogénea, Unidad Asociada al CSIC, CIQSO-Centro de Investigación en Química Sostenible, Departamento de Química, Universidad de Huelva, Campus de El Carmen s/n, 21007 Huelva (Spain).

Corresponding authors' email addresses

josepm.luis@udg.edu; miquel.sola@udg.edu; miquel.costas@udg.edu; perez@dqcm.uhu.es; mmdiaz@dqcm.uhu.es

Content

Computational Section

1. Computational details	2
2. Generation of the carbene moiety	3
3. Iron-carbene conformers. Geometric and electronic structure	4
4. Mechanistic Insights in benzene functionalization I. Concerted insertion versus stepwise mechanism	12
5. Mechanistic Insights in benzene functionalization II. Insertion versus Addition mechanisms	16
6. Spin contamination energy correction	18
7. XYZ coordinates	19
References	20

COMPUTATIONAL SECTION

1. Computational Details

The experimental reaction starts with the $[\text{Fe}^{\text{II}}\text{X}_2(\text{L}1)]$ complex, where $\text{X}=\text{Cl}^-$ or CF_3SO_3^- . However, the high amount of halide scavenger ($\text{NaBAR}_4^{\text{F}}$) that has to be experimentally used to obtain high reaction yields, together with the lack of catalytic activity experimentally observed for pentadentate ligands,¹ suggests that the dicationic species $[\text{Fe}(\text{L}1)]^{2+}$ with two free labile positions is the active form. Therefore, the $[\text{Fe}^{\text{II}}(\text{L}1)]^{2+}$ species was chosen as starting species to study the mechanism.

All structures were optimized with the Gaussian 09 program,^{1,2} using the spin-unrestricted Kohn-Sham formalism employing the B3LYP functional,^{3,4} with the 6-31G(d) basis set^{5,6} for all atoms. Optimizations were performed in dichloromethane solvent, using the SMD solvation model,⁷ and also taking into account dispersion effects with the Grimme and coworkers DFT-D3BJ correction.^{8,9} Collectively, this combination of 6-31G(d) basis set, with the use of the SMD(dichloromethane) solvent model and the B3LYP-D3BJ approach will subsequently be referred to as B1. After geometry optimization, frequency calculations were done at the B1 level for all species to evaluate enthalpy and entropy corrections at 298.15K ($G_{\text{corr.}(B1)}$) and to ensure that all local minima have only real frequencies while transition states have a single imaginary frequency. For all transition states, intrinsic reaction coordinate (IRC) calculations were performed to connect them with their corresponding reactants and products.

At the optimized B1 geometries, the electronic energies were improved performing single point energy calculations using the cc-pVTZ basis set^{10,11} for all atoms, including the D3BJ dispersion correction and SMD solvation effects to reproduce the solvent mixture (see below). Collectively, this new combination will be referred to as B2. In B2, to mimic the experimental solvent mixture with a molar fraction ratio of 58:42 of benzene:dichloromethane, the values of the solvent descriptors used in the SMD solvation model were re-defined on the basis of a linear behavior with the molar fraction. Using the "Solvent=(Generic.Read)" options of the Gaussian09 SCRF keyword, the solvent mixture was defined employing the following solvent descriptors: Dynamic Dielectric Constant=2.17574; Static Dielectric Constant=4.49845; Abraham's hydrogen bond acidity=0.0419; Abraham's hydrogen bond basicity=0.1023; Surface Tension=40.0038; Carbon Aromaticity=0.5808; Electronegativity Halogenicity=0.2796 ($G_{\text{solv.}(B2)}$). All electronic energy values at the B2 level that presented spin-contamination error were corrected using Yamaguchi correction,^{12,13} ($E_{\text{spin-corr}(B2)}$). Finally, the free energy change associated with moving from a standard-state gas phase pressure of 1 atm to a standard-state gas phase concentration of $1.70 \times 10^{-3} \text{M}$ for $[(\text{L}1)\text{Fe}^{\text{II}}]^{2+}$, of 5.61 M for benzene and $3.33 \times 10^{-2} \text{M}$ for ethyl diazoacetate was also included in the final free energies ($\Delta G^{o/*}$). These concentrations are in agreement with the experimental conditions described in Table 1 (in the main manuscript). It has been assumed that the concentration of H_2O -dimer is the same as $[\text{Fe}^{\text{II}}(\text{L}1)]^{2+}$, i.e. $1.70 \times 10^{-3} \text{M}$. Then, the final total Gibbs energy (G) is given by:

$$G = E_{\text{spin-corr}(B2)} + E_{\text{disp}} + G_{\text{solv}(B2)} + G_{\text{corr}(B1)} + \Delta G^{o/*} \text{ (Eq.1)}$$

For **C** and **C'** species, the electronic structure was checked by analyzing MOs, NBOs and the effective oxidation states (effOS) at the B2 level. The NBO 6.0 program¹⁴ was used to perform the natural bond orbital analysis and the APOST-3D v-2.0 program¹⁵ was employed to carry out the effective oxidation states analysis. Non-covalent interaction analyses were done using the NCIPLOT v-3.0 program.^{16,17}

2. Generation of the carbene moiety

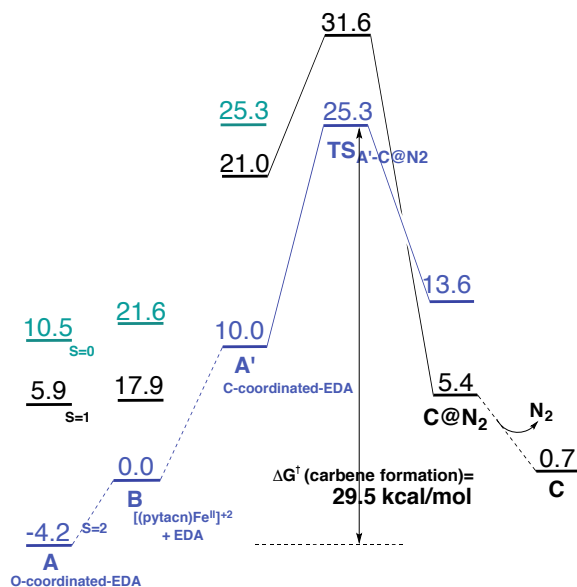


Figure S1: Gibbs energy profile, ΔG , ($\text{kcal}\cdot\text{mol}^{-1}$) of the metal-carbene bond formation. Blue, black and green profiles correspond to quintet, triplet and singlet multiplicities, respectively. In the figure, Gibbs energy values of all possible spin states of the free catalyst, **B**, and adducts **A** and **A'**, as well as the energy barriers of the carbene-formation at quintet and triplet multiplicities are represented.

2.1 Differences between L1 and L2 catalysts

Table S1: Gibbs free energies, ΔG , of the carbene formation for the two isomers of **L2** catalyst (carbene parallel or perpendicular to the plane of pyridyl ring) (in $\text{kcal}\cdot\text{mol}^{-1}$).

	ΔG (B1) ($\text{kcal}\cdot\text{mol}^{-1}$)
^5B	0.0
$^5\text{TS}_{\text{A-C@N2}}$ (parallel Py)	26.7
$^5\text{C@N2}$ (parallel Py)	15.5
$^5\text{TS}_{\text{A-C@N2}}$ (perpendicular Py)	27.4
$^5\text{C@N2}$ (perpendicular Py)	7.8

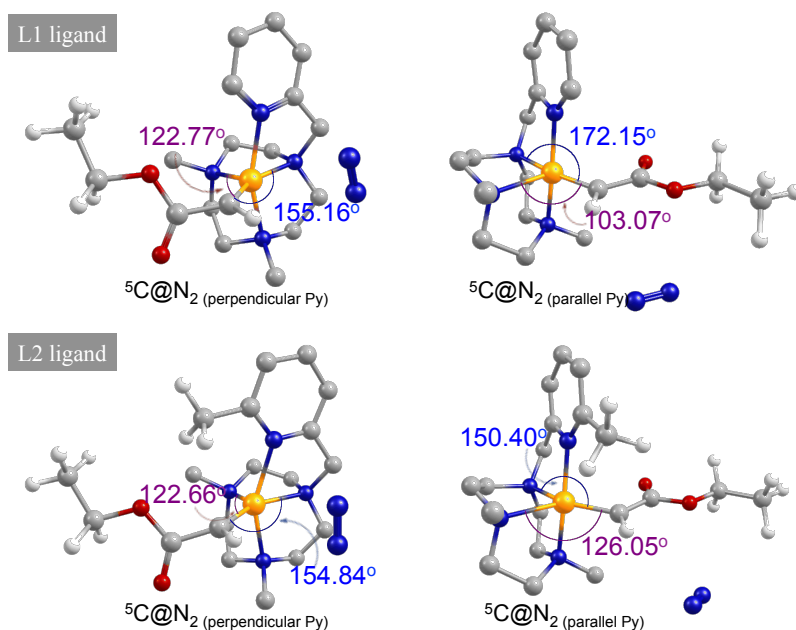


Figure S2: Comparison between the optimized structures of the ${}^5\text{C}@N_2$ isomers (carbene perpendicular or parallel to the plane of pyridyl ring) for the **L1** (top) and **L2** (bottom) complexes. Hydrogen atoms of the pytacn ligand have been omitted for clarity (C: grey, N: blue, O: red, Fe: yellow, H: white).

3. Iron-carbene conformers. Geometric and electronic structure.

3.1 C conformer

The spin densities for ${}^3\text{C}$ reveal 0.824 beta electrons on the carbene carbon coupled in an antiferromagnetic way with 2.835 alpha electrons on iron. Thus, the spin densities in conjunction with the long $\text{Fe}-\text{C}_{\text{carb}}$ bond length reported in the main document point **C** species present a carbene radical character, as opposed to the classical metal carbene with a double bond between metal and the carbon. In some recent studies about cobalt^{18,19} and iron²⁰ porphyrin carbene complexes, it is shown that the carbene moiety in that compounds is best described as a carbene radical as opposed to a common metal carbene double bond. However, only a few examples of carbenes radicals have been described on literature, and all of them have a porphyrin ligand. Thus, the **C** species is the first non-heme iron radical carbene described. To gain more insight about the electronic nature of our carbene moiety and to provide further support to the radical character of the carbene moiety, additional studies of the bonding between the iron and the carbene were done, such as the analyses of molecular orbitals (MOs), natural bond orbitals (NBO)²¹ and the effective oxidation states (effOS).^{22,23}

· effOS analysis

According effOS analysis, the pytacn ligand has a neutral character and, consequently, an oxidation number of 0; the iron is described as an Fe^{III} and the carbene moiety has an effective oxidation state of -1, thus acting as a formal alkyl substituent in the form $-\text{CHCO}_2\text{Et}$. Then, effOS analysis also indicates the radical character of the **C** Fe-carbene.

Table S2: Effective Oxidation State (EOS) analysis of the conformer C.^[a]

Fragment	EOS	$\lambda_{LO}^\alpha / \lambda_{FU}^\alpha$	$\lambda_{LO}^\beta / \lambda_{FU}^\beta$	$R_\alpha(\%) / R_\beta(\%)$
Fe	+3	0.875 / 0.469	0.887 / 0.282	
carbene	-1	0.559 / 0.061	0.686 / 0.027	59.04 / 90.39
pytacn ligand	0	0.705 / 0.038	0.755 / 0.052	

[a]

Analysis performed using the ρ generated at the B2 level of theory. Occupations of the last occupied and first unoccupied spin-resolved effective atomic/fragment orbitals (eff-AOs) are presented for each fragment. The occupations of *frontier* alpha and beta eff-AOs are in bold. These are the values used in the R index (Eq. 1) to quantify the reliability of the formal oxidation states determined.

$$R_\sigma(\%) = 100 \cdot \min(1, \max(0, \lambda_{LO}^\sigma - \lambda_{FU}^\sigma + 1/2)) \quad (\text{Eq.1})$$

· MO and NBO analysis

MOs and NBO analysis are more complex because alpha and beta electrons present different behaviors and orbital interaction diagrams. To analyze MOs, we are going to focus our attention on the molecular spinorbitals obtained combining the *d* orbitals of the initial Fe(II) catalyst and the σ and π orbitals of the carbene moiety. These MOs contain 8 electrons, which come from the d^6 of the initial Fe(II) and the σ^2 lone pair of the carbene moiety. Taking into account a S=1 spin state for the Fe(II) catalyst, we examine the molecular spinorbitals occupied by 5 α and 3 β electrons. Figure S3 introduces schematic orbital interaction diagrams for the alpha and beta electrons, and Figure S4 shows the computed DFT MOs. On one hand, if we analyze the β molecular spinorbitals, we observe the typical carbene-orbital interactions. Carbene's σ bonding MO ($\sigma_{1(\text{Fe-C})}$) is formed as linear combination of iron $d_{x^2-y^2}$ orbital and carbene p_x orbital, and carbene π bonding MO ($\pi_{(\text{Fe-C})}$) is formed by the overlap of iron d_{xy} and carbene p_y orbitals. However, as it can be seen in Figure S4, the $\pi_{(\text{Fe-C})}$ MO is highly polarized toward the carbene C atom. Two of the three analyzed β electrons are in $\sigma_{1(\text{Fe-C})}$ and $\pi_{(\text{Fe-C})}$ MOs just described. The third β electron is in the non-bonding MO d_{xz} . On the other hand, in the case of α molecular spinorbitals, no pure $\sigma_{1(\text{Fe-C})}$ and $\pi_{(\text{Fe-C})}$ molecular orbitals are formed; but a mixture between iron $d_{x^2-y^2}$ and d_{xy} atomic orbitals and carbene p_y and p_x atomic orbitals compose all Fe-C MOs. However, the two bonding α orbitals formed between the iron and the carbene have a predominant σ character, and we label them as $\sigma_{1(\text{Fe-C})}(\alpha)$ and $\sigma_{2(\text{Fe-C})}(\alpha)$, accordingly (Figure S3). The occupied $\sigma_{1(\text{Fe-C})}(\alpha)$ and

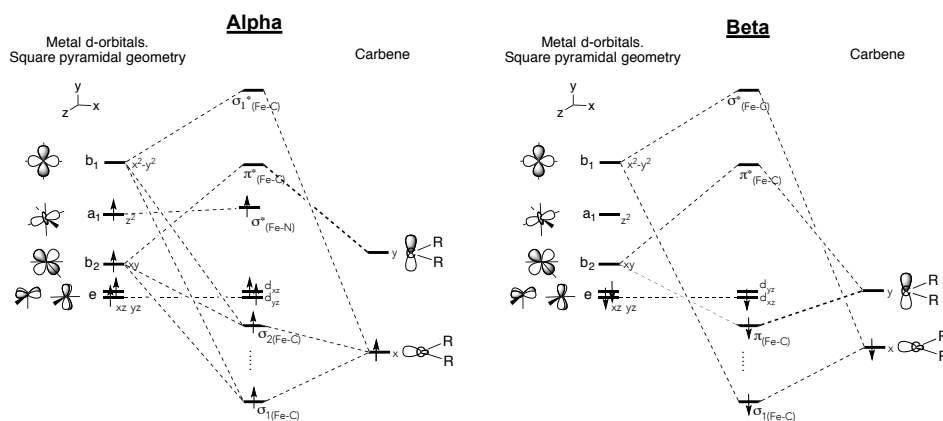


Figure S3: Schematic alpha (right) and beta (left) molecular spinorbital diagrams of **C**. *d* spinorbitals of Fe and p_x and p_y spinorbitals of C_{carb} atom are taken into account to generate iron-carbene and the main iron-ligand molecular spinorbitals.

$\sigma_{2(\text{Fe-C})}(\alpha)$ molecular orbitals are mainly formed as linear combination of iron $d_{x^2-y^2}$ and d_{xy} atomic orbitals and carbene p_x atomic orbital. The $\sigma_{2(\text{Fe-C})}(\alpha)$ orbital is highly polarized toward the Fe because the carbene p_x atomic orbital mainly contributes in the formation of $\sigma_{1(\text{Fe-C})}(\alpha)$. The remaining three α electrons are in the non-bonding MO d_{yz} , d_{xz} , and in the antibonding MO $\sigma_{(\text{Fe-N})}^*(\alpha)$, which is the α HOMO. Thus, the different symmetry and polarization of α and β occupied MOs describe a different bonding for the Fe- C_{carb} moiety, which results in the presence of an Fe(III) and a formal radical alkyl substituent in compound **C**.

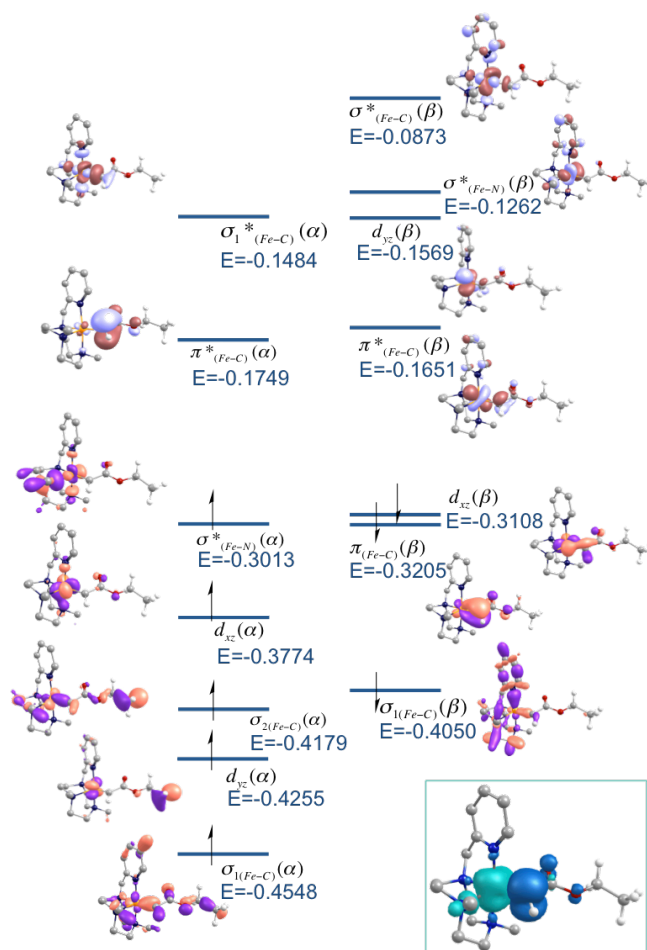


Figure S4: Kohn-Sham molecular spinorbitals of **C** determined with B3LYP functional. On the right: alpha spinorbitals and their energies; on the left: beta spinorbitals and their energies. Only molecular spinorbitals that account for main Fe-carbene and Fe-ligand interactions and that come from Fe d orbitals and p_x and p_y spinorbitals of C_{carb} atom are represented. Orbital isosurface contour value of 0.05. The image at the right bottom corner shows the spin density difference. The spin density isosurface contour value is 0.0045, teal color accounts for positive values (α density) and blue color accounts for negative values (β density). Hydrogen atoms of the LI ligand have been removed for clarity.

NBO analyses of α and β electrons also lead to the same description of the electronic structure of **C**; thus, pointing the existence of a carbene radical.

Selected NBO data:

SUPPORTING INFORMATION SECTION 4.2

 α electrons

=====**NBO numbering**=====

LP
 Fe: 34(0.981e-), 35(0.978e-), 36(0.976e-),
 37(0.965e-)
 N₂: 38(0.866e-)
 N₅: 39(0.873e-)
 N₁₀: 40(0.941e-)
 N₁₃: 41(0.862e-)
 C₅₄: 33(1.000e-)

BD

Fe-C₅₄: 46(0.987e-)
 C₄₄-C₅₄: 96(0.990e-)
 C₅₄-H₅₅: 104(0.989e-)

non-Lewis: LV*(Fe): 105(0.126e-)
 BD*(Fe-C₅₄): 107(0.244e-)

=====**SECOND ORDER PERTURBATION THEORY**=====

within unit 1

3.CR (Fe)	107.BD*(Fe-C ₅₄)	10.95 kcal/mol
38.LP (N ₂)	107.BD*(Fe-C ₅₄)	14.93 kcal/mol
38.LP (N ₂)	105.LV(Fe)	20.08 kcal/mol
39.LP (N ₅)	107.BD*(Fe-C ₅₄)	21.13 kcal/mol

 β electrons

=====**NBO numbering**=====

LP
 Fe: 34(0.973e-)
 N₂: 35(0.854e-), 36(0.672e-)
 N₅: 37(0.881e-)
 N₁₀: 38(0.843e-)
 N₁₃: 39(0.852e-)

BD

Fe-C₅₄: 44(0.988e-)
 Fe-C₅₄: 45(0.913e-)
 C₄₄-C₅₄: 94(0.990e-)
 C₅₄-H₅₅: 102(0.989e-)

non-Lewis:

LV(Fe): 103(0.245e-), 104(0.104e-), 105(0.052e-)
 BD*(Fe-C₅₄): 107(0.166e-), 108(0.037e-)

=====**SECOND ORDER PERTURBATION THEORY**=====

from unit 2 to unit 1:

35.LP (N ₂)	103.LV(Fe)	39.91 kcal/mol
35.LP (N ₂)	104.LV(Fe)	12.19 kcal/mol
37.LP (N ₅)	107.BD*(Fe-C ₅₄)	27.29 kcal/mol
38.LP (N ₁₀)	103.LV(Fe)	12.66 kcal/mol
38.LP (N ₁₀)	104.LV(Fe)	15.71 kcal/mol
39.LP (N ₁₃)	103.LV(Fe)	35.15 kcal/mol



Figure S5: Schematic representation of the iron coordination and the iron-carbene bonding of conformer **C**. Alpha (left) and beta (right) Lewis structures described by the NBO analysis. Squares with a dot represent non-bonding Lewis pairs (electrons) and X represent non-Lewis orbitals.

By analyzing the delocalization of electrons from filled O₄₅ lone pairs into non-Lewis Fe orbitals we can discard any important interaction between the carbonyl oxygen of the carbene and the iron atom. Second order perturbation theory data that supports this conclusion is shown below:

 α electrons

=====**NBO numbering**=====

LP
 O₄₅: 42(0.987e-), 43(0.932e-)

=====**SECOND ORDER PERTURBATION THEORY**=====

within unit 1

42.LP (O ₄₅)	105.LV(Fe)	0.74 kcal/mol
43.LP (O ₄₅)	105.LV(Fe)	0.78 kcal/mol

 β electrons

=====**NBO numbering**=====

LP
 O₄₅: 40(0.986e-), 41(0.926e-)

=====**SECOND ORDER PERTURBATION THEORY**=====

within unit 1

40.LP (O ₄₅)	104.LV(Fe)	1.02 kcal/mol
41.LP (O ₄₅)	104.LV(Fe)	1.34 kcal/mol

3.2 Comparison of the NCI results by C and C'

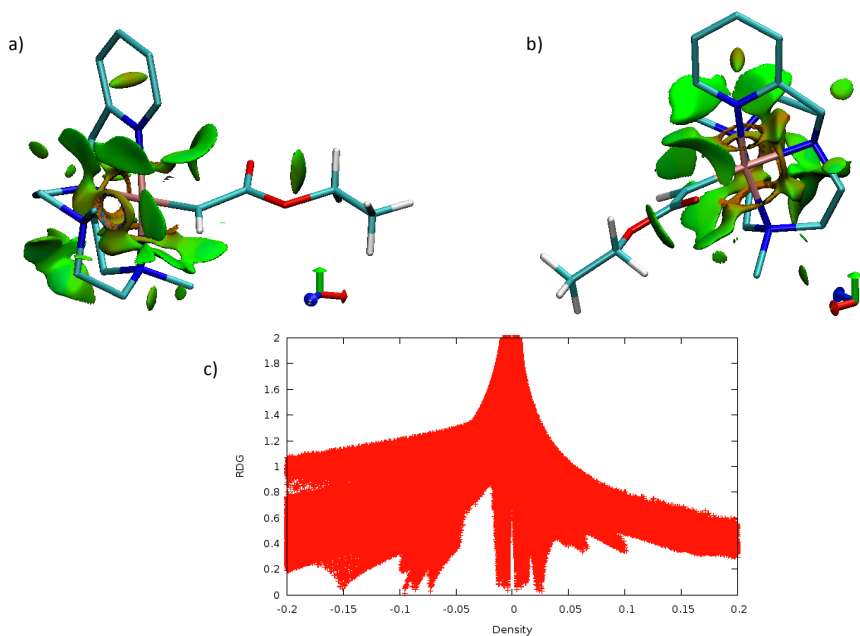


Figure S6: Non-Covalent Interactions (NCI) data of **C** conformer. Density plots (a) and b) with an isosurface reduced density gradient (RDG) value of 0.6. a) and b) differ only in their perspective. c) Graphic of the RDG of C as a function of the density according the NCI index.

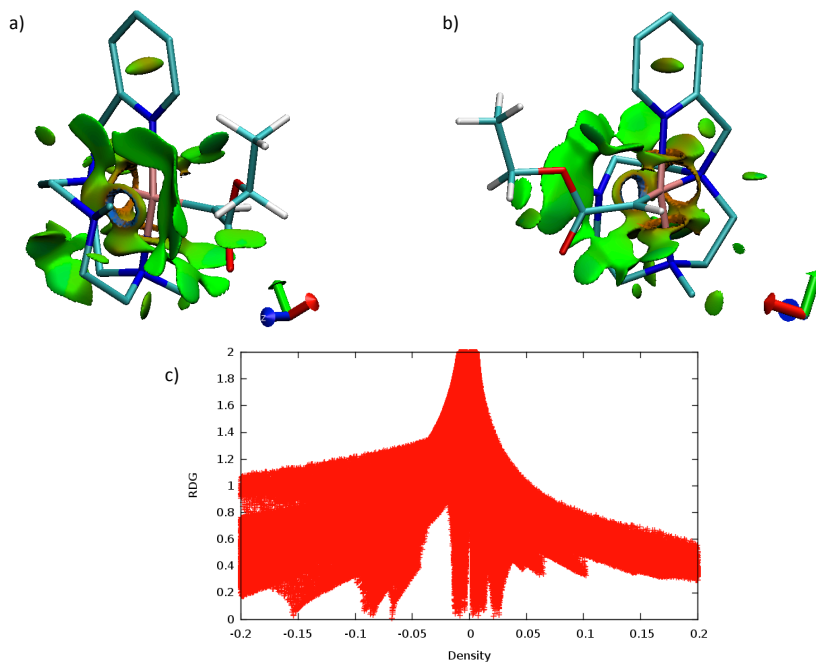


Figure S7: Non-Covalent Interactions (NCI) data of **C'** conformer. Density plots (a) and b) with an isosurface RDG value of 0.6. a) and b) differ only in their perspective. c) Graphic of the RDG of C' as a function of the density according the NCI index.

C and **C'** conformers have similar NCI data. We can sum up the main difference in the following points:

- i) A bonding interaction between the carbonyl oxygen of the carbene's tail and the iron atom is discarded in conformer **C**. Furthermore, it is observed a weak interaction between this oxygen and the nitrogen atom of the pyridine of the pytacn ligand.
- ii) The free-coordination site of iron provides space for the benzene substrate to approach and react with the C_{carb} atom. In the other areas that surround C_{carb} , the benzene approach is sterically hampered. In conformer **C**, this space is more hindered than in conformer **C'**, mainly due to the existence of a weak interaction between the carbonyl oxygen of the carbene's tail and the nitrogen atom of the pyridine of the pytacn ligand.

3.3 C' conformer

C' conformer shares a similar geometric and electronic structure with **C**. **C'** has a Fe- C_{carb} distance of 1.82 Å and its spin density reveals 0.716 beta electrons on C_{carb} coupled in an antiferromagnetic way with 2.671 alpha electrons on iron. Also MOs, NBOs and effOS analyses point to the existence of a carbene radical with just one single sigma bond between the *carbene* moiety and iron. Thus, a Fe^{III} catalyst with the carbene group acting as a formal alkyl substituent in the form $-\dot{\text{C}}\text{HCO}_2\text{Et}$. The corresponding EffOS, NBO, and MO data is presented below.

· effOS analysis

Table S3: Effective Oxidation State (EOS) analysis for the conformer **C'**.^[a]

Fragment	EOS	$\lambda_{LO}^{\alpha}/\lambda_{FU}^{\alpha}$	$\lambda_{LO}^{\beta}/\lambda_{FU}^{\beta}$	$R_{\alpha}(\%) / R_{\beta}(\%)$
Fe	+3	0.861 / 0.436	0.888 / 0.287	
carbene	-1	0.598 / 0.070	0.623 / 0.028	66.21 / 83.59
pytacn ligand	0	0.705 / 0.036	0.760 / 0.051	

^[a] Analysis performed using the p generated at the B2 level of theory. Occupations of the last occupied and first unoccupied spin-resolved effective atomic/fragment orbitals (eff-AOs) are presented for each fragment. The occupations of *frontier* alpha and beta eff-AOs are in bold.

· NBO analysis

Selected NBO data:

α electrons

=====
 LP
 N₁: 34(0.863e-)
 N₄: 35(0.865e-)
 N₉: 36(0.943e-)
 N₁₂: 37(0.860e-)
 Fe: 38(0.984e-), 39(0.982e-), 40(0.979e-),
 41(0.963e-)

BD
 Fe-C₄₄: 92(0.978e-)
 C₄₄-H₄₅: 93(0.979e-)
 C₄₄-C₄₆: 94(0.990e-)

non-Lewis: LV*(Fe): 105(0.130e-)
 LV(C₄₄): 106(0.075e-)
 BD*(Fe-C₄₄): 153(0.245e-)

=====
 SECOND ORDER PERTURBATION
 THEORY =====

from unit 1 to unit 2
 34.LP(N₁) 105.LV(Fe) 20.39 kcal/mol
 34.LP(N₁) 153.BD*(Fe-C₄₄) 12.40 kcal/mol
 35.LP(N₄) 153.BD*(Fe-C₄₄) 22.20 kcal/mol
 37.LP(N₁₂) 105.LV(Fe) 14.66 kcal/mol
 37.LP(N₁₂) 153.BD*(Fe-C₄₄) 12.30 kcal/mol

β electrons

=====NBO numbering =====

LP

N₁: 34(0.854e-), 35(0.675e-)N₄: 36(0.880e-)N₉: 37(0.847e-)N₁₂: 38(0.849e-)

Fe: 39(0.976e-)

BD

Fe-C₄₄: 89(0.971e-)Fe-C₄₄: 90(0.969e-)C₄₄-H₄₅: 91(0.978e-)C₄₄-C₄₆: 92(0.989e-)

non-Lewis:

LV(Fe): 104(0.232e-), 105(0.103e-), 106(0.043e-)

BD*(Fe-C₄₄): 152(0.107e-), 153(0.108e-)===== SECOND ORDER PERTURBATION
THEORY =====

from unit 1 to unit 2:

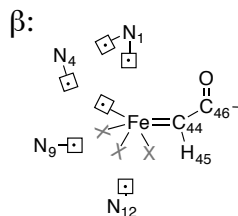
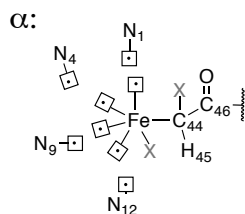
35.LP (N₁) 104.LV(Fe) 37.17 kcal/mol35.LP (N₁) 105.LV(Fe) 10.60 kcal/mol36.LP (N₄) 152.BD*(Fe-C₄₄) 13.72 kcal/mol36.LP (N₄) 153.BD*(Fe-C₄₄) 13.34 kcal/mol37.LP (N₉) 105.LV(Fe) 16.27 kcal/mol38.LP (N₁₂) 104.LV(Fe) 34.69 kcal/mol

Figure S8: Schematic representation of the iron coordination and the iron-carbene bonding of conformer C'. Alpha (left) and beta (right) Lewis structures described by the NBO analysis. Squares with a dot represent non-bonding Lewis pairs(*electrons*) and X represent non-Lewis orbitals.

· MO analysis: (next page)

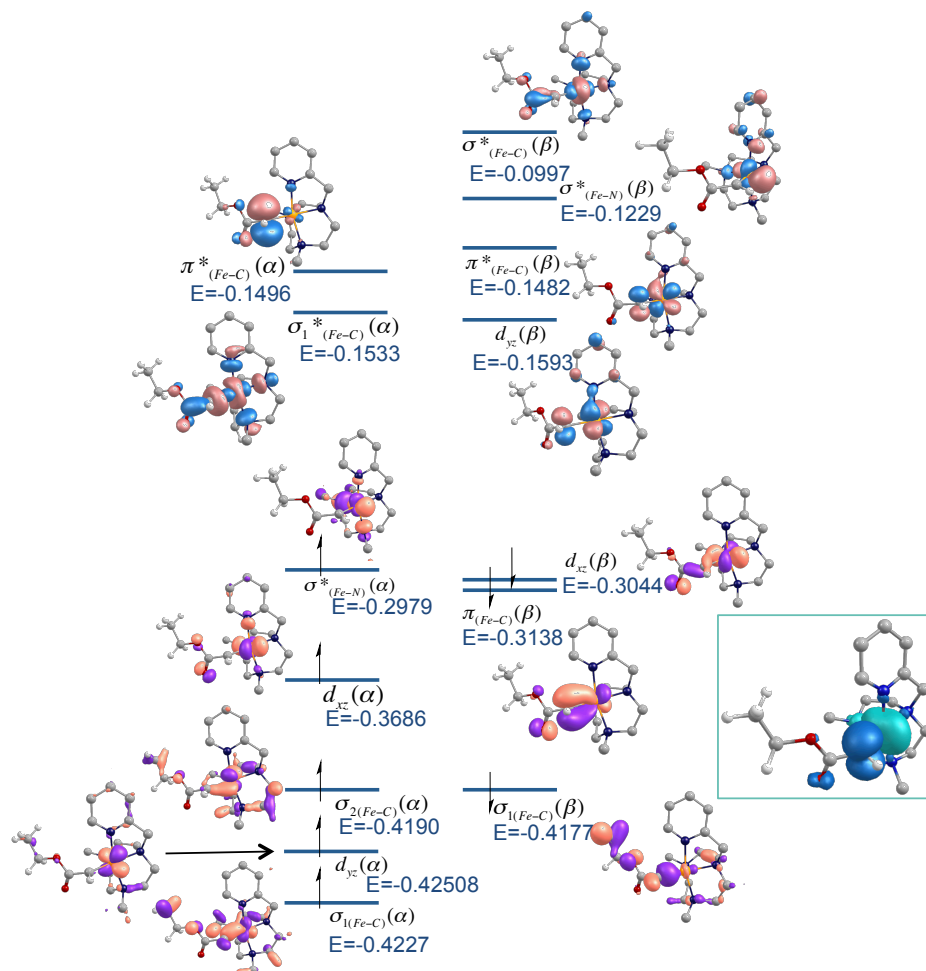


Figure S9: B3LYP Kohn-Sham molecular spinorbitals of C' determined at the B2 level of theory. On the right: alpha spinorbitals and their energies; on the left: beta spinorbitals and their energies. Only molecular spinorbitals that account for main Fe-carbene and Fe-ligand interactions obtained as linear combination of Fe d orbitals and p_x and p_y orbitals of C_{carb} atom are represented. Orbital isosurface contour value of 0.05. The image at the right bottom corner shows the spin density difference. The spin density isosurface contour value is 0.0045, teal color accounts for positive values (α density) and blue color accounts for negative values (β density). Hydrogen atoms of the L1 ligand have been removed for clarity.

4. Mechanistic insights in benzene functionalization I. Concerted insertion versus stepwise mechanism

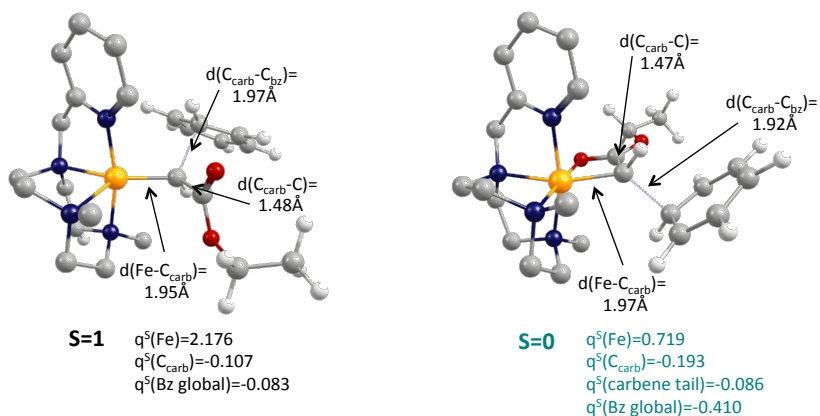


Figure S10: Optimized structures of $\text{TS}_{\text{I,II}}$ (left) and $\text{TS}^k_{\text{I,II}}$ (right) in the ground spin state and for the lowest energy conformer. The key distances related to the transition state are shown as figures insets. Global spin state and localized spin densities are shown below the corresponding structure. Hydrogen atoms of the pytaen ligand have been omitted for clarity (C: grey, N: blue, O: red, Fe: yellow, H: white).

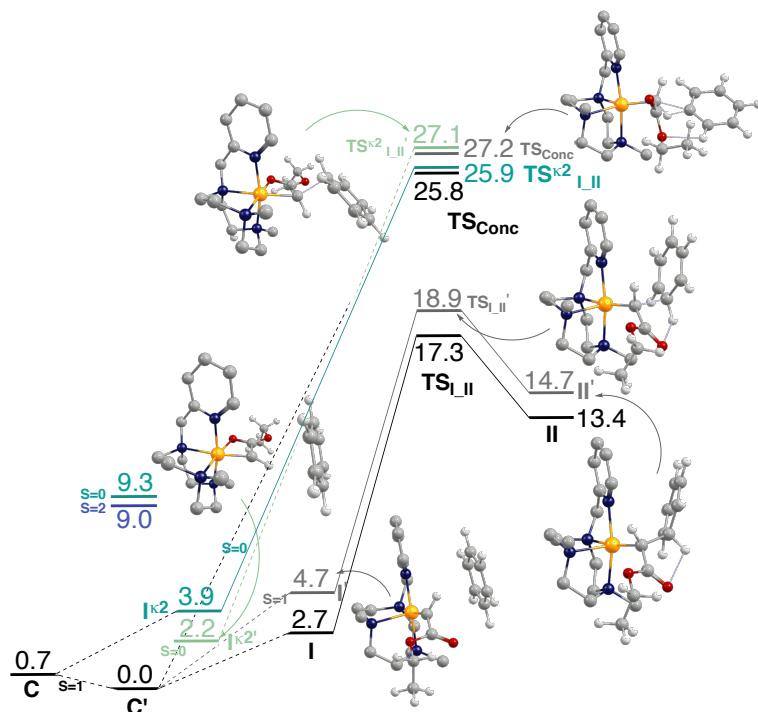


Figure S11: Comparative Gibbs energy profile, ΔG , (kcal·mol⁻¹) of the first step of the concerted and step-wise mechanisms for the reaction between benzene and the iron-carbene for conformers $\text{I}^{\text{k}2}$, $\text{I}^{\text{k}2'}$, I and I' . Pale colors (pale green and grey) are used to represent Gibbs energy profiles for the conformers with higher barriers (i.e. $\text{I}^{\text{k}2'}$ and I'). Black and grey (green and pale green) profiles correspond to triplet (singlet) multiplicities. All the structures presented in the figure correspond to $\text{I}^{\text{k}2'}$ and I' conformers. For C' , the energy value of singlet (green) and quintet (blue) multiplicities are also presented. Hydrogen atoms of the pytaen ligand have been omitted for clarity (C: grey, N: blue, O: red, Fe: yellow, H: white).

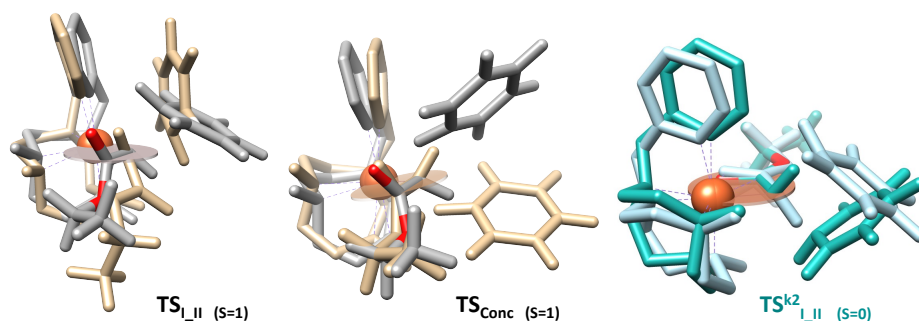


Figure S12: Overlay of $\text{TS}_{\text{I,II}}$ and $\text{TS}_{\text{I,II}'}$ (left), TS_{Conc} and $\text{TS}_{\text{Conc}'}$ (center) and $\text{TS}^{\text{k}2}_{\text{I,II}}$ and $\text{TS}^{\text{k}2}_{\text{I,II}'}$ (right) geometries. The most reactive conformers $\text{TS}_{\text{I,II}}$ and TS_{Conc} ($\text{TS}^{\text{k}2}_{\text{I,II}}$) are depicted in grey (green), while the less reactive conformers $\text{TS}_{\text{I,II}'}$ and $\text{TS}_{\text{Conc}'}$ ($\text{TS}^{\text{k}2}_{\text{I,II}'}$) are depicted in tan (blue) color. The plane formed by Fe, C_{carb} and $\text{C}_{\text{carbonyl}}$ is represented for $\text{TS}_{\text{I,II}}$, TS_{Conc} and $\text{TS}^{\text{k}2}_{\text{I,II}}$.

The sp^2 nature of C_{carb} allows us to define a plane that is formed by C_{carb} , Fe and $\text{C}_{\text{carbonyl}}$. These are the planes represented in Figure S12. The benzene substrate may approach the carbene center from any of the two sides of the plane. This feature has been already reported in previous computational studies about carbene reactivity²⁴ and it has been taken into account in this project in order to ensure a good conformational scope.

If we analyze the structures in Figure S12, we can see that in the transition state geometry the H atom of C_{carb} has come out from the $\text{C}_{\text{carb}}\text{-Fe-C}_{\text{carbonyl}}$ plane, moving away from the benzene substrate. It is also worth noting that in $\text{TS}_{\text{I,II}'}$, the whole carbene moiety reoriented respect to $\text{TS}_{\text{I,II}}$, changing the plane direction (tan color conformer). This can be better seen in Figure S13, where a $\text{Fe-C}_{\text{carb}}\text{-C}_{\text{carbonyl}}$ plane is represented for each conformer. In Figure S13 is easily seen that for $\text{TS}_{\text{I,II}'}$ (tan color) conformer, the benzene substrate approaches the carbene center from below the $\text{Fe-C}_{\text{carb}}\text{-C}_{\text{carbonyl}}$ plane (reddish plane); while in the grey conformer, the benzene substrate approaches the carbene center from above the $\text{Fe-C}_{\text{carb}}\text{-C}_{\text{carbonyl}}$ plane (grey plane).

Grey and green conformers in Figure S12 are the ones that present lower barriers and the ones that have been considered in the main text of the article.

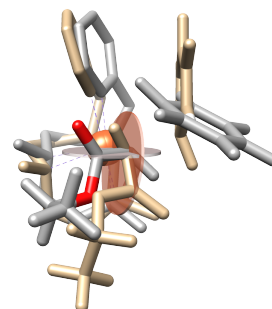


Figure S13: Overlay of the studied conformers for $\text{TS}_{\text{I,II}}$ and $\text{TS}_{\text{I,II}'}$. For each conformer, its $\text{Fe-C}_{\text{carb}}\text{-C}_{\text{carbonyl}}$ plane is represented.

Table S4: Gibbs energy differences, ΔG , of **C**, **C'**, **I** and **I**^{k2} structures (in $\text{kcal}\cdot\text{mol}^{-1}$) in the possible multiplicities.

ΔG ($\text{kcal}\cdot\text{mol}^{-1}$)	C	C'	I ^{k2}	I
Singlet	11.40	9.31	3.93 ^[a]	11.37
Triplet	0.69	0.00 ^[a]	10.17	2.68 ^[a]
Quintet	7.86	8.96	- non minimum -	11.25

^[a] Bold values are the ones that correspond to the lowest energy spin state.

4.1 Triplet-Quintet Spin Splitting for I and TS_{I,II}**Table S5:** Gibbs energy differences (ΔG) and electronic energy differences (ΔE_{elec}) for **I** and **TS_{I,II}** structures using different functionals and approximations, in kcal/mol.^[a]

kcal/mol (\AA^2)	$\Delta G, \text{uB3LYP-GD3B3/SCRF=DCLM}$		$\Delta E_{\text{elec}}, \text{OPT(uB3LYP)-SP(uB3LYP*GD3B3/SCRF=DCLM)}$		$\Delta G, \text{uB3LYP*GD3B3/SCRF=DCLM}$		$\Delta E_{\text{elec}}, \text{OPT(uB3LYP)-SP(uOPBE/SCRF=DCLM)}$		$\Delta G, \text{uOPBE/SCRF=DCLM}$		$\Delta E_{\text{elec}}, \text{OPT(uB3LYP)-SP(uM06L-GD3B3/SCRF=DCLM)}$		$\Delta G, \text{uM06L-GD3B3/SCRF=DCLM}$	
	I	TS _{I,II}	I	TS _{I,II}	I	TS _{I,II}	I	TS _{I,II}	I	TS _{I,II}	I	TS _{I,II}	I	TS _{I,II}
Triplet (S=1)	0.00 (2.586)	17.17 (2.339)	0.00 (2.497)	12.82 (2.346)	0.00 (2.489)	15.59 (2.369)	0.00 (2.398)	10.43 (2.457)	0.00 (2.307)	13.15 (2.464)	0.00 (2.513)	13.15 (2.464)	0.00 (2.507)	13.66 (2.430)
Quintuplet (S=2)	4.37 (6.440)	9.60 (6.131)	5.91 (6.407)	10.53 (6.162)	2.66 (6.467)	8.78 (6.183)	5.07 (6.411)	8.08 (6.306)	-0.88 (6.409)	4.01 (6.348)	-5.26 (6.498)	4.01 (6.348)	-6.81 (6.530)	2.03 (6.415)
$\Delta I, I_{(S=1)} - I_{(S=2)}$	4.37	-7.58	5.91	-2.29	2.66	-6.80	5.07	-2.34	-0.88	-0.88	-5.26	-9.14	-6.81	-11.63
$\Delta \text{TS}_{\text{I,II}} \text{TS}_{\text{I,II}(S=1)} - \text{TS}_{\text{I,II}(S=2)}$														
kcal/mol (\AA^2)	$\Delta E_{\text{elec}}, \text{OPT(uB3LYP)-SP(uBP86-GD3B3/SCRF=DCLM)}$		$\Delta G, \text{OPT(uB3LYP)-GD3B3/SCRF=DCLM}$		$\Delta E_{\text{elec}}, \text{OPT(uB3LYP)-SP(uBLYP-GD3B3/SCRF=DCLM)}$		$\Delta G, \text{uBLYP-GD3B3/SCRF=DCLM}$		$\Delta E_{\text{elec}}, \text{OPT(uB3LYP)-SP(uBPW91/SCRF=DCLM)}$		$\Delta G, \text{uBPW91/SCRF=DCLM}$			
	I	TS _{I,II}	I	TS _{I,II}	I	TS _{I,II}	I	TS _{I,II}	I	TS _{I,II}	I	TS _{I,II}		
Triplet (S=1)	0.00 (2.216)	9.26 (2.278)	0.00 (2.129)	13.41 (2.260)	0.00 (2.507)	15.95 (2.386)	0.00 (2.199)	12.20 (2.258)	0.00 (2.152)	14.80 (2.288)	0.00 (2.194)	21.49 (2.325)		
Quintuplet (S=2)	15.87 (6.302)	19.76 (6.207)	14.89 (6.263)	19.95 (6.234)	1.06 (6.433)	7.61 (6.177)	13.96 (6.284)	19.48 (6.194)	12.34 (6.265)	18.34 (6.267)	12.44 (6.323)	4.27 (6.306)		
$\Delta I, I_{(S=1)} - I_{(S=2)}$	15.87	15.87	14.89	14.89	1.06	1.06	13.96	13.96	12.34	12.34	12.44	4.27		
$\Delta \text{TS}_{\text{I,II}} \text{TS}_{\text{I,II}(S=1)} - \text{TS}_{\text{I,II}(S=2)}$	10.50	10.50	6.54	6.54	-8.33	-8.33	7.27	7.27	3.55	3.55	4.20	-0.38		

^[a] To obtain the Gibbs energy values (ΔG) for I and TS_{I,II} structures, they have been optimized using the corresponding functional.

[#] The shaded column shows the uB3LYP results at the optimization level of theory used in the project (B1 level). Thus, this column presents the data at a level of theory that is comparable to the one used in the main manuscript.

^[a] Calculation performed at the B1 level of theory. Values in brackets are the expected values for the operator S_z^2 . The stability of triplet state over quintet state is shown for I and TS_{I,II} (positive values indicate that triplet state is more stable than the quintet, and vice versa).

% HF exchange included in each functional: **B3LYP**=20%; **B3LYP***=15%; **OPBE**=0%; **M06L**=0%; **BLYP**=0%; **BP86**=0%; **BPW91**=0%.

Several articles have reported B3LYP's problems for the description of first-row-transition-metal – carbon bonds,²⁵ mainly in the Co-C bond of cobalamins.^{18,26-30} These studies are based on the analysis of the homolytic metal-carbon bond dissociation energy (BDE), and, in all of them, it is concluded that hybrid DFT functionals present a poor ability to reproduce the experimental Co-C bond strength. Specifically, when in a hybrid functional the amount of exact exchange increases, the Co-C BDEs decrease leading to values smaller than their experimental counterparts. On the contrary, the experimental absolute BDEs could be correctly reproduced by semilocal (GGA or meta-GGA) density functionals. Among GGA functionals, those that use the gradient-corrected exchange functional Becke88 (B) present better performances, being BP86 the functional that displays the better overall performance.

SUPPORTING INFORMATION SECTION 4.2

In the present study, a good description of the Fe-C bond strength is crucial on the first reaction between the iron-carbene and benzene, **TS_{I,II}**. According to B3LYP results (first column of the upper table), a spin crossing from triplet to quintet spin state takes place in this reaction step. However, the GGA functionals with Becke88 exchange functional suggested by literature to describe this type of metal-carbene bonds (bottom table) do not present the spin crossing from triplet to quintet spin state (e.g. uBP86 and uBLYP). Therefore, taking into account the bibliographic references and the values of Table S5, the spin crossing from triplet to quintet in **TS_{I,II}** is not considered in our study.

Another evidence that also supports a better performance of uBP86 and uBLYP to describe the metal-carbene structure is the spin contamination, which is lower for this two functionals. It is widely accepted that hybrid functionals present higher extent of spin contamination than GGA or meta-GGA functionals when systems cannot be properly described by Hartree-Fock (single-determinant) wave functions.³¹

Finally, we also want to notice that ³TS_{I,II} energy barriers of uBP86 and uBLYP are around 2.4-3.8 kcal·mol⁻¹ lower in energy than the equivalent energy barrier of uB3LYP. Thus, the C_{carb}-C_{bz} bond formation energy barrier of 17.3 kcal·mol⁻¹ obtained in this study could be overestimated.

Table S6: Gibbs energy differences (ΔG) for **I** and **TS_{I,II}** structures using different basis sets, in kcal·mol⁻¹.

kcal/mol (\dot{S}^2)	ΔG , OPT(uB3LYP-B1) -SP(B2: cc-pVTZ/SCRF=mixture)	ΔG , uB3LYP-B1 (6-311+G(d,p))	ΔG , OPT(uB3LYP-B1/6-311+G(d,p)) -SP(cc-pVTZ/SCRF=mixture)	ΔG , uB3LYP-B1 (Def2-SVP)	ΔG , OPT(uB3LYP-B1/Def2-SVP) -SP(cc-pVTZ/SCRF=mixture)
Triplet I	0.00 (2.630)	0.00 (2.576)	0.00 (2.545)	0.00 (2.562)	0.00 (2.524)
(S=1) TS_{I,II}	12.54 (2.103) ^{a)}	14.65 (2.172)	12.13 (2.122)	13.00 (2.176)	11.48 (2.125)

[·] First column corresponds to the level of theory used in the main manuscript.

[·] Values in brackets are the expected values for the \dot{S}^2 operator.

[·] The spin contamination has not been corrected in any case.

^{a)} The difference between this value and the one presented in the paper is due to the correction of spin contamination.

4.2 Electronic structure of ³II

Table S7: Comparison of spin density values of the ³II structure obtained by different functionals.^[a]

Level of theory of ³ II	\dot{S}^2	Mulliken Spin Densities			Mulliken charge of benzyl	Hirshfeld Spin Densities			Hirshfeld charge of benzyl
		Fe	C _{carb}	Benzyl (global)		Fe	C _{carb}	Benzyl (global)	
B3LYP (B2)	3.115	3.1040	-0.2169	-0.9145	+0.1300	2.8959	-0.1222	-0.9038	+0.0987
B3LYP* (B1)	3.079	3.0691	-0.2181	-0.8850	+0.1174				
M06L (B1)	2.971	3.0565	-0.2270	-0.7736	+0.1943				
OPBE (B1)	2.909	2.9571	-0.2022	-0.7358	+0.2028				
BLYP (B1)	2.665	2.5933	-0.1013	-0.5791	+0.3309				
BP86 (B1)	2.645	2.6484	-0.1106	-0.6078	+0.3040				
BPW91 (B1)	2.736	2.6898	-0.1187	-0.6346	+0.2823				

^[a] First row includes the data at the level of theory used in the main manuscript. The other data is obtained by using the uB3LYP/B1 geometry. Besides spin density values, Mulliken charges of benzyl are also reported for all situations.

5. Mechanistic insights in benzene functionalization II. Insertion versus Addition mechanisms

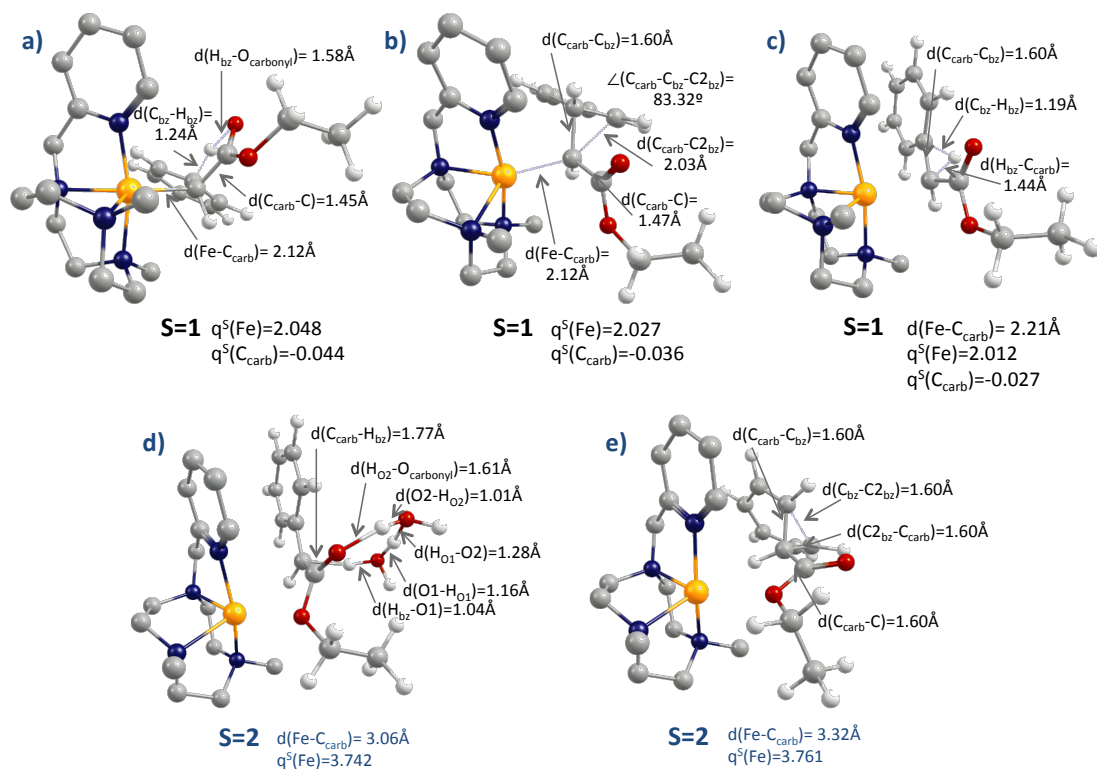


Figure S14: Optimized structures of TS_{II_V} (a), $\text{TS}_{\text{II}_{IV}}$ (b), $\text{TS}_{1,2\text{H-shift}}$ (c), $\text{TS}_{\text{III}_{V(2w)}}$ (d) and $\text{TS}_{\text{IV}_{VI}}$ (e) in the ground spin state and for the lowest energy conformer. The key distances related to the transition state are shown as figures insets. Global spin state, localized spin densities and Fe-C_{carb} distances are shown below the corresponding structure. Hydrogen atoms of the pytacn ligand have been omitted for clarity (C: grey, N: blue, O: red, Fe: yellow, H: white).

Table S8: Comparison between electronic (ΔE_{elec}) and Gibbs free energies (ΔG) for the C-H insertion ($\text{TS}_{\text{II}_{III}}$) and addition ($\text{TS}_{\text{II}_{IV}}$) energy barriers.

	ΔE_{elec} (B2) ($\text{kcal}\cdot\text{mol}^{-1}$)	ΔG (B2) ($\text{kcal}\cdot\text{mol}^{-1}$)
II	0.4	13.4
TS_{II_III}	3.4	14.6
TS_{II_IV}	2.7	16.3
³III	-32.1	-18.6
⁵III	-42.2	-30.7
³IV	-8.7	5.3
⁵IV	-21.9	-9.7

Table S9: Gibbs energy barriers, ΔG , of the enol-ester tautomerism at the $S=2$ spin state (in $\text{kcal}\cdot\text{mol}^{-1}$).

	$\Delta G_{\text{III-TS(III_V)}} (\text{kcal}\cdot\text{mol}^{-1})$
Non-assisted tautomerism	46.6
Assisted by 1 water molecule	23.3
Assisted by 2 water molecules	10.0

Table S10: Absolute and relative Gibbs energy barriers, ΔG , for the formation of insertion and addition products (in $\text{kcal}\cdot\text{mol}^{-1}$).

$(\text{kcal}\cdot\text{mol}^{-1})$	Benzene	D₃-1a^[a]	D₃-1b^[a]
$\Delta G_{\text{insertion}} (\text{TS}_{\text{II_III}}-\text{II})$	1.2	1.1	2.0
$\Delta G_{\text{addition}} (\text{TS}_{\text{II_IV}}-\text{II})$	2.9	2.7	2.8
$\Delta\Delta G_{\text{add.-inser}}$	1.7	1.6	0.8

^[a] Nomenclature in agreement with Scheme 6 of the article.

5.1 Comparison between the chemoselectivity achieved by EDA and 4-Br-phenyldiazoacetate

Table S11: Energy differences between the addition and the insertion transition states, $\text{TS}_{\text{II_IV}}$ and $\text{TS}_{\text{II_III}}$ respectively, obtained using EDA and 4-Br-phenyldiazoacetate as carbene source (in $\text{kcal}\cdot\text{mol}^{-1}$).

	$\Delta\Delta G_{(\text{TS}_{\text{II_IV}}-\text{TS}_{\text{II_III}})}$ (B2) ($\text{kcal}\cdot\text{mol}^{-1}$)	Mulliken charge of $\text{O}_{\text{carbonyl}}$ in ${}^3\text{II}$
EDA	1.7	-0.5221 ^[a]
4-Br-phenyldiazoacetate	1.4	-0.5009

· Low energy differences favor the formation of addition products over insertion products.

^[a] The charge of the $\text{O}_{\text{carbonyl}}$ of the carbene tail correlated with the basicity of the carbonyl group. More negative charge, more basic is the carbonyl.

6. Spin contamination energy correction

All electronic energy values at the B2 level that presented spin-contamination error larger than 10% were corrected using the following expressions (Yamaguchi correction):

$$a = \frac{\langle S_S^2 \rangle - S \cdot (S+1)}{\langle S_{(S+1)}^2 \rangle - S \cdot (S+1)} \quad (\text{Eq. 2})$$

$$E_{spin\ corr} = \frac{E_S - a \cdot E_{(S+1)}}{1 - a} \quad (\text{Eq. 3}),$$

where:

E_S and $\langle S_S^2 \rangle$ are the electronic energy and square total spin angular momentum of the S spin state that presents spin-contamination error (B2 level). $E_{(S+1)}$ and $\langle S_{(S+1)}^2 \rangle$ are the electronic energy and square total spin angular momentum obtained for the (S+1) spin state at the S spin state equilibrium geometry at the same level of theory (B2). And $E_{spin\ corr}$ is the spin corrected electronic energy.

Table S12: Values of the square total spin angular momentum, $\langle S_S^2 \rangle$, the a correction-index (Eq. 2), and $E_{spin\ corr} - E_S$ electronic energy values (ΔE_{elec}), for all the structures presented in this study that show spin-contamination error larger than 10%.^[a]

	$\langle S_S^2 \rangle$	a	ΔE_{elec} ^[b]
A _(S=0)	0.5523	0.273186	0.003
B _(S=0)	0.5791	0.286513	3.72
A _(S=0)	0.6110	0.302460	0.41
C@N₂ _(S=1)	2.5972	0.147268	-2.11
C _(S=1)	2.6863	0.169227	-1.76
TS_{C-Ca} _(S=1)	2.5262	0.129823	-2.36
C_a _(S=1)	2.6204	0.152751	-2.09
TS_{Ca-Cb} _(S=1)	2.5212	0.128425	-2.61
C_b _(S=1)	2.6077	0.149961	-2.40
TS_{Cb-C'} _(S=1)	2.6898	0.170052	-1.81
C _(S=1)	2.5109	0.116270	-2.28
C _(S=0)	0.1904	0.078177	-0.05
I^{k2} _(S=0)	0.6550	0.322184	-4.01
I^{k2'} _(S=0)	0.6687	0.328907	-4.03
TS^{k2}_{I II} _(S=0)	0.6504	0.312182	-2.59
TS^{k2}_{I II} _(S=0)	0.6859	0.331705	-2.56
I _(S=1)	2.6298	0.155311	-2.06
I' _(S=1)	2.5291	0.130333	-2.45
II _(S=1)	3.1146	0.265735	-2.06
II' _(S=1)	2.9127	0.218407	-1.58

^[a] Green and black entries correspond to singlet and triplet multiplicities situations, respectively.

^[b] Negative values of the correction (ΔE_{elec}) indicate that the inclusion of the spin-contamination energy correction stabilizes the structure. Positive energy corrections indicate that the corrected electronic energy of the structure is higher in energy than the spin-contaminated energy, E_S .

7. XYZ coordinates

The Cartesian coordinates of all computed structures are given in a separate text file in a .xyz format that can be directly read by Mercury.

REFERENCES

- (1) Conde, A.; Sabenya, G.; Rodríguez, M.; Postils, V.; Luis, J. M.; Díaz-Requejo, M. M.; Costas, M.; Pérez, P. J. *Angew. Chem.* **2016**, *128*, 6640–6644.
- (2) Frisch, M. J.; Trucks, G. W.; Schlegel, H. B.; Scuseria, G. E.; Robb, M. A.; Cheeseman, J. R.; Scalmani, G.; Barone, V.; Mennucci, B.; Petersson, G. A.; Nakatsuji, H.; Caricato, M.; Li, X.; Hratchian, H. P.; Izmaylov, A. F.; Bloino, J.; Zheng, G.; Sonnenberg, J. L.; Hada, M.; Ehara, M.; Toyota, K.; Fukuda, R.; Hasegawa, J.; Ishida, M.; Nakajima, T.; Honda, Y.; Kitao, O.; Nakai, H.; Vreven, T.; Jr; Peralta, J. E.; Ogliaro, F.; Bearpark, M.; Heyd, J. J.; Brothers, E.; Kudin, K. N.; Staroverov, V. N.; Kobayashi, R.; Normand, J.; Raghavachari, K.; Rendell, A.; Burant, J. C.; Iyengar, S. S.; Tomasi, J.; Cossi, M.; Rega, N.; Millam, J. M.; Klene, M.; Knox, J. E.; Cross, J. B.; Bakken, V.; Adamo, C.; Jaramillo, J.; Gomperts, R.; Stratmann, R. E.; Yazyev, O.; Austin, A. J.; Cammi, R.; Pomelli, C.; Ochterski, J. W.; Martin, R. L.; Morokuma, K.; Zakrzewski, V. G.; Voth, G. A.; Salvador, P.; Dannenberg, J. J.; Dapprich, S.; Daniels, A. D.; Farkas, Foresman, J. B.; Ortiz, J. V.; Cioslowski, J.; Fox, D. J. *Gaussian 09 Revision D.01*; Gaussian Inc. Wallingford CT 2009, 2009.
- (3) Becke, A. J. *Chem. Phys.* **1993**, *98*, 5648–5652.
- (4) Lee, C.; Yang, W.; Parr, R. G. *Phys. Rev. B* **1988**, *37*, 785–789.
- (5) Hariharan, P. C.; Pople, J. A. *Theor. Chim. Acta* **1973**, *28*, 213–222.
- (6) Rassolov, V. A.; Pople, J. A.; Ratner, M. A.; Windus, T. L. *J. Chem. Phys.* **1998**, *109*, 1223.
- (7) Marenich, A. V.; Cramer, C. J.; Truhlar, D. G. *J. Phys. Chem. B* **2009**, *113*, 6378–6396.
- (8) Grimme, S.; Antony, J.; Ehrlich, S.; Krieg, H. *J. Chem. Phys.* **2010**, *132*, 154104.
- (9) Grimme, S.; Ehrlich, S.; Goerigk, L. *J. Comput. Chem.* **2011**, *32*, 1456–1465.
- (10) Dunning, T. H. *J. Chem. Phys.* **1989**, *90*, 1007–1023.
- (11) Balabanov, N. B.; Peterson, K. A. *J. Chem. Phys.* **2005**, *123*, 64107.
- (12) Yamaguchi, K.; Jensen, F.; Dorigo, A.; Houk, K. N. *Chem. Phys. Lett.* **1988**, *149*, 537–542.
- (13) Wittbrodt, J. M.; Schlegel, H. B. *J. Chem. Phys.* **1996**, *105*, 6574–6577.
- (14) Glendening, E. D.; Badenhop, J. K.; Reed, A. E.; Carpenter, J. E.; Bohmann, J. A.; Morales, C. M.; Landis, C. R.; Weinhold, F. Theoretical Chemistry Institute, University of Wisconsin, Madison. NBO 6.0, 2013.
- (15) Salvador, P.; Ramos-Cordoba, E. Program APOST-3D, 2014.
- (16) Johnson, E. R.; Keinan, S.; Mori-Sánchez, P.; Contreras-García, J.; Cohen, A. J.; Yang, W. *J. Am. Chem. Soc.* **2010**, *132*, 6498–6506.
- (17) Contreras-García, J.; Johnson, E. R.; Keinan, S.; Chaudret, R.; Piquemal, J.-P.; Beratan, D. N.; Yang, W. *J. Chem. Theory Comput.* **2011**, *7*, 625–632.
- (18) Dzik, W. I.; Xu, X.; Zhang, X. P.; Reek, J. N. H.; de Bruin, B. *J. Am. Chem. Soc.* **2010**, *132*, 10891–10902.
- (19) Das, B. G.; Chirila, A.; Tromp, M.; Reek, J. N. H.; Bruin, B. de. *J. Am. Chem. Soc.* **2016**, *138*, 8968–8975.
- (20) Sharon, D. A.; Mallick, D.; Wang, B.; Shaik, S. *J. Am. Chem. Soc.* **2016**, *138*, 9597–9610.
- (21) Weinhold, F.; Landis, C. R. *Valency and bonding: a natural bond orbital donor-acceptor perspective*; Cambridge University Press: Cambridge, U.K., 2005.
- (22) Ramos-Cordoba, E.; Postils, V.; Salvador, P. *J. Chem. Theory Comput.* **2015**, *11*, 1501–1508.
- (23) Skara, G.; Gimferrer, M.; De Proft, F.; Salvador, P.; Pinter, B. *Inorg. Chem.* **2016**, *55*, 2185–2199.
- (24) Braga, A. A. C.; Maseras, F.; Urbano, J.; Caballero, A.; Díaz-Requejo, M. M.; Pérez, P. J. *Organometallics* **2006**, *25*, 5292–5300.
- (25) Jensen, K. P.; Ryde, U. *J. Phys. Chem. A* **2003**, *107*, 7539–7545.
- (26) Kuta, J.; Patchkovskii, S.; Zgierski, M. Z.; Kozłowski, P. M. *J. Comput. Chem.* **2006**, *27*, 1429–1437.
- (27) Kobylanski, I. J.; Widner, F. J.; Krätzler, B.; Chen, P. *J. Am. Chem. Soc.* **2013**, *135*, 13648–13651.
- (28) Qu, Z.; Hansen, A.; Grimme, S. *J. Chem. Theory Comput.* **2015**, *11*, 1037–1045.
- (29) Qi, X.-J.; Li, Z.; Fu, Y.; Guo, Q.-X.; Liu, L. *Organometallics* **2008**, *27*, 2688–2698.
- (30) Hirao, H. *J. Phys. Chem. A* **2011**, *115*, 9308–9313.
- (31) Menon, A. S.; Radom, L. *J. Phys. Chem. A* **2008**, *112*, 13225–13230.
- (32) a) Company, A.; Gómez, L.; Güell, M.; Ribas, X.; Luis, J. M.; Que Jr., L.; Costas, M. *J. Am. Chem. Soc.* **2007**, *129*, 15766–15767; b) Garcia-Bosch, I.; Company, A.; Fontrodona, X.; Ribas, X.; Costas, M. *Org. Lett.* **2008**, *10*, 2095–2098.
- (33) Hu, M.; Rong, J.; Miao, W.; Ni, C.; Han, Y.; Hu, J. *Org. Lett.* **2014**, *16*, 2030–2033.
- (34) McKervey, M. A.; Russell, D. N.; Twohig, M. F. *J. Chem. Soc., Chem. Commun.* **1985**, 491–492.

Supporting Information Chapter 6

Supporting Information

On the existence and characterization of molecular electrides

Verònica Postils, Marc Garcia-Borràs, Miquel Solà, Josep M. Luis and Eduard Matito**

* Institut de Química Computacional i Catàlisi (IQCC), Univ. Girona, Campus de Montilivi s/n, Girona, Spain. Tel: +34 972 418 357; E-mail: *josepm.luis@udg.edu; ematito@gmail.com*.

Contents

COMPUTATIONAL DETAILS	S1
TCNQLi₂	S2
TCNQNa₂	S3
Li@calix[4]pyrrole	S4
Li···NCH	S5
Li···HCN	S6
Li@B₁₀H₁₄	S7
e-@C₆₀F₆₀	S8
LINEAR AND NONLINEAR OPTICAL PROPERTIES	S9
IONIZATION POTENTIALS	S9
REFERENCES	S10

Computational Details

Geometry optimization

All geometry and single-point calculations have been performed using the Gaussian09 suite of programs.¹ Geometry optimizations employed the density functional theory (DFT) Becke's three-parameter nonlocal exchange and Lee-Yang-Parr 1988 nonlocal correlation functional (B3LYP)² functional and 6-31+G(d) basis set.³ In order to ensure an accurate account of the molecular geometry, cutoffs on forces and the stepsize have been tightened;^a to improve the description of the wavefunction, the self-consistent field (SCF) convergence has also been tightened to $1 \cdot 10^{-9}$ a.u., and the grid to compute two-electron integrals and their derivatives has been augmented.^b These thresholds were applied to all systems excepting for e-@C₆₀F₆₀, whose geometry was taken from Ref. 4 and the thresholds of convergence for the SCF procedure were not tightened due to its prominent molecular size. However, the accuracy of this calculation was assessed by other means (*vide infra*).

Topological analysis and characterization of electrides

The topological quantum theory of atoms in molecules (QTAIM),⁵ electron localization function (ELF)⁶ and Laplacian of the electron density⁵ analyses were repeated at the same geometry for all the molecules but e-@C₆₀F₆₀ using aug-cc-pVDZ Dunning basis set⁷ in order to corroborate the results found. In addition, for TCNQLi₂ and TCNQNa₂ molecules additional computations at higher ab initio levels (namely, CISD and MP2 calculations in conjunction with the aug-cc-pVDZ basis set) were performed. In all cases, the qualitative results remained the same.

QTAIM and Laplacian calculations used the AIMPACK⁸ and AIMAll⁹ packages and the ToPMoD¹⁰ Package developed by Bernard Silvi and coworkers was used to compute the values of the ELF. In addition, the calculation of the electron delocalization and localization¹¹ indices was done using the results from the previous programs and the *Electron Sharing Indices Program for 3D Molecular Space Partition (ESI-3D)* developed in our group.¹²

The single-point calculation of the e-@C₆₀F₆₀ species was done using the basis of Simon et al. (used originally for the geometry optimization) that employed four s and four p functions placed in the center of the cage. In order to rule out the possibility of a basis set artifact, we performed an additional calculation using basis sets not explicitly located in the center of the structure. Namely, we placed sixty groups of three sp functions at 2.6 Å of the center of the cage, mimicking a smaller C₆₀ structure encapsulated in the cage. Both analyses of the QTAIM structure provided a NNA in the center of the cage, as well as similar pictures of ELF and the Laplacian, thus confirming the validity of the methodology employed in Ref. 4.

In the following pages we collect the full topological analyses performed in this communication.

^a We used the *verytight* option in G09 package that sets the following convergence thresholds: $1 \cdot 10^{-6}$ and $4 \cdot 10^{-6}$ a.u. for force's root mean square (RMS) and displacement's RMS values, respectively.

^b We used the *ultrafine* option in G09 package that sets a (99, 590) *pruned* grid.

TCNQLi₂

Figure S1. [top left] Topological analysis of the electron density including: the atomic positions (see labeled atoms), the bond (BCP) and ring (RCP) critical points (small spheres in grey), and the non-nuclear attractor (NNA; in red). [top right] ELF=0.75 isosurface picture indicating atomic core basins (small red spheres), valence basins (light grey) and the relevant basins for the present study (marked in green tone). [bottom] $\nabla^2\rho=-0.001$ isosurface values.

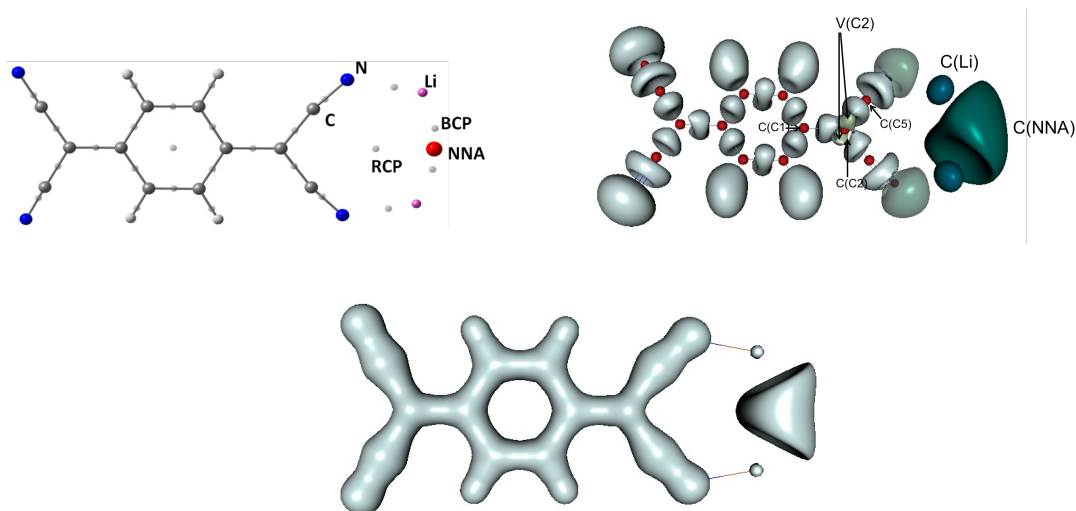


Table S1a. QTAIM and Laplacian analyses, including the distance of the lithium atoms to the NNA, ($|\vec{r}_{(NNA-Li)}|$), the values of the density ($\rho(\Omega)$) and the Laplacian of the electron density ($\nabla^2\rho$) at the Ω position, electron population of Ω ($N(\Omega)$), localization (LI) and delocalization (δ) indices and percentage of electron localization (%LI) from the total electron population. Atomic units employed.

TCNQLi ₂	Ω	$ \vec{r}_{(NNA-Li)} $	$\rho(\Omega)$	$\nabla^2\rho$	$N(\Omega)$	LI	%LI	$\delta(\text{Li},\text{NNA})$	$\delta(\text{N},\text{NNA})$
B3LYP	NNA	3.083	$9.41\cdot 10^{-3}$	$-7.37\cdot 10^{-3}$	0.52	0.28	51	0.20	0.05
	Li		$1.31\cdot 10^{+1}$	$-1.70\cdot 10^{+4}$	2.23	2.02	91		
UMP2	NNA	3.117	$9.75\cdot 10^{-3}$	$-7.87\cdot 10^{-3}$	0.70	0.46	67	0.16	0.06
	Li		$1.32\cdot 10^{+1}$	$-1.70\cdot 10^{+4}$	2.16	2.00	93		
CISD	NNA	3.147	$9.51\cdot 10^{-3}$	$-7.60\cdot 10^{-3}$	0.71	0.49	69		
	Li		$1.31\cdot 10^{+1}$	$-1.70\cdot 10^{+4}$	2.15	2.00	93		

Table S1b. Analysis of the ELF basins, Ω , including the electron population, $N(\Omega)$, the variance of the electron population, $\sigma^2(\Omega)$, the percentage of the basin's fluctuation, $\% \lambda_{\text{f}}(\Omega)$, and the contribution analysis of each ELF basin to the covariance with other ELF basins. Atomic units employed.

Ω	$N(\Omega)$	$\sigma^2(\Omega)$	$\% \lambda_{\text{f}}(\Omega)$	Contribution Analysis ($\geq 10\%$)
C(NNA)	0.92	0.20	22	C(Li) (18%), V(N, Li) (18%)
C(Li)	2.02	0.08	4	V(N, Li) (50%), C(NNA) (50%)
V(C2)	0.45	0.38	84	V(C5, C2) (24%), V(C1, C2) (21%)

TCNQNa₂

Figure S2. [top left] Topological analysis of the electron density including: the atomic positions (see labeled atoms), the bond (BCP) and ring (RCP) critical points (small spheres in grey), and the non-nuclear attractor (NNA; in red). [top right] ELF=0.75 isosurface picture indicating atomic core basins (small red spheres), valence basins (light grey) and the relevant basins for the present study (marked in green tone). [bottom] $\nabla^2\rho=-0.001$ isosurface values.

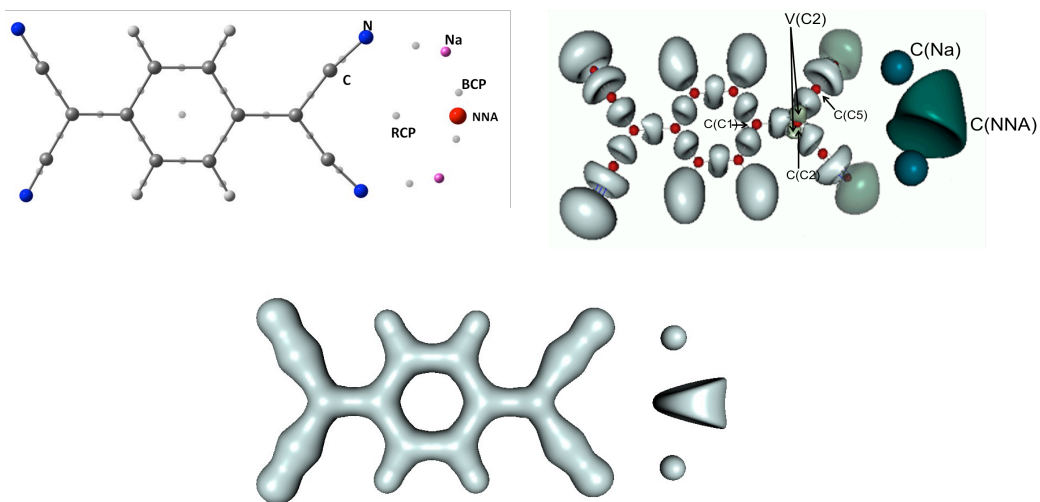


Table S2a. QTAIM and Laplacian analyses, including the distance of the sodium atoms to the NNA, ($|\vec{r}_{(NNA-Li)}|$), the values of the density ($\rho(\Omega)$) and the Laplacian of the electron density ($\nabla^2\rho$) at the Ω position, electron population of Ω ($N(\Omega)$), localization (LI) and delocalization (δ) indices and percentage of electron localization (%LI) from the total electron population. Atomic units employed.

TCNQNa ₂	Ω	$ \vec{r}_{(NNA-Li)} $	$\rho(\Omega)$	$\nabla^2\rho$	$N(\Omega)$	LI	%LI	$\delta(Li,NNA)$	$\delta(N,NNA)$
B3LYP	NNA	3.525	$6.14 \cdot 10^{-3}$	$-3.67 \cdot 10^{-3}$	0.23	0.05	22	0.16	0.02
	Na		$8.04 \cdot 10^{+2}$	$-1.78 \cdot 10^{+7}$	10.39	10.10	97		
UMP2	NNA	3.429	$6.70 \cdot 10^{-3}$	$-4.50 \cdot 10^{-3}$	0.44	0.19	43	0.22	0.02
	Na		$8.04 \cdot 10^{+2}$	$-1.78 \cdot 10^{+7}$	10.29	10.05	98		

Table S2b. Analysis of the ELF basins, Ω , including the electron population, $N(\Omega)$, the variance of the electron population, $\sigma^2(\Omega)$, the percentage of the basin's fluctuation, $\% \lambda_f(\Omega)$, and the contribution analysis of each ELF basin to the covariance with other ELF basins. Atomic units employed.

Ω	$N(\Omega)$	$\sigma^2(\Omega)$	$\% \lambda_f(\Omega)$	Contribution Analysis ($\geq 10\%$)
C(NNA)	0.89	0.26	29	C(Na) (33%)
C(Na)	10.03	0.14	1	V(N,Na) (33%), C(NNA) (67%)
V(C2)	0.44	0.38	86	V(C5,C2) (24%), V(C1,C2) (21%)

Li@calix[4]pyrrole

Figure S3. [top left] Topological analysis of the electron density including: the atomic positions (see labeled atoms), the bond (BCP) and ring (RCP) critical points (small spheres in grey), the cage critical points (small spheres in yellow) and the non-nuclear attractor (NNA; in red). [top right] ELF=0.75 isosurface picture indicating atomic core basins (small red spheres), valence basins (light grey) and the relevant basins for the present study (marked in green tone). [bottom] $\nabla^2\rho=-0.001$ isosurface values.

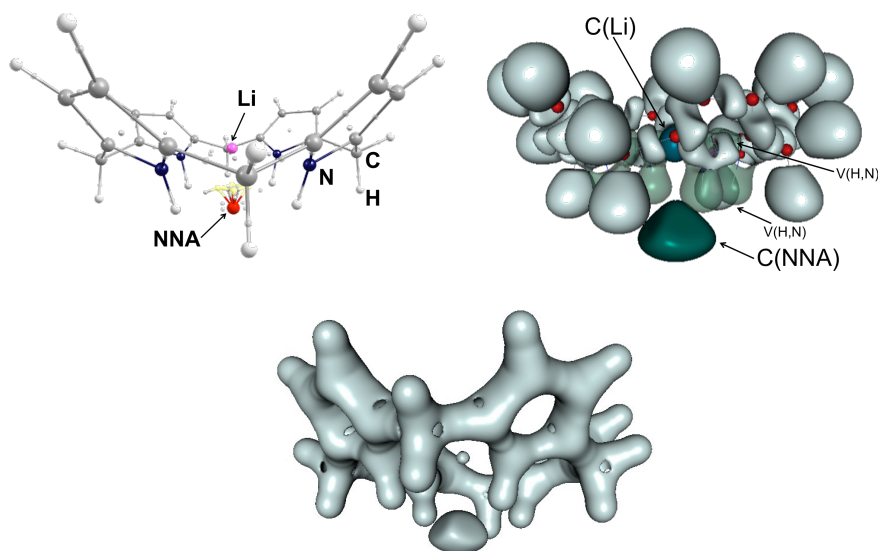


Table S3a. QTAIM and Laplacian analyses, including the distance of the lithium atom to the NNA, ($|\vec{r}_{(NNA-Li)}|$), the values of the density ($\rho(\Omega)$) and the Laplacian of the electron density ($\nabla^2\rho$) at the Ω position, electron population of Ω ($N(\Omega)$), localization (LI) and delocalization (δ) indices and percentage of electron localization (%LI) from the total electron population. Atomic units employed.

Li@calix[4]pyrrole (Ω)	$ \vec{r}_{(NNA-Li)} $	$\rho(\Omega)$	$\nabla^2\rho$	$N(\Omega)$	LI	%LI	$\delta(\text{Li},\text{NNA})$	$\delta(\text{N},\text{NNA})$
NNA		$5.61 \cdot 10^{-3}$	$-3.67 \cdot 10^{-3}$	0.15	0.02	13	0.004	0.01
Li	2.998	$1.31 \cdot 10^{+1}$	$-1.78 \cdot 10^{+7}$	2.11	1.98	94		

Table S3b. Analysis of the ELF basins, Ω , including the electron population, $N(\Omega)$, the variance of the electron population, $\sigma^2(\Omega)$, the percentage of the basin's fluctuation, $\% \lambda_f(\Omega)$, and the contribution analysis of each ELF basin to the covariance with other ELF basins. Atomic units employed.

Ω	$N(\Omega)$	$\sigma^2(\Omega)$	$\% \lambda_f(\Omega)$	Contribution Analysis ($\geq 10\%$)
C(NNA)	0.63	0.34	54	V(H,N) (17%)
C(Li)	2.03	0.08	4	V(N, Li) (20%), C(NNA) (20%)

Li...NCH

Figure S4. [top left] Topological analysis of the electron density including: the atomic positions (see labeled atoms) and the bond (BCP) critical points (small spheres in grey). [top right] ELF=0.75 isosurface picture indicating atomic core basins (small red spheres), valence basins (light grey) and the relevant basins for the present study (marked in green tone). [bottom] $\nabla^2\rho=-0.001$ isosurface values.

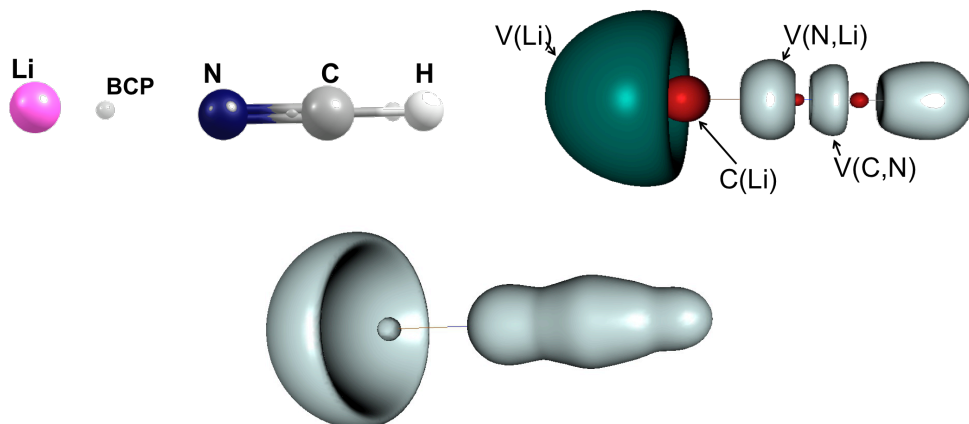


Table S4a. Analysis of the ELF basins, Ω , including the electron population, $N(\Omega)$, the variance of the electron population, $\sigma^2(\Omega)$, the percentage of the basin's fluctuation, $\% \lambda_f(\Omega)$, and the contribution analysis of each ELF basin to the covariance with other ELF basins. Atomic units employed.

Ω	$N(\Omega)$	$\sigma^2(\Omega)$	$\% \lambda_f(\Omega)$	Contribution Analysis ($\geq 10\%$)
V(Li)	0.91	0.16	18	V(N,Li) (46%), C(Li) (38%), V(C,N) (15%)
C(Li)	2.02	0.08	4	V(N, Li) (37%), V(Li) (62%)

Li...HCN

Figure S5. [top left] Topological analysis of the electron density including: the atomic positions (see labeled atoms) and the bond (BCP) critical points (small spheres in grey). [top right] ELF=0.75 isosurface picture indicating atomic core basins (small red spheres), valence basins (light grey) and the relevant basins for the present study (marked in green tone). [bottom] $\nabla^2\rho=-0.002$ isosurface values.

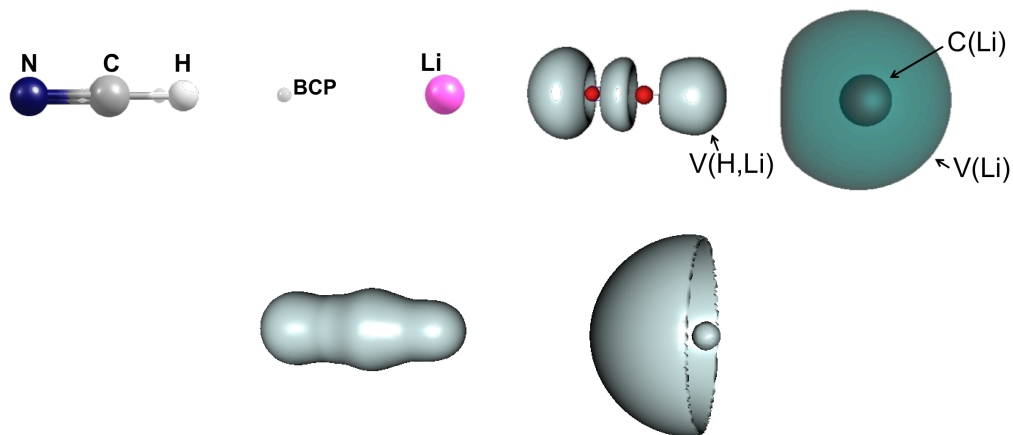


Table S5a. Analysis of the ELF basins, Ω , including the electron population, $N(\Omega)$, the variance of the electron population, $\sigma^2(\Omega)$, the percentage of the basin's fluctuation, $\% \lambda_f(\Omega)$, and the contribution analysis of each ELF basin to the covariance with other ELF basins. Atomic units employed.

Ω	$N(\Omega)$	$\sigma^2(\Omega)$	$\% \lambda_f(\Omega)$	Contribution Analysis ($\geq 10\%$)
V(Li)	0.95	0.11	12	C(Li) (75%), V(H,C) (25%)
C(Li)	2.01	0.06	3	V(Li) (98%)

Li@B₁₀H₁₄

Figure S6. [top left] Topological analysis of the electron density including: the atomic positions (see labeled atoms), the bond (BCP) and ring (RCP) critical points (small spheres in grey) and the cage critical points (small spheres in yellow). [top right] $\nabla^2\rho=-0.001$ isosurface values. [bottom] ELF=0.75 isosurface picture (left) and ELF=0.20 isosurface picture (center) indicating atomic core basins (small red spheres), valence basins (light grey) and the relevant basins for the present study (marked in green tone). (right) 2D contour plot of the ELF function.

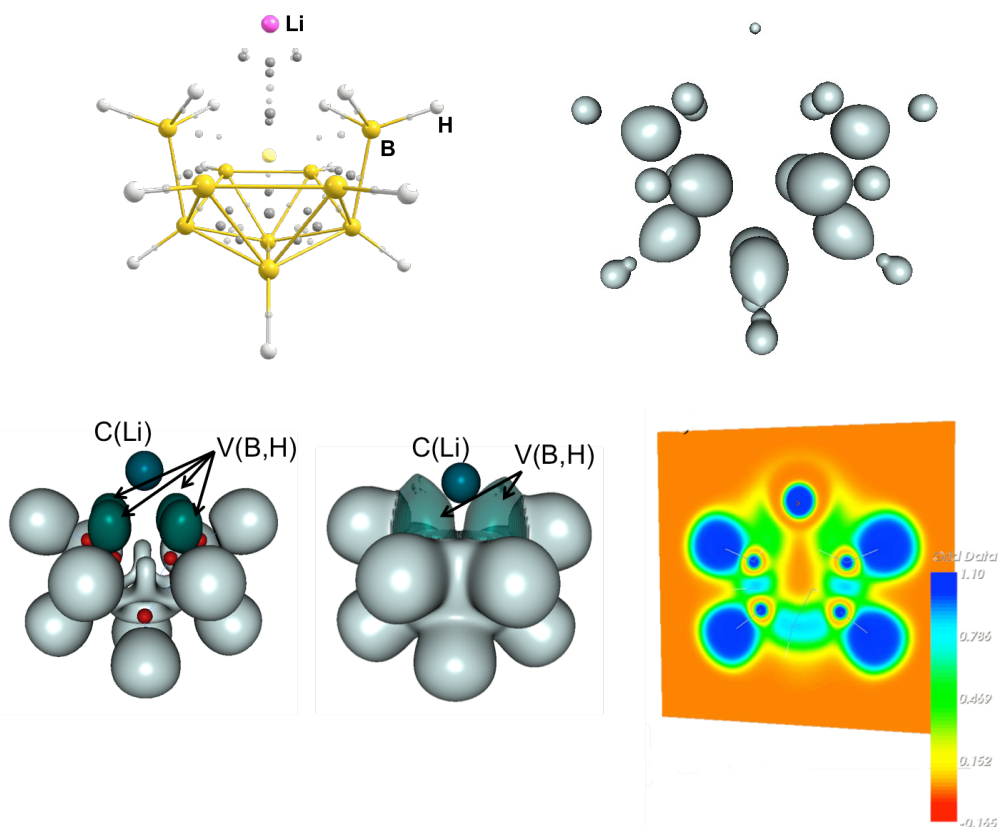


Table S6a. Analysis of the ELF basins, Ω , including the electron population, $N(\Omega)$, the variance of the electron population, $\sigma^2(\Omega)$, the percentage of the basin's fluctuation, $\% \lambda_r(\Omega)$, and the contribution analysis of each ELF basin to the covariance with other ELF basins. Atomic units employed.

Ω	$N(\Omega)$	$\sigma^2(\Omega)$	$\% \lambda_r(\Omega)$	Contribution Analysis ($\geq 10\%$)
C(Li)	2.02	0.06	3	V(B,H) (25%) each
V(B,H)	2.04	0.84	41	V(B,H) (14%), others not relevant

e-@B₁₀H₁₄

Figures S7. [top left] Topological analysis of the electron density including: the atomic positions (see labeled atoms), the bond (BCP) and ring (RCP) critical points (small spheres in grey), the cage critical points (small spheres in yellow) and the non-nuclear attractor (NNA; in red). [top right] ELF=0.75 isosurface picture indicating valence basins (light grey) and the isolated-electron of the electride basin (marked in green). [bottom] $\nabla^2\rho=-0.001$ isosurface values.

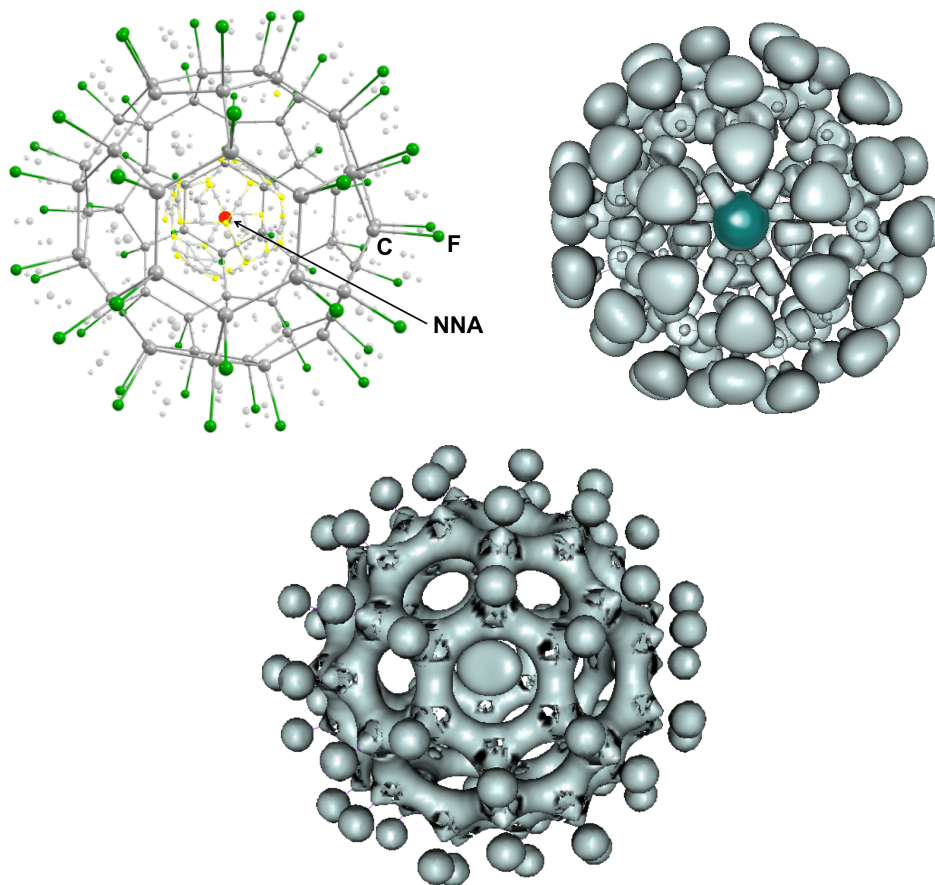


Table S7a. QTAIM and Laplacian analyses for the e-@C₆₀F₆₀ including: the values of the density ($\rho(\Omega)$) and the Laplacian of the electron density ($\nabla^2\rho$) at the Ω position, electron population of Ω ($N(\Omega)$), the localization (LI) index and the percentage of electron localization (%LI) from the total electron population. Atomic units employed.

e-@C ₆₀ F ₆₀ (Ω)	$\rho(\Omega)$	$\nabla^2\rho$	$N(\Omega)$	LI	%LI
NNA	$1.74 \cdot 10^{-3}$	$-2.63 \cdot 10^{-4}$	0.19	0.03	18

Linear and Nonlinear Optical Properties

Table S8. Electronic contribution to linear and nonlinear optical properties (NLOP) for the molecules studied in this communication. ^aData from Ref. 13. ^bData from Ref. 4. ^cData from Ref. 14. ^dValues computed at the UB3LYP/aug-cc-pVDZ level of theory.

properties	TCNQLi ₂ ^a	TCNQNa ₂ ^a	Li@Calix ^a	Li@B ₁₀ H ₁₄ ^a	Li⋯HCN ^c	HCN⋯Li ^c	Li ₂ (S=0)	Li ₂ (S=0)
$\alpha_{zz}(0;0)$					212.6	158.2	263.2	583.0
$\tilde{\alpha}(0;0)$	371.9	389.7	381.6	150.3	181.9	239.1	198.5	340.0
$\beta_{zzz}(0;0,0)$					-2791	-3640		
$\gamma_{zzzz}(0;0,0,0)$							1.2·10 ⁶	9.2·10 ⁵
$\gamma_{ }(0;0,0,0)$	1.4·10 ⁶	1.3·10 ⁶	4.8·10 ⁶	4.8·10 ⁵				

Ionization Potentials

Table S9. Ionization Potentials for the molecules studied in this work computed at the B3LYP/aug-cc-pVDZ level of theory. ^aComputed at the level of theory of Ref. 4.

molecule	PI (eV)
TCNQLi ₂	(S=1 → S=1/2) 6.32
	(S=1 → S=3/2) 7.80
TCNQNa ₂	(S=1 → S=1/2) 6.11
	(S=1 → S=3/2) 7.47
Li@Calix	(S=1/2 → S=0) 3.82
Li@B ₁₀ H ₁₄	(S=1/2 → S=0) 6.39
e-@C ₆₀ F ₆₀ ^a	(S=1/2 → S=0) 3.99
Li⋯HCN	(S=1/2 → S=0) 5.98
HCN⋯Li	(S=1/2 → S=0) 4.35

References

- [1.] M. J. FRISCH, G. W. TRUCKS, H. B. SCHLEGEL, G. E. SCUSERIA, M. A. ROBB, J. R. CHEESEMAN, G. SCALMANI, V. BARONE, B. MENNUCCI, G. A. PETERSSON, H. NAKATSUJI, M. CARICATO, X. LI, H. P. HRATCHIAN, A. F. IZMAYLOV, J. BLOINO, G. ZHENG, J. L. SONNENBERG, M. HADA, M. EHARA, K. TOYOTA, R. FUKUDA, J. HASEGAWA, M. ISHIDA, T. NAKAJIMA, Y. HONDA, O. KI-TAO, H. NAKAI, T. VREVEN, J. A. MONTGOMERY, JR., J. E. PERALTA, F. OGLIARO, M. BEARPARK, J. J. HEYD, E. BROTHERS, K. N. KUDIN, V. N. STAROVEROV, R. KOBAYASHI, J. NORMAND, K. RAGHAVACHARI, A. RENDELL, J. C. BURANT, S. S. IYENGAR, J. TOMASI, M. COSSI, N. REGA, J. M. MILLAM, M. KLENE, J. E. KNOX, J. B. CROSS, V. BAKKEN, C. ADAMO, J. JARAMILLO, R. GOMPERTS, R. E. STRATMANN, O. YAZYEV, A. J. AUSTIN, R. CAMMI, C. POMELLI, J. W. OCHTERSKI, R. L. MARTIN, K. MOROKUMA, V. G. ZAKRZEWSKI, G. A. VOTH, P. SALVADOR, J. J. DANNENBERG, S. DAPPRICH, A. D. DANIELS, Å. FARKAS, J. B. FORESMAN, J. V. ORTIZ, J. CIOSŁOWSKI, and D. J. FOX, Gaussian 09 Revision A.1, Gaussian Inc. Wallingford CT 2009.
- [2.] A. D. BECKE, *J. Chem. Phys.* **98**, 5648 (1993).
- [3.] R. DITCHFIELD, W. J. HEHRE, and J. A. POPLÉ, *J. Chem. Phys.* **54**, 724 (1971). ; W. J. HEHRE, R. DITCHFIELD, and J. A. POPLÉ, *J. Chem. Phys.* **56**, 2257 (1972). ; P. C. HARIHARAN and J. A. POPLÉ, *Theor. Chim. Acta (Berlin)* **28**, 213 (1973). ; M. M. FRANCL, W. J. PIETRO, W. J. HEHRE, J. S. BINKLEY, M. S. GORDON, D. J. DEFREES, and J. A. POPLÉ, *J. Chem. Phys.* **77**, 3654 (1982).
- [4.] Y.-F. WANG, Z.-R. LI, D. WU, C.-C. SUN, and F.-L. GU, *J. Comput. Chem.* **31**, 195 (2010).
- [5.] R. F. W. BADER and T. T. NGUYEN-DANG, Quantum Theory of Atoms in Molecules –Dalton Revisited, in *Advances in Quantum Chemistry*, volume 14, pp. 63–124, Academic Press, New York, 1981.
- [6.] A. D. BECKE and K. E. EDGECOMBE, *J. Chem. Phys.* **92**, 5397 (1990).
- [7.] R. A. KENDALL, T. H. DUNNING JR, and R. J. HARRISON, *J. Chem. Phys.* **96**, 6796 (1992).
- [8.] F. W. BIEGLER-KONIG, T. T. NGUYEN-DANG, Y. TAL, and R. F. W. BADER, *J. Phys. B: Atom. Molec. Phys.* **14**, 2739 (1981). ; F. W. BIEGLER-KÖNIG, R. F. BADER, and T.-H. TANG, *J. Comput. Chem.* **3**, 317 (1982).
- [9.] T. A. KEITH, AIMall (Version 14.11.23), 2014, TK Gristmill Software, Overland Park KS, USA (aim.tkgristmill.com).
- [10.] S. NOURY, X. KROKIDIS, F. FUSTER, and B. SILVI, TopMoD package, 1997.
- [11.] E. MATITO and M. SOLÀ, *Coord. Chem. Rev.* **253**, 647 (2009); E. MATITO, M. DURAN, and M. SOLÀ, *J. Chem. Phys.* **122**, 014109 (2005); E. MATITO, M. SOLÀ, P. SALVADOR, and M. DURAN, *Faraday Discuss.* **135**, 325 (2007); F. FEIXAS, E. MATITO, M. DURAN, M. SOLÀ, and B. SILVI, *J. Chem. Theory Comput.* **6**, 2736 (2010).
- [12.] E. MATITO, ESI-3D: Electron Sharing Indices Program for 3D Molecular Space Partitioning; Institute of Computational chemistry and Catalysis, University of Girona, Catalonia, Spain, 2006.
- [13.] M. GARCIA-BORRÀS, M. SOLÀ, J. M. LUIS, and B. KIRTMAN, *J. Chem. Theory Comput.* **8**, 2688 (2012).
- [14.] W. CHEN, Z.-R. LI, D. WU, R.-Y. LI, and C.-C. SUN, *J. Phys. Chem. B* **109**, 601 (2005).